UNIVERSIDADE FEDERAL DO PARANÁ

GUSTAVO SCHEID PRASS

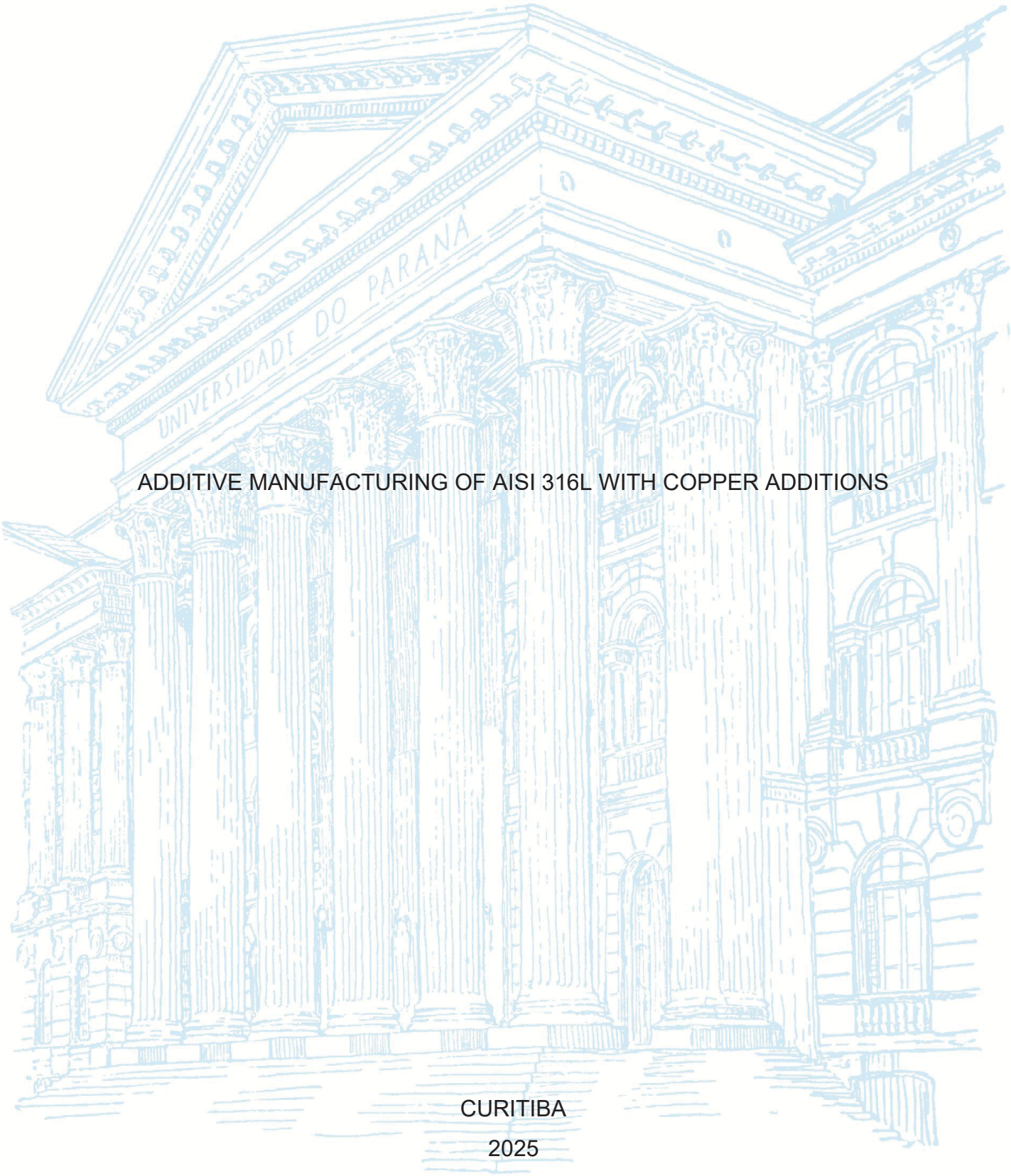

ADDITIVE MANUFACTURING OF AISI 316L WITH COPPER ADDITIONS

CURITIBA

2025

GUSTAVO SCHEID PRASS

ADDITIVE MANUFACTURING OF AISI 316L WITH COPPER ADDITIONS

Tese de doutorado apresentada ao Programa de Pós-Graduação em Engenharia e Ciências dos Materiais (PIPE) do Setor de Tecnologia da Universidade Federal do Paraná (UFPR), como requisito parcial à obtenção do título de Doutor em Engenharia e Ciência dos Materiais.

Orientadora: Profa. Ana Sofia C.M. d'Oliveira, PhD.

Supervisor do doutorado sanduíche: Prof. Moataz M. Attallah, PhD.

CURITIBA

2025

DADOS INTERNACIONAIS DE CATALOGAÇÃO NA PUBLICAÇÃO (CIP)
UNIVERSIDADE FEDERAL DO PARANÁ
SISTEMA DE BIBLIOTECAS – BIBLIOTECA DE CIÊNCIA E TECNOLOGIA

Prass, Gustavo Scheid
Additive manufacturing of AISI 316L with copper additions / Gustavo Scheid Prass. – Curitiba, 2025.
1 recurso on-line : PDF.

Tese (Doutorado) - Universidade Federal do Paraná, Setor de Tecnologia, Programa de Pós-Graduação em Engenharia e Ciências dos Materiais.

Orientador: Ana Sofia Clímaco Monteiro de Oliveira
Coorientador: Moataz M. Attallah

1. Processos de fabricação. 2. Aço inoxidável. 3. Nanopartículas. I. Universidade Federal do Paraná. II. Programa de Pós-Graduação em Engenharia e Ciências dos Materiais. III. Oliveira, Ana Sofia Clímaco Monteiro de. IV. Attallah, Moataz M.. V. Título.

Bibliotecário: Douglas Lenon da Silva CRB-9/1892

MINISTÉRIO DA EDUCAÇÃO
SETOR DE TECNOLOGIA
UNIVERSIDADE FEDERAL DO PARANÁ
PRÓ-REITORIA DE PÓS-GRADUAÇÃO
PROGRAMA DE PÓS-GRADUAÇÃO ENGENHARIA E CIÊNCIA DOS MATERIAIS - 40001016033P9

TERMO DE APROVAÇÃO

Os membros da Banca Examinadora designada pelo Colegiado do Programa de Pós-Graduação ENGENHARIA E CIÊNCIA DOS MATERIAIS da Universidade Federal do Paraná foram convocados para realizar a arguição da tese de Doutorado de **GUSTAVO SCHEID PRASS**, intitulada: **ADDITIVE MANUFACTURING OF AISI 316L WITH COPPER ADDITIONS**, sob orientação da Profa. Dra. ANA SOFIA CLÍMACO MONTEIRO DE OLIVEIRA, que após terem inquirido o aluno e realizada a avaliação do trabalho, são de parecer pela sua APROVAÇÃO no rito de defesa.

A outorga do título de doutor está sujeita à homologação pelo colegiado, ao atendimento de todas as indicações e correções solicitadas pela banca e ao pleno atendimento das demandas regimentais do Programa de Pós-Graduação.

CURITIBA, 06 de Agosto de 2025.

Assinatura Eletrônica
11/08/2025 12:02:21.0
ANA SOFIA CLÍMACO MONTEIRO DE OLIVEIRA
Presidente da Banca Examinadora

Assinatura Eletrônica
11/08/2025 23:35:37.0
OSVALDO MITSUYUKI CINTHO
Avaliador Externo (UNIVERSIDADE ESTADUAL DE PONTA GROSSA)

Assinatura Eletrônica
11/08/2025 15:25:45.0
DANTE HOMERO MOSCA JÚNIOR
Avaliador Interno (UNIVERSIDADE FEDERAL DO PARANÁ)

Assinatura Eletrônica
12/08/2025 16:03:45.0
RODRIGO PERITO CARDOSO
Avaliador Externo (UNIVERSIDADE DE SANTA CATARINA)

Assinatura Eletrônica
11/08/2025 11:31:21.0
HAROLDO DE ARAÚJO PONTE
Avaliador Interno (UNIVERSIDADE FEDERAL DO PARANÁ)

I dedicate this doctoral thesis to my father Marcos Aurélio Scheid Prass and to my mother Rosane Maria Siqueira Prass.

ACKNOWLEDGEMENTS

I extend my appreciation to the Federal University of Paraná (UFPR) for providing me with the necessary resource, infrastructure, and a conducive academic environment to pursue my doctoral research.

The orientation and support provided by Professor Ana Sofia C. M. d'Oliveira, Ph.D., were invaluable in helping me transition into the world of academic research. The guidance and assistance I received during this phase helped me to shape my personal and professional life.

I would like to extend my gratitude to Professor Moataz M. Attallah, Ph.D. for hosting me in his research group at the University of Birmingham in the United Kingdom. His guidance and expertise have been invaluable for my research. And special thanks for all the support and care received by my colleagues at the AMPLab (Advance Materials Processing Laboratory).

The collaborative atmosphere in our laboratory LAMSE (Laboratory of Advanced Materials and Surface Engineering) has been of great importance to this research. I am grateful to my laboratory colleagues for their friendship and shared insights, which have contributed to the success of our collective and individual works.

I must also acknowledge SENAI Innovation Institute in Manufacturing Systems and Laser Processing (ISI Laser), which was my professional home during 3 years of the PhD, providing me with practical knowledge on additive manufacturing and applied research. I want to express my gratitude to my work colleagues for their friendship and support. Balancing work and my doctoral research would have been far more difficult without their support.

I also wish to thank TWI (The Welding Institute) for being my professional home during the final months of my PhD, especially at LAM (Laser Additive Manufacturing) section. At TWI, I had the opportunity to apply my academic knowledge to real-word projects and to launch myself into an international career as an engineer in laser additive manufacturing. The new friends I have made and the experiences I had significantly contributed to my professional growth and broadened my perspective on applied research and industrial collaboration.

I would like to thank the members of the evaluation panels for their rigorous assessment and constructive feedback. The quality of this research will be greatly enriched by their invaluable academic experience.

And my deepest gratitude goes to my family and friends for the unconditional support, love, and encouragement throughout my journey. Having my father Marcos, my mother Rosane, my dog Louie and all my friends by my side during all the challenging moments provided me with the strength to move forward.

I feel privileged to have been surrounded by such a supportive network. I truly appreciate all the contributions.

Inventar é imaginar o que ninguém pensou;
é acreditar no que ninguém jurou;
é arriscar o que ninguém ousou;
é realizar o que ninguém tentou.
Inventar é transcender.

Alberto Santos Dumont.

RESUMO

Aços inoxidáveis austeníticos são ligas metálicas à base de Ferro, que se destacam por sua elevada resistência a corrosão, atribuída à da presença de Cromo e Níquel em sua composição. Estas ligas são empregadas em uma gama diversificada de aplicações, desde implantes médicos e instrumentos cirúrgicos, componentes automotivos, navais e aeroespaciais, até equipamentos para exploração de petróleo offshore. Entretanto, os aços inoxidáveis mais comumente empregados na fabricação de componentes diversos utilizados em ambientes públicos, não inibem o crescimento e proliferação de microrganismos em sua superfície. Impulsionado pela pandemia da Covid-19, o desenvolvimento de materiais com propriedades antimicrobianas tornou-se imperativo, respondendo à urgência de conter a propagação de vírus em superfícies de uso comum, como maçanetas de porta, botões de elevador e corrimãos. O Cobre (Cu), reconhecido por sua propriedade antimicrobiana, pode ser incorporado em pequenas quantidades aos aços inoxidáveis austeníticos para promover a ação antimicrobiana, entretanto, permanece como desafio o equilíbrio com as demais propriedades destes aços. Neste contexto, a Manufatura Aditiva (MA) destaca-se pela capacidade de fabricar peças metálicas com geometrias diversas, desde válvulas a próteses customizadas. Além disso, permite a customização da composição química dos materiais recorrendo a síntese *in-situ* de ligas através de fusão de misturas de pós metálicos, abrangendo partículas micrométricas e nanométricas. Esta pesquisa concentra-se na modificação do aço inoxidável AISI 316L com Cu, utilizando dois processos de MA, a Deposição por Energia Direcionada com Plasma de Arco Transferido (PTA-DED) e a Fusão em Leito de Pó a Laser (L-PBF). De maneira inovadora, micropartículas de Cu (Cu MP), nanopartículas de Cu (Cu NP) e nanopartículas de Óxido de Cobre (CuO NP) foram incorporadas individualmente ao aço inoxidável atomizado a gás. São explorados os efeitos da adição de Cu na processabilidade, características metalúrgicas e propriedades do aço inoxidável 316L. As peças sólidas resultantes foram caracterizadas quanto à composição química, microestrutura, propriedades mecânicas, resistência ao desgaste, resistência à corrosão e propriedades antimicrobianas. Com objetivo de estabelecer o tripé processamento-microestrutura-propriedades, abrangendo as diferentes quantidades de Cu adicionadas (1 e 5 % em massa), forma de adição (Cu MP, Cu NP e CuO NP) e técnicas de processamento (PTA-DED e L-PBF). Nesta pesquisa demonstrou-se a viabilidade do uso de pós modificados com Cu, incorporando micropartículas e nanopartículas, ao aço inoxidável 316L atomizado, para o processamento de multicamadas por PTA-DED e L-PBF, possibilitando a produção de componentes densos e livre de defeitos, com composição química personalizada. Os resultados revelam que as adições de Cu influenciam diretamente na interação entre o arco de plasma e o material de adição, especialmente nos processamentos contendo nanopartículas. As adições de Cu também alteram a geometria da poça de fusão e promovem o refino da microestrutura, embora reduzam a dureza devido a presença de Cu em solução sólida. O desempenho ao desgaste foi influenciado pela adição de Cu, com maiores teores favorecendo a formação de tribocamadas de óxido e resultando na redução dos coeficientes de atrito e de desgaste.

Palavras-chave: Manufatura Aditiva; Plasma de Arco Transferido; Fusão em Leito de Pó a Laser; AISI 316L; Nanopartículas de Cu e CuO.

ABSTRACT

Austenitic stainless steels are iron-based metallic alloys known for their high corrosion resistance, attributed to the presence of Chromium and Nickel in their composition. These alloys find applications in a diverse range of uses, from medical implants and surgical instruments, automotive, naval, and aerospace components to equipment for offshore oil exploration. However, the most commonly employed stainless steels do not inhibit the growth and proliferation of microorganisms on their surface. Driven by the Covid-19 pandemic, the development of materials with antimicrobial properties has become imperative, responding to the urgency to contain the virus spread on common use surfaces, such as door handles, elevator buttons and handrails. Copper (Cu), recognized for its antimicrobial property, can be incorporated in small quantities into austenitic stainless steels to enhance antimicrobial action, however, balancing it with the other properties of these steels remains a challenge. In this context, Additive Manufacturing (AM) stands out for its ability to manufacture metallic parts with diverse geometries, from valves to customized prostheses. Additionally, it allows for the customization of the chemical composition of materials through the *in-situ* synthesis of alloys by melting mixtures of metallic powders, encompassing micrometer and nanometer-sized particles. This research focuses on the modification of AISI 316L stainless steel with Cu, using two AM processes: Directed Energy Deposition with Plasma Transferred Arc (PTA-DED) and Laser Powder Bed Fusion (L-PBF). Innovatively, microparticles of Cu (Cu MP), nanoparticles of Cu (Cu NP), and nanoparticles of Copper Oxide (CuO NP) were individually incorporated into gas-atomized stainless steel. The effects of Cu addition on processability, metallurgical characteristics, and properties of 316L stainless steel are explored. The resulting solid parts were characterized by chemical composition, microstructure, mechanical properties, wear resistance, corrosion resistance, and antimicrobial properties. With the objective of establishing the tripod of processing-microstructure-properties, covering different quantities of added Cu (1 and 5 wt%), forms of addition (Cu MP, Cu NP, and CuO NP), and processing techniques (PTA-DED and L-PBF). This research demonstrated the feasibility of using Cu-modified powders, incorporating microparticles and nanoparticles, in atomized 316L stainless steel for processing of multilayers via PTA-DED and L-PBF, enabling the production of dense, defect-free components with customized chemical composition. The results show that Cu additions directly affect the interaction between the plasma arc and the feedstock material, especially in processing involving nanoparticles. Cu additions also altered the melt pool geometry and promoted microstructural refinement, although Cu additions reduced hardness due to the presence of Cu in solid solution. Wear performance was influenced by the Cu content, with higher levels promoting the formation of oxide tribolayers and leading to reduced friction and wear coefficients.

Keywords: Additive Manufacturing; Plasma Transferred Arc; Laser Powder Bed Fusion; AISI 316L; Cu and CuO nanoparticles.

LIST OF FIGURES

LIST OF TABLES

LIST OF SYMBOLS, ABBREVIATIONS AND ACRONYMS

ABNT - Associação Brasileira de Normas Técnicas
AISI - American Iron and Steel Institute
AM - Additive Manufacturing
ANOVA - Analysis of Variance
ASTM - American Society for Testing and Materials
BCC - Body-Centered Cubic
BSD - Backscattered Electron
CLSM - Confocal Laser Scanning Microscopy
COF - Coefficient of Friction
DED - Directed Energy Deposition
DIA - Dynamic Image Analysis
DoE - Design of Experiments
EBSD - Electron Backscatter Diffraction
ECA - Equivalent Circular Area
EDM - Electrical Discharge Machining
EDS - Energy-Dispersive X-ray Spectrometry
EDX - Energy-Dispersive X-ray Spectroscopy
FCC - Face-Centered Cubic
FEG - Field Emission Gun
HCl - Hydrochloric Acid
HT - Heat Treatment
HV - Vickers Hardness
HVOF - High Velocity Oxy-Fuel
LAM - Laser Additive Manufacturing
LCM - Laser Confocal Microscopy
L-PBF - Laser Powder Bed Fusion
MP - Microparticles
NP - Nanoparticles
OM - Optical Microscopy
PCE - Powder Catchment Efficiency
PFR - Powder Feed Rate
PSA - Particle Size Analysis

PTA - Plasma Transferred Arc

ROS - Reactive Oxygen Species

SD - Standard Deviation

SE - Secondary Electron

SEM - Scanning Electron Microscopy

SSS - Saturated Solid Solution

UTS - Ultimate Tensile Strength

XRD - X-Ray Diffraction

XRF - X-Ray Fluorescence Spectrometry

TABLE OF CONTENTS

1 INTRODUCTION

1.1 CONTEXT AND MOTIVATION

In recent years, attention has been directed toward the development of practices that combat the spread of microorganisms (Tang *et al.,* 2020). Notably, there has been a growing interest in developing surfaces capable of eliminating or preventing the attachment of microbial and viral entities (Balasubramaniam *et al.,* 2020), ranging from medical to engineering applications. AISI 316L is one of the most widely used austenitic stainless steels, due to its high corrosion resistance and excellent biocompatibility (Kayali; Talaş, 2019). It is extensively employed across diverse industries, including petrochemical, chemical, marine, biomedical, automotive, pharmaceutical and food processing (d'Andrea, 2023). However, as viruses can stay viable on stainless steel surfaces for durations spanning from 4 to 72 hours (Kampf *et al.,* 2020; van Doremalen *et al.,* 2020), the need for enhanced antimicrobial properties is emphasized.

Copper is well-known for its good antimicrobial properties, effectively targeting fungi, viruses, and bacteria in contact with its surface (Grass; Rensing; Solioz, 2011; Mathews; Kumar; Solioz, 2015; Silva *et al.,* 2019; Wu *et al.,* 2020). Two mechanisms are responsible for its antimicrobial action. One mechanism involves the release of Cu ions, which interact with the cell membrane of microorganisms, disrupting protein structure and impeding their survival (Xi *et al.,* 2017). Additionally, a second mechanism involves the generation of reactive oxygen species (ROS), which can interact and adversely affect vital biomolecules, such as DNA, proteins, and lipids (Warnes; Little; Keevil, 2015; Slavin *et al.,* 2017). To enhance the release of metallic ions and ROS, nanoparticles (NP) can be employed. Typically, NP exhibit greater antimicrobial properties compared to their bulk counterparts, owing to their small size and high surface-to-volume ratio (Slavin *et al.,* 2017).

The addition of small quantities of Cu (up to 7.5 wt%) to AISI 316L during casting and additive manufacturing processes has shown to improve both antimicrobial properties and corrosion resistance (Wang *et al.,* 2016; Xi *et al.,* 2017; Liu *et al.,* 2018; Zhao *et al.,* 2022; Lian *et al.,* 2023). The form in which Cu is present in these alloys, whether as an alloying element in solid solution or in copper-rich precipitates, influences these properties and may require solubilization and aging

heat treatment for optimal performance (Xi *et al.,* 2016; Du *et al.,* 2022; Huang *et al.,* 2022). The choice of the processing technique and processing parameters for Cu-containing stainless steels plays a crucial role, as they affect not only the microstructure, but also the overall performance of these materials.

The development of new materials is often accompanied by the adoption of innovative processing techniques. Additive manufacturing (AM) techniques, such as laser powder bed fusion (L-PBF) and directed energy deposition (DED), have increasingly explored AISI 316L owing to its favorable mechanical properties, corrosion resistance and processability (Saboori *et al.,* 2020; d'Andrea, 2023) despite some limitations regarding low hardness and poor wear performance (Kayali; Talaş, 2019). In addition, AM techniques can be used to in situ alloy AISI 316L and elemental Cu powders (Wang *et al.,* 2016; Zhao *et al.,* 2022). In this context, directed energy deposition with plasma transferred arc as a heat source (PTA-DED) stands out as a competitive technique, capable of producing coatings and thin walls (Alberti; Bueno; d'Oliveira, 2015). In addition, PTA-DED enables the deposition powder mixtures with different range of morphologies, ensuring good powder catchment efficiency due to the strong interaction between the plasma arc and the feedstock (Cardozo *et al.,* 2018; Prass; d'Oliveira, 2023). Moreover, PTA-DED can be cost-effective in comparison to laser-based DED processes (Sawant; Jain, 2018; Sadasivam; Amirthalingam, 2022).

Limited research has been published on the AM of stainless steel modified with Cu, but recent studies have demonstrated the viability of AM techniques for processing these materials (Foadian *et al.,* 2023; Behjat *et al.,* 2024; Yang *et al.,* 2024). However, there remains a lack of detailed information regarding the effects of Cu addition on the processability and resulting properties of AISI 316L, particularly in the context of different AM techniques such as PTA-DED. To the best of our knowledge, aside from our own work (Prass; d'Oliveira, 2023), there are no published studies that investigated the use of PTA-DED on the processing of stainless steel powder modified with Cu microparticles (Cu MP), Cu nanoparticles (Cu NP), and CuO nanoparticles (CuO NP). The influence of Cu on microstructure, mechanical properties, and wear resistance, continues underexplored, especially when comparing different Cu particle size (MP and NP) and chemical form (Cu and CuO).

To address this gap in the literature, this research investigates the AM of AISI 316L stainless steel with Cu additions employing two distinct AM techniques, PTA-

DED and L-PBF. Powder mixtures comprising AISI 316L and Cu MP were processed using both PTA-DED and L-PBF to evaluate the impact of Cu on the processability and resulting material properties. Additionally, nanocomposite powders were prepared by individually mixing Cu NP and CuO NP with AISI 316L, and these were deposited using PTA-DED to assess the influence of Cu particle size and chemical form on processing and material behavior.

1.2 OBJECTIVES

The main objective of this research is to develop an austenitic stainless steel utilizing additive manufacturing techniques, assessing the impact of Cu additions on processability, metallurgical characteristics, and overall performance of the processed materials. This overarching objective is further supported by a set of specific objectives, outlined below:

1. To understand how the characteristics of powder mixtures, consisting of gas atomized stainless steel powder and various forms of Cu particles (Cu microparticles, Cu nanoparticles and CuO nanoparticles), interfere with the deposition process and the resulting material density.
2. To comprehend the influence of processing parameters on the geometrical features of single-track coatings of stainless steel deposited by PTA-DED.
3. To discuss how the addition of different Cu particles impact on the processability and metallurgical features of stainless steel coatings processed by PTA-DED, addressing the interaction between powder feedstock and plasma arc during deposition.
4. To understand the role of Cu content, particle type and post-fabrication heat treatment on the microstructure, mechanical properties, and wear performance of stainless steel single-walls fabricated by PTA-DED.
5. To assess the role of Cu content and type of Cu particle on the corrosion resistance and antimicrobial properties of modified stainless steel single-walls deposited by PTA-DED.
6. To establish the relationship between processing parameters, microstructure and mechanical properties of Cu-modified stainless steel specimens, with a focus on the effects of multiple remelting cycles during L-PBF processing.

2 LITERATURE REVIEW

Despite the growing interest in additive manufacturing (AM) of austenitic stainless steels, little is known about the influence of copper additions on processability, microstructure, and properties of this material. This Chapter provides a brief review on stainless steels, the effects of Cu additions and the AM techniques, to better understand motivations, challenges, and opportunities relevant to this study.

2.1 STAINLESS STEELS

Stainless steels belong to a family of iron-based alloys primarily based on the Fe-Cr, Fe-Cr-C, and Fe-Cr-Ni systems. According to ASTM A941-15: Standard Terminology Relating to Steel, Stainless Steel, Related Alloys, and Ferroalloys, an alloy must contain a minimum of 10.5 wt% Chromium content to be classified as stainless steel. This elevated Chromium content enables the formation of a stable, passive oxide layer on the surface that protects the underlying material from corrosion under ambient conditions. Furthermore, the oxide layer prevents oxidation at temperatures as high as 1000 °C (Lippold; Kotecki, 2005).

The invention of stainless steel cannot be attributed to a single individual, as parallel and simultaneous experiments and discoveries were made in different parts of the world. Early attempts to produce corrosion-resistant steel trace back to the early 1800s, when alloys containing small amounts of Cr (around 1.5 wt%) were proposed for cutlery applications. However, the limitation of that time revolved around the inability to produce steels with low Carbon content, and as a result, increasing Cr content drastically compromised the formability. With advances in the production of low-carbon steels, interest in corrosion-resistant steel resurged in the early 1900s. In May 1912, Harry Brearly, a metallurgist based in Sheffield, United Kingdom, was tasked to investigate the premature failure of rifle barrels made from 5 wt% Cr steel which had failed due to corrosion. In August 1913, Brearly successfully cast a stainless steel ingot composed of 12.86 wt% Cr, 0.24 wt% C, 0.20 wt% Si, and 0.44 wt% Mn. In March 1915, the age of stainless steel began, with the first patent for cutlery grade steel being granted to Breatly, which covered compositions with Cr content ranging from 9 to 16 wt% (Lippold; Kotecki, 2005).

Over the years, stainless steels have become widely used in everyday items, like cookware, cutlery, fasteners and decorative fittings, as well as in demanding industrial applications, including petrochemical, chemical, marine, automotive, building, biomedical, pharmaceutical, and food processing (d'Andrea, 2023). For each application, the composition of stainless steel is often modified to facilitate production and to meet specific performance requirements. Stainless steels can be classified into families based on their characteristic crystallographic microstructures, which result from variations in chemical composition and heat treatment used. The families include ferritic, martensitic, austenitic, duplex, and precipitation-hardening stainless steels (Davis, 1999). The designation of the wrought grades of stainless steels is commonly based on the American Iron and Steel Institute (AISI) numbering system. Most grades use a three-digit code, the 200 and 300 series correspond to austenitic stainless steels, while the 400 series include ferritic or martensitic stainless steels. The stainless steel family of alloys is presented in Figure 1.

Figure 1 - Stainless steel family of alloys: compositional and properties linkages

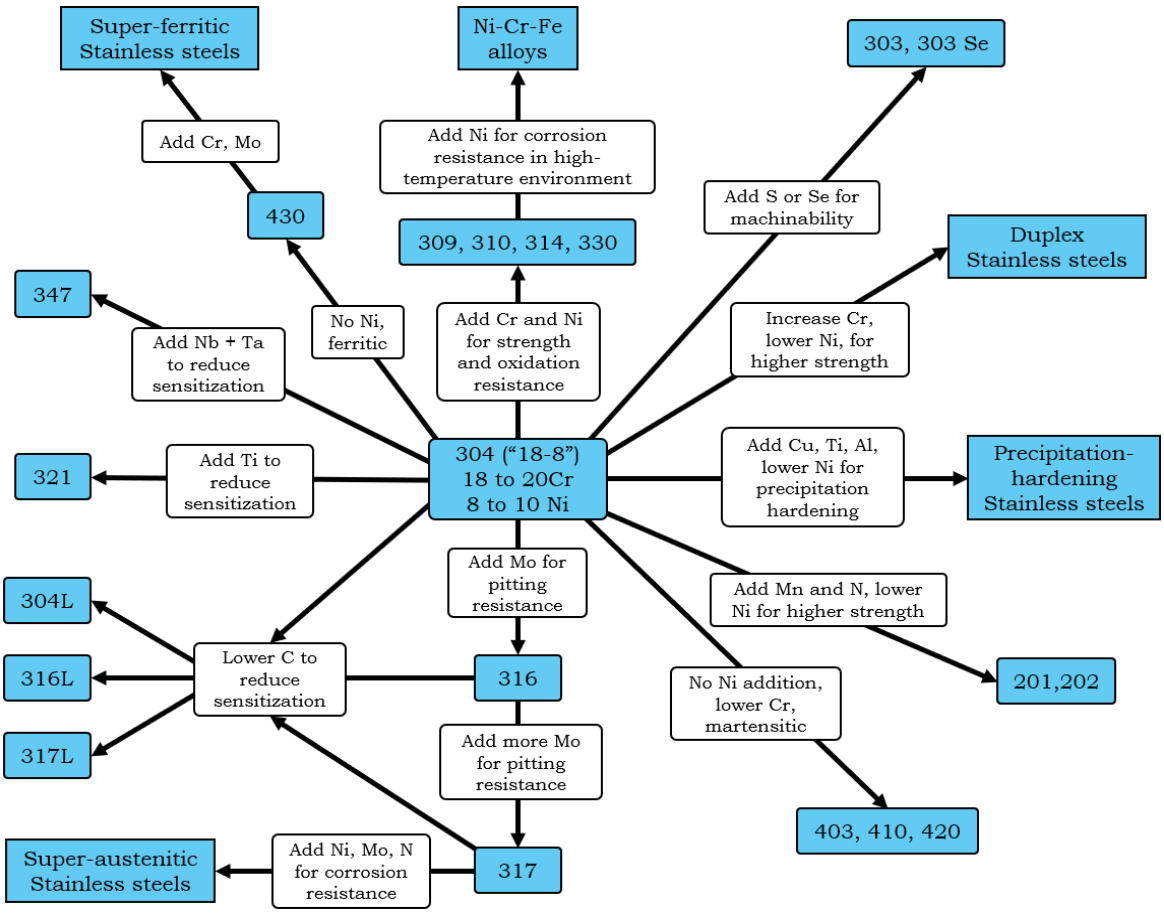

Source: Adapted from Davis (1999).

One of the most widely used austenitic stainless steels is the AISI 304, which contains 18 to 20 wt% Cr and 8 to 10 wt% Ni, and is shown at the center of the diagram in Figure 1. In general, the austenitic family offers excellent ductility, formability and toughness, in addition to good corrosion resistance (Davis, 1999). To obtain different stainless steel families with tailored properties, the chemical composition can be adjusted (Figure 1). For example, adding Molybdenum improves pitting resistance, while reducing Carbon content reduces the risk of sensitization. A result of this compositional modification is the AISI 316L, which contains 16 to 18 wt% Cr, 10 to 14 wt% Ni, 2 to 3 wt% Mo, and a maximum of 0.030 wt% C. By contrast, removing austenite-stabilizing elements such as Nickel leads to the formation of ferritic stainless steels, while reducing Nickel and increasing Chromium results in duplex stainless steel, which has a balance between austenitic and ferritic phases. Additionally, the introduction of Copper, Titanium and Aluminum enables the development of precipitation-hardening stainless steels, where the distribution and size of precipitates can be controlled by heat treatment (Davis, 1999; Xi *et al.,* 2017).

2.1.1 Copper in Stainless Steels

The presence of Cu in stainless steel is not a recent development, as it can be found on commercially available alloys such as AISI 17-4PH, a martensitic precipitation-hardening stainless steel. However, as discussed in Section 1.1, recent studies (Wang *et al.,* 2016; Xi *et al.,* 2017; Liu *et al.,* 2018; Du *et al.,* 2022; Huang *et al.,* 2022; Zhao *et al.,* 2022; Lian *et al.,* 2023; Mirzababaei *et al.,* 2023; Behjat *et al.,* 2024) have explored the addition of Cu to austenitic stainless steels with the aim to improve antimicrobial properties, mechanical properties, thermal conductivity and corrosion resistance.

A brief literature review relating processing technique, material composition and objectives is presented in Table 1. The main challenge in adding Cu to austenitic stainless steels is to enhance a specific property, such as antimicrobial performance, without compromising the alloy original characteristics, such as mechanical strength and corrosion resistance. As shown in Table 1, most studies have focused on the addition of Cu in relatively small amounts, up to 7.5 wt%. The exceptions on the list include the works of Rankouhi *et al.* (2021) and Mirzababaei *et al.* (2023). The former investigated the fabrication of functionally graded materials, transitioning from AISI

316L to pure Cu, while the latter explored the production of AISI 316L alloys with high Cu content (up to 60 wt%) aiming at enhancing thermal conductivity.

Table 1 - Brief literature review relating processing technique, material composition and objectives

Reference	Processing Technique	Material Composition (weight %)	Objectives
Wang et al., 2016	Laser Powder Bed Fusion	316L + 4.5 % Cu	Antimicrobial properties and biocompatibility
Xi et al., 2016	Casting and Heat Treatment	316L + 4.36 % Cu	Precipitate formation and mechanical properties
Xi et al., 2017	Casting and Heat Treatment	316L + 2.5 and 3.5 % Cu	Antimicrobial properties, mechanical properties and corrosion resistance
Liu et al., 2018	Casting	316L + 4.46 % Cu	Antimicrobial properties and corrosion resistance
Liu et al., 2021	Laser Directed Energy Deposition	316L + 1.5, 4.5 and 7.5 % Cu	Corrosion resistance
Rankouhi et al., 2021	Laser Powder Bed Fusion	316L + 25, 50, 75, 100 % Cu	Compositional grading
Du et al., 2022	Casting and Heat Treatment	316L + 4.5 % Cu	Precipitate formation and recrystallization
Huang et al., 2022	Casting and Heat Treatment	304L + 4 % Cu	Mechanical properties
Zhao et al., 2022	Laser Directed Energy Deposition	316L + 1.5, 4.5 and 7.5 % Cu	Corrosion resistance
Foadian et al., 2023	Laser Powder Bed Fusion	316L + 1 and 5 % Cu	Mechanical properties
Lian et al., 2023	Cold Spray	304L + 5 % Cu	Antimicrobial properties and corrosion resistance
Mirzababaei et al., 2023	Laser Powder Bed Fusion and Hot Isostatic Pressing	316L + 20, 30, 50, 60 % Cu	Thermal conductivity
Romero-Resendiz et al., 2023	Casting and Heat Treatment	316L + 3 % Cu	Antimicrobial properties and mechanical properties
Behjat et al., 2024	Laser Powder Bed Fusion	316L + 3.5 % Cu	Antimicrobial properties
Behjat et al., 2024	Laser Powder Bed Fusion	316L + 2.5 % Cu	Mechanical properties

Source: Authors (2025).

The Fe-Cu phase diagram (Figure 2) highlights the limited mutual solubility between Fe and Cu in the solid state. At elevated temperatures near 1500°C, the maximum solubility of Cu in δ-ferrite (δFe) is approximately 8.1 wt%. Both γ-austenite (γFe) and Copper (Cu) share a face-centered cubic (FCC) crystal structure, which allows for a maximum solubility of Cu in γ-austenite of around 13 wt%. However, Cu

solubility decreases as temperature decreases. In the body-centered cubic (BCC) α-ferrite, Cu solubility drops below 2.2 wt% and eventually falls below 1 wt% at room temperature (ASM International, 1992). In applications involving rapid cooling rates, such as welding and additive manufacturing, solidification occurs under non-equilibrium conditions. The high cooling rates can suppress the formation of Cu-rich precipitates, resulting in a saturated solid solution (Lippold; Kotecki, 2005). In addition, posterior heat treatment can control the precipitation and growth of Cu-rich phases (Xi *et al.*, 2016; Xi *et al.*, 2017; Mirzababaei *et al.*, 2023).

Figure 2 - Fe-Cu phase diagram

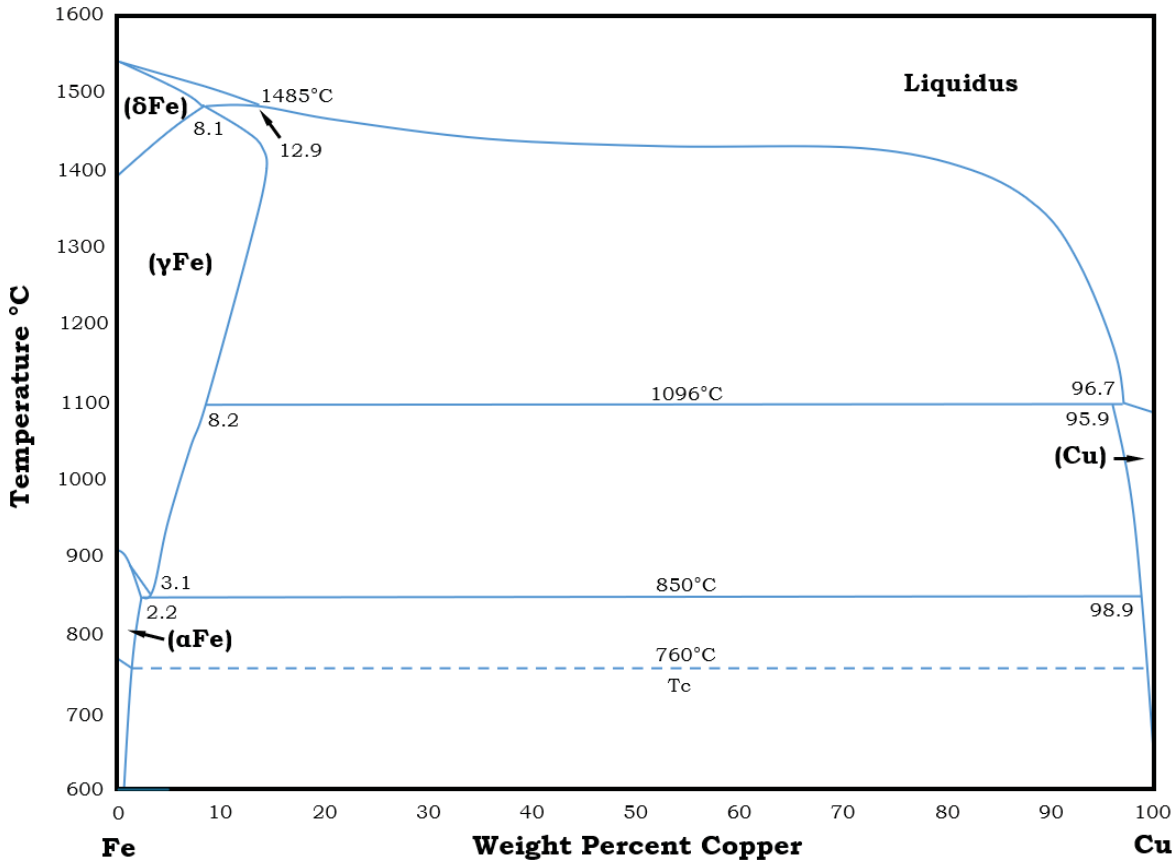

Source: Adapted from ASM International (1992).

Not only does the material composition influence on the crystallographic microstructure and resulting properties, but the processing technique employed also has a significant impact. For example, works from Xi *et al.* (2017) and Romero-Resendiz *et al.* (2023) investigated the impact of heat treatment in cast 316L modified with Cu. Their studies identified how variations of time and temperature influence the formation of Cu-rich precipitates and mechanical properties. They also

demonstrated that the precipitate size and distribution have a direct impact on both antimicrobial properties and corrosion resistance. Regarding the impact of processing techniques, Zhao *et al.* (2022) and Behjat *et al.* (2024) explored the use of additive manufacturing methods (described in Section 2.2) for producing 316L alloys with Cu additions. The rapid colling rates associated with both Directed Energy Deposition and Powder Bed Fusion techniques promoted the refinement of the microstructure when compared to conventional casting, and in turn, induced changes in the corrosion resistance and antimicrobial properties of the alloys.

The solidification mode of an alloy can be planar, cellular, columnar dendritic, or equiaxed dendritic (Figure 3a), depending on the chemical composition of the alloy and the thermal conditions during solidification. As solidification occurs, solute is rejected at the solid-liquid interface, creating a composition gradient in the liquid ahead the interface, that lowers the local liquidus temperature. If the actual temperature of the liquid ahead of the interface falls below this local liquidus temperature, constitutional supercooling occurs. This condition causes the initially stable planar interface to became unstable and transition to cellular or dendritic mode (Kou, 2002).

Figure 3 - a) Effect of temperature gradient and growth rate on the microstructure and b) schematic showing solidification and post-solidification transformations in Fe-Cr-Ni welds

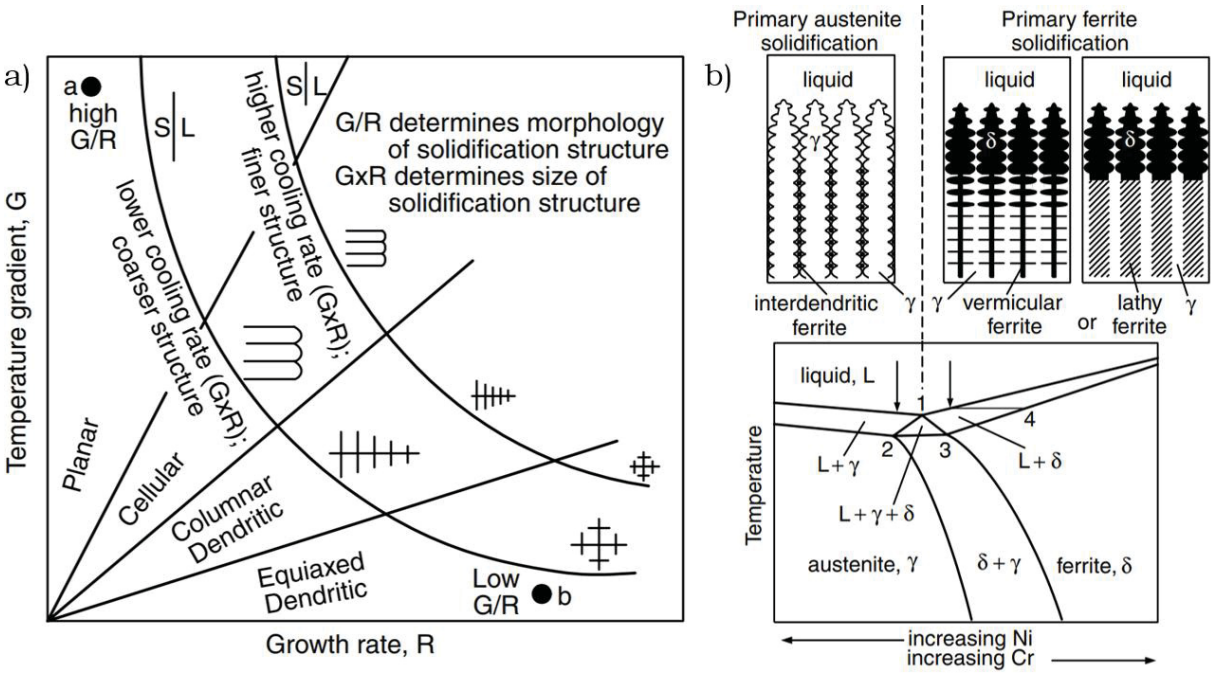

Source: Kou (2002).

Figure 3a summarizes how the temperature gradient (G) and the growth rate (R) effect the resulting microstructure. The ratio G/R controls the solidification morphology, while the product G×R (cooling rate) governs the refinement of the microstructure. Higher cooling rates result in shorter solidification times and, consequently, finer microstructural features (Kou, 2002). The addition of Cu increases the thermal conductivity of stainless steel, as mentioned by Mirzababaei *et al. (*2023). As a result, it is expected that higher cooling rates will occur during solidification, promoting grain refinement and favoring dendritic formation in alloys containing Cu.

Figure 3b illustrates the solidification and post-solidification transformations in Fe-Cr-Ni welds. After solidification, austenitic stainless steels typically exhibit a γ-austenite matrix with small amounts of δ-ferrite. The primary solidification mode and the amount of δ-ferrite depend on the chemical composition of the alloy. In alloys rich in austenite-stabilizing elements, such as Ni and Cu, primary austenite solidification occurs, forming γ-austenite dendrites with small amounts of δ-ferrite in the interdendritic region. In contrast, in alloys rich in ferrite-stabilizing elements, like Cr, primary ferrite solidification occurs, with the formation δ-ferrite dendrites with a core rich in Cr. As temperature decreases, the outer core of the dendrites, having less Cr, transform into γ-austenite, while the Cr-rich core remains as δ-ferrite in a network-like structure, called vermicular ferrite (Kou, 2002; Lippold; Kotecki, 2005).

In order to predict the ferrite content and solidification mode in austenitic stainless steel welds, the WRC-1992 diagram developed by Kotecki and Siewert (1992) can be employed (Figure 4). The diagram is based on the concepts on Ni equivalent and Cr equivalent, and the ratio between them enables the prediction of solidification mode and ferrite number. Solidification modes are classified as A (primary austenite solidification with no ferrite formation), AF (primary austenite solidification with ferrite formation in the interdendritic regions), FA (primary ferrite solidification followed by austenite transformation), and F (primary ferrite solidification with minimal austenite formation). The addition of Cu to the AISI 316L stainless steel affects the solidification mode and reduces the ferrite content, as Cu acts as an austenite-stabilizing element.

Figure 4 presents the WRC-1992 diagram with the plotted positions of both 316L and 316L + 5 wt% Cu. The addition of Cu has a twofold effect, it increases the Ni equivalent value due to its austenite-stabilizing behavior and reduces the Cr

equivalent value, as Cr content reduces with Cu additions. According to the diagram, the addition of Cu shifts the solidification mode from FA to AF and reduces the predicted ferrite number from 4 to 1. As indicated by Kou (2002), the reduction of δ-ferrite to values below 5 vol % increases the risk of solidification cracking, consequently, increasing Cu content above 5 wt% could increase the possibility of crack formation during solidification.

Figure 4 - Prediction of weld ferrite content and solidification mode for 316L and 316L + 5% Cu using the WRC-1992 diagram

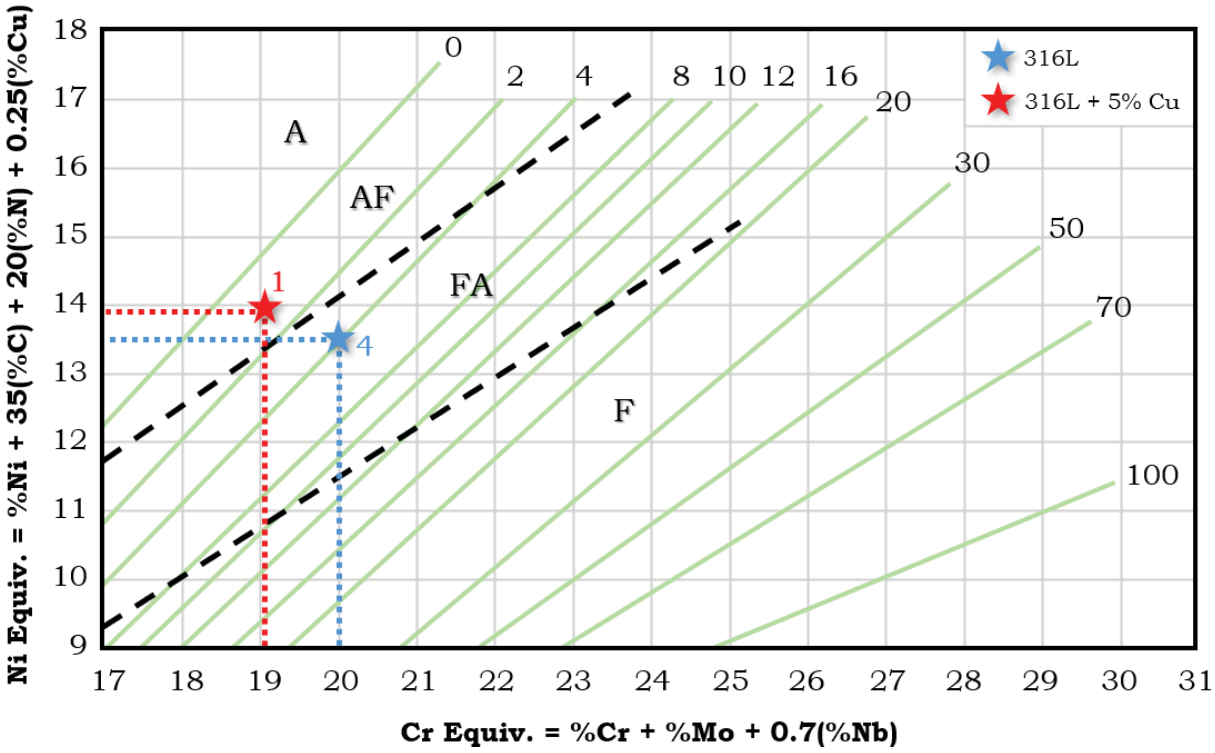

Source: Adapted from Kotecki and Siewert (1992).

The WRC-1992 diagram (Figure 4) only provides a prediction of ferrite content for single-pass welds or single-bead coatings. However, in multi-pass welds or multilayer deposition processes, such as those of additive manufacturing, the thermal cycles induced by subsequent layer deposition can cause the dissolution of δ-ferrite, as the previously solidified metal is reheated above the transformation temperature.

2.2 ADDITIVE MANUFACTURING

The ISO/ASTM 52900:2021 standard defines Additive Manufacturing (AM) as the process of joining materials to make parts from a three-dimensional (3D) model data, usually on a layer-by-layer manner, contrasting with traditional manufacturing methods, such as subtractive and formative techniques. The AM techniques can be divided into 7 process categories, as shown in Table 2, each process is distinguished by the type of feedstock used and the method by which material is joined.

Table 2 - Additive manufacturing process categories according to ISO/ASTM 52900:2021

AM process category	**Description**
Binder Jetting - BJT	A liquid bonding agent is selectively deposited to join powder materials
Directed Energy Deposition - DED	Thermal energy is used to fuse materials by melting as they are being deposited
Material Extrusion - MEX	Material is selectively dispensed through a nozzle or orifice
Material Jetting - MTJ	Droplets of feedstock material are selectively deposited
Powder Bed Fusion - PBF	Thermal energy selectively fuses regions of a powder bed
Sheet Lamination - SHL	Sheets of material are bonded to form a part
Vat Photopolymerization - VPP	Liquid photopolymer in a vat is selectively cured by light-activated polymerization

Source: Adapted from ISO/ASTM (2021).

One of the advantages of the AM techniques is the ability to produce components with complex geometries in a single process, allowing the reduction of the number of parts in multicomponent assemblies by consolidating them into a single monolithic object. This approach eliminates assembly time, reduces inventory costs, and improves equipment performance (Bahnini *et al.*, 2018; Debroy *et al.*, 2017). Through its layer-by-layer processing approach, the AM techniques stand out by enabling the simultaneous fabrication of both the material and the geometry of the part. This allows for customization of the chemical composition and the development of composite materials, tailoring properties locally within the component. The layer-by-layer fabrication also enables variations in composition and/or microstructure across different regions of a part. By selecting appropriate materials, processing parameters, and build orientation, it is possible to control the microstructure and resulting properties, improving the functionality of a part (Thompson *et al*., 2016).

Table 3 presents a comparison of the general characteristics of both AM methods. DED stands out for its ability to use both powder and/or wire as feedstock material, its higher building rate, minimal size constraints (limited primarily by the

handling system), and its suitability for repair operations. In contrast, PBF excels at producing highly complex geometries, including intricate internal features, with superior dimensional accuracy (Brandt, 2017).

Table 3 - Comparison of the general characteristics of DED and PBF

Characteristic	**DED**	**PBF**
Feedstock material	Powder, wire	Powder
Energy source	Laser beam, electron beam, electric arc	Laser beam, electron beam
Part dimensions	Limited by the handling system	Limited by the processing chamber
Part complexity	Limited	Practically unlimited, excellent for hollow geometries, i.e. lattices and complex cooling channels
Building rate	10-80 cm^3 / h	2-40 cm^3 / h
Can be built on	Tridimensional surfaces, preexisting parts, excellent for repair operations	Plan surfaces, plan preexisting parts
Surface roughness	60-500 µm	10-50 µm

Source: Adapted from Brandt (2017).

In this work, two categories of AM process were explored for processing the AISI 316L stainless steel with the addition of Cu particles, Directed Energy Deposition (DED) and Powder Bed Fusion (PBF). Both techniques utilize metal powder as feedstock material but differ in their energy source. DED was performed using Plasma Transferred Arc (PTA), while PBF employed a Laser Beam.

2.2.1 Directed Energy Deposition

Figure 5 presents a schematic of a generic DED process. In this technique, a deposition head, or nozzle, delivers both heat source and the feedstock material to a precise location. The heat source melts the material that is being fed along with the substrate, forming a local melt pool. As the deposition head moves, the molten material solidifies, forming a single track. Depositing adjacent tracks side by side, a layer is formed. Repeating this process layer-by-layer enables the fabrication of three-dimensional components.

Table 4 provides a brief comparison of powder DED applications using laser beam and electric arc as energy sources. Typically, laser DED (L-DED) can operate at lower power levels, allowing for the fabrication of finer geometrical features, such as thin walls. In contrast, electric arc DED methods, such as PTA-DED, offer

competitive building rates but generally require post-processing machining to achieve the required final geometry and surface finish (Debroy *et al.*, 2017). Generally, arc-based DED processes incur lower initial and running costs, and are considered more energy-efficient than laser-based processes with similar productivity (Kumar; Jain, 2022; Sadasivam; Amirthalingam, 2022).

Figure 5 - Schematic of a generic Directed Energy Deposition process

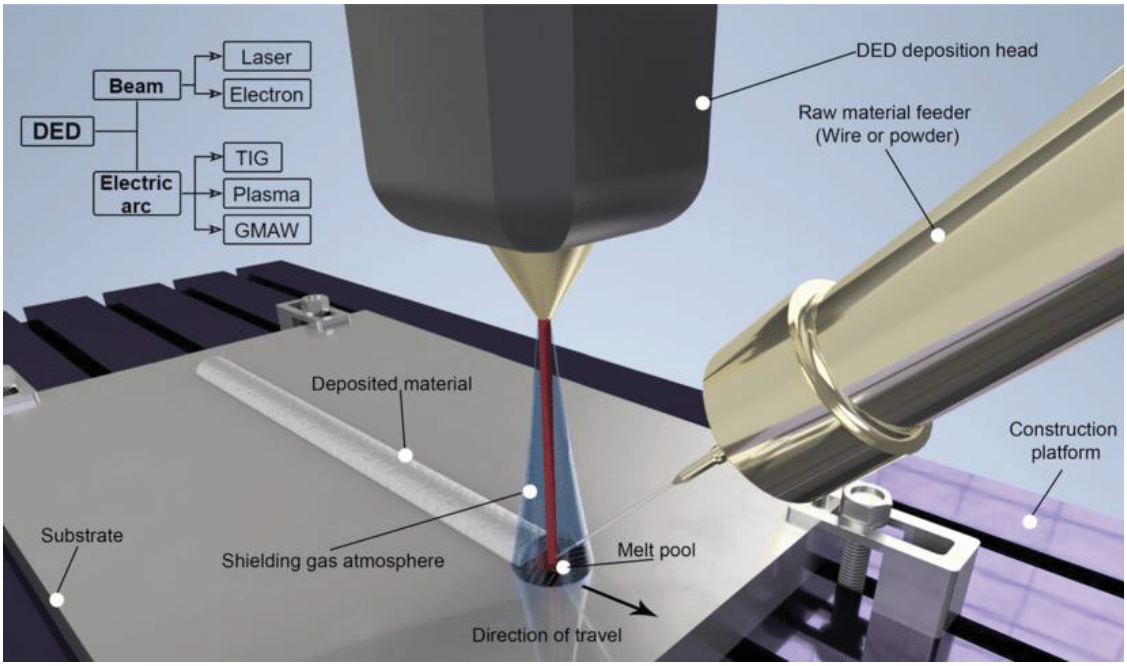

Source: Dávila et al. (2020).

Table 4 - Brief comparison of powder DED applications: laser beam and electric arc

Characteristic	**Laser beam**	**Electric arc**
Power (W)	100 - 3000	1000 - 3000
Speed (mm/min)	300 - 1500	100 - 900
Building rate (g/min)	6 - 60	12 - 168
Surface roughness	4 - 10 µm	Usually require machining

Source: Adapted from Debroy *et al.* (2017).

PTA is a DED technique that employs a nozzle-constricted plasma arc as a heat source to melt and deposit metallic feedstock onto a substrate (described in Section 3.2). The process was originally developed for hardfacing, being capable of processing a wide range of alloys, including hard-to-weld, corrosion and wear resistant materials (Cardozo *et al.,* 2018). Due to its characteristics, PTA-DED has gained attention in the field of AM, in recent years, as briefly summarized in Table 5.

Table 5 - Brief literature review of the potential uses of PTA in additive manufacturing applications

Reference	Feedstock; Process	Remarks
Alberti, Bueno and d'Oliveira, 2015	Nickel-based superalloys; powder; PTA-DED	The study successfully processed defect-free thin walls with PTA-DED. Chemical composition of the alloy and preheating influenced the wall geometry.
Jhavar, Paul and Jain, 2016	AISI P20 low-alloy tool steel; wire; µPTA-DED	µPTA-DED is a viable, economical, and cleaner methodology for industrial applications. The process was found advantageous in terms of low initial and running costs with comparable properties when compared to high-energy density beam processes. It confirmed the process capability for cost-effective for die and mold remanufacturing.
Cardozo et al., 2018	Inconel 625; powder and wire; PTA-DED	PTA offers superior energy efficiency compared to laser-based processes. The choice of feedstock material form (wire and powder) affects the microstructure and mechanical properties, mainly because different processing parameters are required for each.
Sawant and Jain, 2018	Ti6Al4V titanium alloy; powder; µPTA-DED	Deposition usings a dwell-time yielded higher effective wall width, deposition efficiency, yield strength, ultimate strength, microhardness, and surface straightness, along with lower strain, wear volume, and friction coefficient. µPTA-DED process was found to be cost-effective compared to laser-based processes and energy efficient compared to pulsed plasma arc process.
Rojas et al., 2018	6030 Nickel Alloy with WC particles; PTA-DED	WC particle homogeneity was maintained due to the rapid solidification rate of the layer-by-layer processing. The average density was 99.60%. The study confirms the feasibility of the process for AM purposes. The technology is suitable for applications requiring high wear resistance, like in the mining, oil, and gas industries.
Nikam, Jain and Sawant, 2019	AISI P20 low-alloy tool steel; wire; µPTA-DED	The study optimized parameters to minimize aspect ratio and increase productivity. Optimized parameters resulted in very good quality and accuracy of deposition, with excellent bonding to the substrate material and no internal defects.
Kumar and Jain, 2022	Stellite-6; powder and wire; µPTA-DED	Surface roughness increases with increased power supply and material feed rate and decreases with increased traverse speed for both powder and wire forms. Surface roughness of the powder was smaller (118 to 149 µm) than the wire (195 to 227 µm).
Pacheco and d'Oliveira, 2023	Superduplex Stainless Steel 2507; powder; PTA-DED	The deposition heat cycle poses a significant challenge to microstructure control, especially for alloys with complex metallurgy like duplex stainless steels. Achieving the adequate proportion of ferrite and austenite phases require careful consideration for each process and condition, and post-processing heat treatment.
Abreu-Castillo and d'Oliveira, 2024	Ni and Al mixed with WC-NPs; powder; PTA-DED	Tungsten carbide nanoparticles (WC-NPs) were used to limit grain growth, but their effectiveness was challenged by the formation of a molten film around the Ni particles (carrier particles) during processing, compromising the synthesis of aluminides.
Chen et al., 2025	PTA-DED	For typical PTA-DED, the arc efficiency is approximately 60%, due to energy loss by convection and radiation. Higher current intensity increased plasma column stiffness. Increasing Plasma Gas Flow Rate increases arc efficiency due to arc column contraction. Longer arc lengths resulted in less concentrated power.

Source: Authors (2025).

PTA-DED has demonstrated several advantages for AM applications, as shown by recent studies (Table 5). It enables the deposition of defect-free parts using a wide range of materials, including nickel-based superalloys, tool steels, titanium alloys, and stainless steels. PTA-DED stands out for its energy efficiency and its lower operational costs, particularly when compared to laser-based processes (Jhavar; Paul; Jain, 2016; Chen et al., 2025) The process can produce coatings and AM parts using both powder and wire feedstocks, providing flexibility on the choice of materials (Kumar; Jain, 2022). Additionally, when the process is optimized, it results in excellent mechanical properties, microstructural control, and high material density (Pacheco; d'Oliveira, 2023). However, to achieve optimal results, careful selection of process parameters is required, especially for complex alloys containing nanoparticle reinforcements (Abreu-Castillo; d'Oliveira, 2024).

2.2.2 Powder Bed Fusion

Figure 6 illustrates a schematic representation of a Laser Powder Bed Fusion process (L-PBF), including details of melt pool dynamics during processing. To produce additive manufactured parts using L-PBF, a thin layer of metal powder, with a typical layer thickness between 15 to 90 μm, is evenly spread over a substrate, which is attached onto the build platform. A laser beam, which is focused on the surface of the powder bed, is guided by the scan head optic system, and selectively melts the powder according to the geometry of each slice of the part. The molten material rapidly solidifies to form a single layer with the desired shape. Subsequent layers are formed by moving the build platform down, reapplying a layer of powder, and scanning the laser. Once the building is complete, the remaining powder and the consolidated part, still attached to the substrate, are removed from the building platform. The remaining powder can be sieved and reused, while the fabricated part can be post-processed, such as heat treatment and machining, to meet specific application requirements (Haferkamp, 2022).

During the L-PBF process, the laser beam interacts with the metal powder particles, heating them to temperatures above the melting point and generating a melt pool that typically is deeper than the powder layer thickness. As the laser moves forward, the temperature decreases, leading to the formation of a solidified melt track. In some cases, the local temperature, under laser irradiation, exceeds the

boiling point, causing localized vaporization. The resulting vapor pressure can depress the melt pool surface and induce spattering of surrounding powder particles. The L-PBF process involves complex interaction among multiple physical phenomena, making accurate simulation highly challenging. Consequently, structured experimental approaches are often preferred to optimize processing parameters, tailor the microstructure and control the resulting material properties.

Figure 6 - Schematic of a Laser Powder Bed Fusion process

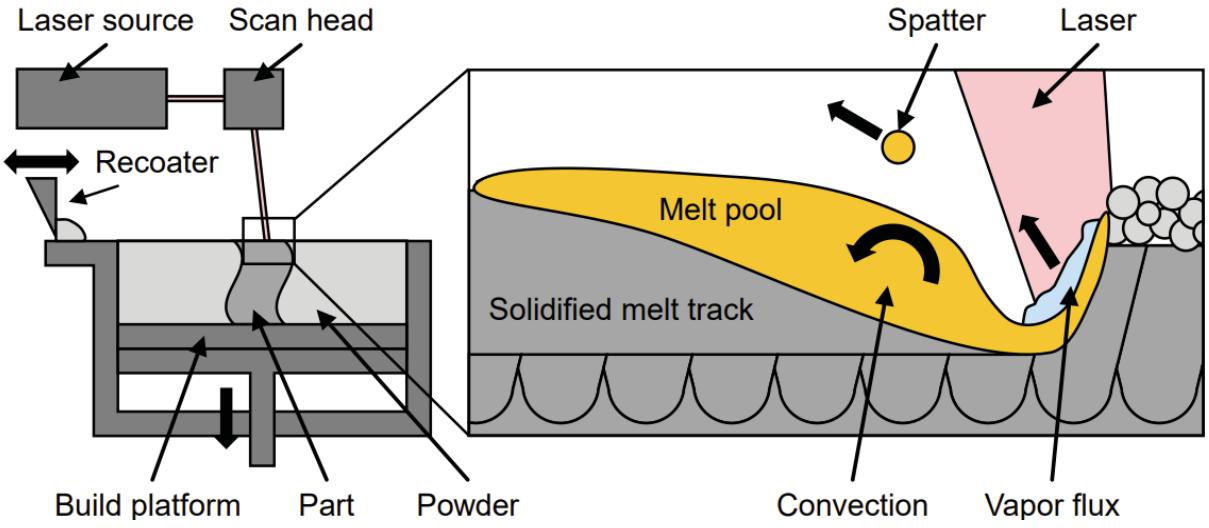

Source: Haferkamp (2022).

Figure 7 shows a schematic representation of the thermal history in AM processes, including L-PBF and PTA-DED. At any given point inside the final part, the thermal history comprises a series of repeated thermal cycles. The first temperature peak occurs when the powder feedstock is initially melted and solidified to form a solidified melt track. To build a complete layer, adjacent tracks are produced with a degree of overlap, resulting in a second temperature peak and a partial remelting of the initial track. As subsequent layers are produced, along the build direction, the initial track experiences addition remelting from the heat coming from above. This results in multiple thermal cycles for each region, which significantly influences the final microstructure of the AM part (Xiong *et al.* 2022).

Figure 7 - Thermal history in Laser Powder Bed Fusion

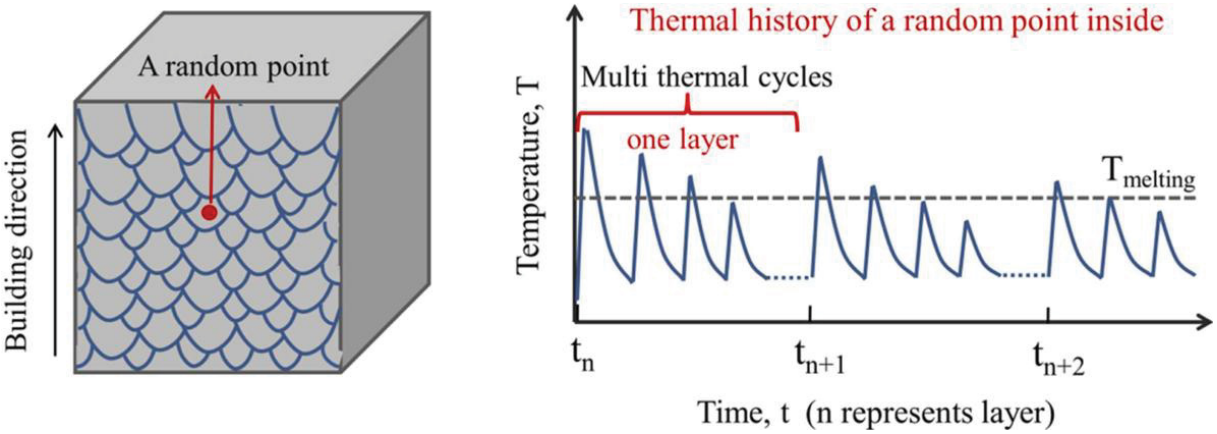

Source: Adapted from Xiong *et al.* (2022).

As with other powder-based AM techniques, L-PBF allows for the in-situ alloying of powder mixtures. In recent years, this capability has been increasingly explored for the fabrication of stainless steel alloys modified with Cu additions, as summarized previously in Table 1. Research has shown the feasibility of in-situ alloying AISI 316L with Cu. However, further investigation needs to be done regarding the optimization of processing parameters, particularly focused on reducing porosity in the alloys containing Cu. Additionally, the influence of energy input on melt pool geometry and its relationship with the resulting mechanical properties remains to be addressed. These topics are explored in more detail in Section 4.5.

2.2.3 Feedstock Material

For AM processes that use powder as feedstock, selecting materials with appropriate characteristics is mandatory, as the quality of the produced parts is directly influenced by the properties of the powder. Figure 8 presents a cause-and-effect diagram (Ishikawa diagram) illustrating some of the parameters influencing the metal powder properties applied to AM applications. The first powder property is the alloy composition, followed by the optical material properties, especially when interacting with laser beam. Particle shape, size and morphology are determined by the powder production method. In addition, powder behavior characteristics, such as flowability and tap density, are dictated by the interactions between individual particles (Spierings *et al.*, 2015).

Figure 8 - Ishikawa diagram with parameters influencing metal powder for additive manufacturing

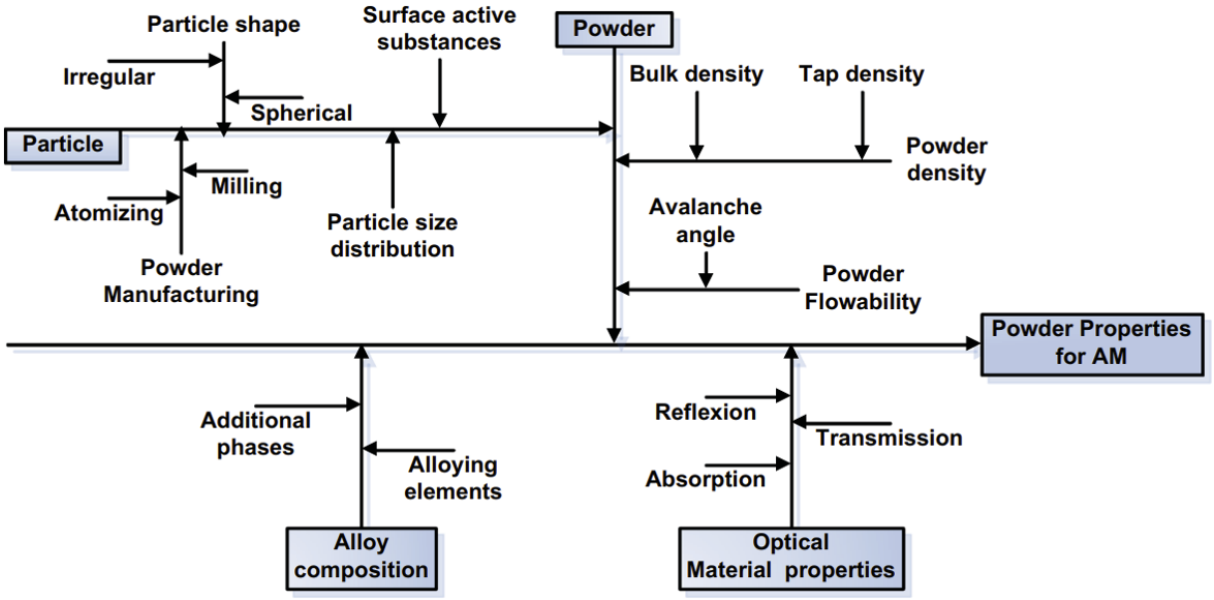

Source: Spierings *et al.* (2015).

For AM applications, a powder is considered suitable when its particle size falls within the specified range, its chemical composition meets the standard specifications, and its surface is free of contaminants such as oxidation. In addition, both DED and PBF processes require good powder flowability, which is strongly related to particle size distribution and morphology. In general, the more spherical the powder particles are, the better their flow behavior. The production method determines the powder morphology while sieving can be used to control the particle size range (Spierings *et al.*, 2015; Gutjahr, 2022).

Figure 9 presents an overview of the main powder production methods used for AM metallic powders. Atomization processes are the most used, as they produce powders with very high sphericity, which is an important characteristic for most AM techniques (Nie *et al.*, 2020). However, refractory materials, for example, cannot be easily obtained through most atomization processes, and often require alternative methods, such as mechanical processes. Figure 10 illustrates the typical morphology of powders obtained by different production methods. Both powder quality and production costs increase from left to right in the image. Due to the focused nature of the laser beam, laser-based AM processes usually require fine powders with high sphericity. In contrast, PTA-DED can accommodate the deposition of powders with a broader range of particle morphologies, due to the strong interaction provided by the plasma arc (Cardozo *et al.,* 2018).

Figure 9 - Powder production methods and processes used for metallic powders for additive manufacturing applications

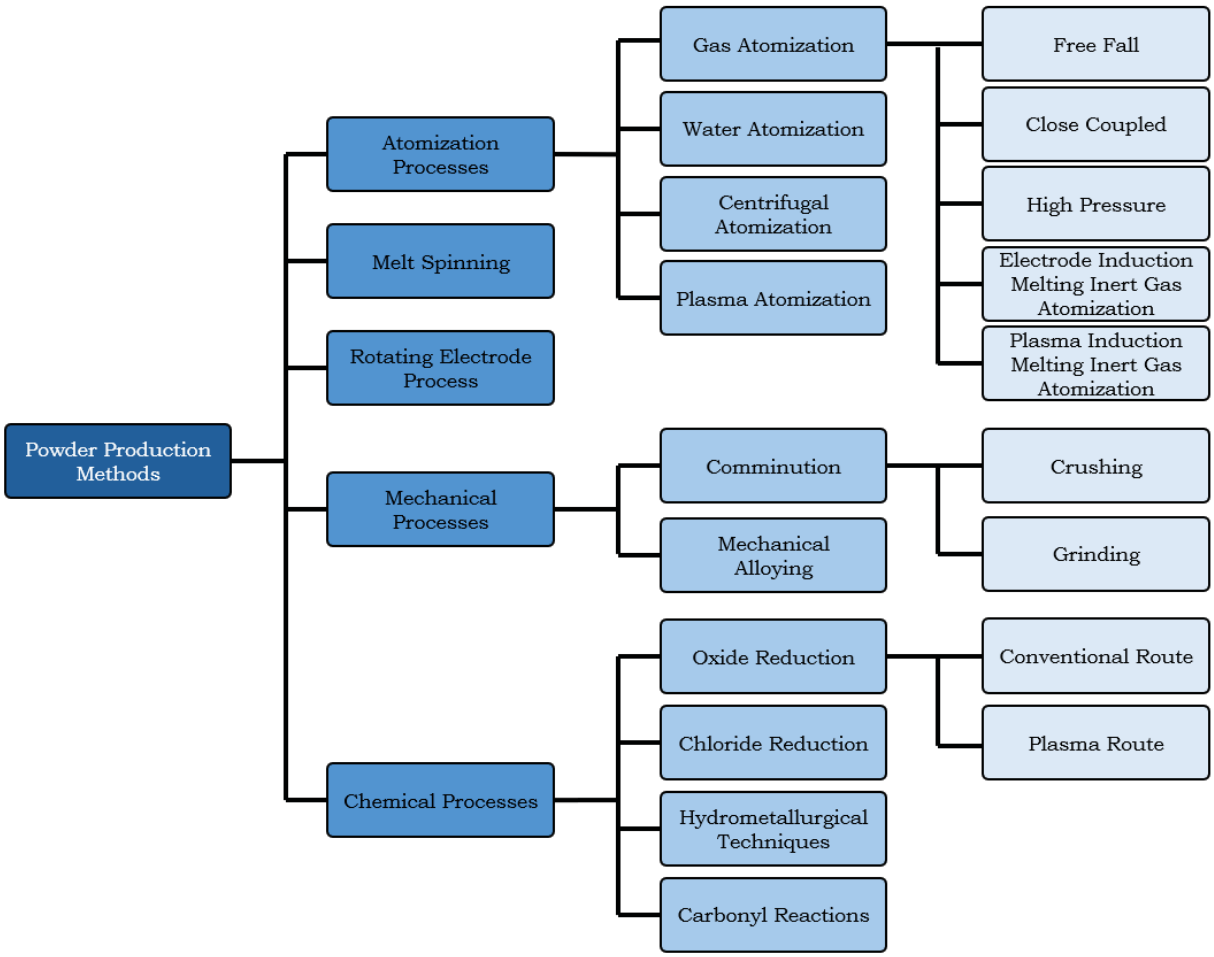

Source: Adapted from Kassym and Perveen (2020).

Figure 10 - Powder morphology obtained by different production methods

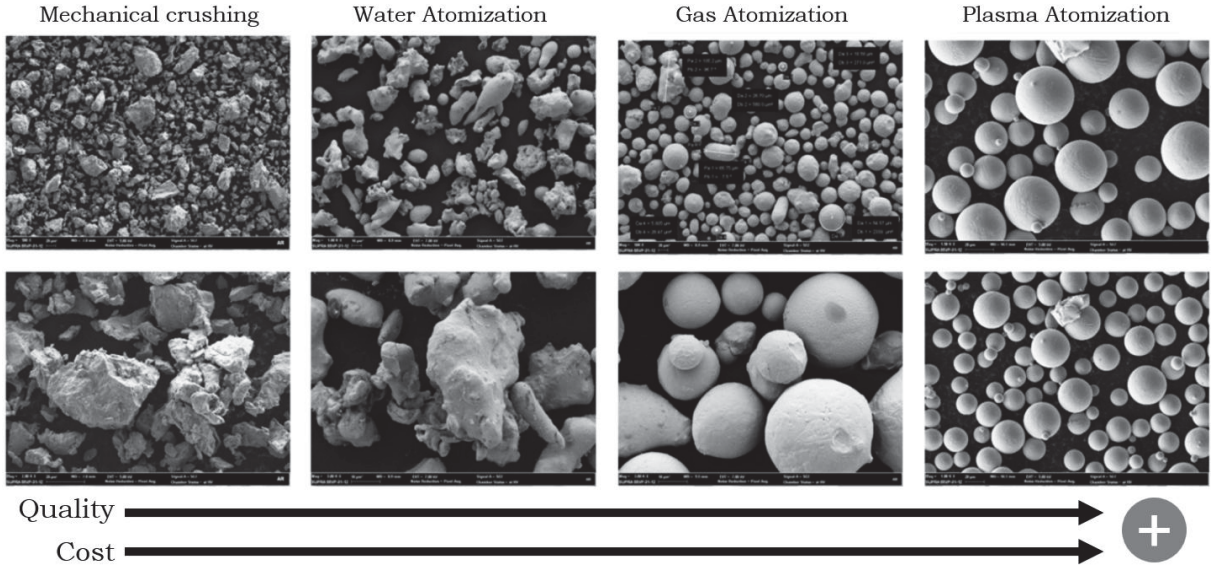

Source: Adapted from Gutjahr (2022).

During powder production, individual particles solidify with varying sizes and shapes. Some particles may contain internal defects, such as pores formed by gas entrapment, while others exhibit external imperfections or irregular geometrical features. These surface defects can be detrimental to powder flowability, which in turn may affect processability and the overall quality of the manufactured part (Nie *et al.*, 2020; Chu *et al.,* 2021). Figure 11 illustrates the types of defects observed in an AISI 316L powder produced by gas atomization. These defects promote mechanical interlocking between particles during relative movement, thereby reducing powder flowability.

Figure 11 - Types of defects on gas-atomized particles

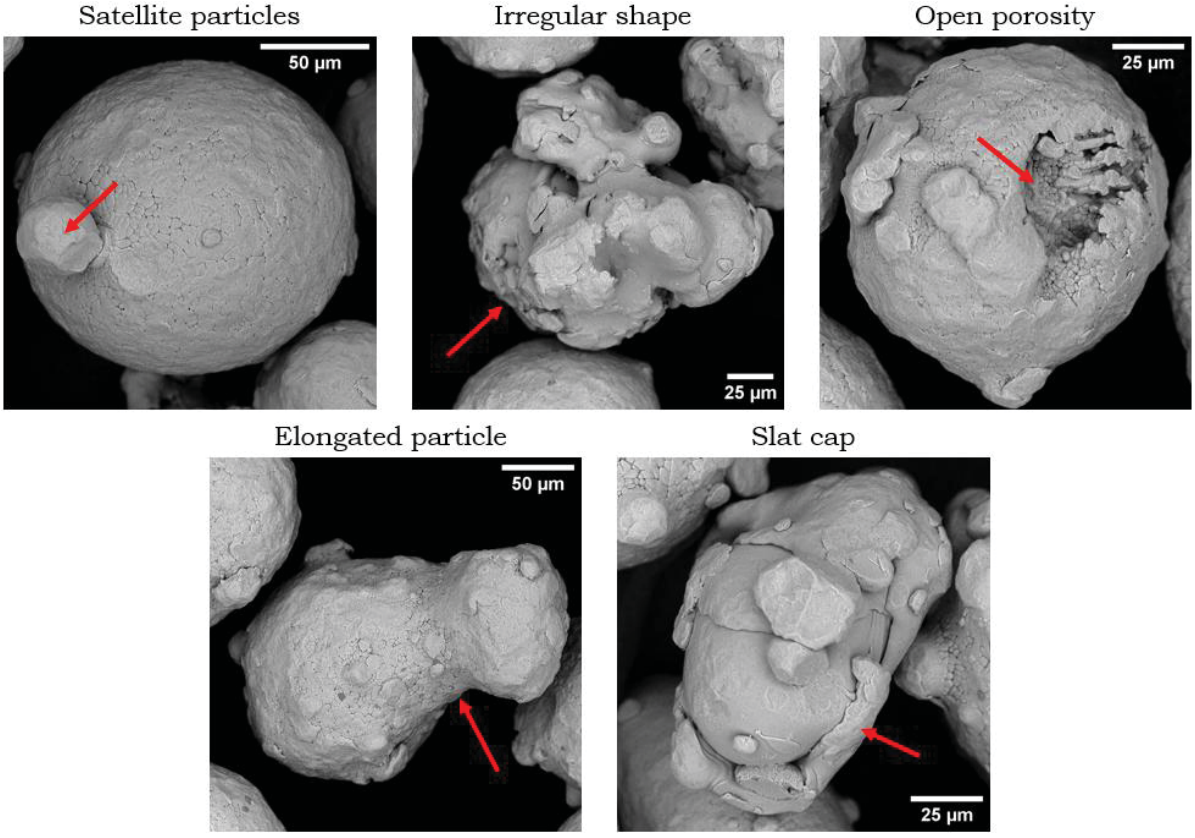

Source: Authors (2025).

Using powders as feedstock material in AM offers flexibility for designing alloys with customized chemical compositions, enabling the development of advanced materials with tailored properties (Li *et al.,* 2019; Dong *et al.,* 2020; Cui *et al.,* 2022). The control over composition can be achieved by mixing different powder prior to processing or, in some DED system, by simultaneously feeding multiple

powder through the nozzle during processing, allowing for in-flight mixing. However, the deposition of nanoparticles (NPs) on their own is not possible, due to their limited flowability. Among the innovative approaches to employ NPs to AM processes, is the generation of nanocomposite powders, where guest NPs are dispersed onto the surface of carrier particles, usually microparticles (MPs), to form a nanocomposite powder system (Zhuang *et al.,* 2020; Soulier *et al.,* 2022). The attachment of the guest NPs on the surface of the carrier particle occurs when the adhesive interactions are stronger than the gravitational forces acting over the NPs.

Mixing NPs with MPs to produce nanocomposite powder, particularly for AM applications, presents several challenges. These are primarily associated with achieving a homogeneous dispersion of NPs and preserving the original powder properties, such as flowability (Yin *et al*., 2022; Zhai; Zhou; Nai, 2022a; Javidi *et al*., 2023; Wei *et al*., 2025; Wang *et al*., 2025). If not prepared properly, the prepared powder mixture can affect the processability, compromising the quality of the produced parts and altering the resulting material properties (Zhai; Zhou; Nai, 2022b; Wang *et al*., 2022).

One of the main challenges in preparing nanocomposite powders is the tendency of NPs to agglomerate. Due to their high surface-area-to-volume ratio, NPs are prone to clustering, which can result in a non-uniform distribution across the matrix powder (Yin *et al*., 2022; Zhai; Zhou; Nai, 2022a; Wang *et al*., 2025). The agglomeration of NPs, combined with the strong interactions forces between particles, can significantly reduce the flowability of the powder mixture (Javidi *et al*., 2023; Yin *et al*., 2022; Zhai; Zhou; Nai, 2022a), hindering the formation of uniform powder layers in PBF and impairing consistent powder feeding rate in DED. Additional issues have also been reported, such as the loss of NPs during the mixing and subsequent material handling and delivery process (Zhai; Zhou; Nai, 2022a; Prass; d'Oliveira, 2023), and changes in the morphology of the larger MPs during mixing, particularly when ball milling is employed, reducing overall powder flowability (Wang *et al*., 2022; Javidi *et al*., 2023).

3 METHODOLOGY

This research used a commercially available stainless steel atomized powder that was modified with the addition of different content and types of Cu particles. To evaluate the impact of Cu on the processability, metallurgical characteristics and overall performance of austenitic stainless steel, two distinct AM techniques were employed, PTA-DED and L-PBF. Figure 12 shows a summarized flowchart of the methodology adopted in this work.

Figure 12 - Methodology flowchart

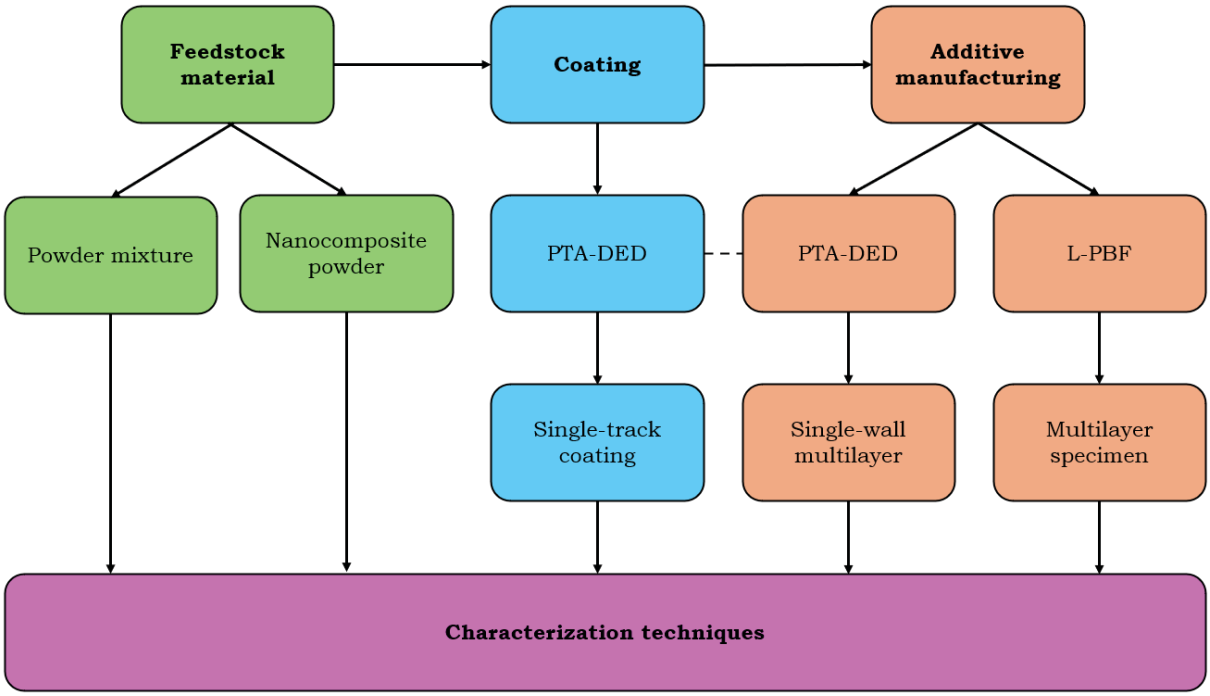

Source: Authors (2025).

The following sections present the feedstock preparation methods, the manufacturing techniques used to process the modified stainless steel, and the characterization techniques employed. Details of the material suppliers and equipment manufacturers used in this thesis are provided in Appendix D.

3.1 FEEDSTOCK MATERIALS PREPARATION

Four primary feedstock materials were used in the PTA-DED studies, gas atomized stainless steel powder (AISI 316L) with particle size ranging from 85 to 150

μm, Cu microparticles (Cu MP) varying from 89 to 143 μm, Cu nanoparticles (Cu NP) and CuO nanoparticles (CuO NP) sized approximately 500 nm and 40 nm, respectively. To obtain the distinct powder mixture compositions, various Cu contents were added to the stainless steel. In Table 6, a summary of the powder mixture compositions used in the PTA-DED studies are presented, including references to the corresponding sections where these compositions are discussed.

Table 6 - Powder mixture compositions used in the PTA-DED studies in weight percentage

Powder composition	**Used in**	**Sections it appears**
AISI 316L	Single-track coating, single-wall multilayer	4.1, 4.2, 4.3, 4.4
99 % AISI 316L + 1 % Cu MP	Single-track coating, single-wall multilayer	4.1, 4.4
99 % AISI 316L + 1 % Cu NP	Single-track coating, single-wall multilayer	4.1, 4.4
99 % AISI 316L + 1 % CuO NP	Single-track coating, single-wall multilayer	4.1, 4.4
95 % AISI 316L + 5 % Cu MP	Single-track coating, single-wall multilayer	4.3, 4.4
95 % AISI 316L + 5 % Cu NP	Single-track coating	4.3
95 % AISI 316L + 5 % CuO NP	Single-track coating	4.3

Source: Authors (2025).

Figure 13 brings a schematic diagram of the preparation steps for obtaining powder mixtures (composed of only microparticles) and nanocomposite powders (composed of microparticles and nanoparticles) used for PTA-DED processing. The preparation of powder mixtures (Figure 13a) involves drying both powders (i.e. AISI 316L and Cu MP) for 2 h at 80°C, followed by mixing in a Y-type blender for 2 h. As a result, it is expected that the guest particles (i.e. Cu MP) are uniformly distributed within the host powder (i.e. AISI 316L).

Due to the tendency of NPs to cluster together, the preparation of nanocomposite powder (Figure 13b) is more complex and requires a few more steps. The process starts with the dispersion of the nanoparticles (i.e. Cu NP) in an ultrasonic bath in ethanol for at least 300 s. After which, the host powder (i.e. AISI 316L) is added to the mixture and mechanically stirred for 2 h. Ethanol is evaporated in a furnace for 24 h at 50 °C, to avoid boiling the ethanol abruptly. After drying, the powders are mixed in a Y-type blender for 2 h. Consequently, it is anticipated that most of the guest nanoparticles are uniformly adhered to the host particle surface. The characterization of the nanocomposite powder was crucial for comprehending the impact of different Cu additions in the deposition process, allowing improved

selection of processing parameters to produce defect-free parts. This aspect is further explored in Section 4.1.

Figure 13 - Preparation steps for (a) powder mixtures and (b) nanocomposite powders

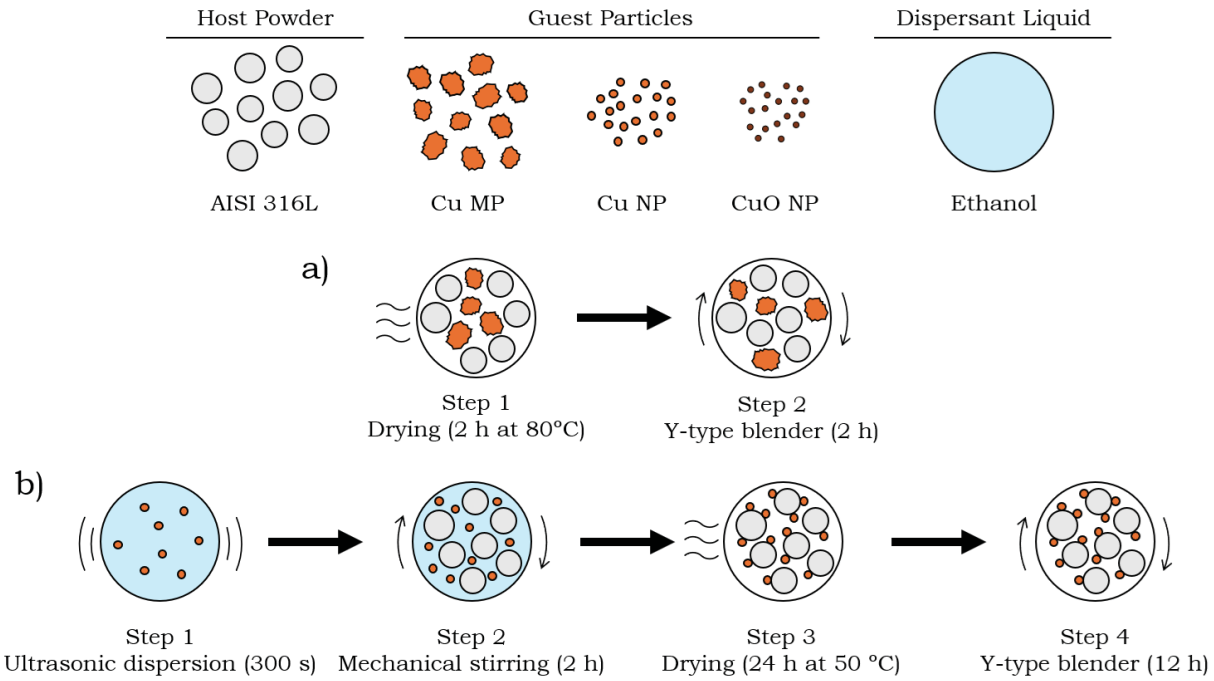

Source: Authors (2025).

Two primary feedstock materials were used in the L-PBF studies, gas atomized stainless steel powder (AISI 316L) and Cu powder (Cu), with particle sizes ranging from 15 to 53 µm and 15 to 45 µm, respectively. Two powder compositions were prepared, commercially available AISI 316L and AISI 316L modified with 5 wt% Cu. The powders were kept under argon atmosphere, and mixing was conducted in a 3D powder mixer for 1 h to ensure a homogeneous distribution of Cu particles within the stainless steel powder. The processing and characterization of this material are detailed in Section 4.5.

3.2 PLASMA TRANSFERRED ARC - DIRECTED ENERGY DEPOSITION

PTA process was employed as a DED technology, enabling the deposition of powder feedstock as solid metallic coatings and multilayers. Figure 14 shows a schematic diagram illustrating the PTA nozzle and a photograph of the PTA deposition process. The plasma arc formed between the Tungsten electrode and the

substrate consists of a high-temperature ionized gas that allows the passage of electric current through it. The plasma arc is used as the heat source to melt the feedstock material and substrate. Additionally, shielding gas forms a protective environment, insulating the melt pool from ambient air, while the carrier gas protects and transports the powder throughout the feeding system. As the feedstock material is delivered into the plasma arc, it interacts with the heat source before reaching the substrate, allowing for melting and effective in-situ synthesis of powder mixtures.

Figure 14 - a) Schematic diagram of PTA nozzle and b) photograph of PTA deposition

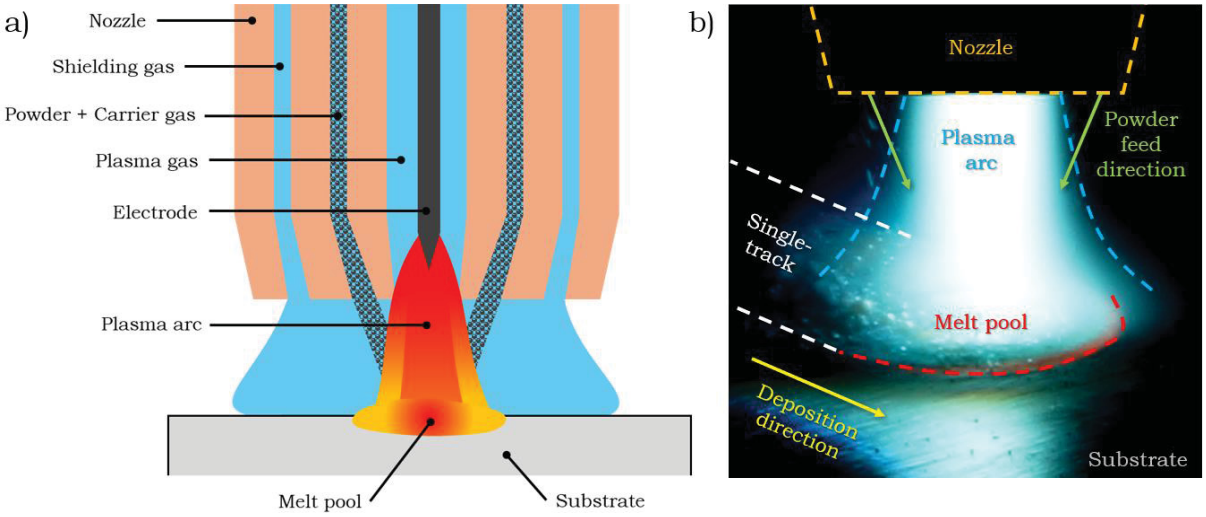

Source: Authors (2025).

PTA-DED processing was carried out to manufacture single-track coatings (Figure 15a) and single-wall multilayers (Figure 15b), employing the powder compositions presented in Table 6 as feedstock material. Investigating the manufacturing of coatings provided better understanding of the correlation between PTA-DED processing parameters and the resulting geometry of stainless steel single-track coatings. This aspect is elaborated upon in Section 4.2. Furthermore, the deposition of single-track coatings allowed for the understanding of the impact of adding Cu MP, Cu NP and CuO NP in the processability, hardness and solidification structure of the stainless steel coatings. These aspects are further explored in Section 4.3.

The deposition of single-track coatings was carried out with the stainless steel substrate positioned horizontally (Figure 15a), whereas for the deposition of single-wall multilayers, the substrate was oriented vertically (Figure 15b). The vertical

orientation was used to simulate the heat transfer conditions similar to those experienced by a preexisting wall. The single-walls were built by the deposition of successive layers on top of each other, keeping the same direction throughout the deposition process. Temperature between successive depositions was kept bellow 150 °C to prevent overheating. The effect of Cu additions on the wear performance of AISI 316L multilayers obtained by PTA-DED is explored in Section 4.4, while the antimicrobial assessment and corrosion behavior of these materials are discussed in Appendix A and Appendix B, respectively.

Figure 15 - PTA deposition process for (a) single-track coatings and (b) single-wall multilayer

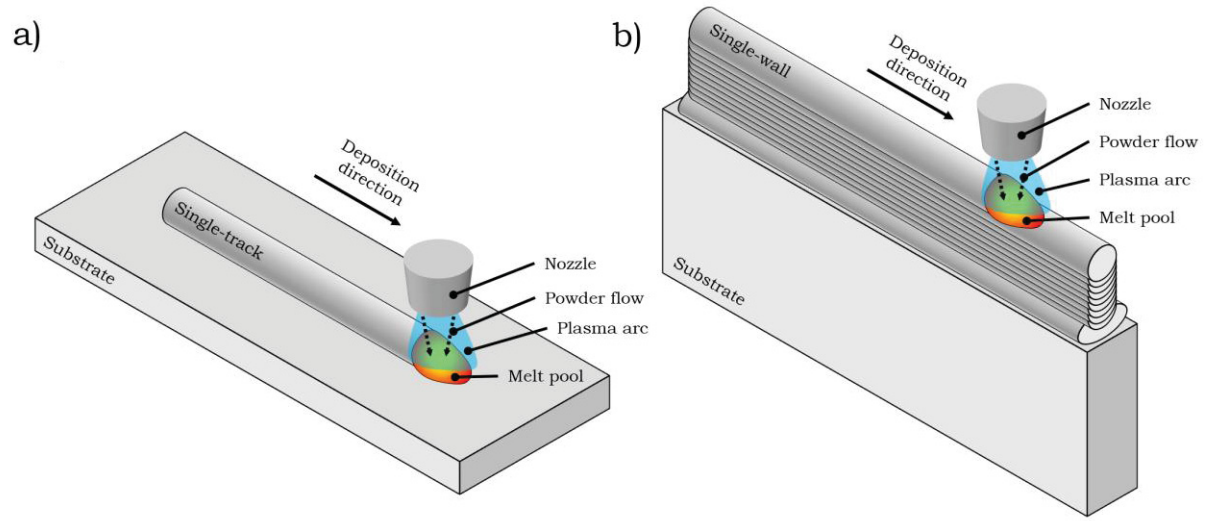

Source: Authors (2025).

3.3 LASER POWDER BED FUSION

L-PBF is an AM technology that is capable of manufacturing solid metallic parts with complex geometry with precision. In this process, the feedstock material is distributed across a powder bed and selectively melted using a focused heat source, in contrast to DED technologies, where powder is fed through the nozzle. A visual representation of the L-PBF process is depicted in Figure 16a.

The process begins with the distribution of powder supply over the build plate by the recoater. This device spreads layers of powder with controlled thickness, forming the powder bed. Any excess powder displaced by the recoater (powder overflow) goes into a separated chamber to be used in future builds. A focused laser beam scans the designated area of the powder bed, selectively melting the powder

layer to build the desired solid-part geometry. During processing, the whole system remains submerged in inert gas, usually Argon, to protect the melt pool from reactive gases such as oxygen. Successive layers of powder are distributed by the coordinated movement of the powder platform and build platform, which ascend and descend, respectively.

Figure 16 - Schematic diagrams of (a) L-PBF process and (b) scanning strategy adopted

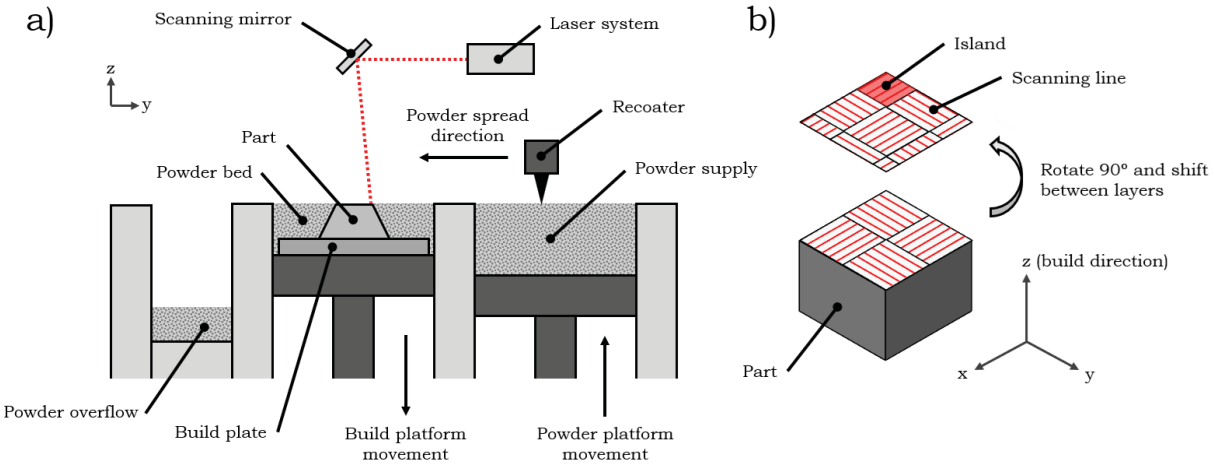

Source: Authors (2025).

The laser scanning strategy employed in this study is shown in Figure 16b. The strategy consists of partitioning the cross-section area of the part into small square islands with a controlled size of 5 x 5 mm. The laser scans an individual island at a time, altering the scanning line direction for each adjacent island. The laser scan pattern changes as the layers are built, as two adjustments occur. Firstly, the scanning line direction within the islands rotates by 90º, and secondly, all islands shift by 1 mm in both x and y directions.

As described in Section 3.1, two powder compositions were used to produce parts with L-PBF, AISI 316L and AISI 316L with 5 wt% Cu. Given the time constraints of the sandwich doctorate period for material processing and characterization, a fixed Cu content was used. To maximize the effects of Cu addition on processability, microstructure and mechanical properties, a 5 wt% Cu content was chosen, as this concentration previously enabled the production of dense, defect-free stainless steel multilayers using PTA-DED. The relationship between chemical composition, processing parameters, microstructure and mechanical properties are further discussed in Section 4.5.

3.4 CHARACTERIZATION TECHNIQUES

3.4.1 Characterization of Feedstock Materials

As described in Section 3.1, the feedstock materials used in this work consisted of powder mixtures of AISI 316L stainless steel and different Cu-based particles, including Cu MP, Cu NP and CuO NP. Due to the significant size differences between these particles, a combination of characterization techniques was employed to better understand the properties of the feedstock.

The feedstock materials were characterized in terms of their morphology, size and shape distribution, flowability, and chemical composition, as illustrated in Figure 17. These techniques aimed to assess the characteristics of the individual powder grains, the homogeneity of the powder mixture, the attachment of NP to the carrier AISI 316L powder, as well as particle shape, surface defects, and their potential influence on powder flow behavior during PTA-DED and L-PFB processing.

Figure 17 - Feedstock characterization

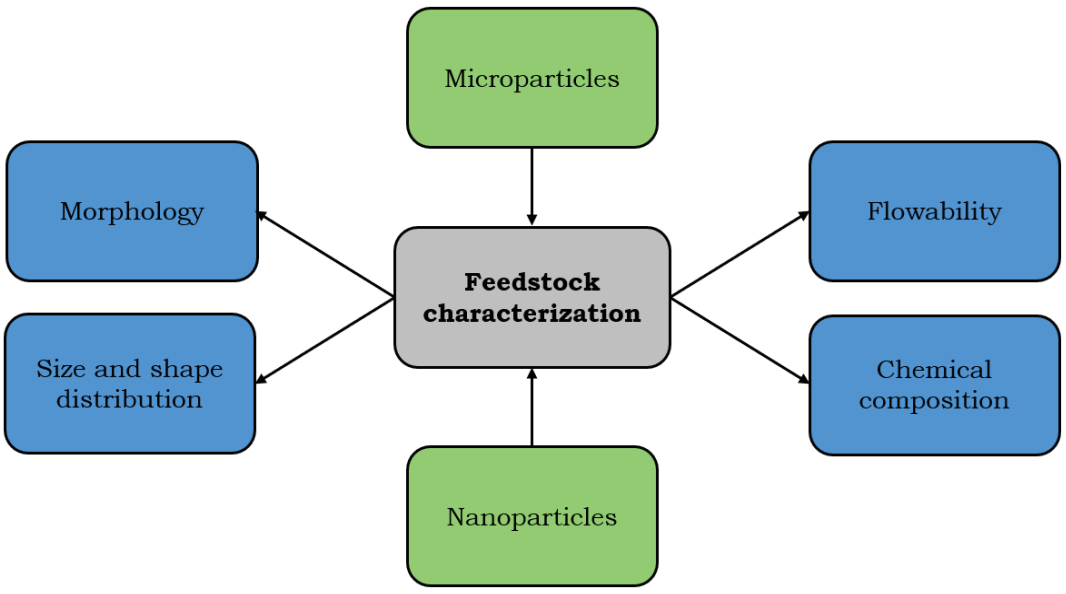

Source: Authors (2025).

- ✓ Morphology:

Powder morphology and powder mixtures were assessed using Confocal Laser Scanning Microscopy (CLSM) and Scanning Electron Microscopy (SEM). Both

techniques enable the visualization of the characteristics of individual particles, such as surface defects, satellite particles, and particle shape. Additionally, they can be used to evaluate the homogeneity of powder mixtures and verify the attachment of NP onto the carrier stainless steel microparticles.

CLSM operates at lower magnifications compared to SEM, however, it offers the advantage of capturing true-color images, similar to conventional Optical Microscopy (OM). Moreover, CLSM can generate a high depth-of-field image comparable to that of SEM, by acquiring and stacking a large number of images. Figure 18a shows a CLSM micrograph of an AISI 316L particle with Cu NP attached, the image was obtained by stacking approximately 1500 images. The contrast in color allows for the clear distinction between the orange-red Cu NP from the gray surface of the stainless steel particle.

Figure 18 - Micrographs of an AISI 316L particle covered with Cu NP obtained by a) CLSM and b) SEM

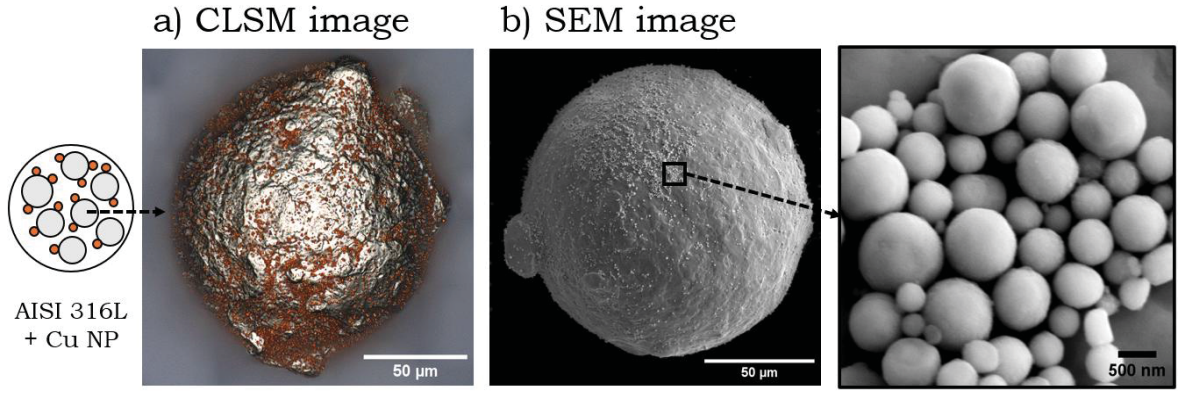

Source: Authors (2025).

In contrast, SEM uses a focused beam of electrons to scan the surface of the sample. Since electrons do not carry color information like visible light photons, the resulting SEM images are rendered in grayscale. However, SEM offers significantly higher magnification and resolution, making it suitable to assess the morphology of nanoparticles in detail, as illustrated in Figure 18b.

- ✓ Size and shape distribution:

The powder feedstock material consists of a collection of individual particles, each with distinct size and shape. To understand the collective behavior of a powder,

it is essential to evaluate the distribution of both size and shape across a large number of particles. This information can be collected by the analysis of powder micrographs or, more efficiently, by using specialized techniques such as Dynamic Image Analysis (DIA). In this work, DIA was performed in accordance with ASTM B822-20 - Standard Test Method for Particle Size Distribution of Metal Powders and Related Compounds by Light Scattering. As shown in Figure 19, the DIA process involves three main stages, image acquisition, image processing, and particle classification by size and shape.

Figure 19 - Dynamic Image Analysis: a) image acquisition, b) image processing, and c) particle classification by size and shape

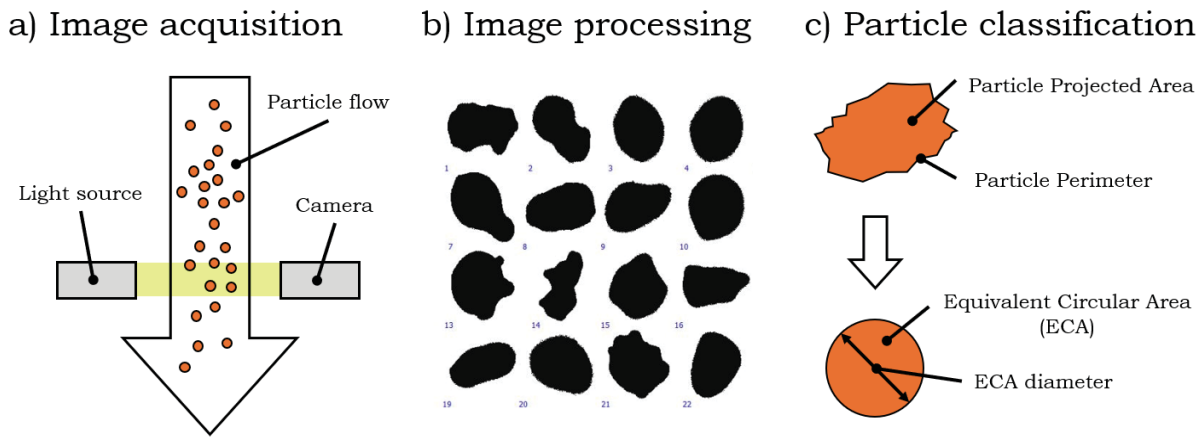

Source: Authors (2025).

In the first stage, a powder sample is fed into the system, where particles flow individually in front of a light source. As the particles interrupt the light path, a camera captures the 2D projection of each particle. This process continues until thousands of particle images have been captured and recorded by the computer. In the second stage, the captured images are converted into binary images, and a dedicated software analyses them, extracting the geometrical information of the particle's 2D projection.

In the third stage, the particles are classified by size and shape, based on two parameters, Equivalent Circular Area (ECA) diameter and circularity. The ECA diameter describes the particle size as the diameter of a circle with the same area as the particle projected area (Figure 19c). Additionally, circularity quantifies how close to a perfect circle a particle shape is. It is calculated according to Equation 1:

$$Circularity = (4 \times \pi \times A) / (P^2) \quad (1)$$

where A is the particle projected area (μm²) and P is the particle perimeter (μm). A perfect circle has a circularity of 1.0. As particle shape deviates further away from circular, the particle perimeter increases relative to the area, resulting in lower circularity values approaching zero.

✓ Flowability:

It is well known that highly spherical particles exhibit better flowability, a critical requirement in powder-based AM processes, including DED and PBF. In addition to powder morphology, particle size distribution also plays an important role in flow behavior. As particle size decreases, the surface-area-to-volume ratio increases, intensifying the interaction forces between particles, resulting in poorer flowability in finer powders.

To measure powder flowability, two standardized procedures can be employed, the Hall flowmeter funnel and the Carney funnel, Figure 20. In this work, flowability tests were carried out in accordance with both ASTM B213-20 - Standard Test Methods for Flow Rate of Metal Powders Using the Hall Flowmeter Funnel, and ASTM B964-16 - Standard Test Methods for Flow Rate of Metal Powders Using the Carney Funnel.

Figure 20 - a) Hall Funnel (ASTM B213-20) and b) Carney funnel (ASTM B964-16)

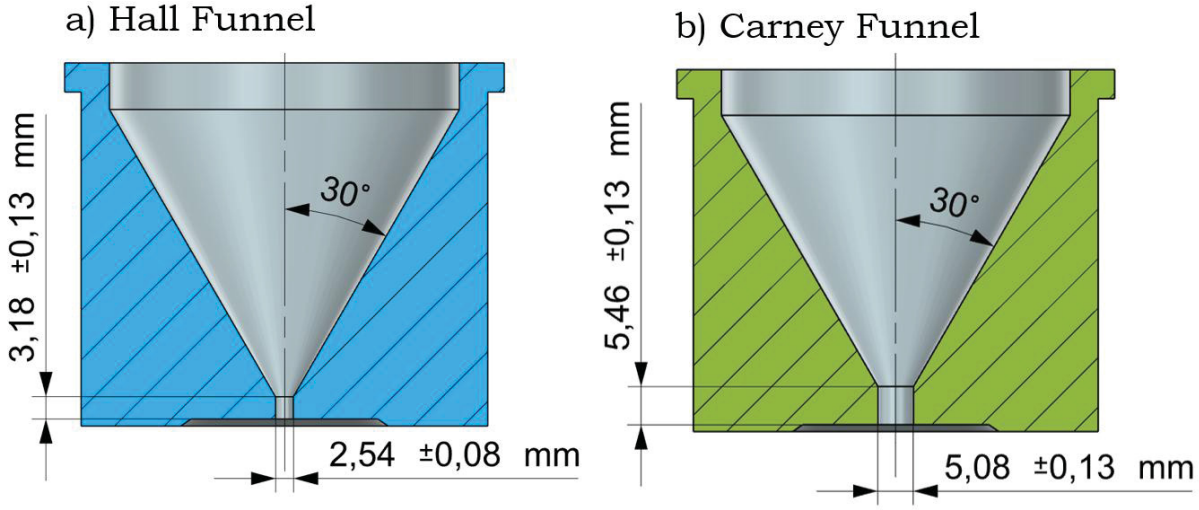

Source: Authors (2025).

The procedure involves measuring the time required for specific mass of powder or powder mixture (50 g) to flow through the funnel orifice under gravity. Shorter flow times indicate better flowability. The dimensions of the Hall Funnel and the Carney Funnel are presented in Figure 20. According to standard testing protocols, the flowability tests should begin with the Hall funnel, which features a smaller orifice. If the powder does not flow through the Hall Funnel, it has insufficient flowability, and the test should then be repeated using a Carney Funnel, which has a larger orifice and is better suited for powders with poor flow characteristics.

✓ Chemical composition:

The chemical composition of powder mixtures was assessed using X-ray Fluorescence Spectrometry (XRF) and Energy-Dispersive X-ray Spectrometry (EDS) attached to a SEM. XRF provides quantitative analysis of the chemical composition of bulk powder samples. In contrast, EDS allows for semi-quantitative elemental analysis of individual particles and provides elemental mapping across selected regions, which allows for the evaluation of the homogeneity of powder mixtures.

As illustrated in Figure 21, XRF was used to confirm and quantify the bulk chemical composition of AISI 316L powder. Additionally, EDS mapping was conducted to verify the distribution of the added Cu-based particles between the stainless steel powder, assessing the homogeneity of the powder mixture. These analyses contributed to the optimization of the feedstock preparations procedures presented in Section 3.1.

Figure 21 - XRF and EDS mapping used for feedstock characterization

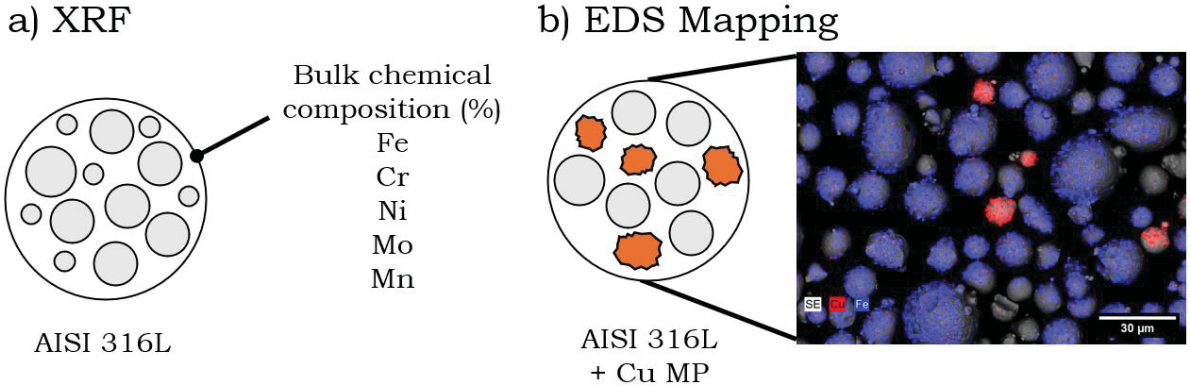

Source: Authors (2025).

3.4.2 Characterization of Processed Materials

As described in Sections 3.2 and 3.3, the feedstock material was processed using two different AM techniques, PTA-DED and L-PBF, resulting in solid metallic components. A set of characterization techniques was used to investigate the relationship between processing parameters, microstructure and properties of the Cu-modified stainless steel specimens. The processed materials were characterized in terms of geometrical features, cross-section porosity analysis, Archimedes density, chemical composition, microstructure, crystalline structure, mechanical testing and wear performance, as summarized in Figure 22.

Figure 22 - Processed material characterization

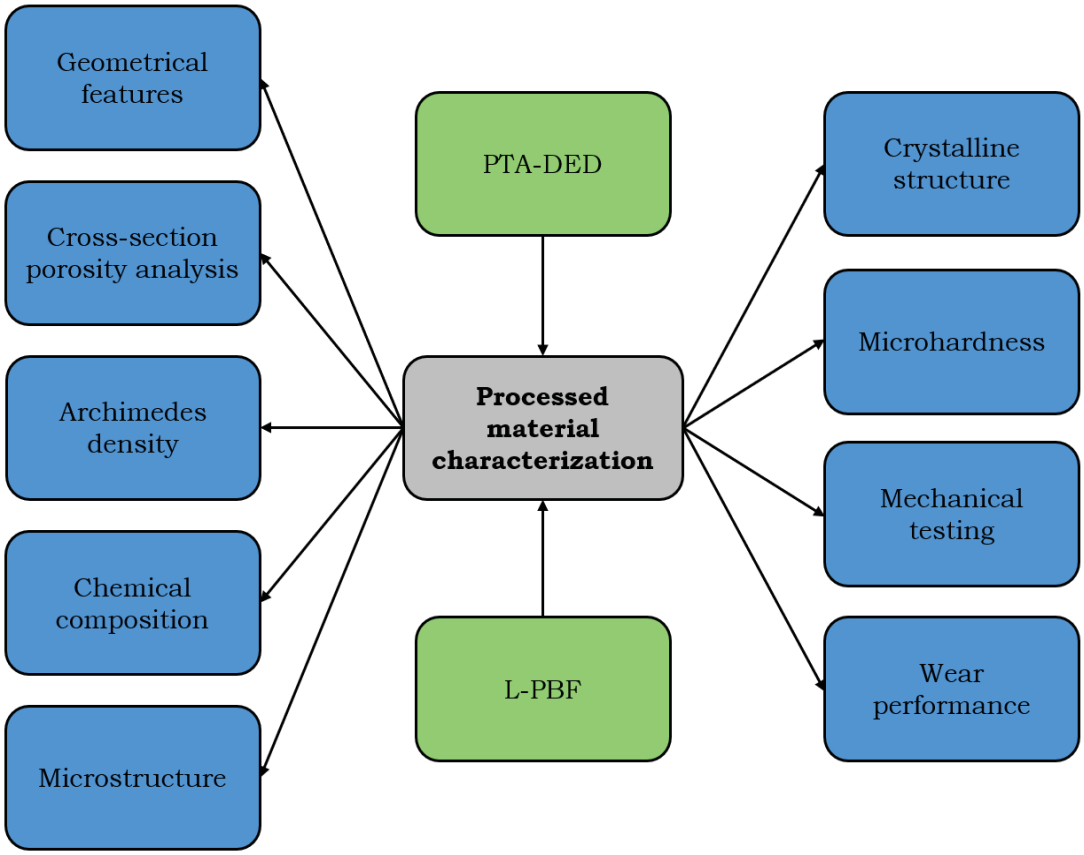

Source: Authors (2025).

- ✓ Geometrical features:

To investigate the relationship between chemical composition, processing parameters and resulting geometrical features, the single-tracks manufactured by

PTA-DED were cross-sectioned, as described on Figure 23. The cross-sectioned specimens were mounted in Bakelite, ground with 1200-grit SiC abrasive paper, polished with 1 µm alumina suspension and etched (as detailed in each corresponding Section). OM was used to capture micrographs of the cross-section, which were analyzed using ImageJ software to quantify geometrical dimensions.

Figure 23 - AISI 316L single-track: a) top view and b) cross-section view

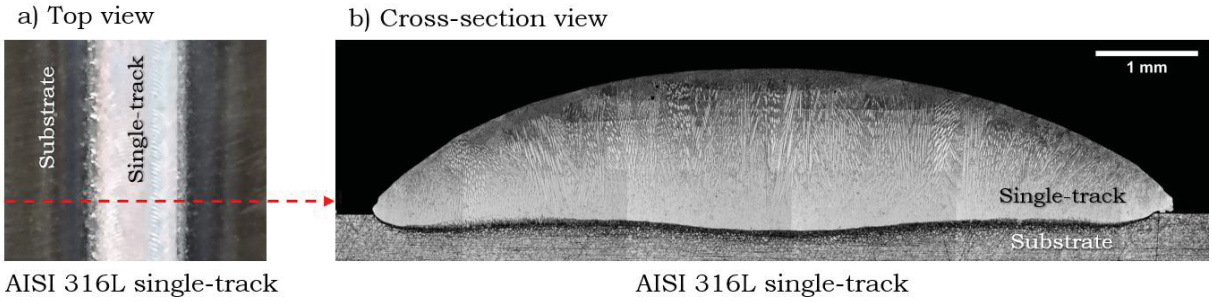

Source: Authors (2025).

The geometrical features measured on the cross-sections of the PTA-DED single-tracks included track height, width, reinforcement area, penetration area, and wettability angle, as illustrated in Figure 24. Based on these measurements, two key parameters can be calculated, dilution and Powder Catchment Efficiency (PCE). Dilution relates the quantity of material on the melt pool originated from the substrate and can be calculated using Equation 2:

$$Dilution\ (\%) = (P / (P + R)) \times 100\% \qquad (2)$$

where P is the penetration area (mm²) and R is the reinforcement area (mm²).

PCE assesses the efficiency of powder utilization during the deposition process, comparing the measured area of deposited material to the quantity of powder delivered by the feeding system. PCE can be calculated according to Equation 3, adapted from literature (Koti *et al.,* 2023):

$$PCE\ (\%) = ((R \times V \times \rho \times D_{IMAGE}) / (PFR)) \times 100\% \qquad (3)$$

where R is the reinforcement area (mm²), V is the deposition speed (mm/min), ρ is the theoretical density of the solidified material (g/mm³), D_{IMAGE} is the cross-sectional density determined by image analysis (%), and PFR is the powder feed rate (g/min).

Figure 24 - Geometrical features evaluated on the PTA-DED single-tracks

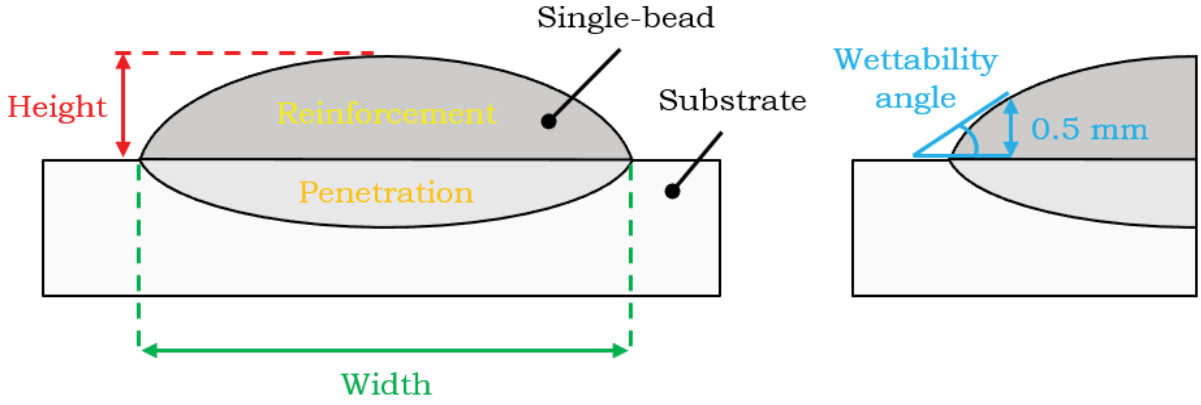

Source: Authors (2025).

Unlike PTA-DED, the melt pool geometrical features of L-PBF specimens were evaluated on the cross-section of the top layers, as illustrated in Figure 25. The melt pool width and depth are influenced by both the processing parameters and chemical composition of the feedstock. The melt pool dimensional analysis provides insights into defect formation mechanism, such as key-hole pores and lack of fusion pores, associated respectively with excessive and insufficient energy density.

Figure 25 - Micrograph and geometrical features evaluated on L-PBF melt pools

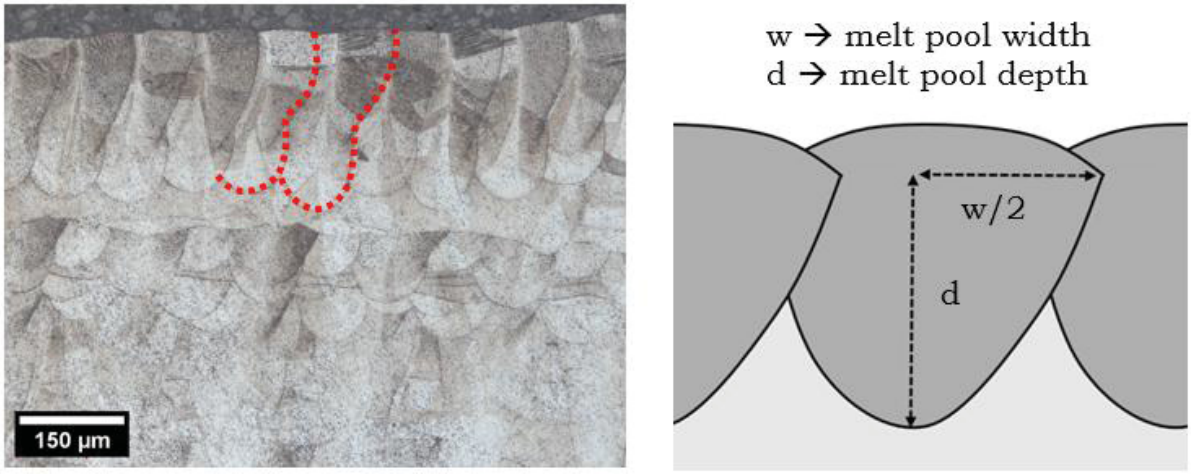

Source: Authors (2025).

✓ Cross-section porosity analysis:

The analysis of polished cross-section from both PTA-DED and L-PBF specimens allows for the inspection of defects, such as pores and cracks. The micrograph images can be obtained using OM and SEM. While OM provides a broader overview of the entire cross-section of the specimen, SEM offers higher resolution, making it preferable to detailed pore analysis at higher magnifications. Identification and quantification of pores from polished cross-section micrographs can be performed using image analysis software (ImageJ). The sequence of steps used for porosity analysis is presented in Figure 26.

Figure 26 - Cross-section porosity analysis sequence

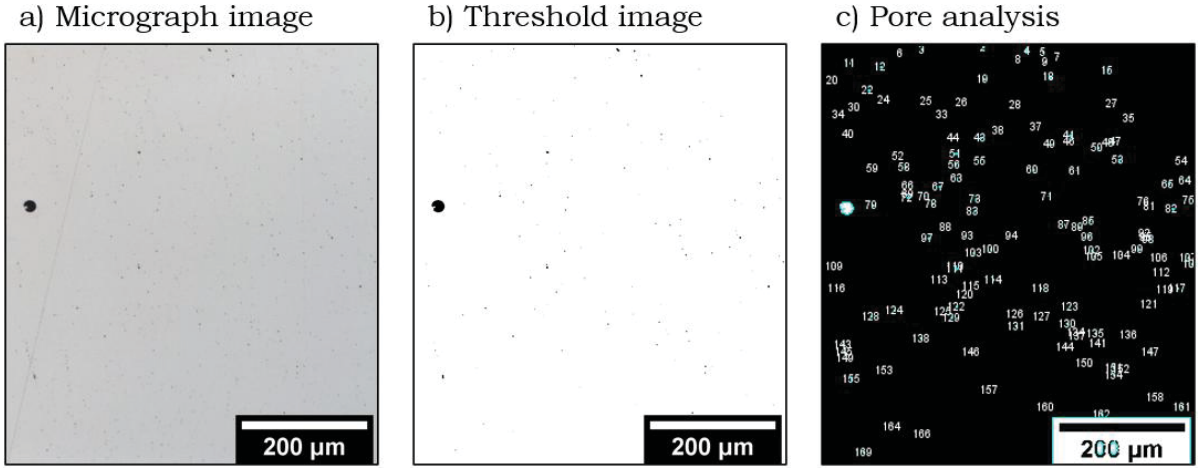

Source: Authors (2025).

First, a large number of micrographs are acquired from the specimen's cross-section. When OM is used, it is possible to capture the whole cross-section area. In the second step, the images are processed using the image analysis software by applying a thresholding technique, which converts color or grayscale images into binary format (black and white), contrasting the pores (black) from the surrounding material (white). In the third step, the software detects and measures individual pores, recording information on quantity, size and shape.

From the porosity analysis data, key metrics can be calculated, including cross-sectional porosity (%) and cross-sectional density (%). In addition, pore count (pore/mm²) and average pore size (µm²) can be determined. Providing information on

the influence of processing parameters and feedstock material on the integrity of the processed material.

✓ Archimedes density:

The cross-sectional density determined by imaging analysis represents the proportion of solid material area relative to pore area within a slice of the specimen, expressed in percentage. To determine the overall density of a specimen in g/cm³, the Archimedes method can be applied. The method involves using a precision laboratory balance equipped with density determination kit, as illustrated in Figure 27.

Figure 27 - Measuring density with laboratory balance

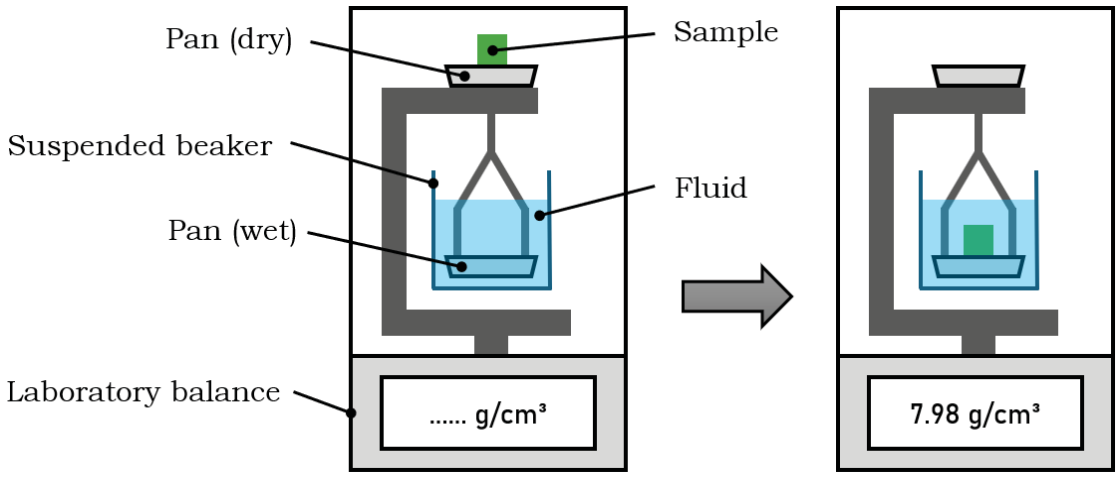

Source: Authors (2025).

The setup consists of a suspended beaker filled with a fluid of known density, along with two weighting pans, one for measuring the sample under dry condition (in air) and another under wet condition (fully submerged in the fluid). Following the Archimedes principle, the sample density can be obtained according to Equation 4, adapted from the literature (Mettler Toledo, 2025):

$$Density\ (g/cm^3) = ((\ m_d\ /\ (m_d - m_w)) \times (\rho_f - \rho_{air})) + \rho_{air} \qquad (4)$$

where m_d is the dry weight of the sample (g), m_w is the wet weight of the sample (g), which is reduced due to the buoyance force, ρ_f is the density of the fluid (g/cm³) at a controlled temperature, and ρ_{air} is the density of air (g/cm³). In this work, ethanol was

used as the immersion fluid, avoiding the formation of air bubbles, which are usually seen when using tap water.

✓ Chemical composition:

Similar to the methodology applied to feedstock characterization, the chemical composition of the processed materials was assessed using XRF and EDS coupled with SEM. XFR provided the quantitative analyses of the bulk composition of the processed material, enabling comparison between the original feedstock material. This is particularly relevant for powder mixtures containing NP, especially when processed by PTA. The interaction of Cu NP and CuO NP with the high temperatures of the plasma arc column might lead to the selective evaporation of finer particles with small volume, resulting in a reduced content of these elements in the melt pool and in the solidified material, further discussion on this topic is provided in Section 4.3.

Combining the EDS semi-quantitative elemental analysis capabilities with high-resolution SEM imaging, enables the assessment of chemical composition in specific regions within the microstructure. As exemplified in Figure 28, EDS was carried out on an etched AISI 316L + 1 wt% Cu specimen processed by PTA-DED.

Figure 28 - EDS analysis from AISI 316L + 1 wt% Cu processed by PTA-DED

a) Micrograph of etched specimen

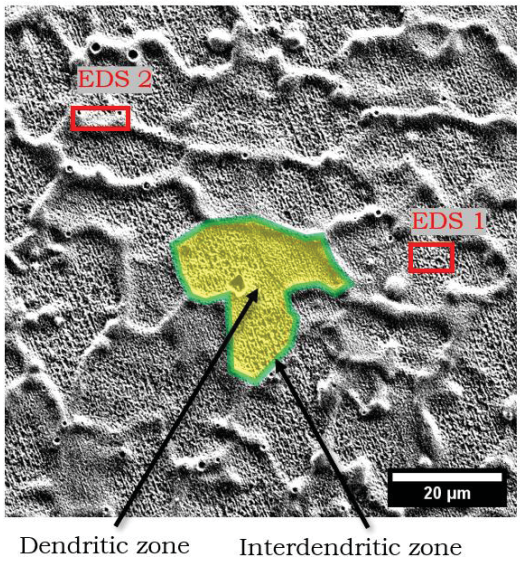

b) EDS spectrum and chemical composition

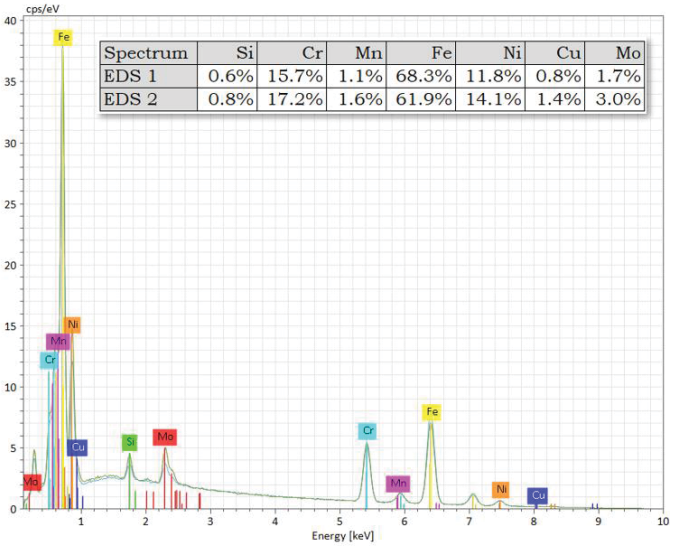

Spectrum	Si	Cr	Mn	Fe	Ni	Cu	Mo
EDS 1	0.6%	15.7%	1.1%	68.3%	11.8%	0.8%	1.7%
EDS 2	0.8%	17.2%	1.6%	61.9%	14.1%	1.4%	3.0%

Source: Authors (2025).

The etching provides contrast between the dendritic and interdendritic zones, allowing for EDS to be targeted to these regions to obtain their chemical composition. In this example, EDS revealed the segregation of elements, offering insight on the solidification sequence and indicating a preferential accumulation of solute, including the added Cu, in the interdendritic regions.

- ✓ Microstructure:

As previously described in the geometrical features section of this chapter, the cross-sectioned specimens were mounted, ground, polished and etched to reveal their microstructural features. For all feedstock material analyzed in this study, Marble's reagent was used as the chemical etchant, which is commonly used for austenitic stainless steels, due its effectiveness in revealing dendritic structures and elemental segregation. The reagent was prepared by mixing 4 g $CuSO_4$, 20 ml HCl and 20 mL of H_2O.

The etching procedure involved repolishing the specimen to remove any protective oxide layer, followed by ultrasonic cleaning in ethanol to eliminate any contaminants from the surface. Etching was then carried out by immersing the specimen in Marble's reagent for no more than 10 seconds. After etching, the specimens were rinsed with running water and subsequently ultrasonically cleaned in ethanol to remove any residual etchant from pores and edges. The sequence of steps followed for microstructural analysis is illustrated in Figure 29.

Figure 30 presents examples of micrographs of AISI 316L processed by L-PBF, obtained using OM, SEM, and Electron Backscatter Diffraction (EBSD). OM and SEM were utilized to characterize the etched specimens. OM enables the identification of melt pool boundaries in both horizontal (hatch distance) and vertical (layer height) directions. SEM, with higher resolution and magnification, reveals finer details, such as dendritic structures within individual grains.

In contrast, EBSD analysis was done on polished specimens, as the technique requires a low roughness, high quality surface finish for accurate data acquisition. EBSD provides information on grain orientation, grain size and crystallographic texture. The combinations of these characterization techniques allow for the understanding of the relationship between chemical composition, processing parameters, resulting microstructure and material performance.

Figure 29 - Sequence of steps followed for microstructural analysis

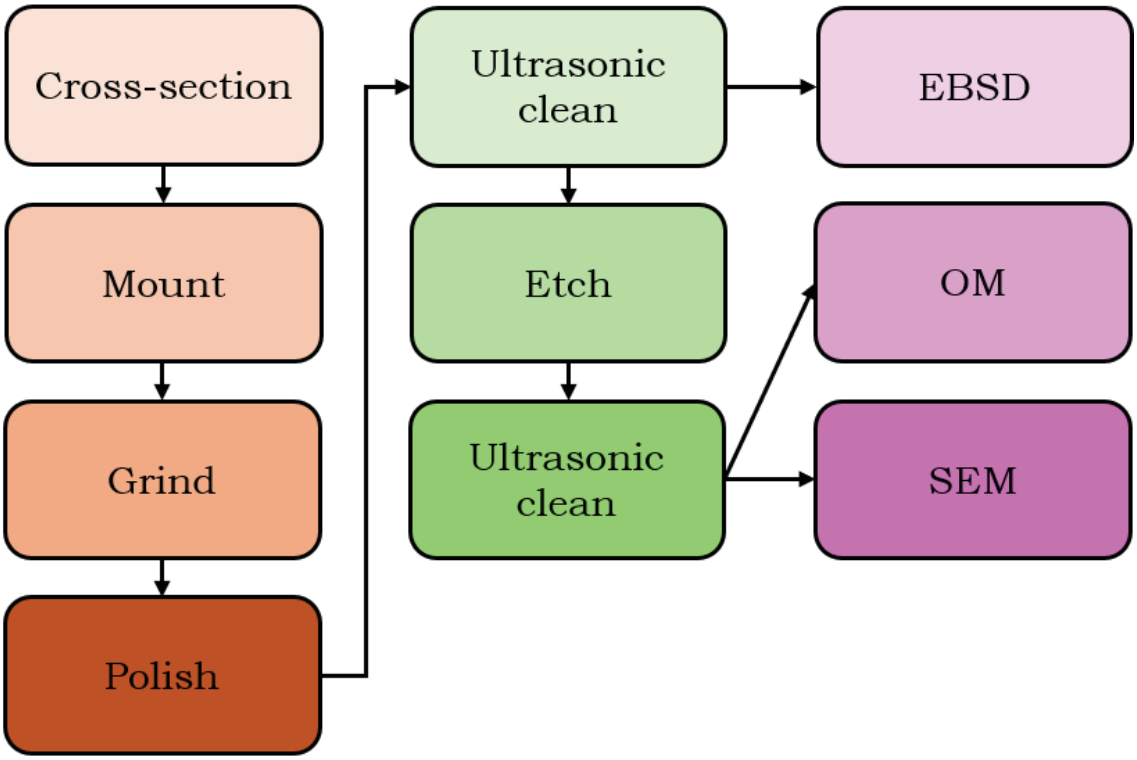

Source: Authors (2025).

Figure 30 - Comparison of micrographs obtained using a) OM, b) SEM, and c) EBSD

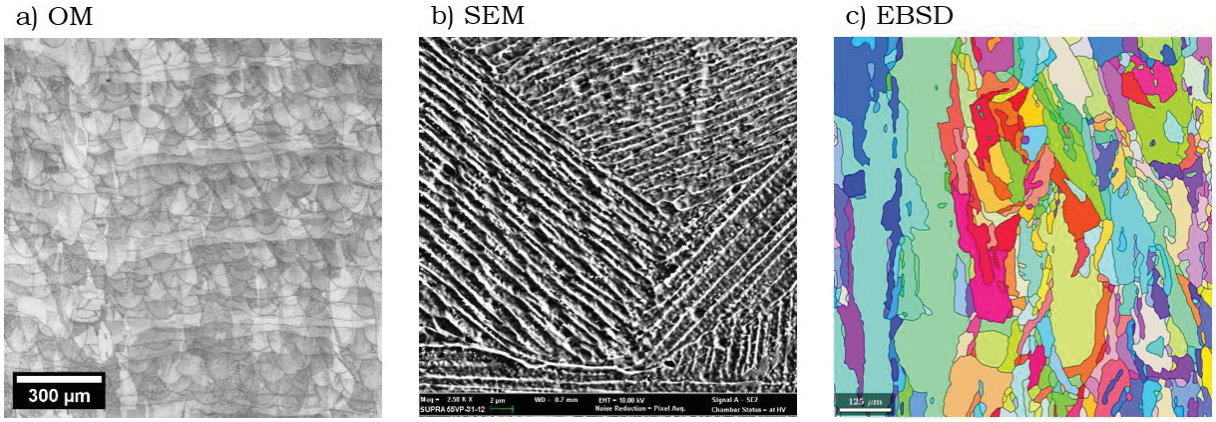

Source: Authors (2025).

✓ Crystalline structure:

The crystalline structure of materials processed by both PTA-DED and L-PBF was analyzed by X-ray diffraction (XRD). To avoid interference in the results, the substrates were removed from the specimens, including the single-track coatings. Prior to analysis, the specimens were ground and polished but not mounted on

Bakelite, to avoid noise from the mounting material. XRD provides information on crystalline structure, phase composition, and lattice parameters. This allows for the analysis of the phase transformations induced by the rapid solidification during processing, as well as changes in phase composition and lattice parameter resulting from post-processing heat treatments.

✓ Microhardness:

Microhardness profiles were obtained using a micro-indentation tester equipped with a Vickers indenter. A micrograph of a Vickers indentation is provided in Figure 31a. Different loads were applied depending on the processing technique, 300 or 500 g for PTA-DED and 1000 g for L-PBF, all with a dwell time of 10 seconds. Measurements were performed on polished cross-section of the specimens, as illustrated in Figure 31.

For the PTA-DED single-walls, three parallel hardness profiles were measured, starting on the substrate and moving with 0.5 mm steps in both the horizontal and vertical directions. This approach enables the calculation of an average hardness profile, relative to the distance from the interface between the substrate and deposited material.

Figure 31 - a) Micrograph of a Vickers indentation and hardness profiles on the cross-section of b) PTA-DED single-wall and c) L-PBF cube

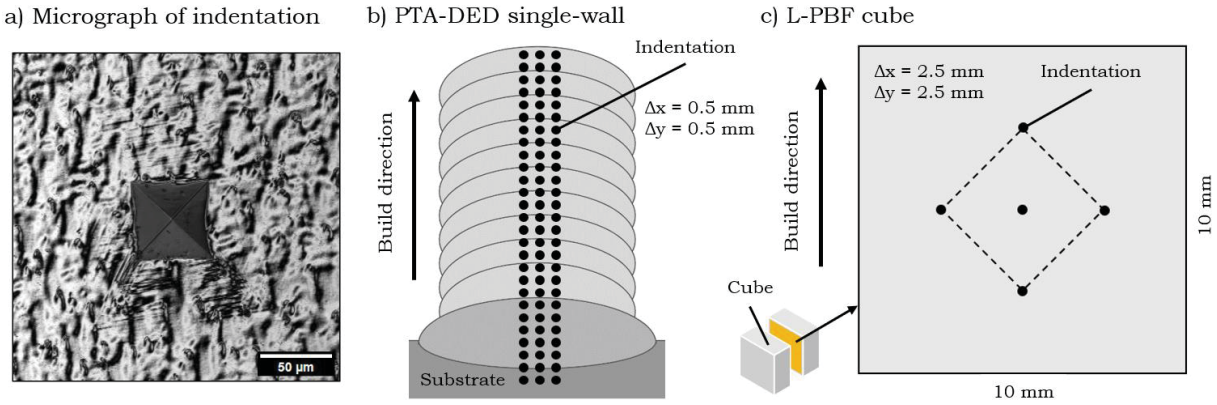

Source: Authors (2025).

As for the L-PBF cubes, hardness was measured at five locations, one at the center of the cube cross-section and in four indentations surrounding it. A total of 27 sets of processing parameters were tested for two different feedstock materials,

resulting in 54 cube specimens. The use of a higher load (1000 g) and measurement of five indentations points per specimen provided a reliable assessment of average hardness. This procedure allows for a comparative evaluation of the effects of Cu addition and processing parameters on the mean hardness of the L-PBF processed materials.

- ✓ Mechanical testing:

Mechanical testing of the materials processed by L-PBF was carried out in accordance with ASTM E8/E8M - Standard Test Methods for Tension Testing of Metallic Materials. Subsize rectangular specimens were employed in this study, with dimensions shown in Figure 32a. Both as-built and heat-treated samples were machined to required dimensions using Electrical Discharge Machining (EDM), followed by surface preparation using 600-grit SiC abrasive paper, as illustrated in Figure 32b. Tensile tests were performed on a universal testing machine equipped with a clip-on extensometer to measure displacement during testing, as shown in Figure 32c.

Figure 32 - a) Test testing sub size specimen dimensions, b) photo of tensile specimens prepared by EDM, and c) photo of tensile testing setup

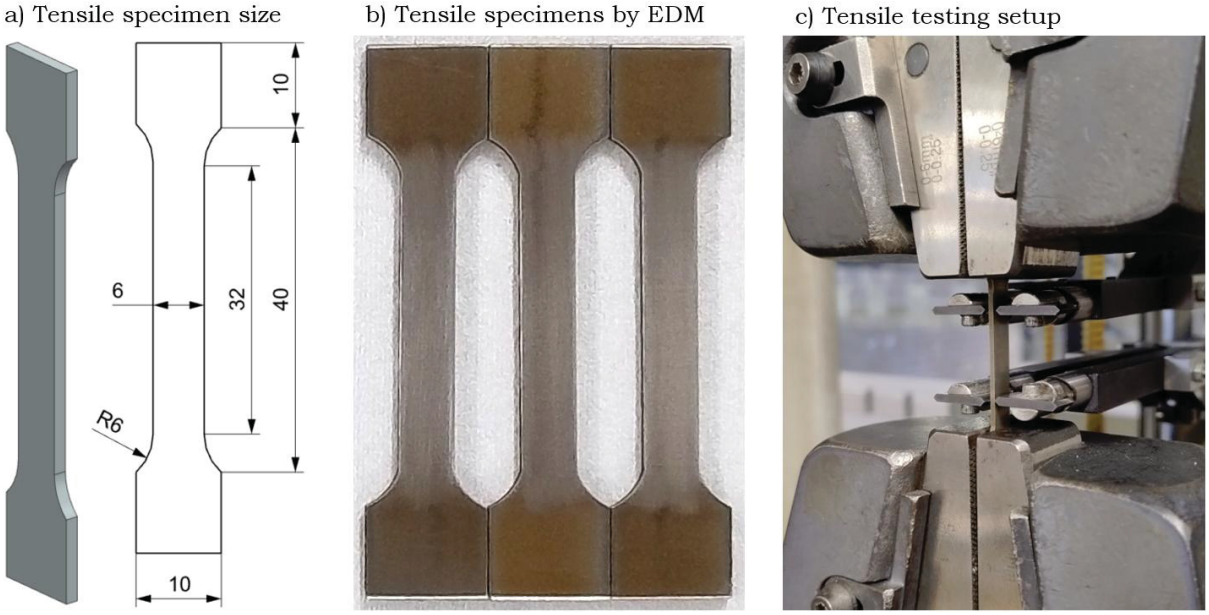

Source: Authors (2025).

The data collected enables the calculation of yield strength, ultimate tensile strength (UTS) and strain at UTS. After testing, the fractured regions and fractured surfaces were examined using a stereo microscope and SEM to assess the fracture mechanisms associated with Cu addition, energy input levels and the effects of heat treatment.

✓ Wear performance:

The wear performance was evaluated on a ball-on-disk tribometer using a 3 mm diameter 100Cr6 steel ball as the counter body. The sliding wear tests were performed under dry conditions at room temperature. Specimens were tested in both as-built and heat-treated conditions, and their cross-sections were prepared by grinding with 1200-grit SiC abrasive paper followed by ultrasonic cleaning in acetone. The wear performance test details are presented in Section 4.4.

The profiles of the wear track cross-sections were measured using CLSM, as described in Figure 33. Measurements were taken at 12 evenly distributed locations along the circumference of the wear track. The coefficient of friction (COF) was continuously monitored and recorded in real-time using the load cell integrated into the tribometer.

Figure 33 - Circular wear track on the single-wall cross-section and b) procedure used for wear track profile measurements

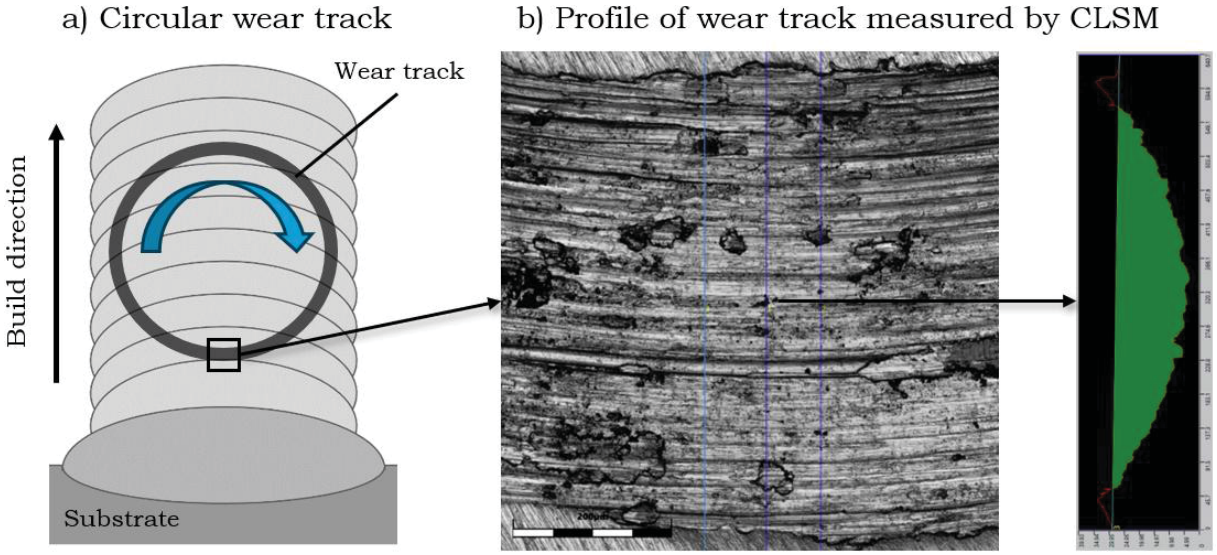

Source: Authors (2025).

After obtaining the profile measurements, the wear coefficient can be determined using Equation 5, based on the Archard's wear model (Archard, 1953):

$$\text{Wear coefficient } (mm^3 / (N \times m)) = (2 \times \pi \times r \times S) / (F \times D) \quad (5)$$

where r is the wear track radius (mm), S is the average cross-section profile area of the wear track (mm^2), F is the normal load applied (N) and D is the total sliding distance (m).

Post-testing analysis of the worn surface was carried out using SEM equipped with a secondary electron (SE) detector at 15 kV with a 60 μm aperture. In addition, SEM with a backscattered electron detector (BSD) and EDS at 10 kV with a 60 μm aperture were used to assess the extent of tribolayer formation and its chemical composition.

4 RESULTS AND DISCUSSIONS

The results and discussions are organized into sections that align with the key topics assessed in published and forthcoming papers. These contributions include a conference paper, a book chapter, and a journal paper that have already been published during the course of this research. In addition, other significant findings are presented in the form of a submitted journal paper currently under review, and a journal paper in preparation for submission. The structure of this chapter follows the methodology flowchart (Figure 12), with the sequence of papers illustrated in Figure 34. Section 4.1 addresses the feedstock material (highlighted in green), Sections 4.2 and 4.3 focus on coatings produced by PTA-DED (blue), and Sections 4.4 and 4.5 examine, respectively, PTA-DED and L-PBF as additive manufacturing techniques (orange).

Figure 34 - Chapter structure organized as a sequence of papers

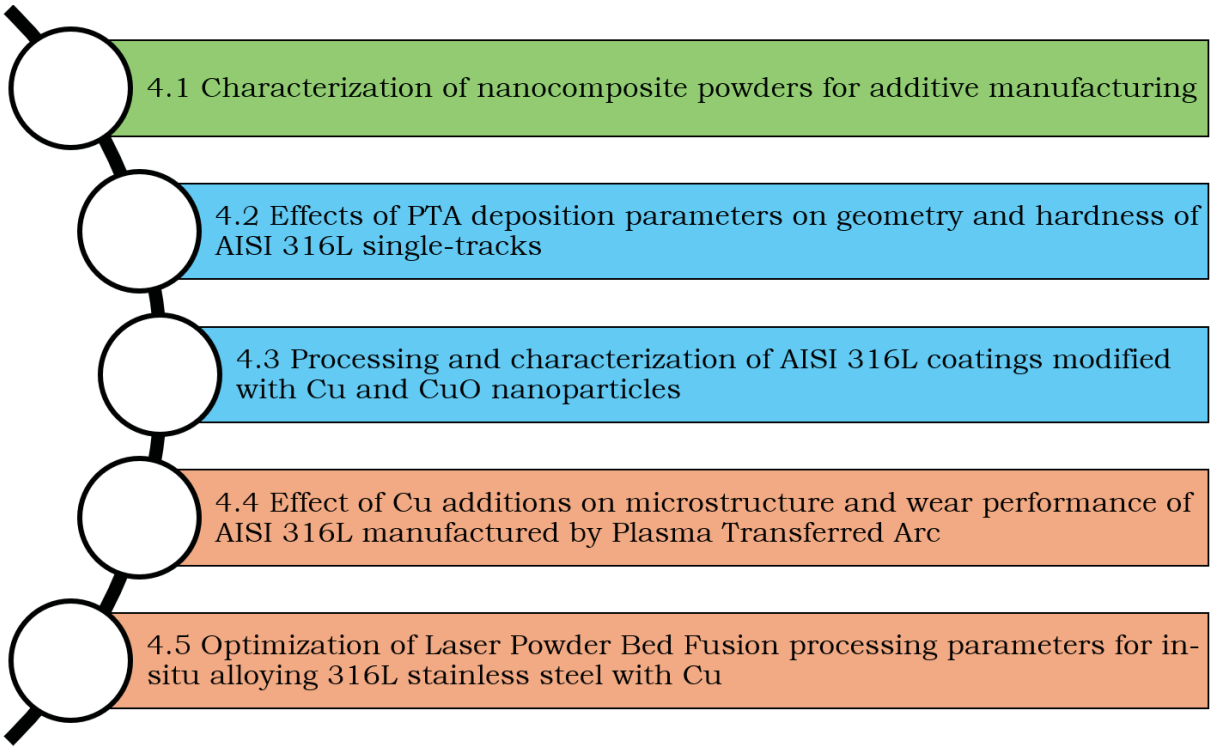

Source: Authors (2025).

The following sections describe the activities undertaken and their contributions to the research, emphasizing how each paper supports the overall findings.

Characterization of nanocomposite powders for additive manufacturing

The conference paper, presented in Section 4.1, was developed in collaboration with the SENAI Innovation Institute in Manufacturing Systems and Laser Processing. Authored by Gustavo Scheid Prass[1,2], Victor Lira Chastinet[2] and Ana Sofia C. M. d'Oliveira[1], from [1]Federal University of Paraná and [2]SENAI Innovation Institute in Manufacturing Systems and Laser Processing, this paper was presented at the **27th International Congress of Mechanical Engineering**, organized by the Brazilian Society of Mechanical Sciences and Engineering - ABCM (*Associação Brasileira de Engenharia e Ciencias Mecânicas*). Held in December 2023 in Florianopolis-SC, Brazil.

This paper investigates the preparation and characterization of powder mixtures and nanocomposite powders for AM using gas atomized 316L stainless steel as the carrier powder, with Cu MP, Cu NP, and CuO NP as host particles. Contributing to the understanding on how the characteristics of these powder mixtures, each containing various forms of Cu particles, impact the deposition process, and the resulting material density and chemical composition.

The study found that nanoparticles notably influence flowability and processability, stressing the need for specific procedures in the mixing, handling, and processing of powders with nanoparticles. Nonetheless, customized powders achieved a homogeneous distribution between the carrier and guest particles, indicating that PTA-DED can be used as an effective technique for processing these materials as coatings and AM parts.

Effects of PTA deposition parameters on geometry and hardness of AISI 316L single-tracks

The book chapter, presented in Section 4.2, was developed with contributions from an undergraduate research student enrolled in our project. Authored by Gustavo Scheid Prass, Pedro Weiss Mattioli and Ana Sofia C. M. d'Oliveira, from Federal University of Paraná, the book chapter originated from a paper presented at the **12th Brazilian Manufacturing Engineering Congress** - 12th COBEF (12º *Congresso Brasileiro de Engenharia de Fabricação*) in May 2023, Brasília-DF, Brazil. After being presented in the 12th COBEF, the paper was selected

to be published as a chapter in the book **ABCM Series on Mechanical Science and Engineering**, edited by Déborah de Oliveira (University of Brasília), Maksym Ziberov (University of Brasília) and Alisson Rocha Machado (Pontifical Catholic University of Paraná). The book was published by Springer Nature in September 2023, with DOI: 10.1007/978-3-031-43555-3_13.

This study addresses the effects of deposition current and deposition speed on the geometry and hardness of single-track 316L coatings produced by PTA-DED. The design of experiments (DoE) approach was employed to systematically organize data in a comprehensive manner, and to facilitate a deeper understanding of how processing parameters govern the geometrical features of single-track coatings.

Results demonstrate a clear relationship between processing parameters on both hardness and geometrical features, while the DoE provides reliable predictive estimates on the interaction between substrate and the deposited material. The resulting process window mapping provides a foundation for selecting optimal parameters to achieve high-quality single-track coatings with controlled geometry, a significant step forward in establishing PTA-DED as a robust AM technique.

Processing and characterization of AISI 316L coatings modified with Cu and CuO nanoparticles

The journal paper, featured in Section 4.3, was developed by Gustavo Scheid Prass[1,2] and Ana Sofia C. M. d'Oliveira[1], from [1]Federal University of Paraná and [2]SENAI Innovation Institute in Manufacturing Systems and Laser Processing. Preliminary results were initially presented at the **XX B-MRS Meeting**, organized by the Brazilian Materials Research Society - SBPMat (*Sociedade Brasileira de Pesquisa em Materiais*), held in September 2022 in Foz do Iguaçu-PR, Brazil. The authors received the **Bernhard Gross Award** for the best oral presentation of Symposium U - Surface Science and Engineering. The complete research paper was submitted to **Surface & Coating Technology** scientific journal and was later published in March 2023, with DOI: 10.1016/j.surfcoat.2023.129465.

This paper explores the processing and characterization of 316L stainless steel coatings produced by PTA-DED with addition of 5 wt% Cu MP, 5 wt% Cu NP, and 5 wt% CuO NP, individually. Contributing to the understanding of how the interaction between the powder feedstock and the plasma arc during deposition

affects the processability and metallurgical features of stainless steel coatings. Additionally, a hypothesis regarding the behavior of the powder mixtures within the plasma arc is proposed.

The results indicate that the addition of both Cu NP and CuO NP require higher energy to avoid lack of fusion. Notably, the increased vaporization of nanoparticles, as they interact with the plasma arc leads to a significant loss of Cu. Regardless of the feedstock composition, the Cu-containing coatings exhibited lower hardness, which can be attributed to Cu being in solid solution in the as-deposited condition. Following this initial assessment of the effects on processability and the loss of Cu content associated with the addition of 5 wt% NP to the stainless steel, subsequent studies were conducted with a reduced NP content of 1 wt%.

Effect of Cu additions on microstructure and wear performance of AISI 316L manufactured by Plasma Transferred Arc

Section 4.4 assesses a complete research paper submitted to a scientific journal in 2025. The authors are Gustavo Scheid Prass and Ana Sofia C. M. d'Oliveira, from Federal University of Paraná. Preliminary findings from this study were presented at the **XXI B-MRS Meeting**, organized by the Brazilian Materials Research Society - SBPMat (*Sociedade Brasileira de Pesquisa em Materiais*), which took place in October 2023 in Maceio-AL, Brazil.

In this paper, PTA-DED was employed to fabricate single-wall multilayers, as described in Section 3.2, using powder mixtures that included 316L stainless steel, Cu MP, Cu NP and CuO NP. The wear performance of the stainless steel multilayers was evaluated by examining the effects of varying Cu contents (1 and 5 wt%), the Cu particle size (micro and nanoparticles) and post-fabrication heat treatments. The analysis provided an advance in the current knowledge of how Cu content, particle type and post-fabrication heat treatment influence the microstructure, mechanical properties, and wear performance of stainless steel single-walls fabricated by PTA-DED.

PTA-DED demonstrated excellent powder catchment efficiency while producing dense, defect-free single-walls, indicating it as a competitive AM technique when compared to laser-based DED techniques. Regarding wear performance, the addition of 5 wt% Cu microparticles to the stainless steel significantly reduced both

the coefficient of friction and the wear rate. Following solubilization, the subsequent aging heat treatment of the Cu-containing stainless steel specimens resulted in increased hardness, indicating the formation of Cu-rich precipitates.

However, while the heat treatments had no significant impact on wear performance, they could influence other properties, such as antimicrobial activity. In this sense, an antimicrobial assessment is being carried out.

Optimization of Laser Powder Bed Fusion processing parameters for in-situ alloying 316L stainless steel with Cu

Section 4.5 addresses a study carried out during a sandwich doctorate period at the Advanced Material Processing Laboratory (AMPLab) at the University of Birmingham, United Kingdom, under the guidance of Professor Moataz M. Attallah, PhD. The section provides an overview of the key findings from the study, as a complete research paper is currently in preparation.

In previous sections, PTA-DED was used to process stainless steel coatings and multilayers with varying forms and contents of Cu. This section introduces another AM technique to *in-situ* alloy AISI 316L with Cu from powder mixtures, laser powder bed fusion (L-PBF), which allows for the manufacture of complex geometries using powder as feedstock, as detailed in Section 3.3. Unlike PTA-DED, L-PBF employs a highly focused heat source, enabling lower heat input and faster cooling rates. Additionally, L-PBF can induce multiple remelting cycles depending on the selected processing parameters. The relationship between processing parameters microstructure and mechanical properties of Cu-modified stainless steel specimens are further explored in this study.

Through an optimization process for both 316L and 316L with 5 wt% Cu, parameter sets were identified and enabled the fabrication of dense, defect-free specimens. At lower energy densities, both materials showed a refined microstructure that improved the mechanical properties of 316L, though this same energy level caused incomplete Cu homogenization in the matrix due to a shallower melt pool that limited full remelting of previous layers. This observation aligns with findings in PTA-DED coatings, indicating that Cu-containing powders require higher energy input to prevent lack of fusion.

Appendices

Antimicrobial assessment

Appendix A presents some preliminary findings of the antimicrobial assessment for 316L and 316L with Cu addition, specifically single-wall multilayers processed by PTA-DED. This study is being conducted at the "*Laboratório de Bacteriologia Clínica*" at Federal University of Paraná, with contributions from Professor Wesley Mauricio de Souza and his team.

The single-walls, which were previously evaluated for wear performance, are test for antimicrobial activity against *E. coli* and *S. aureus* to elucidate the effects of Cu content (1 and 5 wt%), Cu particle size (MP and NP), and heat treatment. Preliminary results, for specimen in the as-deposited condition, indicate that the addition of Cu to the stainless steel reduces the number of *E. coli* colonies after a 24-hour incubation period, although it does not significantly affect *S. aureus*. Therefore, an increased Cu content, combined with heat treatment, is expected to enhance the observed antimicrobial activity, although results for the heat-treated specimens are still pending.

In addition to evaluating wear performance and antimicrobial activity, the multilayers deposited by PTA-DED are also assessed for their corrosion resistance.

Corrosion resistance

Appendix B addresses selected results from corrosion resistance studies on 316L stainless steel processed by PTA-DED and HVOF (High Velocity Oxy-Fuel) with varying Cu additions. This work was conducted with contributions from Professor Juliane Ribeiro da Cruz Alves, formerly a postdoctoral researcher at the Federal University of Paraná and currently an Assistant Professor at the University of São Paulo.

This study investigates the effect of Cu content and particle type on the corrosion resistance of modified stainless steel single-walls deposited by PTA-DED, comparing these AM materials to those produced by high-velocity oxy-fuel (HVOF) and conventional bulk materials.

L-PBF with heat treatment

Additionally, a brief preview of the results from the ongoing investigation on the “**Impact of heat treatments on mechanical properties and wear resistance of in-situ alloyed Cu-bearing 316L stainless steel produced by Laser Powder Bed Fusion”** is presented in Appendix C.

4.1 CHARACTERIZATION OF NANOCOMPOSITE POWDERS FOR ADDITIVE MANUFACTURING

ABSTRACT

Additive manufacturing (AM) of metallic parts includes a set of techniques where three-dimensional objects are built up layer by layer using metallic powder or wire as feedstock. The use of metallic powder has its own advantages, such as the ability to blend different powders to obtain customized chemical compositions, which drives innovation in the development of new materials. In this context, nanocomposite powders can be introduced to AM processes to take advantage of their unique properties. Nanocomposite powders are materials consisting of a carrier powder, generally microparticles (MPs), and one or more types of nanoparticles (NPs) that are distributed on the MPs surface. Characterization of the nanocomposite powders is important to understand their behavior during the additive manufacturing process and to select processing parameters, leading to the production of defect-free parts with desired properties. In this study, different powder compositions were obtained by individually mixing AISI 316L with 1 wt% Cu MPs, Cu NPs, and CuO NPs. The mixtures with NPs were carried out in two steps, the first mixture was done in a mechanical mixer with pure ethanol to avoid agglomeration of the NPs and the second mixture was done in a Y-type mixer after drying (50°C for 24 h). AISI 316L and Cu MPs both range from 75 to 150 μm as measured by dynamic image analysis (DIA). Cu NPs and CuO NPs have average particle sizes of 500 nm and 30 nm, respectively, according to the manufacturer. Scanning electron microscopy (SEM) was used to analyze powder morphology, SEM images showed that the electrolytic Cu MPs are irregular with a dendritic-like morphology and gas-atomized AISI 316L particles are mostly spherical, with satellite particles. The MPs had some porosity that was not observed in the multilayers processed by plasma transferred arc (PTA). Cu NPs and CuO NPs adhered to the surface of the carrier particles in a well-distributed manner. Energy-dispersive X-ray spectroscopy (EDS) confirmed the composition of powder mixtures. Powder flowability was evaluated using a Hall funnel with dried (80°C for 2 h) and non-dried powder mixtures. Results showed that powder mixtures containing NPs required drying before the deposition to mitigate the negative impact of humidity on powder flowability. Deposited multilayers processed

with nanocomposite powder mixtures have a similar density to those processed with atomized stainless steel, whereas powder mixtures containing Cu MPs resulted in denser multilayers.

Keywords: Additive Manufacturing, Nanocomposite Powder, AISI 316L, Cu, CuO.

INTRODUCTION

Additive manufacturing (AM) is a technology that allows for the fabrication of complex metallic parts, in a process which involves processing the feedstock layer-by-layer (Huang *et al.,* 2014). Among the available feedstock options, powders offer versatility in creating customized chemical compositions, enabling the development of advanced materials with tailored properties (Li *et al.,* 2019; Dong *et al.,* 2020; Cui *et al.,* 2022). A particularly promising approach is the generation of nanocomposite powders, where guest nanoparticles (NPs) are incorporated into the carrier powder matrix (Zhuang *et al.,* 2020; Soulier *et al.,* 2022). During this process, the guest NPs adhere to the carrier particle surface, if their adhesion force surpasses their gravity force. However, this introduces changes in the interaction between the carrier particles, altering critical properties, such as cohesion and flowability (Sharma; Setia, 2019).

In the context of AM, Powder Bed Fusion (PBF) and Directed Energy Deposition (DED) are two techniques where the powder characteristics play an important role in processability. In PBF, successive thin layers of powder must be evenly spread across the powder bed to create fully dense parts (Avrampos; Vosniakos, 2022; Abu-Lebdeh *et al.,* 2022). Similarly, in DED, a consistent powder flow through a feeding system is crucial for deposition (Mellin *et al.,* 2017; Garg *et al.,* 2023). Thus, the development of advanced materials for AM requires a thorough understanding of the interaction between the microparticles (MPs) and NPs, elucidating their impact on processability and the resulting properties of the fabricated parts.

As part of an ongoing project aiming to enhance the antimicrobial properties of stainless steel by adding Cu particles to the metal matrix. This study approaches the preparation and characterization of nanocomposite powder for AM. The deposition of powder mixtures, consisting of stainless-steel powder and different Cu

particles, were carried out using the plasma transferred arc (PTA) deposition process. Notably, the effect of powder characteristics on flowability and part density were assessed.

MATERIALS AND METHODS

Four primary materials were used to investigate the characteristics of nanocomposite powders for AM. Commonly applied in AM, gas atomized AISI 316L powder (85 - 150 μm) served as the carrier powder. As guest powder, Cu was provided in the form of Cu microparticles (Cu MP, 89 - 143 μm), Cu nanoparticles (Cu NP, about 500 nm) and CuO nanoparticles (CuO NP, about 40 nm). The stainless-steel powder was individually mixed with 1 wt% of Cu MP, Cu NP and CuO NP to obtain the powder mixtures.

For the powder mixture containing Cu MPs, the powders were dried in a furnace at 80 °C for 2 h before being mixed in a Y-type mixer for 2 h, ensuring uniform distribution of Cu particles within the stainless-steel powder. The preparation of nanocomposite powders is more complex, as NPs tend to agglomerate in clusters, not adhering to the carrier particle surface. The dispersion of NPs was performed in an ultrasonic bath with ethanol for 300 s. The stainless-steel powder was added to the ethanol-dispersed NPs and mechanically stirred for 2 h. The ethanol was evaporated in a furnace at 50 °C for 24 h. Finally, the dried powders were mixed in a Y-type mixer for 12 h to guarantee strong adhesion between the guest NPs and the surface of the carrier MPs.

Powder mixtures and particles morphology were assessed by optical microscopy (OM), scanning electron microscopy (SEM) and field emission gun equipped SEM (FEG-SEM). Particle size distribution, particle shape and circularity of AISI 316L powder and Cu MP were performed by dynamic image analysis (DIA) in accordance with ASTM B822-20, while their cross-section density was measured by SEM. Flow behavior of the non-dried (shelf condition) and dried (80 °C for 2h) powder mixtures was characterized using a Hall flowmeter funnel, following ASTM B213-20.

Plasma transferred arc (PTA) was employed to deposit the powder mixtures on AISI 304L plates. Single-bead walls with 11 layers and length of 150 mm were deposited using a mass flow rate of 6 g/min, deposition speed of 100 mm/min and

deposition current of 120 A (first layer) and 80 A (other layers). Argon was used as carrier gas (0.8 L/min), plasma gas (2 L/min) and shield gas (15 L/min). The single-bead wall cross-sections were ground and polished with alumina (1 μm) to achieve a mirror-like finish. The density and chemical composition of the PTA-deposited materials were assessed by OM and X-ray fluorescence (XRF), respectively.

RESULTS AND DISCUSSION

XRF analysis was performed for AISI 316L powder and calculated for the powder mixtures, incorporating 1 wt% of Cu MP, 1 wt% of Cu NP and 1 wt% CuO NP. When comparing the powder mixtures, it is evident that the addition of the different Cu particles has low impact on the elemental percentage of AISI 316L. However, it should be noted that 1.0 g of CuO adds approximately 0.8 g of Cu and 0.2 g of O to the mixture. Table 7 presents the chemical composition of the powder mixtures in weight percentage.

Table 7 - Chemical composition of the powder mixtures in weight percentage

Powder mixture	Fe	Cr	Ni	Mo	Mn	S	Si	P	Cu	O	Source
AISI 316L	Bal.	17.64	12.52	3.34	1.72	0.69	0.53	0.09	-	-	XRF
AISI 316L + Cu MP	Bal.	17.47	12.40	3.31	1.70	0.69	0.52	0.09	1.00	-	calculated
AISI 316L + Cu NP	Bal.	17.47	12.40	3.31	1.70	0.69	0.52	0.09	1.00	-	calculated
AISI 316L + CuO NP	Bal.	17.47	12.40	3.31	1.70	0.69	0.52	0.09	0.80	0.20	calculated

Source: Authors (2023).

Figure 35 illustrates the OM and SEM images of the AISI 316L powder and AISI 316L + Cu MP powder mixture. Stainless-steel particles are gray (Figure 35a) and exhibit a predominantly spherical shape with some satellite particles (Figure 35b). At a higher magnification, the roughness of the particle surface (Figure 35c) can be seen. The adhesive interactions between the spherical particles are greatly reduced by the surface roughness, improving powder flowability (Sharma; Setia, 2019). As a hypothesis, the surface roughness benefits the generation of nanocomposite powder, since the small wrinkles and groves serve as points of anchorage for the NPs. The Cu MPs are red-orange and are well distributed among the stainless-steel particles (Figure 35d). In contrast, the Cu MPs are irregular in

shape (Figure 35e) and have a higher surface-to-volume ratio (Figure 35f), which could be detrimental to the powder flowability if added in excessive quantities.

Figure 35 - OM and SEM images of (a, b, c) AISI 316L powder and (d, e, f) AISI 316L + Cu MP powder mixture

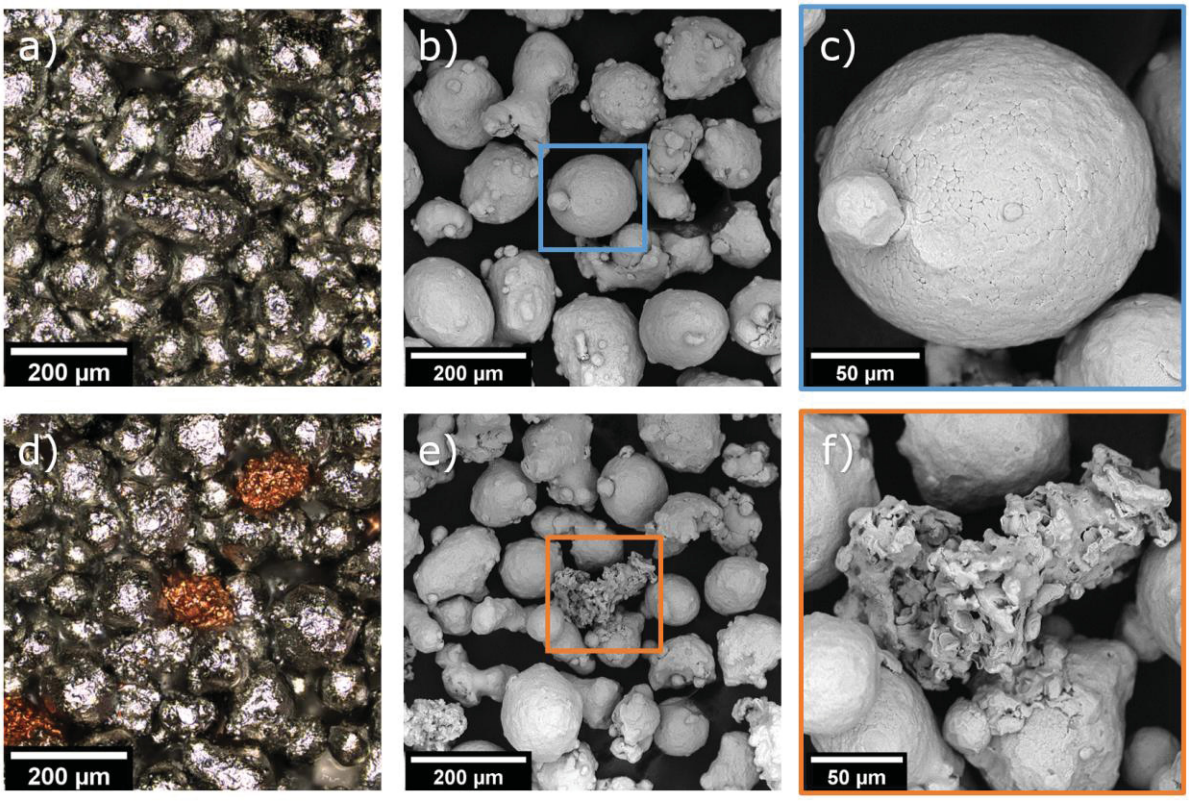

Source: Authors (2023).

Figure 36 presents the OM and FEG-SEM images of the nanocomposite powders of AISI 316L + Cu NP and AISI 316L + CuO NP. The carrier particles, originally gray, acquired a red-orange appearance, showcasing the presence of guest Cu NPs (Figure 36a). The Cu NPs are adhered to the carrier particle in a well-distributed manner, partially covering its surface (Figure 36b). At higher magnifications, the NPs can be seen adhered to the surface individually and in clusters (Figure 36c). The CuO NPs presence changed the color of the carrier particles to a brownish-orange color (Figure 36d). The CuO NPs adhered to the AISI 316L particles surface (Figure 36e). Due to its reduced size of approximately 40 nm, the NPs covered the surface almost completely (Figure 36f).

Figure 36 - OM and FEG-SEM images of (a, b, c) AISI 316L + Cu NP powder mixture and (d, e, f) AISI 316L + CuO NP powder mixture

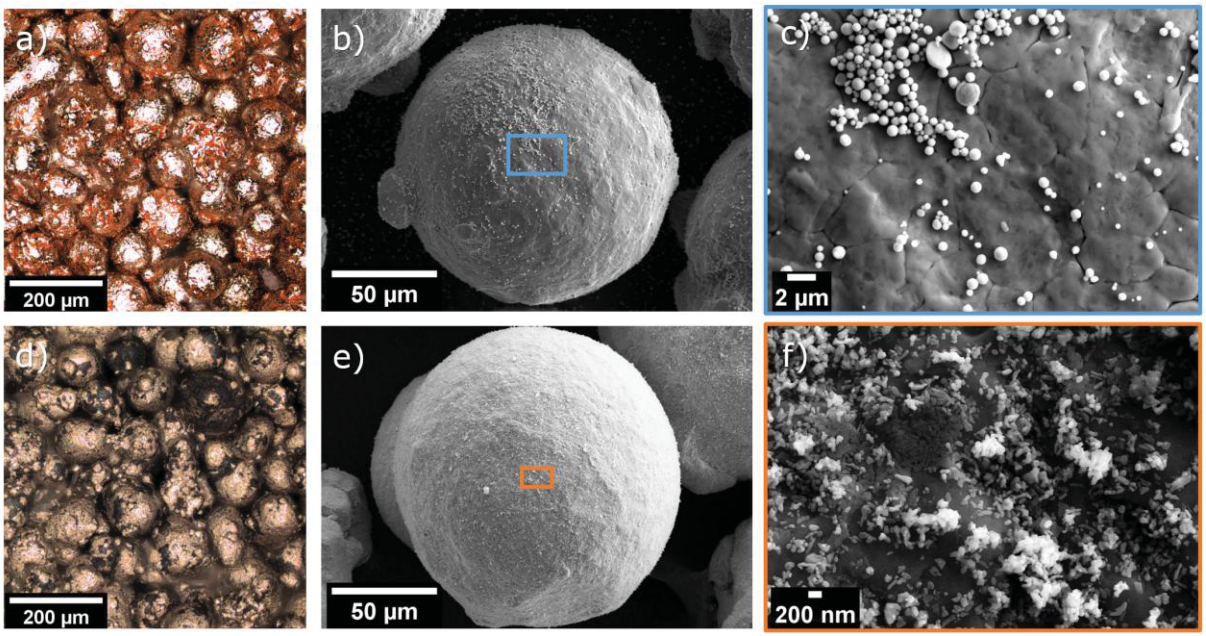

Source: Authors (2023).

Figure 37 provides information about powder size distribution for AISI 316L and Cu MPs, respectively. The equivalent circular area (ECA) diameter can be determined by the average size of particles in volume percentage and in number percentage. The volume distribution of AISI 316L (Figure 37a) shows that 10% of the volume comes from particles smaller than 85.6 µm and 10% of the volume comes from particles bigger than 150.0 µm. The number distribution of AISI 316L (Figure 37b) shows that 10% of the particles are smaller than 20.9 µm and 10% of the particles are bigger than 120.3 µm. This behavior is expected in for powders with satellite particles, since the satellites can break from the bigger particles during transportation and handling, forming new, but smaller particles. Although, due to their small size, these particles represent an insignificant volume in the powder distribution.

In comparison, the volume distribution of Cu MP (Figure 37c) shows that 10% of the volume comes from particles smaller than 89.6 µm and 10% of the volume comes from particles bigger than 143.1 µm. This result shows that the size distributions of the stainless-steel and Cu powders are in the same range, resulting in a uniform particle distribution when mixed, as seen on Figure 35d. However, the number distribution of Cu MP (Figure 37d) shows that 10% of the particles are

smaller than 4.9 µm and 10% of the particles are bigger than 112.2 µm. The presence of a substantial number of small particles in the powder mixture could be attributed to the breakdown of irregular Cu particles. Additionally, these smaller particles may lead to disturbances in powder flowability.

Figure 37 - ECA diameter per volume and ECA diameter per number for (a, b) AISI 316L and (c, d) Cu MP.

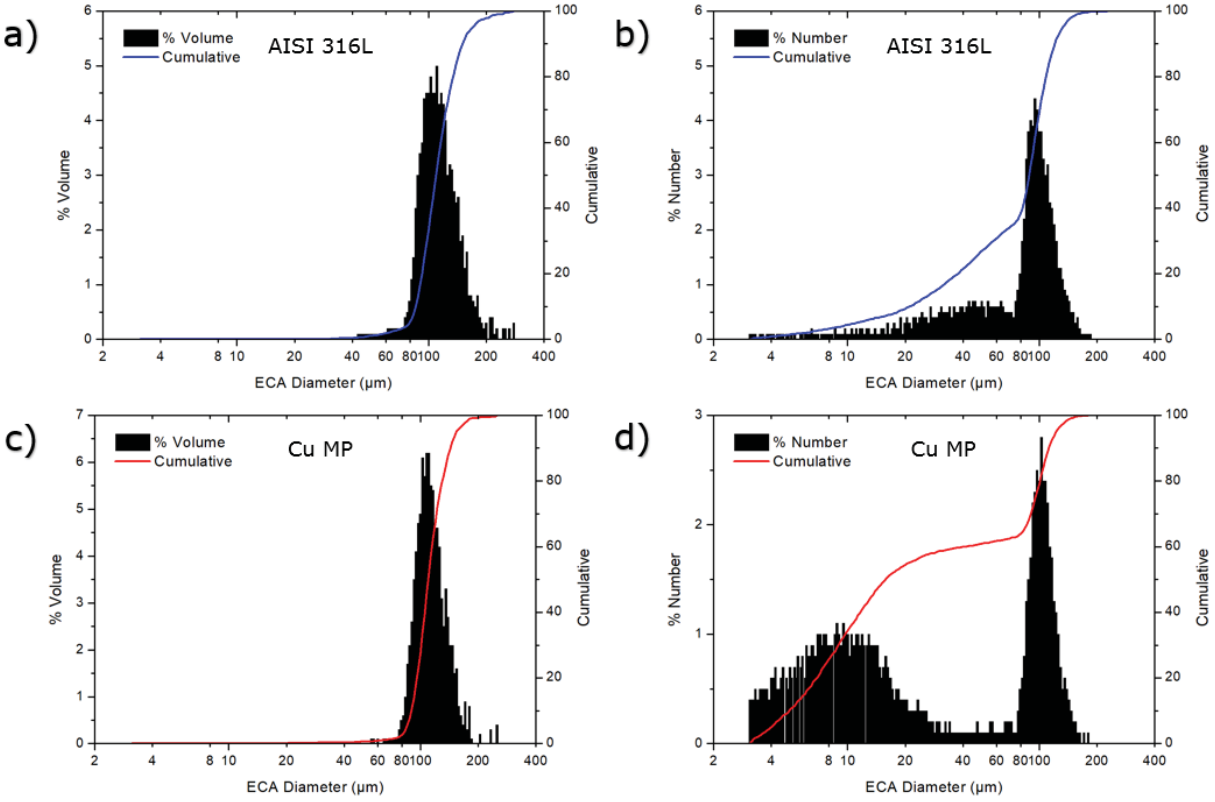

Source: Authors (2023).

Figure 38 offers a visual representation of AISI 316L and Cu MP particles shape and measured particle circularity by DIA. As expected, spherical stainless-steel particles are shown in sharp silhouettes (Figure 38a), on the contrary, irregular Cu particles are represented by blurry silhouettes (Figure 38c). The particles shape can be better described by the circularity, where a value of 1.0 represents a perfect circle. The mean circularity measured for AISI 316L and Cu MP is respectively, 0.642 ± 0.104 and 0.552 ± 0.117. This information is valuable for controlling the powder mixture for consistent powder flow in AM deposition, since higher circularity usually means better flowability.

Figure 38 - Particle shape and particle circularity for (a, b) AISI 316L and (c, d) Cu MP

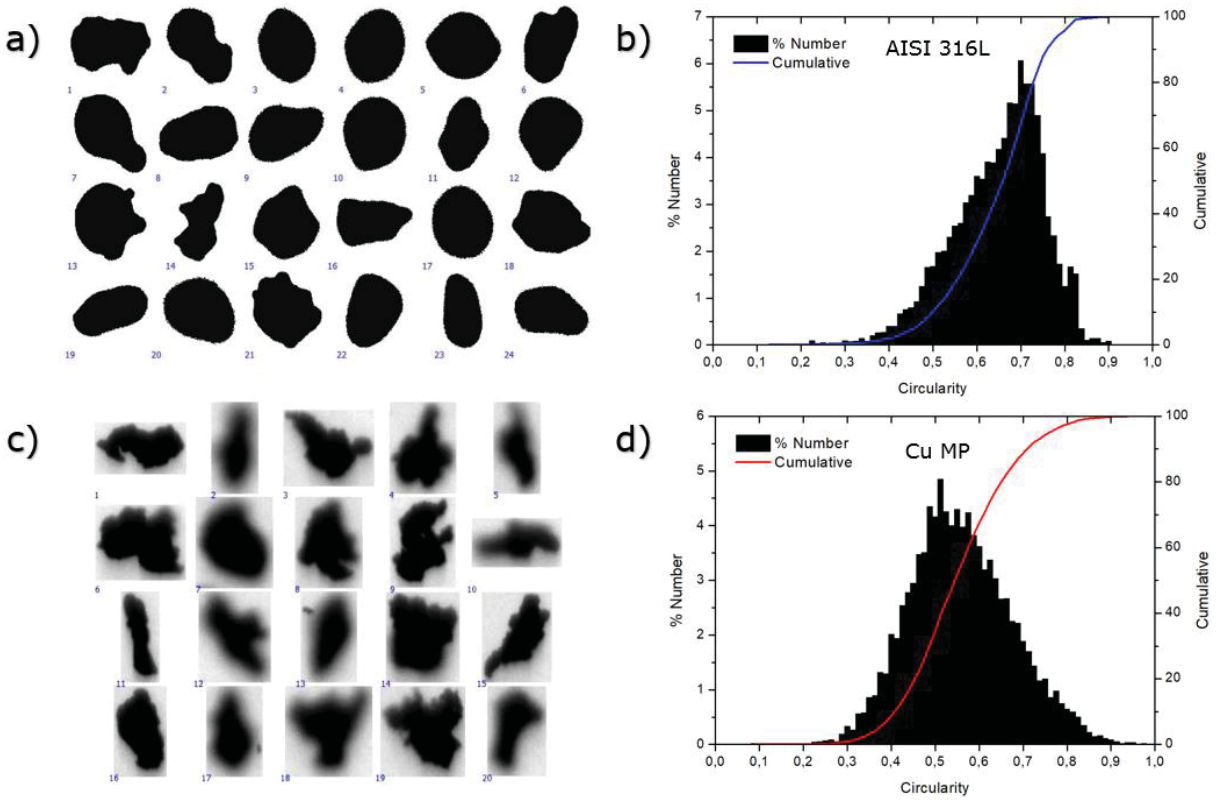

Source: Authors (2023).

The Hall flowmeter funnel was used to measure the flow time of the powder mixtures. Figure 39 shows the results for the non-dried (shelf condition) and dried powders (80 °C for 2h). The lower the time for the powder to flow through the Hall funnel aperture, the better the powder flowability. The mean flow time for AISI 316L was below 35.0 s per 50 g and its flow time was not affected by a potential humidity content. Adding Cu MPs did not change the flow time, despite their irregular shape. This observation suggests that adding small amounts of irregular particles to more spherical particles can be done without hindering powder flowability.

The nanocomposite powder with Cu NP showed similar flow time than the stainless-steel powder in the non-dried condition and lower flow time after dried. This behavior can be explained by the presence of the Cu NPs at the surface of the carrier particles, that can reduce the cohesion between the stainless-steel particles and improve flowability (Sharma; Setia, 2019). Humidity has a negative effect on the flowability of both nanocomposite powders. However, the addition of CuO NP lead to a significant increase in flow time. Due to its high surface-to-volume area, CuO NPs

have high surface free energy and tends to cluster to reduce its energy, increasing the cohesion between particles and slowing down flow.

Figure 39 - Hall funnel flow time for non-dried and dried powder mixtures

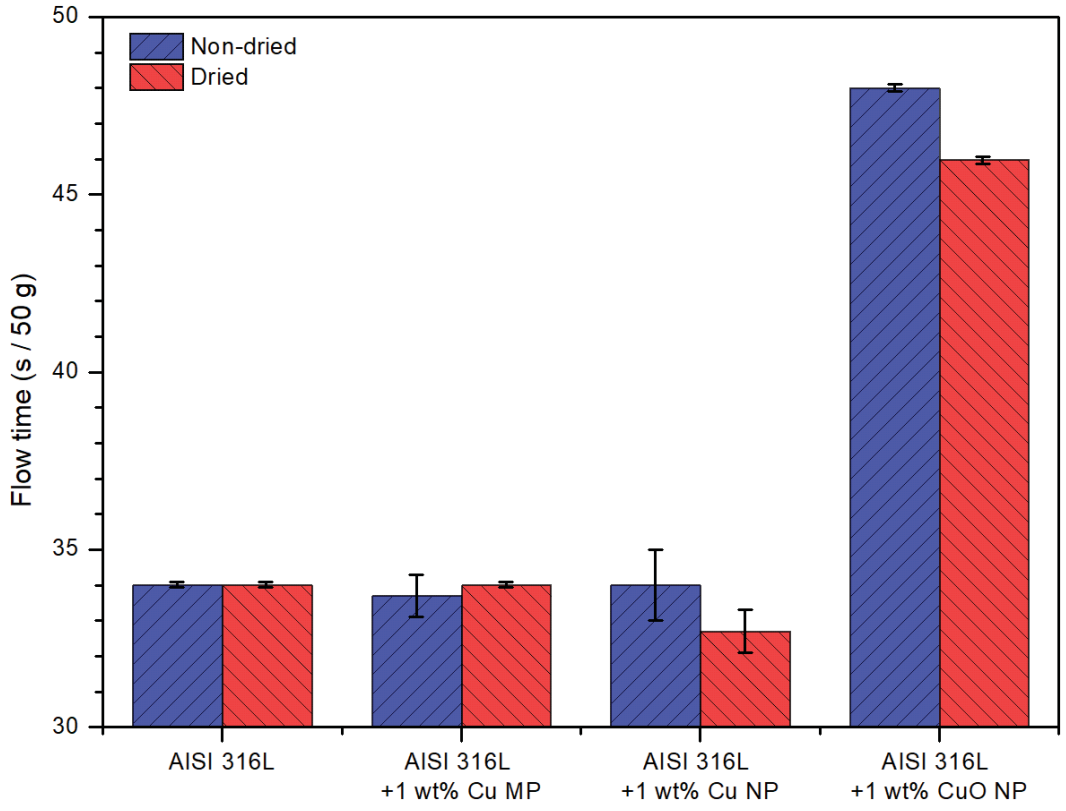

Source: Authors (2023).

To assess the internal features of the MPs, cross-section SEM images of AISI 316L and Cu MP are shown in Figure 40. It is shown that some of the stainless-steel particles have big pores (Figure 40a). In detail (Figure 40b), the pores inside the particle are indicated by arrows, some pores are small (about 1 μm), but others are bigger (about 35 μm). The cross-section of the irregular Cu MPs (Figure 40c) provides insight into the internal structures of this powder. It is possible to observe numerous voids within the particle region. The presence of pores and irregularities in the feedstock can impact the density of the parts build by AM. However, the fine tuning of processing parameters, considering the characteristics of the feedstock, should guarantee the obtention of fully dense parts.

Figure 40 - Cross-section SEM images of (a, b) AISI 316L and (c) Cu MP

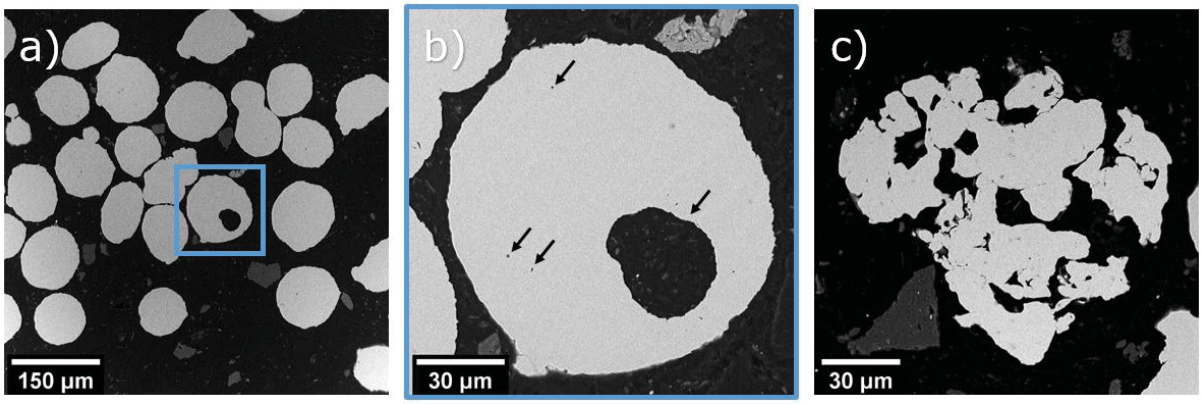

Source: Authors (2023).

Figure 41 shows the density on the cross-section of PTA-deposited material. For all powder mixtures, the mean density measured were at least 99.90 %, which can be considered a good density. Although, some porosity was observed in the particles of AISI 316L powder, the as deposited stainless-steel did not show big porosities. The presence of Cu MPs had a positive impact on part density, rising it to a mean value of 99.93 %. Showing that the irregularities of Cu MPs was not a problem for PTA processing. For the nanocomposite powders of Cu NPs and Cu O NPs, no impact of the mean density was observed.

To evaluate if the nanoparticles were successfully delivered to the melt pool and consequently to the solid part, XRF of the PTA-deposited material was performed. Table 8 displays the chemical composition of the PTA-deposited materials. It is expected some variation between the powder mixture and the deposited material since the deposition process brings elements from the substrate material (AISI 304L) due to dilution. Since AISI 304L does not have Mo in its composition, a reduction in Mo percentage is observed for all powder mixtures. The addition of Cu MPs successfully increased Cu content on the solid part, about 0.94 wt%, slightly shorter than the 1.0 wt% in the powder mixture. Which again, can be explained by the dilution with the substrate material, that does not have Cu in its composition. This result shows that, the mixture between two MPs within the same size distribution range, guarantee the chemical composition of the final part.

Figure 41 - Density of the PTA-deposited material

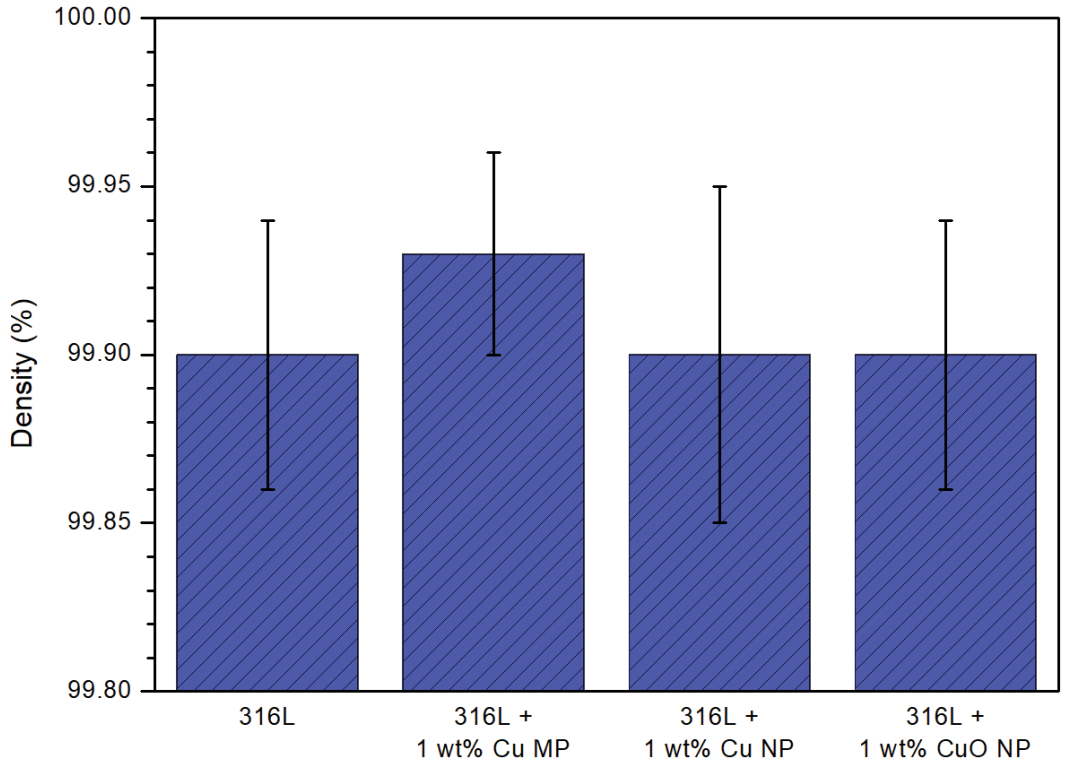

Source: Authors (2023).

For both nanocomposite powder, the chemical composition in the PTA-deposited material falls short on Cu content. For Cu NP and CuO NP nanocomposite powders, the difference on Cu content was 0.27 wt% and 0.10 wt%, respectively. Parts of the NPs could have remained unstable in carrier particle surface, thus parts of it segregated during powder handling and processing. In addition, a partial vaporization of the NPs in the plasma arc is expected to occur, as stated in (Prass; d'Oliveira, 2023).

Table 8 - Chemical composition of the PTA-deposited material in weight percentage

Material	**Fe**	**Cr**	**Ni**	**Mo**	**Mn**	**S**	**Si**	**P**	**Cu**	**O**
AISI 316L	Bal.	17.41	12.38	2.56	1.57	1.05	0.74	-	-	-
AISI 316L + Cu MP	Bal.	17.30	12.29	2.56	1.53	1.03	0.50	-	0.94	-
AISI 316L + Cu NP	Bal.	17.35	12.41	2.59	1.55	1.03	0.56	-	0.73	-
AISI 316L + CuO NP	Bal.	17.26	12.39	2.58	1.38	1.03	0.55	0.08	0.70	*

Source: Authors (2023).

CONCLUSIONS

In this study, the preparation and characterization of nanocomposite powders for additive manufacturing (AM) were investigated. By incorporating Cu microparticles, Cu nanoparticles and CuO nanoparticles into AISI 316L powder, advanced materials with tailored properties can be further developed, opening new opportunities for applications in AM. The major conclusions from the tested conditions are as follows:

- Addition of different Cu particles had minimal impact on the elemental percentage of AISI 316L, enabling customized powder compositions without significantly altering the stainless-steel chemical composition.
- Powder mixture of AISI 316L with 1 wt% Cu MP and nanocomposite powders of AISI 316L with 1 wt% Cu NP and 1 wt% CuO NP were successfully prepared and deposited using plasma transferred arc, resulting in high-density parts (over 99.90 %).
- Morphological analyses showed distinct shape between AISI 316L particles and Cu MP. However, the powder mixture exhibited uniformly distributed Cu particles, facilitated by the powder size distributions, that were in the same range.
- For the nanocomposite powders, successful adhesion of Cu NP and CuO NP onto the carrier particle surface was achieved. The stainless-steel particle surface was partially covered by Cu NP and completely covered by CuO NP due to their different sizes.
- The presence of Cu MP and Cu NP had no impact on powder flow time. While the addition of CuO NPs increased cohesion forces between the carrier particles, increasing flow time.
- Cu content on the PTA-deposited parts remained consistent with the powder mixture containing Cu MPs. However, parts deposited with both nanocomposite powders fall short in Cu content. Requiring specific procedures to mix, handle and process these special powders.

ACKNOWLEDGEMENTS

The authors would like to thank LAMSE and LATECME for providing the equipment used in some of the analyses.

REFERENCES

ABU-LEBDEH, T. M.; DAMPTEY, R.; UNGUREANU, L. M.; PETRESCU, F. I. T. A Ternary Model for Particle Packing Optimization. **Journal of Composites Science**, v. 6, n. 4, p. 113, Apr. 2022. DOI. 10.3390/jcs6040113.

AMERICAN SOCIETY FOR TESTING AND MATERIALS. **ASTM B213-20**: Standard Test Methods for Flow Rate of Metal Powders Using the Hall Flowmeter Funnel. New York, 2020.

AMERICAN SOCIETY FOR TESTING AND MATERIALS. **ASTM B822-20**: Standard Test Method for Particle Size Distribution of Metal Powders and Related Compounds by Light Scattering. New York, 2020.

AVRAMPOS, P.; VOSNIAKOS, G. C. A review of powder deposition in additive manufacturing by powder bed fusion. **Journal of Manufacturing Processes**, v. 74, p. 332-352, Feb. 2022. DOI. 10.1016/j.jmapro.2021.12.021.

CUI, C.; BECKER, L.; GÄRTNER, E.; BOES, J.; LENTZ, J.; UHLENWINKEL, V.; STEINBACHER, M.; WEBER, S.; FECHTE-HEINEN, R. Laser Additive Manufacturing of Duplex Stainless Steel via Powder Mixture. **Journal of Manufacturing and Materials Processing**, v. 6, n. 4, p. 72, Jul. 2022. DOI. 10.3390/jmmp6040072.

DONG, Y.; LI, Y.; EBEL, T.; YAN, M. Cost-affordable, high-performance Ti-TiB composite for selective laser melting additive manufacturing. **Journal of Materials Research**, v. 35, n. 15, p. 1922-1935, Jan. 2020. DOI. 10.1557/jmr.2019.389.

GARG, R.; DHAMI, H. S.; PANDA, P. R.; VISWANATHAN, K. Evaluating gas-driven flow mechanics of non-spherical powders for directed energy deposition. **Journal of Manufacturing Processes**, v. 99, p. 260-271, Aug. 2023. DOI. 10.1016/j.jmapro.2023.04.057.

HUANG, Y.; LEU, M. C.; MAZUMDER, J.; DONMEZ, A. Additive Manufacturing: current state, future potential, gaps and needs, and recommendations. **Journal of Manufacturing Science and Engineering**, v. 137, n. 1, Feb. 2015. DOI. 10.1115/1.4028725.

LI, N.; HUANG, S.; ZHANG, G.; QIN, R.; LIU, W.; XIONG, H.; SHI, G.; BLACKBURN, J. Progress in additive manufacturing on new materials: a review. **Journal of Materials Science & Technology**, v. 35, n. 2, p. 242-269, Feb. 2019. DOI. 10.1016/j.jmst.2018.09.002.

MELLIN, P.; LYCKFELDT, O.; HARLIN, P.; BRODIN, H.; BLOM, H.; STRONDL, A. Evaluating flowability of additive manufacturing powders, using the Gustavsson flow meter. **Metal Powder Report**, v. 72, n. 5, p. 322-326, Sep. 2017. DOI. 10.1016/j.mprp.2017.06.003.

PRASS, G. S.; D'OLIVEIRA, A. S. C. M. Processing and characterization of AISI 316L coatings modified with Cu and CuO nanoparticles. **Surface and Coatings Technology**, v. 461, p. 129465, May 2023. DOI. 10.1016/j.surfcoat.2023.129465.

SHARMA, R.; SETIA, G. Mechanical dry particle coating on cohesive pharmaceutical powders for improving flowability - A review. **Powder Technology**, v. 356, p. 458-479, Nov. 2019. DOI. 10.1016/j.powtec.2019.08.009.

SOULIER, M.; BENAYAD, A.; TEULON, L.; OUDART, Y.; SENOL, S.; VANMEENSEL, K. Nanocomposite powder for powder-bed-based additive manufacturing obtained by dry particle coating. **Powder Technology**, v. 404, p. 117474, May 2022. DOI. 10.1016/j.powtec.2022.117474.

souli, J.; GU, D.; XI, L.; LIN, K.; FANG, Y.; WANG, R. Preparation method and underlying mechanism of MWCNTs/Ti6Al4V nanocomposite powder for selective laser melting additive manufacturing. **Powder Technology**, v. 368, p. 59-69, May 2020. DOI. 10.1016/j.powtec.2020.04.041.

4.2 EFFECTS OF PTA DEPOSITION PARAMETERS ON GEOMETRY AND HARDNESS OF AISI 316L SINGLE-TRACKS

ABSTRACT

Directed Energy Deposition (DED) is an Additive Manufacturing (AM) technology involving the layer-by-layer building of components close to their final geometry. One of the main applications of DED is the repair of metallic components, since the technique offers good control over composition and microstructure, minimizing the impact on the existing part. However, the control of geometrical features is more demanding than in machining processes, a consequence of the nature of the feedstock, the heat Source, and the process itself. In repair operations, the impact of the deposition process on the damaged component should be minimized. Within this context, Plasma Transferred Arc (PTA) is a well-known process for applying coating on metallic materials, guaranteeing a good metallurgical bond between the substrate and the deposited material. PTA-DED process has a low carbon footprint when compared with other processes and offers significant competitive advantages for which a known behavior of processing variables is required. This study is part of an ongoing project, and it addresses the effects of deposition current and deposition velocity on the geometry of single-track AISI 316L. The relationship between processing parameters, processability, and hardness is identified and discussed as a useful database to select AM maintenance procedures. A Design of Experiment (DoE), for single-track AISI 316L, deposited on AISI 304L plates, varying two factors were adopted, deposition current (4 levels) and deposition velocity (3 levels), totaling 12 sets of parameters. Statistical analysis showed that both factors alter the dilution with the substrate, while a higher current increased the dilution the velocity had the opposite effect. The results also revealed that both deposition parameters greatly affected the wettability, hence the geometry of the single tracks. The DoE allowed for a good predictive estimate of the interaction with a part being repaired and the re-furbishing of its geometry by AM. This research points out that the geometry, microstructure, and hardness of the first deposited track play an important role in the quality and properties of subsequent multilayer builds, required to recover the part geometry or even add functionalities.

Keywords: Additive Manufacturing, Directed Energy Deposition, Plasma Transferred Arc, Design of Experiments.

INTRODUCTION

Additive manufacturing (AM) technology allows components with complex geometry to be manufactured using a layer-by-layer construction. As feedstock, the technology enables the processing of powders or wires from different metallic materials, such as nickel alloys, titanium, aluminum, and stainless steel (Benakis; Costanzo; Patran, 2020; Karapuzha *et al.,* 2021; Lashgari *et al.,* 2021; Oropeza *et al.,* 2020; Park *et al.,* 2021; Riquelme *et al.,* 2021; Wan *et al.,* 2022). With the capability of processing different metallic alloys, AM can be employed in repairing and remanufacturing damaged parts. This becomes relevant for complex and high-value parts, which would be ex-pensive and time-consuming to be replaced (Priarone *et al.,* 2021). In refurbishing components, directed energy deposition (DED) is used to add layers of materials to rebuild worn areas of operating parts (Chen *et al.,* 2022; Sahoo; Tripathy, 2020).

DED is an AM technology in which the deposited material is directed by a nozzle and is melted by an energy Source, which can be a plasma arc, laser beam, and electron beam (TWI, 2023). As a general observation, the use of metal powder provides better accuracy and surface finish, but at a lower deposition rate than those used for depositing wire feedstock. Although for both materials (powder and wire) post-processing machining is essential for obtaining the final geometry and surface finish (Priarone *et al.,* 2021). Notwithstanding the advantages of processing near final geometries without the need for expensive tooling, it is of relevance to control the presence of common defects in AM including crack formation, pores, inclusions, and delamination that strongly depend on the processing parameters must be considered (Li; Jin; Paquit, 2021).

Processing parameters also affect the geometrical features of the deposited layer, namely layer height and width, penetration and consequently dilution, in repair operations, these contribute to control the deposit geometry. Furthermore, processing parameters influence the microstructure of the deposited material and have a significant impact on the properties of the material, such as hardness and wear resistance. To make the most of the technology, research has endeavored to

optimize the processing parameters for different materials deposited with a variety of energy Sources (Bharath *et al.,* 2008; Kumar; Sawant; Jain, 2021; Momin *et al.,* 2023; Sadasivam; Amirthalingam, 2022; Wei *et al.,* 2018; Yadav *et al.,* 2020).

In comparison with the laser beam, plasma arc techniques, such as plasma transferred arc (PTA), offer higher deposition rates, good homogeneity, and low oxides content, being a competitive alternative for repairing damaged parts (Cardozo *et al.,* 2018). However, there is a lack of a systematic investigation on the PTA-DED of AISI 316L that offers information on the processing parameters selection. In particular, for repair operations, the first deposited layer has a two-fold impact on a successful refurbishing of a part: interaction with the original material and it sets a reference for subsequently deposited layers. Thus, in the present study, PTA is used to deposit single tracks of AISI 316L on AISI 304L. A design of experiments (DoE) is carried out to assess the effects of deposition current and speed on the coating hardness and geometry.

MATERIALS AND METHODS

Single layers of gas-atomized AISI 316L stainless steel powder (75-250 μm) were deposited by PTA on AISI 304L plates (70 x 30 x 10 mm). To evaluate the effects of deposition parameters on geometry and hardness, four levels of deposition current and three levels of deposition speed were selected, the processing parameters are shown in Table 9.

Table 9 - PTA deposition parameters

Parameter	**Value**
Protective gas	Argon 99%
Carrier gas flow (L/min)	0.8
Plasma gas flow (L/min)	2.0
Shield gas flow (L/min)	15.0
Nozzle-plate distance (mm)	10
Powder flow rate (g/min)	10
Deposition current (A)	60, 90, 120, 150
Deposition speed (mm/min)	100, 150, 200

Source: Authors (2023).

Figure 42 shows the geometrical features measured in the cross-section of the single-track, namely height, width, penetration, reinforcement, dilution, and wettability. The hardness and the geometrical features were measured for all experiments in the full factorial design of experiments.

Figure 42 - Single-track geometric features

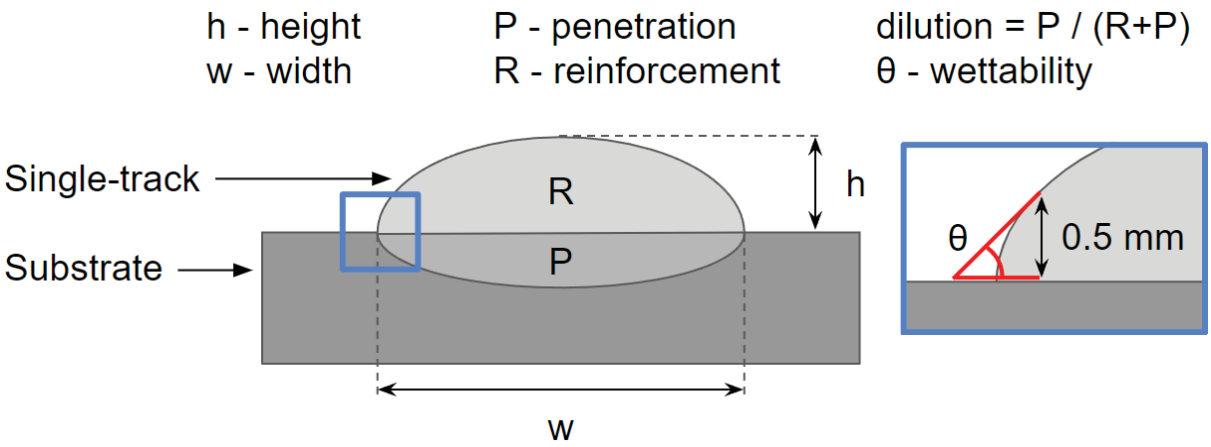

Source: Authors (2023).

RESULTS AND DISCUSSION

The full factorial experiment was carried out at various combinations of deposition parameters by varying deposition current and speed. Table 10 presents the measured responses of the deposited single-tracks obtained at 12 combinations of parameters, which were repeated in 3 different cross-sections.

The optical microscopies of the single-track cross-sections are shown in Figure 43. It reveals a lack of fusion for the tracks deposited at a lower current (60 A) that are detached from the substrate. Lack of fusion was also identified at the following deposition with 90 A, and the faster speeds tested, 150 and 200 mm/min, as a consequence of insufficient energy per unit length. The cross-sections of the processed layers reveal that both current and speed have a great impact on the geometry of the deposited single-tracks.

Table 10 - Experimental conditions and measured responses

Experiment	Speed (mm/min)	Current (A)	Height (mm)	Width (mm)	Wettability (°)	Reinforcement (mm²)	Penetration (mm²)	Dilution (%)	Vickers Hardness (HV 0.3)
			2.524	3.712	-	10.254	-	-	169
1	100	60	2.531	3.704	-	10.169	-	-	174
			2.512	3.735	-	10.310	-	-	178
			2.269	5.931	73.11	11.315	0.251	2.17	190
2	100	90	2.276	5.938	52.80	12.123	0.231	1.87	174
			2.281	5.856	51.00	11.822	0.181	1.51	178
			1.863	9.484	36.90	12.460	1.552	11.08	193
3	100	120	1.856	9.413	40.32	12.422	1.587	11.33	175
			1.863	9.475	42.96	12.679	1.521	10.71	178
			1.505	12.036	22.90	12.635	6.053	32.39	189
4	100	150	1.499	11.972	22.56	12.610	5.904	31.89	189
			1.508	11.999	25.75	12.804	5.998	31.90	179
			1.975	3.075	-	5.873	-	-	189
5	150	60	1.983	3.065	-	5.798	-	-	174
			1.971	3.095	-	5.901	-	-	172
			1.724	5.253	58.93	7.161	-	-	186
6	150	90	1.758	5.039	61.19	7.084	-	-	168
			1.725	5.268	53.18	7.210	-	-	177
			1.422	7.631	34.68	8.288	0.815	8.95	184
7	150	120	1.415	7.591	32.10	8.207	0.756	8.43	183
			1.436	7.583	33.51	8.359	0.776	8.49	177
			1.222	9.444	22.43	8.062	4.430	35.46	193
8	150	150	1.243	9.480	25.30	8.379	4.438	34.63	187
			1.219	9.462	22.32	8.163	4.453	35.30	183
			1.596	3.275	-	4.755	-	-	173
9	200	60	1.587	3.265	-	4.686	-	-	169
			1.599	3.283	-	4.781	-	-	177
			1.520	4.862	39.73	5.913	-	-	189
10	200	90	1.532	4.450	46.99	5.601	-	-	173
			1.532	4.450	46.99	5.601	-	-	173
			1.183	6.663	33.18	5.918	0.800	11.91	178
11	200	120	1.169	6.649	27.11	5.867	0.805	12.07	181
			1.160	6.707	25.95	5.917	0.768	11.49	183
			1.017	8.448	17.81	6.087	3.695	37.77	196
12	200	150	1.036	8.485	18.82	6.369	3.388	34.72	180
			1.025	8.476	17.83	6.227	3.316	34.75	183

Source: Authors (2023).

Figure 43 - Optical microscopies of the single-track cross-sections

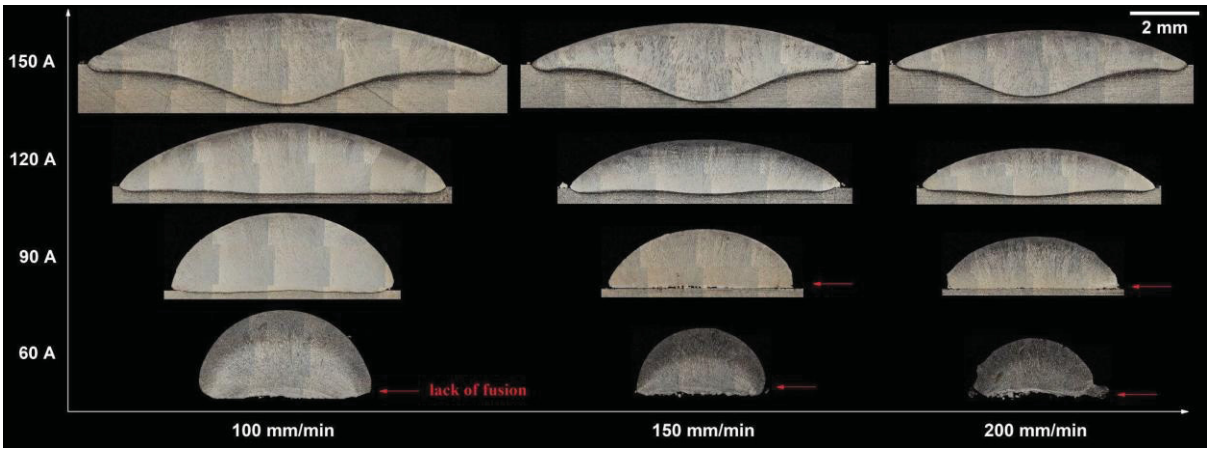

Source: Authors (2023).

Process maps of deposition current and speed, Figure 44 shows the contour plots of the measured geometrical features and hardness. When deposition speed is increased, less powder is fed into the melt pool per length unit, since the powder flow rate (10 g/min) is kept constant. As a result, higher deposition speeds lead to lower track heights (Figure 44a) and lower track widths (Figure 44b). As expected, a decrease in reinforcement area (Figure 44d) is observed with an increase in deposition speed. Further-more, higher deposition speed causes a reduction in energy per unit length, slightly decreasing the penetration area measured (Figure 44e). For the tested conditions, dilution (Figure 44f) remains almost constant with changes in speed, since both reinforcement and penetration decrease with higher deposition speed (Santos *et al.,* 2019).

Alongside speed, deposition current also highly impacts the single-track geometry. When the deposition current is increased, more energy is available per unit length, leading to higher temperatures in the melt pool. As a consequence, higher deposition currents lead to lower wettability angles (Figure 44c), decreasing track height (Figure 44a), and substantially increasing the measured track width (Figure 44b). Although keeping the powder flow rate constant, increasing deposition current slightly increases reinforcement area (Figure 44d), this can be explained by the better capturing of the metallic pow-der, since higher temperatures lead to a wider melt pool (Figure 43). Higher currents lead to an increase in both penetration and dilution (Figure 44e and Figure 44f) since more energy is available at the melt pool (Yaedu; d'Oliveira, 2005; Takano; Queiroz; d'Oliveira, 2008).

Figure 44 - Contour plot of (a) height, (b) width, (c) wettability, (d) reinforcement, (e) penetration, (f) dilution, and (g) Vickers hardness

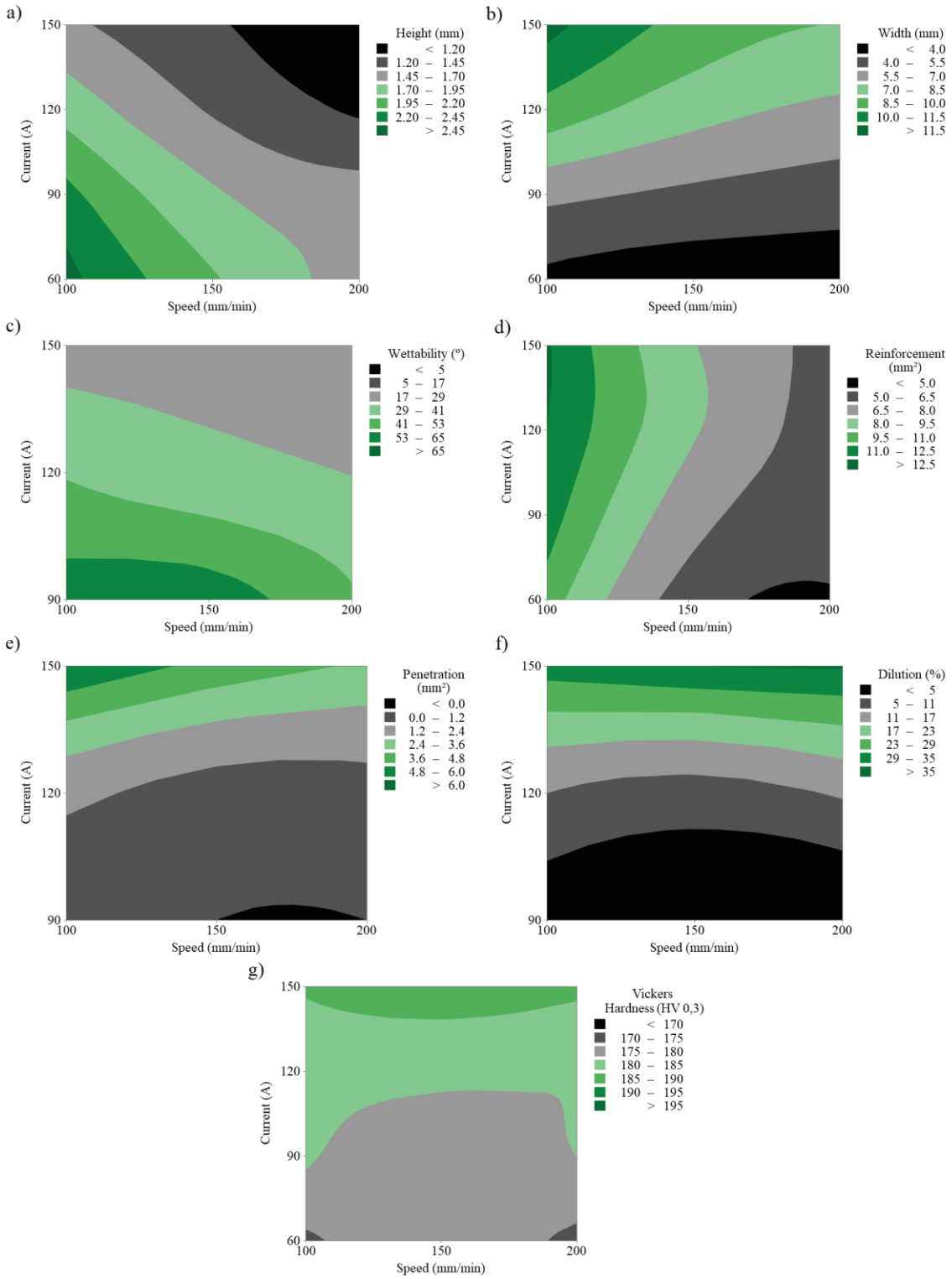

Source: Authors (2023).

Analysis of variance (ANOVA) was used to quantify the impact of both individual and combined deposition parameters. Tables 6-12 show the ANOVA data for the measured responses. At Table 11, it is seen that both speed (46.66%) and

current (50.65%) significantly contributed to the track height response. Whereas track width (Table 12) and wettability (Table 13) were mainly influenced by deposition current (86.73% and 91.92%, respectively), which highlights the effect of the energy input on these variables. The fact that the powder flow rate per length unit depends on the speed is emphasized in Table 14, where reinforcement is highly impacted by deposition speed (89.94%). In turn, penetration (Table 15) and dilution (Table 16) were shown to be dependent on heat input, since deposition current has the maximum contribution (92.08% and 99.22%, respectively).

Since the feedstock and the substrate have different chemical compositions, the coating hardness is directly impacted by dilution (Takano; Queiroz; d'Oliveira, 2008). As aforementioned, dilution was not impacted by deposition speed, therefore hardness measured at the single-track cross-section was not affected by deposition speed in the tested range (Figure 44g). Increasing deposition current increases the measured hardness (Figure 44g). This is a surprising result because a higher heat input leads to a slower cooling rate compromising the refinement of the solidification structure accounting for a lower hardness (Kumar *et al.,* 2014). However, results showed that the increase in hardness is associated with an increase in dilution with the substrate material suggesting that alloying elements from the substrate increased solid solution saturation and the hardness of the coatings (Ramakrishnan *et al.,* 2021).

The ANOVA data for the measured hardness is shown in Table 17. As expected, deposition speed has no significant effect on the measured hardness, since the P-value of 0.93 > 0.05. Also, the deposition current contribution on hardness is lower than the standard deviation contribution (33.24% and 62.37%, respectively), which means that the standard deviation of the measured hardness surpassed the variation with the selected range of deposition parameters tested.

Table 11 - Analysis of variance data for height

Source	DF	Sum of Squares	Mean Square	F-Value	P-Value	Contribution %
Model	11	6.58	0.60	3419.47	<0.001	-
Speed	2	3.07	1.54	8780.89	<0.001	**46.66**
Current	3	3.34	1.11	6354.55	<0.001	**50.65**
Speed*Current	6	0.17	0.03	164.80	<0.001	2.63
Error	24	0.00	0.00			0.06
Total	35	6.59				100.00

Source: Authors (2023).

Table 12 - Analysis of variance data for width

Source	DF	Sum of Squares	Mean Square	F-Value	P-Value	Contribution %
Model	11	263.95	24.00	4256.28	<0.001	-
Speed	2	25.50	12.75	2261.09	<0.001	9.65
Current	3	229.04	76.35	13542.03	<0.001	**86.73**
Speed*Current	6	9.42	1.57	278.47	<0.001	3.57
Error	24	0.14	0.01			0.05
Total	35	264.09				100.00

Source: Authors (2023).

Table 13 - Analysis of variance data for wettability

Source	DF	Sum of Squares	Mean Square	F-Value	P-Value	Contribution %
Model	11	14151.30	1286.48	71.89	<0.001	-
Speed	2	448.90	224.47	12.54	<0.001	3.08
Current	3	13402.80	4467.60	249.65	<0.001	**91.92**
Speed*Current	6	299.60	49.93	2.79	0.033	2.05
Error	24	429.50	17.90			2.95
Total	35	14580.80				100.00

Source: Authors (2023).

Table 14 - Analysis of variance data for reinforcement

Source	DF	Sum of Squares	Mean Square	F-Value	P-Value	Contribution %
Model	11	267.97	24.36	1007.46	<0.001	-
Speed	2	241.52	120.76	4994.19	<0.001	**89.94**
Current	3	24.66	8.22	340.00	<0.001	9.18
Speed*Current	6	1.78	0.30	12.27	<0.001	0.66
Error	24	0.58	0.02			0.22
Total	35	268.55				100.00

Source: Authors (2023).

Table 15 - Analysis of variance data for penetration

Source	DF	Sum of Squares	Mean Square	F-Value	P-Value	Contribution %
Model	11	139.46	12.68	3041.51	<0.001	-
Speed	2	4.91	2.45	588.69	<0.001	3.52
Current	3	128.51	42.83	10276.40	<0.001	**92.08**
Speed*Current	6	6.04	1.01	241.67	<0.001	4.33
Error	24	0.10	0.00			0.07
Total	35	139.56				100.00

Source: Authors (2023).

Table 16 - Analysis of variance data for dilution

Source	DF	Sum of Squares	Mean Square	F-Value	P-Value	Contribution %
Model	11	6995.12	635.92	2049.48	<0.001	-
Speed	2	5.72	2.86	9.21	<0.001	0.08
Current	3	6948.18	2316.06	7464.34	<0.001	**99.22**
Speed*Current	6	41.22	6.87	22.14	<0.001	0.59
Error	24	7.45	0.31			0.11
Total	35	7002.57				100.00

Source: Authors (2023).

Table 17 - Analysis of variance data for hardness

Source	DF	Sum of Squares	Mean Square	F-Value	P-Value	Contribution %
Model	11	705.64	64.15	1.32	0.275	-
Speed	2	7.06	3.53	0.07	0.93	0.38
Current	3	623.19	207.73	4.26	0.015	33.24
Speed*Current	6	75.39	12.57	0.26	0.951	4.02
Error	24	1169.33	48.72			**62.37**
Total	35	1874.97				100.00

Source: Authors (2023).

CONCLUSIONS

A systematic investigation on the PTA-DED of AISI 316L was carried out in this study. The key findings for the tested conditions are as follows:

- AISI 316L powder was successfully deposited by PTA, resulting in sound single-track coatings. The exception was the coatings processed with 60 A, which resulted in insufficient dilution, detaching the coating from the substrate.
- The contour plots can be used to predict the hardness and the geometric response of AISI 316L coating to process parameters within the tested range.
- Single track height is governed by both deposition current and speed, which decreases by increasing any of the two tested factors.
- Deposition current was found to be the most influential parameter affecting width, as a result of a decrease in wettability angle. In addition, penetration, and consequently dilution, is mostly influenced by deposition current.
- On the other hand, deposition speed was discovered to be the most significant factor influencing reinforcement area, since the powder flow rate was kept constant.

- For the tested conditions, the variation in deposition speed did not change the hardness of the AISI 316L coating. However, the dispersion of the measured hardness is very significant for the test conditions used.

ACKNOWLEDGEMENTS

The authors acknowledge CAPES, CNPq and the Laboratory of Additive Manufacturing and Surface Engineering (LAMSE) of UFPR.

REFERENCES

BENAKIS, M.; COSTANZO, D.; PATRAN, A. Current mode effects on weld bead geometry and heat affected zone in pulsed wire arc additive manufacturing of Ti-6-4 and Inconel 718. **Journal of Manufacturing Processes**, v. 60, p. 61-74, Dec. 2020. DOI. 10.1016/j.jmapro.2020.10.018.

BHARATH, R. R.; RAMANATHAN, R.; SUNDARARAJAN, B.; SRINIVASAN, P. B. Optimization of process parameters for deposition of Stellite on X45CrSi93 steel by plasma transferred arc technique. **Materials & Design**, v. 29, n. 9, p. 1725-1731, Out. 2008. DOI. 10.1016/j.matdes.2008.03.020.

CARDOZO, E. P.; RÍOS, S.; GANGULY, S.; D'OLIVEIRA, A. S. C. M. Assessment of the effect of different forms of Inconel 625 alloy feedstock in Plasma Transferred Arc (PTA) additive manufacturing. **The International Journal of Advanced Manufacturing Technology**, v. 98, n. 5-8, p. 1695-1705, Jun. 2018. DOI. 10.1007/s00170-018-2340-z.

CHEN, X.; WANG, C.; DING, J.; BRIDGEMAN, P.; WILLIAMS, S. A three-dimensional wire-feeding model for heat and metal transfer, fluid flow, and bead shape in wire plasma arc additive manufacturing. **Journal of Manufacturing Processes**, v. 83, p. 300-312, Nov. 2022. DOI. 10.1016/j.jmapro.2022.09.012.

KARAPUZHA, A. S.; FRASER, D.; ZHU, Y.; WU, X.; HUANG, A. Effect of solution heat treatment and hot isostatic pressing on the microstructure and mechanical properties of Hastelloy X manufactured by electron beam powder bed fusion. **Journal of Materials Science & Technology**, v. 98, p. 99-117, Jan. 2022. DOI. 10.1016/j.jmst.2021.04.059.

KUMAR, P.; SAWANT, M. S.; JAIN, N. K. Optimization of process parameters in micro-plasma transferred arc deposition process for cobalt-based alloy. **Materials Today**: Proceedings, v. 44, p. 1681-1686, 2021. DOI. 10.1016/j.matpr.2020.11.840.

KUMAR, R.; ARYA, H. K. Experimental Determination of Cooling Rate and its Effect on Microhardness in Submerged Arc Welding of Mild Steel Plate (Grade c-25 as per

IS 1570). **Journal of Material Science & Engineering**, v. 03, n. 02, 2013. DOI. 10.4172/2169-0022.1000138.

LASHGARI, H. R.; LI, S.; KONG, C.; ASNAVANDI, M.; ZANGENEH, S. Rotary friction welding of additively manufactured 17-4PH stainless steel. **Journal of Manufacturing Processes**, v. 64, p. 1517-1528, Apr. 2021. DOI. 10.1016/j.jmapro.2021.03.008.

LI, R.; JIN, M.; PAQUIT, V. C. Geometrical defect detection for additive manufacturing with machine learning models. **Materials & Design**, v. 206, p. 109726, Aug. 2021. DOI. 10.1016/j.matdes.2021.109726.

MOMIN, A. G.; KHATRI, B. C.; CHAUDHARI, M.; SHAH, U. V.; VALAKI, J. Parameters for cladding using plasma transfer arc welding - A critical. **Materials Today**: Proceedings, v. 77, p. 614-618, 2023. DOI. 10.1016/j.matpr.2022.11.009.

OROPEZA, D.; HOFMANN, D. C.; WILLIAMS, K.; FIRDOSY, S.; BORDEENITHIKASEM, P.; SOKOLUK, M.; LIESE, M.; LIU, J.; LI, X. Welding and additive manufacturing with nanoparticle-enhanced aluminum 7075 wire. **Journal of Alloys and Compounds**, v. 834, p. 154987, Sep. 2020. DOI. 10.1016/j.jallcom.2020.154987.

PARK, S. H.; SON, S. J.; LEE, S. B.; YU, J. H.; AHN, S. J.; CHOI, Y. S. Surface machining effect on material behavior of additive manufactured SUS 316L. **Journal of Materials Research and Technology**, v. 13, p. 38-47, Jul. 2021. DOI. 10.1016/j.jmrt.2021.04.031.

PRIARONE, P. C.; CAMPATELLI, G.; CATALANO, A. R.; BAFFA, F. Life-cycle energy and carbon saving potential of Wire Arc Additive Manufacturing for the repair of mold inserts. **CIRP Journal of Manufacturing Science and Technology**, v. 35, p. 943-958, Nov. 2021. DOI. 10.1016/j.cirpj.2021.10.007.

RAMAKRISHNAN, A.; RAMESHKUMAR, T.; RAJAMURUGAN, G.; SUNDARRAJU, G.; SELVAMUTHUKUMARAN, D. Experimental investigation on mechanical properties of TIG welded dissimilar AISI 304 and AISI 316 stainless steel using 308 filler rod. **Materials Today**: Proceedings, v. 45, p. 8207-8211, 2021. DOI. 10.1016/j.matpr.2021.03.502.

RIQUELME, A.; CANDELA, C. S. R.; RODRIGO, P.; RAMS, J. Influence of process parameters in additive manufacturing of highly reinforced 316L / SiCp composites. **Journal of Materials Processing Technology**, v. 299, p. 117325, Jan. 2022. DOI. 10.1016/j.jmatprotec.2021.117325.

SADASIVAM, P.; AMIRTHALINGAM, M. Design and fabrication of micro-plasma transferred wire arc additive manufacturing system. **CIRP Journal of Manufacturing Science and Technology**, v. 37, p. 185-195, May 2022. DOI. 10.1016/j.cirpj.2022.01.014.

SAHOO, A.; TRIPATHY, S. Development in plasma arc welding process: a review. **Materials Today**: Proceedings, v. 41, p. 363-368, 2021. DOI. 10.1016/j.matpr.2020.09.562.

SANTOS, A. X.; MACIEL, T. M.; COSTA, J. D.; SOUSA, M. B.; PRASAD, S.; CAMPOS, A. R. N.; SANTANA, R. A. C. Study on influence of the PTA-P welding process parameters on corrosion behavior of Inconel 625 coatings. **Matéria (Rio de Janeiro)**, v. 24, n. 1, 2019. DOI. 10.1590/s1517-707620190001.0619.

TAKANO, E. H.; QUEIROZ, D.; D'OLIVEIRA, A. S. C. M. Avaliação dos Parâmetros de Processamento por PTA nas Superfícies Processadas. **Soldagem & Inspeção**, v. 13, n. 3, p. 210-218, Sep. 2008.

TWI. What is directed energy deposition (DED). Available at: https://www.twi-global.com/technical-knowledge/faqs/directed-energy-deposition. Accessed on 21 May 2023.

WAN, H. Y.; YANG, W. K.; WANG, L. Y.; ZHOU, Z. J.; LI, C. P.; CHEN, G. F.; LEI, L. M.; ZHANG, G. P. Toward qualification of additively manufactured metal parts: tensile and fatigue properties of selective laser melted inconel 718 evaluated using miniature specimens. **Journal of Materials Science & Technology**, v. 97, p. 239-253, Jan. 2022. DOI. 10.1016/j.jmst.2021.04.049.

WEI, Y.; WEI, X. S.; CHEN, B.; ZUO, J. Y.; MA, T. C.; SHEN, J. Parameter optimization for tungsten carbide/Ni-based composite coating deposited by plasma transferred arc hardfacing. **Transactions of Nonferrous Metals Society of China**, v. 28, n. 12, p. 2511-2519, Dec. 2018. DOI. 10.1016/s1003-6326(18)64897-6.

YADAV, S.; JINOOP, A. N.; SINHA, N.; PAUL, C. P.; BINDRA, K. S. Parametric investigation and characterization of laser directed energy deposited copper-nickel graded layers. **The International Journal of Advanced Manufacturing Technology**, v. 108, n. 11-12, p. 3779-3791, Jun. 2020. DOI. 10.1007/s00170-020-05644-9.

YAEDU, A. E.; D'OLIVEIRA, A. S. C. M. Cobalt based alloy PTA hardfacing on different substrate steels. **Materials Science and Technology**, v. 21, n. 4, p. 459-466, Apr. 2005. DOI. 10.1179/174328413x13789824293380.

4.3 PROCESSING AND CHARACTERIZATION OF AISI 316L COATINGS MODIFIED WITH CU AND CUO NANOPARTICLES

ABSTRACT

Nanoparticles (NPs) have been used to benefit from Cu properties, due to their unique physicochemical characteristics caused by a high surface-to-volume ratio. However, to enable the deposition of hardfacing coatings with NPs, it is of interest to evaluate the processability of nanocomposite materials. The processability of hardfacing coatings, measured by their soundness, porosity, hardness, and solidification structure, is particularly relevant to assess the effects of adding Cu NPs and CuO NPs to AISI 316L. This study prepared and deposited powder mixtures of AISI 316L atomized steel with 5 wt% Cu microparticles (MPs), Cu NPs, and CuO NPs, individually, to process coatings by plasma transferred arc. Results showed that Cu additions alter the processability of AISI 316L and that both NPs influenced dilution and wettability of layers, requiring higher deposition energy to avoid lack of fusion. The interaction between the powder and the plasma arc depends on the features of the powder mixtures and a hypothesis for the behavior of the powder mixtures used across the plasma arc is put forward. The more significant evaporation during hardfacing with powder mixtures with NP particles induced a more significant loss in Cu and an increase in porosity in the austenitic coatings. Further impacts of the Cu-based nanoparticles in the deposited powders mixtures are revealed by the finer solidification structure. Regardless of the features of the powder mixtures, Cu-containing coatings showed a lower hardness associated with Cu being in solid solution on the as-deposited condition.

Keywords: Nanoparticles, Coatings, Plasma Transferred Arc, 316L, Cu and CuO.

INTRODUCTION

The search for materials with high resistance to bacterial corrosion aims to extend the service life of equipment exposed to environments where bacteria easily form, such as medical devices, marine transport vehicles, water treatment and storage systems, agriculture machinery, pharmaceutical and food industry, among

others (Macedo, 2000; Durmoo et al., 2008; Kasnowski; Mantilla; Oliveira, 2010; Jia et al., 2019). A step further in the search for materials with enhanced resistance to biological agents was imposed by the recent Covid-19 pandemic which brought the urgency to combat the spread of the virus (Liu et al., 2020; Hasan; Kow; Zaidi, 2021). Developing antimicrobial materials for common-use surfaces that are frequently touched such as doorknobs and handrails might mitigate the contamination by viruses and bacteria. Viruses can remain active for periods ranging from 4 to 72 hours on stainless steel surfaces (Kampf et al., 2020; Van Doremalen et al., 2020). In this scenario, keeping the surface free of pathogens must depend on the material used to fabricate the object and/or its surface.

In hospitals, it is common to find copper and its alloys on surfaces of common use, in order to prevent the spread of contagious diseases (Palza et al., 2018; Colin et al., 2020). Copper is recognized for its antimicrobial action, being able to eliminate fungi, viruses, and bacteria in contact with its surface (Grass; Rensing; Solioz, 2011; Mathews; Kumar; Solioz, 2015; Silva et al., 2019; Wu et al., 2020). One of the mechanisms responsible for the antimicrobial action on copper-containing surfaces is the release of copper ions, which when adhering to the cell of a microorganism reacts with the cell membrane and damages its protein structure, making its survival impossible (Xi et al., 2017). Another mechanism occurs by generating reactive oxygen species (ROS), which attack different parts of bacteria and viruses. In this context, nanoparticles with a high surface-to-volume ratio have been emphasized for their differentiated physicochemical properties, as well as their antimicrobial action (Warnes; Little; Keevil, 2015; Slavin et al., 2017).

It is possible to add Cu to other materials to guarantee antimicrobial properties, research data indicates that small amounts of copper (0.2-4.5 wt%) added to stainless steel show good antimicrobial behavior (Chai et al., 2011; Xi et al., 2016; Chen et al., 2020; Zhang et al., 2021). Adding larger amounts of Cu to a metal matrix increases antimicrobial activity, as it enables a greater release of ions that effectively kill the microorganisms (Xi et al., 2017; Zhang et al., 2021). The dependence on processing features of these alloys is observed as mechanical properties, corrosion resistance, and antimicrobial properties of the Cu-bearing stainless steels are influenced by the form in which Cu is present in the alloys, either as an alloying element in solid solution or in copper-rich precipitates, that might require solubilization and aging heat treatment (Xi et al., 2016; Xi et al., 2017). Antimicrobial

action of parts is required at their surface hence the development of Cu-bearing stainless steel coatings appears as a viable solution to process components with such functionality.

However, there is a gap in the literature regarding the impact of Cu additions on the processability and metallurgical features of stainless steel coatings. This study assesses the impact of Cu additions to a stainless steel on the processability of hardfacing coatings. In an innovative approach, Cu and CuO nanoparticles (NPs) were mixed with the particles of the atomized AISI 316L steel. Correlation with hardfacing coatings processed with mixtures of the atomized steel with Cu microparticles (MPs) is also carried out to discuss the processability and metallurgical features of the modified stainless steel.

MATERIALS AND METHODS

Powder mixtures were prepared using gas-atomized AISI 316L stainless steel powder (particles size ranging from 75 to 250 μm), metallic Cu powder (MPs - particle size ranging from 30 to 175 μm), nanopowders of copper and copper oxide (NPs - particles size of about 500 nm and 40 nm, respectively). The chemical compositions of the powder materials are shown in Table 18, and the prepared powder mixture compositions are presented in Table 19.

The high surface energy of NPs accounts for their tendency to cluster together. Prior to the mixing process, the nanopowder was dispersed in an ultrasonic bath with ethanol. The ethanol-dispersed NPs were added and mixed with AISI 316L powder for 2 h. The wet mixture was dried in a furnace at 50 °C for 12 h. Subsequently, the dry powders were blended in a Y-type mixer to guarantee good adherence between the MPs and NPs for 12 h. The powder mixtures and particle morphology were assessed by optical microscopy and confocal laser microscopy, respectively.

Powder mixtures were deposited by a plasma transferred arc (PTA) equipment (Stellite Starweld 300) as single-bead coatings on AISI 316L plates (13 x 32 x 160 mm). The substrate surfaces were ground, cleaned with ethanol, and dried before PTA deposition. During processing, the plasma arc is established between a tungsten electrode and the substrate and is directed by the torch. In contrast with other directed energy deposition techniques, the feedstock powder is fed in the

proximity of the plasma arc, where it starts to melt before reaching and mixing with the substrate material in the melt pool, Figure 45. As the heat Source moves in the direction of deposition, the melt pool solidifies as a single bead.

Table 18 - Powder chemical composition

(wt %)	Cr	Ni	Mo	Mn	S	Si	Fe	Mg	Cu	Source
316L	17.64	12.52	3.34	1.72	0.69	0.53	Bal.			EDX
Cu MP								0.40	Bal.	EDX
Cu NP	99.8% purity									Manufacturer
CuO NP	99% purity									Manufacturer

Source: Authors (2023).

Table 19 - Composition of powder mixtures used for the coatings

Powder mixture	Powder composition
316L	100 wt% AISI 316L
316L + Cu MP	95 wt% AISI 316L + 5 wt% Cu microparticles
316L + Cu NP	95 wt% AISI 316L + 5 wt% Cu nanoparticles
316L + CuO NP	95 wt% AISI 316L + 5 wt% CuO nanoparticles

Source: Authors (2023).

Figure 45 - PTA powder deposition process

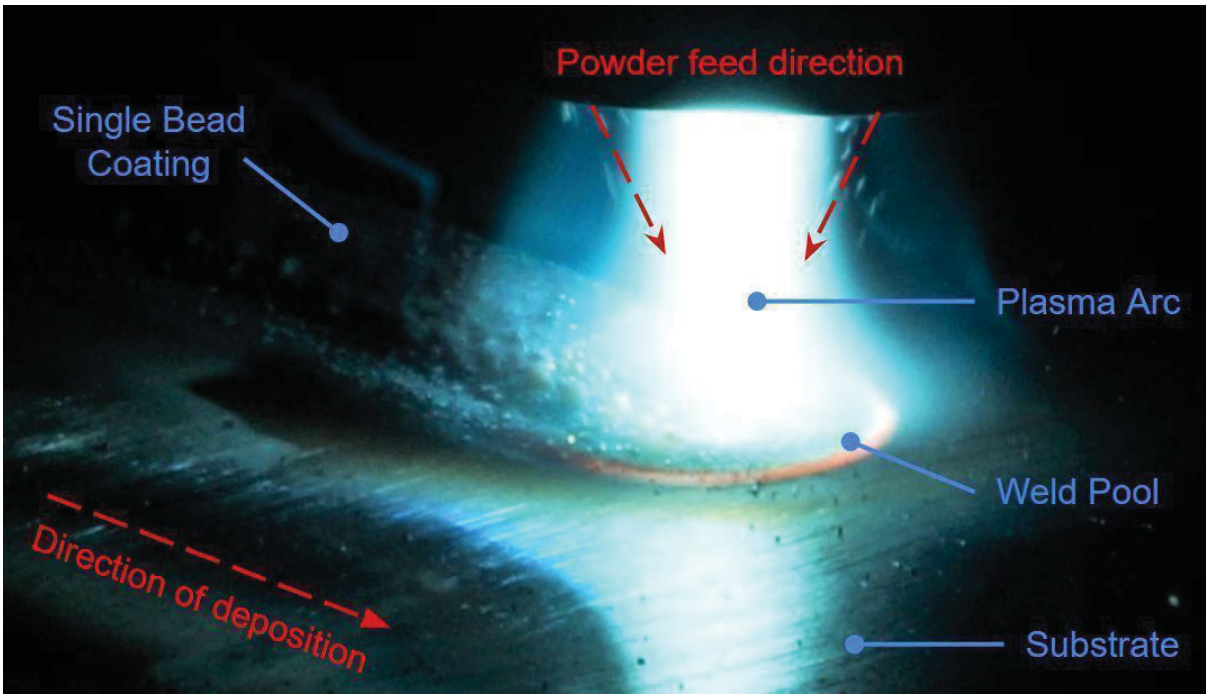

Source: Authors (2023).

The powder mixtures were warmed up in a furnace at 100 °C for 1 h prior to the deposition. Processing parameters were selected for each powder mixture to obtain continuous deposits that required different powder flow rates. For the powder mixtures without NPs, the powder flow rate was 0.167 g/s. When powder mixtures with NPs were tested with the same powder flow rate, the powder supply system clogged during the deposition, resulting in uneven powder delivery to the weld pool. To avoid this problem, the powder mixtures with NPs were processed with a lower powder flow rate of 0.100 g/s, which guaranteed continuous delivery of microparticles and nanoparticles to the plasma arc. Regardless of the feeding rate, two deposition currents were used as shown in Table 20, where the selected processing parameters are presented.

Table 20 - PTA processing parameters

Parameter (unit)	**Value**
Powder flow rate (g/s)	0.100, 0.167
Deposition current (A)	80, 100
Deposition speed (mm/s)	1.667
Nozzle-plate distance (mm)	10
Protective gas	Argon 99%
Carrier gas flow (l/s)	0.013
Plasma gas flow (l/s)	0.033
Shield gas flow (l/s)	0.250

Source: Authors (2023).

For each processed coating, analyses were carried out using two transverse cross-sections that were ground, polished with alumina (1 μm) to attain a mirror-like finish, cleaned ultrasonically in ethanol, and etched with Marbles solution (4 g CuSO4 + 20 ml HCl + 20 mL H2O). The micrographs were obtained in an optical microscope and the analysis of the geometrical features (height, width, dilution, wettability, and porosity) was carried out in analysis software (ImageJ). Micrographs of the mirror-polished specimens for the porosity analysis were obtained at a magnification of 100x, covering all single-bead transverse cross-sections.

The microhardness profiles of the coatings were obtained in a micro indentation tester using a Vickers diamond indenter at a load of 500 g (4.9 N) and a

dwell period of 10 s. The microhardness profiles were measured in the center portion of the coating cross-section, starting from the substrate.

The characterization of coatings included X-ray diffraction (XRD) tests conducted in an X-ray diffractometer, using a scanning speed of 1.0 degrees/min and scanning angle 2θ from 30º to 90º with Cu-Ka radiation (λ = 0.15406 nm) at 40 kV and 20 mA. The polished specimens were separated from the substrate prior to the XRD and were randomly oriented in the sample holder. Characterization of the top region of the coating transverse cross-section was also carried out by scanning electron microscope (SEM) equipped with energy dispersive spectroscopy (EDS) unity.

RESULTS AND DISCUSSION

Micrographs of the powder mixtures and of the powder particles used are shown in Figure 46. Stainless steel powder is gray and its particles are spherical with a few satellite particles (Figure 46a). Cu powder is red-orange and its particles are irregularly shaped (Figure 46b). The Cu NPs present the same red-orange color as the Cu MPs, while CuO exhibits a brownish-orange color. The mixing process between the atomized stainless steel with nanopowders resulted in a “layer” of either Cu nanopowder (Figure 46c) or CuO nanopowder (Figure 46d) adhered to the surface of the former particle.

Coatings processed with the atomized stainless steel and with the mixtures containing Cu MPs, Cu NPs, and CuO NPs did not change the formation of the austenite phase (Figure 47). Nevertheless, in coatings processed with the powder mixture of stainless steel and Cu MPs, detailed analysis reveals a shift to the right on the main peaks for the austenite (Figure 47b). The contributions to the observed shift are due to residual stresses from the solidification of the melt pool, the increase in Cu content in the austenitic matrix, and the formation of Cu-rich precipitates, all factors contributing to lattice distortion.

The atomic radius of Cu (128 pm) is larger than that of Fe (124 pm) and when in a solid solution it increases the lattice constant (Xi et al., 2016). However, using Bragg’s law, the calculated lattice parameter (Table 21) shows a reduction in the lattice parameter after Cu addition, this could indicate that either Cu occupies a position in the crystal lattice that accommodates well the small atomic difference or

that small precipitates might have formed but its dispersion is not dense enough to be identified by the XRD phase analysis. Processing coatings with the powder mixtures containing NPs also induced a shift to the right in the main peaks of austenite (Figure 47c and Figure 47d) and a reduced lattice parameter (Table 21) that varies with the composition of the NPs. For the mixture containing CuO NP, this effect was more significant, which can be explained by the presence of undissolved oxides in the austenitic matrix, although due to its size, it could not be detected by XRD.

Figure 46 - Optical micrographs of powder mixtures and confocal laser micrographs of particles

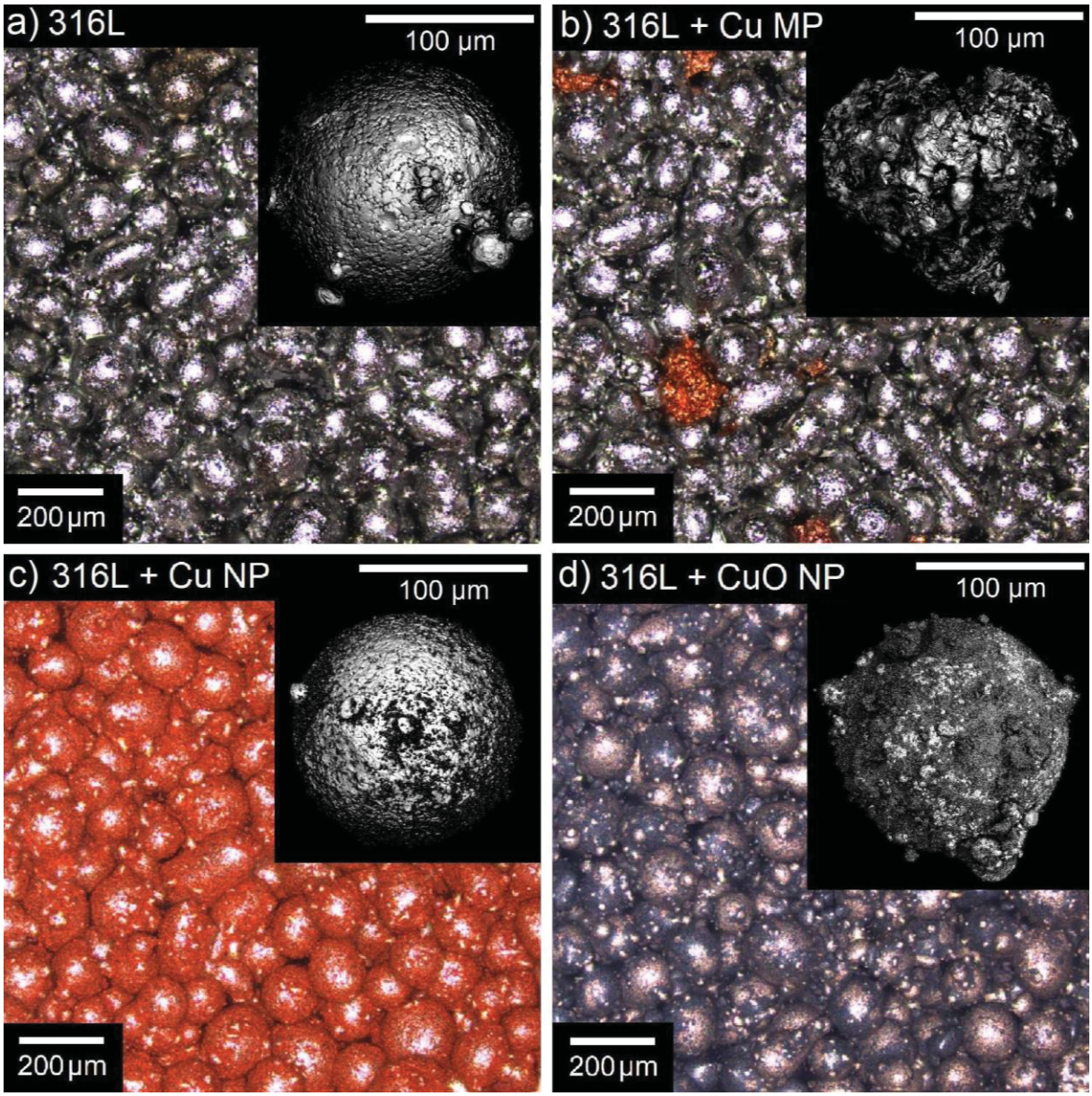

Source: Authors (2023).

Figure 47 - XRD patterns of the coatings with deposition current of 100 A

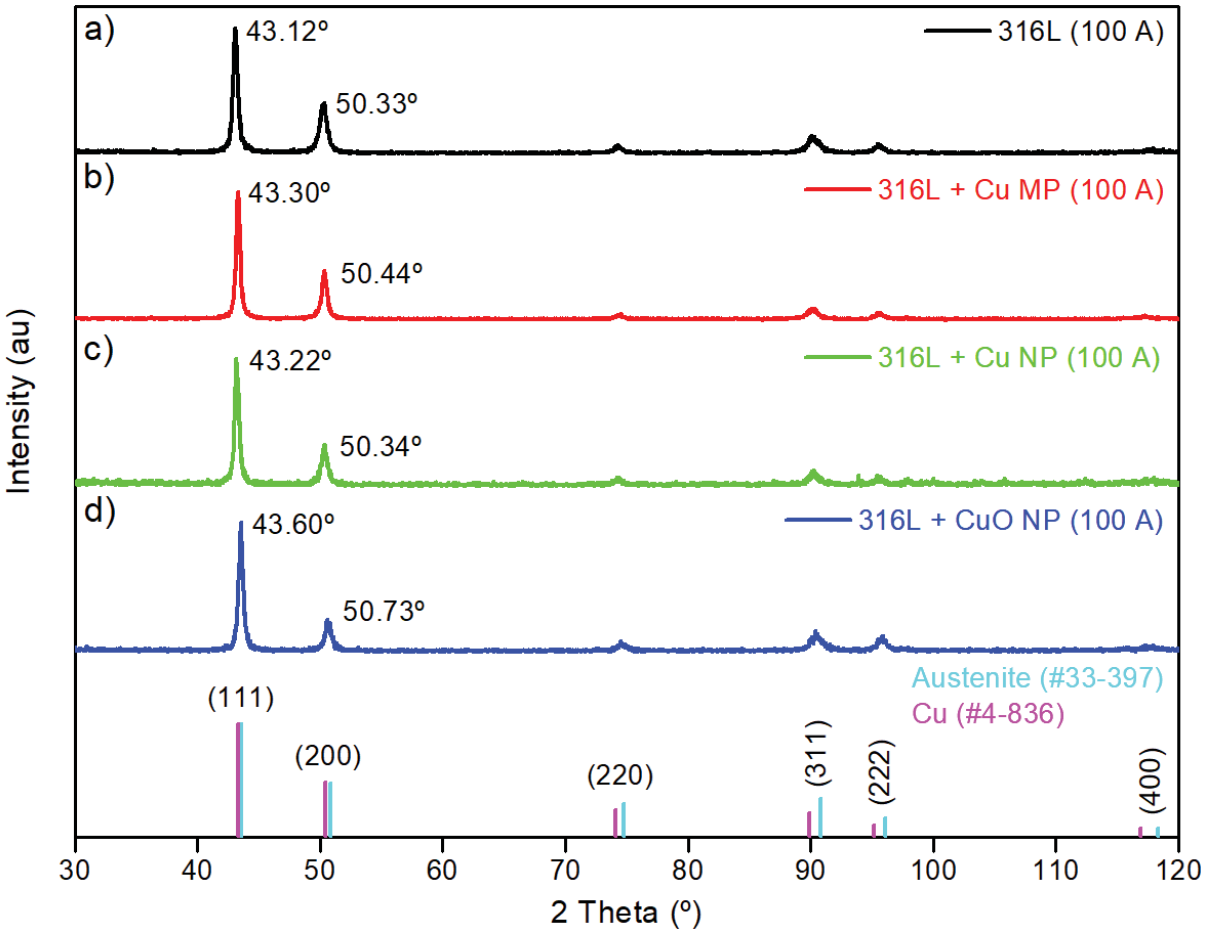

Source: Authors (2023).

Table 21 - Peak angle and lattice parameters

Powder mixture	Crystallographic plane	2 Theta (°)	Lattice Parameter (Å)
316L	(111)	43.12	2.096
	(200)	50.33	1.812
316L + Cu MP	(111)	43.30	2.088
	(200)	50.44	1.808
316L + Cu NP	(111)	43.22	2.092
	(200)	50.34	1.811
316L + CuO NP	(111)	43.60	2.074
	(200)	50.73	1.798

Source: Authors (2023).

Detailed analysis of the chemical composition at the top region of the coating cross-section (Figure 48b) shows that for the coatings processed with the stainless steel mixture containing Cu MPs with a deposition current of 100 A, Cu content is

nearly the same as in the powder mixture. For the conditions used, EDS mapping could not detect preferential Cu position within the austenitic matrix. However, in coatings processed with powder mixtures containing either Cu NPs or CuO NPs, the Cu content in the coating (Figure 48c and Figure 48d) is significantly smaller than in the powder mixture. This can be caused by two main phenomena. The high surface-to-volume ratio of the NPs that causes them to cluster together and adhere to the surface of other materials to reduce their surface energy, namely walls of the powder mixing and feeding systems. Also, some NPs adherent to the surface of the atomized stainless steel particles might evaporate when exposed to high temperatures in the plasma arc. This result is an important contribution to the processing of powder mixtures containing NPs, contributing to the understanding of how to handle NPs powder mixtures and to control the chemical composition of coatings.

Figure 48 - SEM/EDS of the coatings with deposition current of 100 A

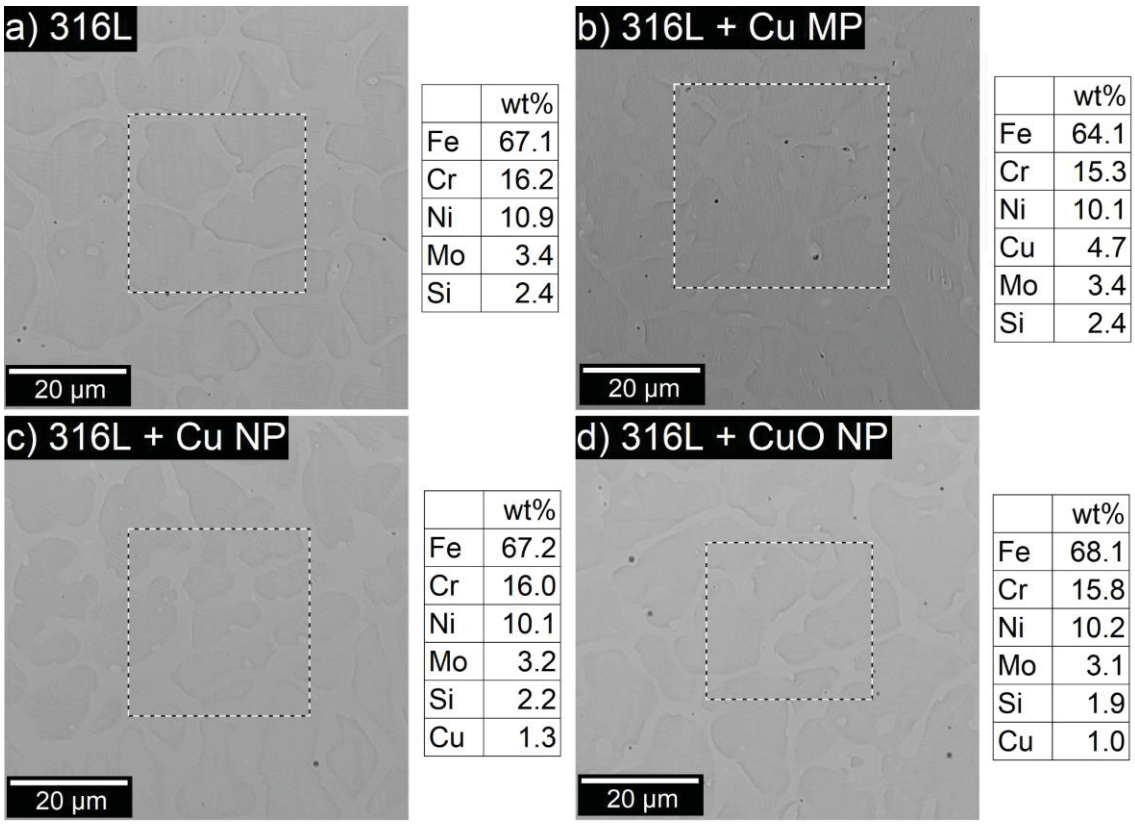

	wt%
Fe	67.1
Cr	16.2
Ni	10.9
Mo	3.4
Si	2.4

	wt%
Fe	64.1
Cr	15.3
Ni	10.1
Cu	4.7
Mo	3.4
Si	2.4

	wt%
Fe	67.2
Cr	16.0
Ni	10.1
Mo	3.2
Si	2.2
Cu	1.3

	wt%
Fe	68.1
Cr	15.8
Ni	10.2
Mo	3.1
Si	1.9
Cu	1.0

Source: Authors (2023).

Further characterization was made at the cross-section of coatings revealing crack-free coating (Figure 49 and Figure 50), but changes associated with each

deposited material were identified. Regardless of the feedstock used, increasing the deposition current leads to a higher dilution (Figure 49), associated with higher heat input that also enhances wettability. As a result of the higher wettability, a reduction in the height and an increase in the width of coatings occurs (Figure 51) following the expected behavior in hardfacings (Takano; Queiroz; d'Oliveira, 2010). Although, the high thermal conductivity of Cu MPs reduces the wettability of coatings processed with powder mixtures, inducing changes in the height and width of coatings (Figure 51), the impact of increasing the deposition current did not change. Particularly, the addition of Cu MP led to a significant reduction in the dilution (Figure 49), this can be associated with the thermal conductivity of Cu (403 W/mK) (Ho; Powell; Liley, 1972) which is higher than that of AISI 316L (13 W/mK) (Gilcrist; Preston, 1985). As a result, a greater heat output at the melt pool is expected, and consequently, the higher solidification rate reduces the interaction between the melted particles and the molten substrate, hence reducing the penetration into the substrate.

Figure 49 - Coatings cross-section micrographs (powder flow rate of 0.167 g/s)

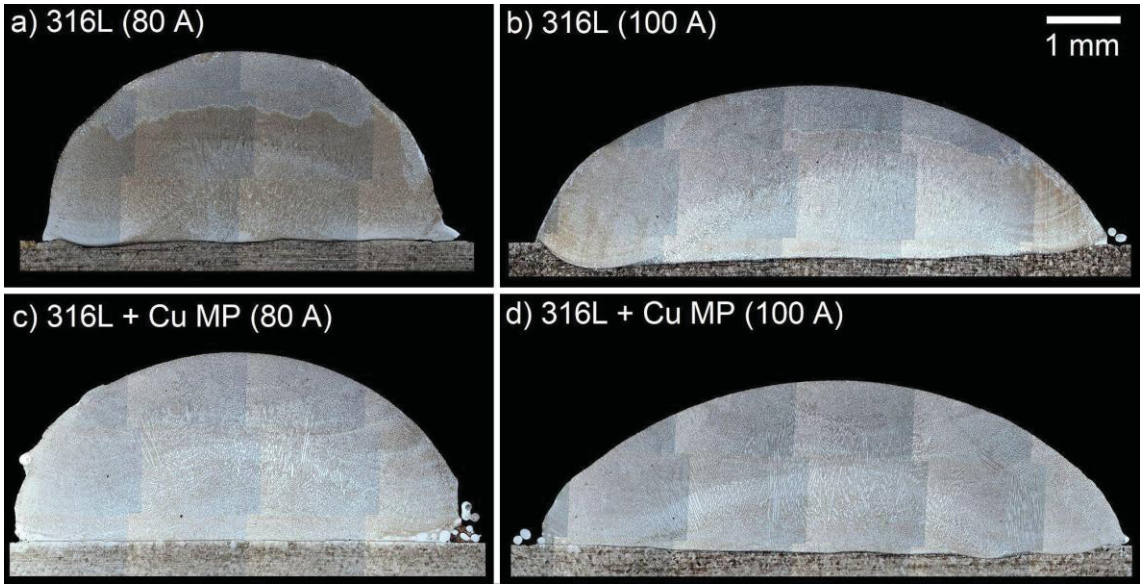

Source: Authors (2023).

Although the processing parameters selection for each powder mixture considered a sound visual analysis of each coating, detailed analysis shows that processing the powder mixtures containing NPs respond differently to the selected parameters (Figure 50 and Figure 51). Lack of fusion for the lower deposition current used (80 A) is observed at the interface with the substrate (Figure 50) in spite of the

lower powder feed rate used, 0.100 g/s as opposed to 0.167 g/s for the previous coatings. As expected, the lower feeding rate used to process the powder mixtures containing NPs with 100 A accounts for a decrease in height and width compared to the stainless steel coating. As measured in coatings containing Cu MPs, the addition of Cu NPs also reduces dilution with the substrate even with a smaller Cu content on the deposited coating. Figure 52 shows a schematic representation of the interaction between the powder mixture and the plasma arc. Due to the dispersion of nano-size particles around the atomized particles, the large surface area, and the high thermal conductivity of Cu, more energy is captured from the plasma arc into the powder feedstock, causing part of the Cu NPs to evaporate. Consequently, less energy from the plasma arc is available to melt the substrate, thus reducing the dilution with the substrate material (Figure 52b).

Figure 50 - Coatings cross-section micrographs (powder flow rate of 0.100 g/s).

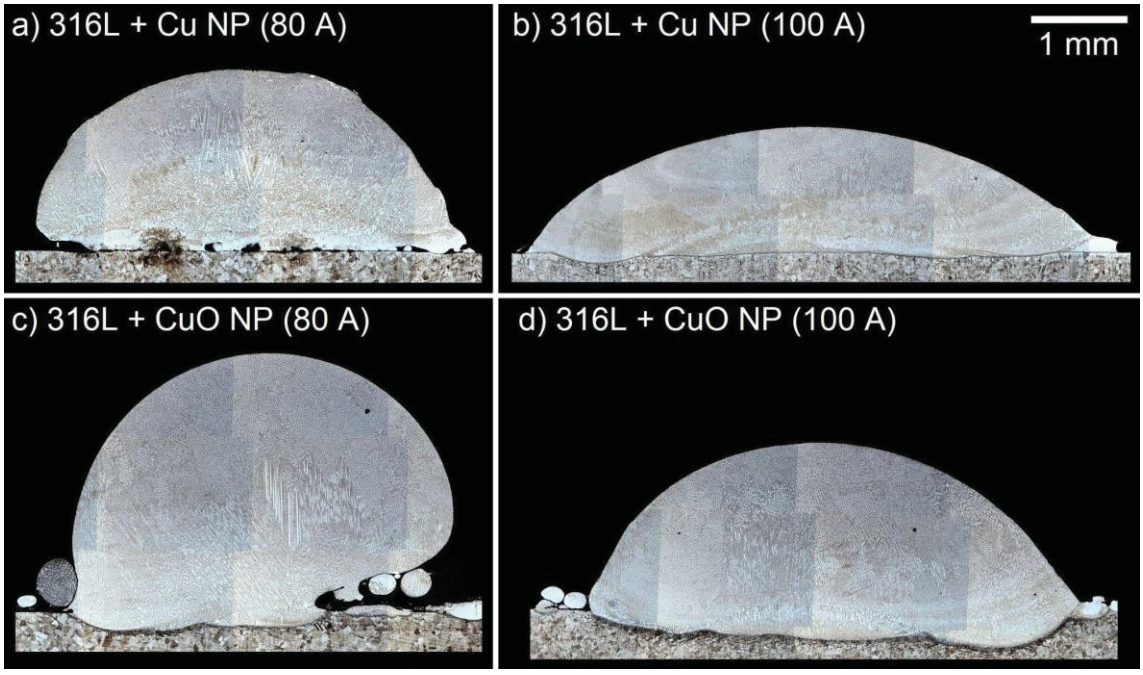

Source: Authors (2023).

A better understanding of the impact of CuO NPs requires a better analysis of the behavior of particles as they cross the plasma arc (Figure 52). The lower thermal conductivity of CuO (33 W/mK) (Liu; Lin; Wang, 2011) does not allow particles to absorb as much energy as metallic surface particles do. As a consequence, when the atomized steel particles covered with CuO NPs (Figure 46d)

cross the plasma arc the NPs layer acts as a thermal barrier (Abreu-Castillo; Bueno; d'Oliveira, 2021). This effect accounts for the lack of fusion (Figure 50c) for the lower deposition current used (80 A). The lower wettability induced by the CuO NPs accounts for the height increase and width decrease compared to coatings processed with Cu NPs. Another contrasting behavior between coatings processed with each NPs is shown by the measured increase in dilution, which is larger than that measured in stainless steel coating processed at 100 A (Figure 51). This behavior might be associated with the mentioned thermal barrier effect of the CuO NPs that increase the energy available to interact with the substrate. Also, under these processing conditions, the reduction of the copper oxide occurs, forming metallic Cu and oxygen molecules (Figure 52c). The presence of oxygen in the melt pool changes the Marangoni convection mode from outward to inward (Zou; Ueji; Fujii, 2014; Zhang et al., 2022), further contributing to the larger dilution measured.

Figure 51 - Geometrical features. (a) Height, (b) width, (c) dilution, and (d) wettability

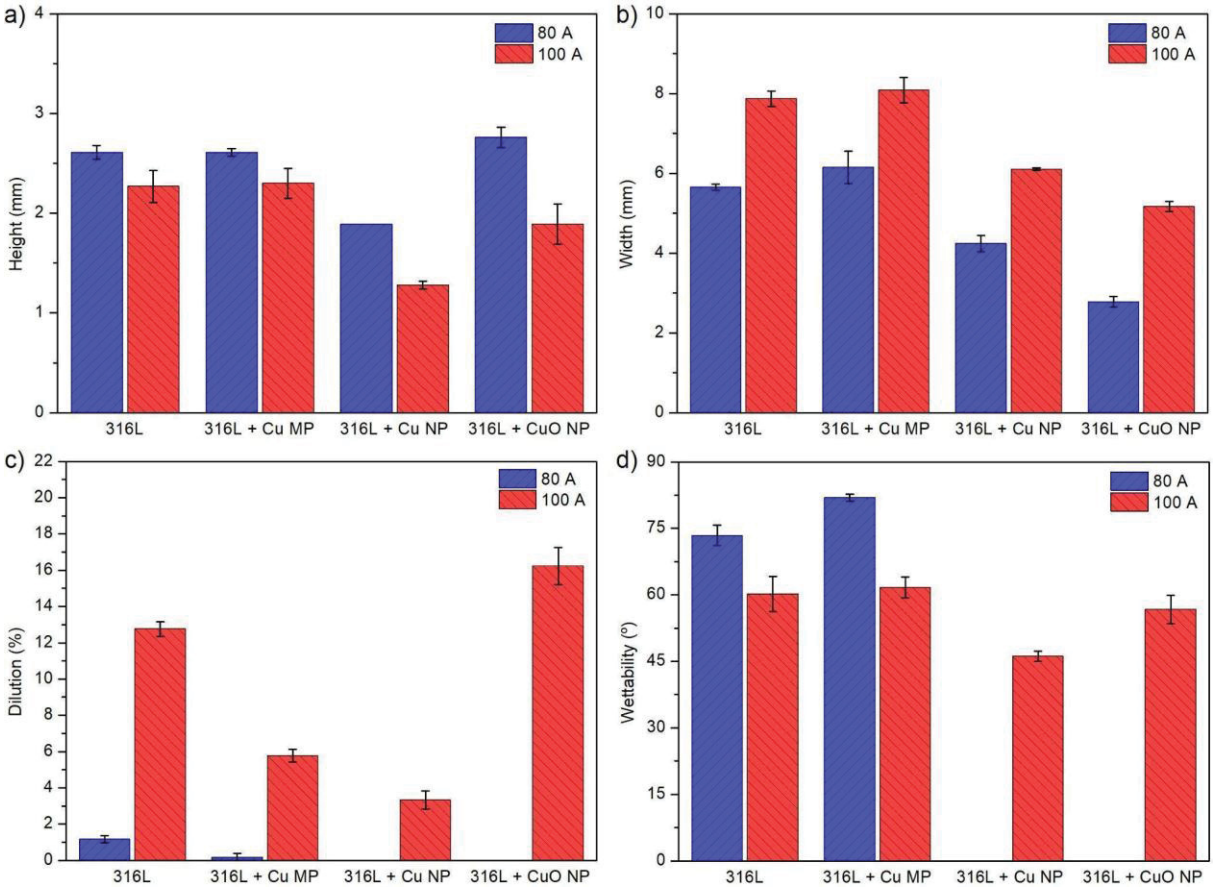

Source: Authors (2023).

Figure 52 - Schematic representation of the interaction between powder feedstock, plasma arc, and melt pool

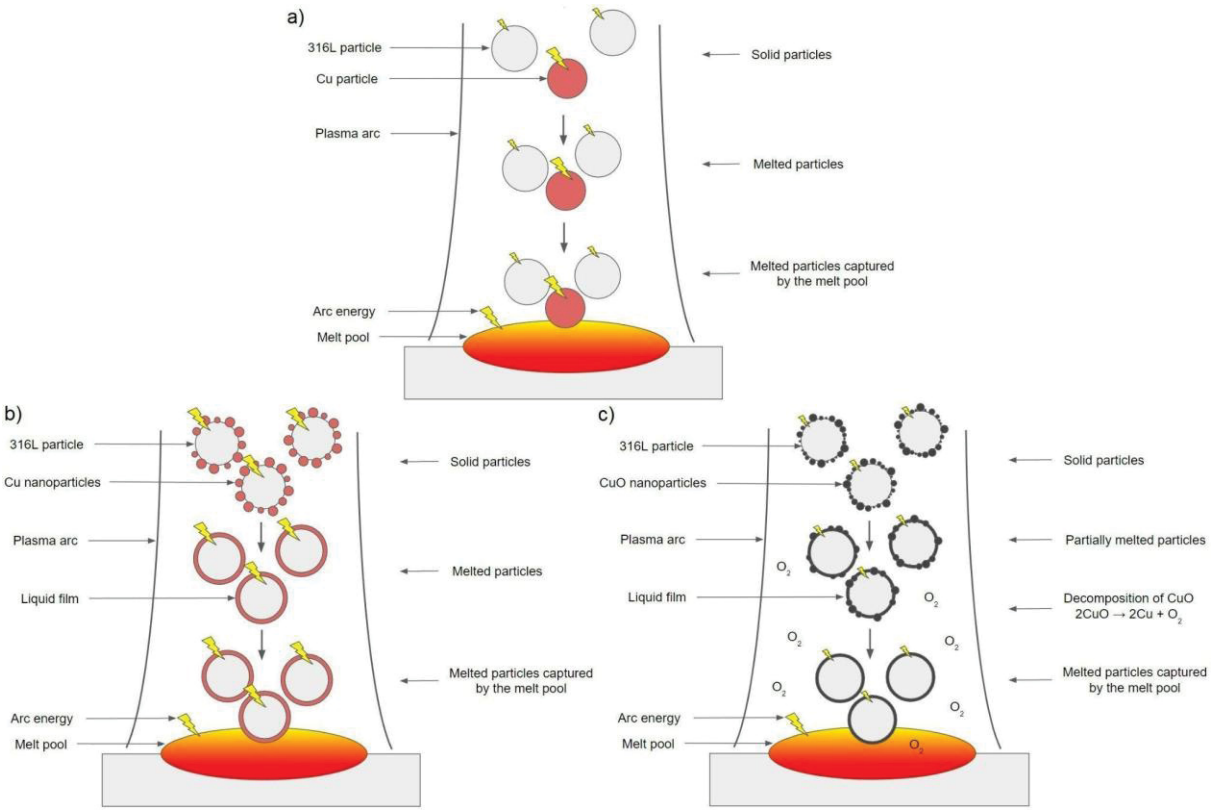

Source: Authors (2023).

Further understanding of the interaction between the different feedstock powders and the plasma arc is given by the analysis of the porosity at the transverse cross-section of coatings. Coatings processed with a deposition current of 80 A, even with the lack of fusion observed, were considered in the porosity analysis to promote a better understanding of the behavior of the powders when they cross the plasma arc, melt and solidify. Figure 53a shows the density of coatings, revealing the atomized 316L stainless steel powder to produce low porosity coatings (density above 99.95%). Adding Cu MPs and Cu NPs preserves the high density of coatings (Figure 53a) although small changes in the pore average size (Figure 53b) and pore count (Figure 53c) were measured. As a general trend, coatings processed with a deposition current of 100 A exhibited higher dilution and increased density.

Figure 53 - Porosity analysis. (a) density, (b) average pore size, and (c) pore count

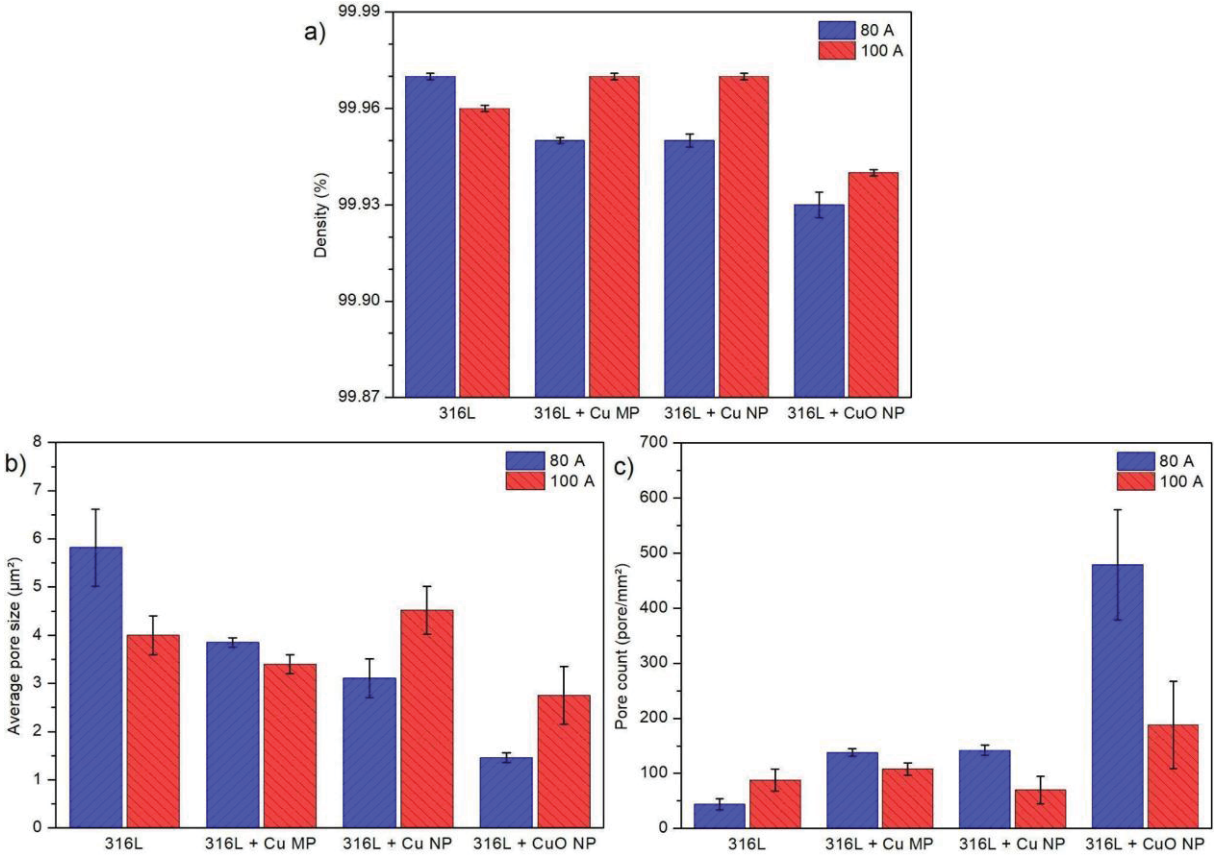

Source: Authors (2023).

The lower density of coatings processed with the CuO NPs powder mixture (99.93%) is coherent with the release of O_2 during the decomposition of CuO and reduced absorbed energy by the powders as they cross the plasma arc, which causes a less efficient melting of these particles. The pore count is much higher in coatings containing CuO NPs (Figure 53c), which is associated with the decomposition of CuO and partially melted particles. It is also possible to raise the hypothesis that there are undissolved oxides in the austenitic matrix (Cooper et al., 2016), and these oxides are counted as porosity in the image analyzer due to the high contrast with the metallic matrix in the mirror-polished condition. With the increase in the deposition current, more energy is available to dissolve the oxides, as a result, powder mixtures with CuO NPs processed with 100 A showed fewer but larger pores.

Microstructures as observed at the transverse cross-section of the single-bead coating show solidification structures typical of welding (Figure 54). Solidification starts at the interface with the substrate (Figure 54a), and the faster

cooling rates near the fusion line account for the cellular growth. As segregation occurs the cellular growth rapidly changes to columnar dendritic, which can be seen throughout the middle of the layer (Figure 54b), growing along the direction of the heat flow and away from the substrate. As the remaining liquid cools down at the top of coatings in contact with air, equiaxed dendrites form (Figure 54c) (Mazur; Mazur; d'Oliveira, 2022). As expected, due to grain refinement associated with PTA processing, the 316L coating showed a higher hardness than the substrate (Figure 55b) (Bond; d'Oliveira, 2012; Gomes; Henke; d'Oliveira, 2012).

Figure 54 - Microstructure of the coatings processed with 100 A

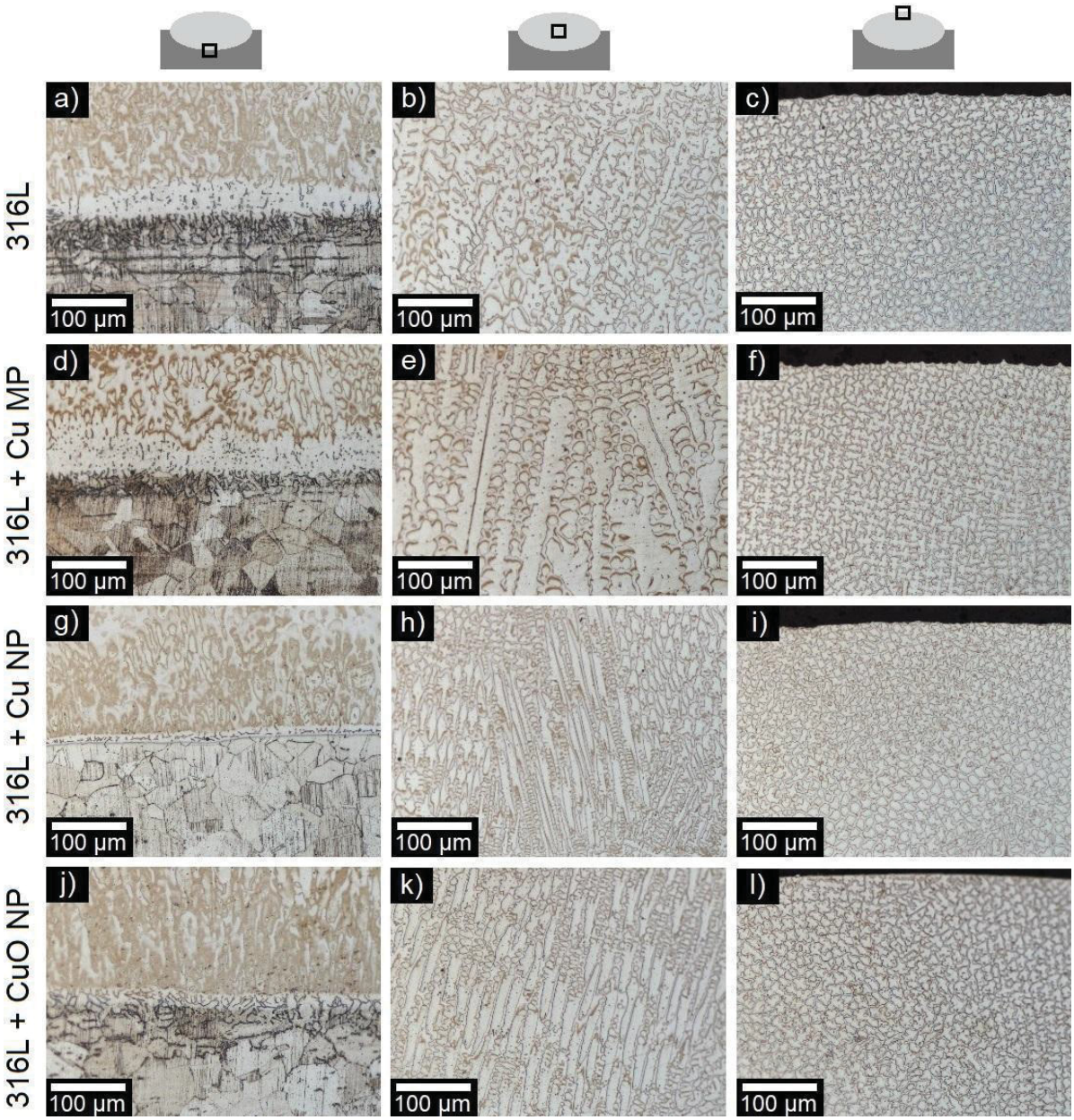

Source: Authors (2023).

Coatings processed with the powder mixture containing Cu MPs exhibited coarser columnar dendrites in the middle section of the layer (Figure 54e). The lower hardness measured in the as-deposit condition (Figure 55a) follows the expected hardness reduction reported for Cu-rich austenitic matrix, although a hardness increase is expected following precipitation hardening (Xi et al., 2016; Xi et al., 2017). In contrast, a smaller zone of cellular growth near the fusion line (Figure 54g), and finer dendrites were observed in coatings processed with powder mixtures containing Cu NPs (Figure 54h), leading to an increase in hardness. The observed structure refinement is a consequence of an increase in the thermal conductivity of coatings containing Cu MPs, inducing a faster solidification rate with higher nucleation and growth rates.

Coatings processed with powder mixtures containing CuO NPs also exhibited a finer microstructure (Figure 54k) than that of coatings processed with Cu MPs (Figure 54e). Microstructure features at the fusion line and center of the deposited layers are coarser than those exhibited by coatings processed with Cu NPs in agreement with the hardness measurements (Figure 55a). As already mentioned, the presence of CuO NPs in the powder mixture influences the processability of the coatings, as a result, a lower density was obtained with the same processing parameters of 316L coating. Oxides and the high number of pores can account for the lower hardness (Cooper et al., 2016).

Results showed that when Cu is mixed with the atomized AISI 316L alloy as MPs, NPs, or even CuO NPs, the processability of coatings is made more difficult. However, as Cu has been mentioned to add antimicrobial action to the AISI 316L stainless steel, results show that the selection of the processing parameters is crucial to allow adding this new functionality to the surface of parts without altering the bulk material.

Figure 55 - Vickers hardness measured in the cross-section. (a) Mean hardness, and (b, c, d, e) hardness profile

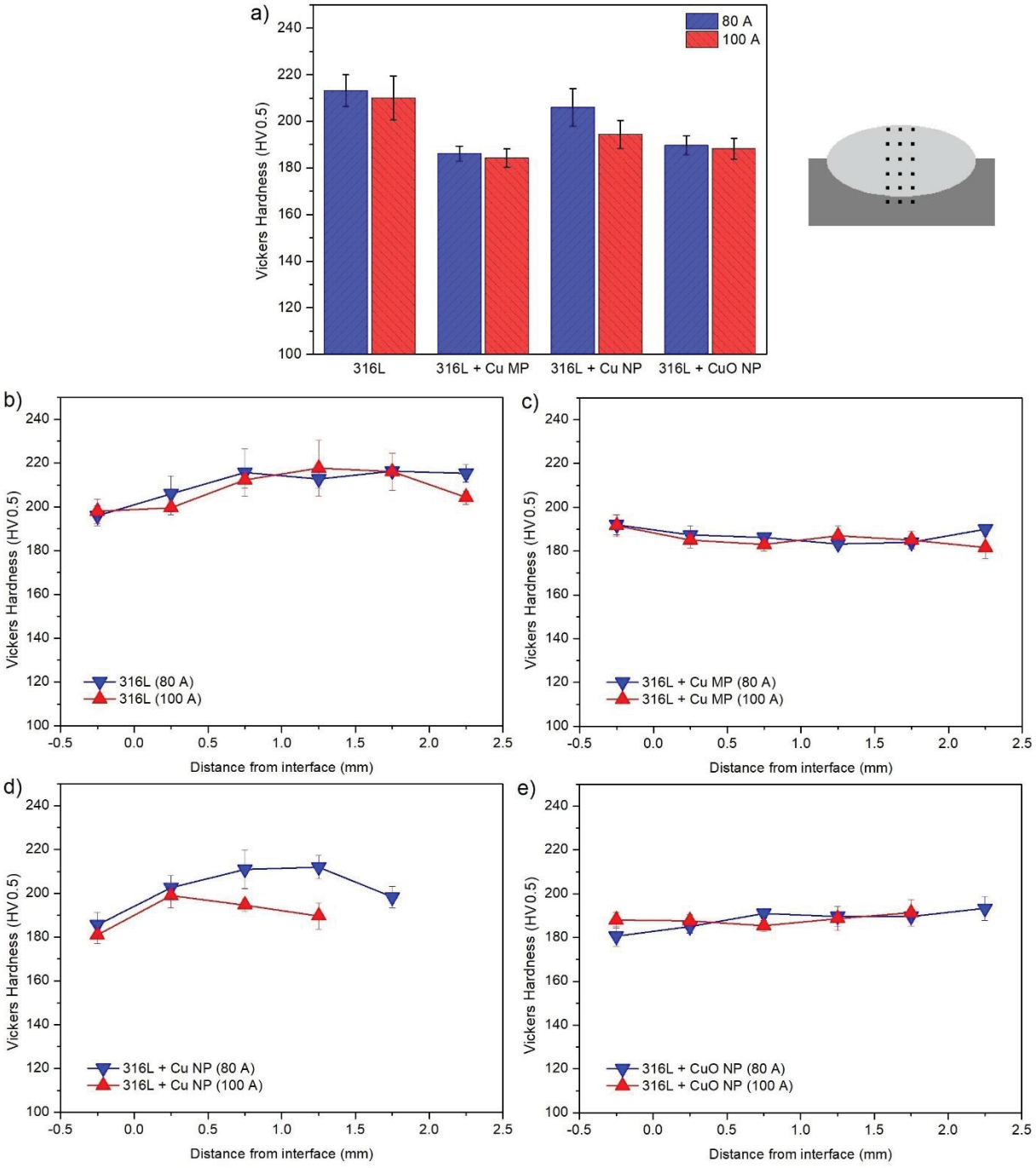

Source: Authors (2023).

CONCLUSIONS

The processability of AISI 316L stainless steel coatings containing Cu MPs, Cu NPs, and CuO NPs was explored in this study. For the tested conditions employed, the major conclusions are as follows:

- AISI 316L powder modified with 5 wt% Cu MPs, Cu NPs, and CuO NPs was successfully prepared and processed by plasma transferred arc, resulting in crack-free high-density coatings (over 99.93%) that did not compromise the formation of the austenite phase.
- Cu content in coatings processed with Cu MPs (4.7 wt%) remained consistent with the powder mixture composition (5.0 wt%). However, the interaction of NPs with the plasma arc and eventual losses during the handling of the powder mixtures required specific procedures to control the chemical composition of coatings.
- Coatings exhibited a similar solidification structure: cellular growth near the interface with the substrate that changed into columnar dendritic, and equiaxed dendritic at the top regions of coatings, regardless of the composition of powder mixtures used.
- High thermal conductivity and the presence of coarse columnar dendrites caused by the addition of Cu MPs resulted in a decrease in coating dilution (5.8 %) and hardness (184 $HV_{0.5}$).
- Cu NPs in the deposited powder mixture resulted in grain refinement and an increase in coating hardness (194 $HV_{0.5}$), and a reduction in coating dilution (3.3 %).
- The decomposition of CuO when processing powder mixtures releases oxygen with a twofold effect, increasing porosity (reducing density to 99.93 %) and changing the dynamics of the molten material. That increases dilution (16.2 %) despite the low wettability of the coatings.

ACKNOWLEDGMENTS

The authors acknowledge CAPES, the National Council for Scientific and Technological Development (CNPq), Instituto Nacional de Engenharia de Superfícies/CNPq, the Laboratory of X-Ray Optics and Instrumentation (LORXI) of UFPR, and the Laboratory of Additive Manufacturing and Surface Engineering (LAMSE) of UFPR.

REFERENCES

ABREU-CASTILLO, H. O.; BUENO, B. P.; D'OLIVEIRA, A. S. C. M. In situ processing aluminide coatings with and without tungsten carbide. **The International Journal of Advanced Manufacturing Technology**, v. 119, n. 1-2, p. 477-488, Nov. 2021. DOI. 10.1007/s00170-021-08032-z.

BOND, D.; D'OLIVEIRA, A. S. C. M. Effect of current and atomized grain size distribution on the solidification of Plasma Transferred Arc coatings. **Materials Research**, v. 15, n. 5, p. 770-774, Aug. 2012. DOI. 10.1590/s1516-14392012005000101.

CHAI, H.; GUO, L.; WANG, X.; FU, Y.; GUAN, J.; TAN, L.; REN, L.; YANG, K. Antibacterial effect of 317L stainless steel contained copper in prevention of implant-related infection in vitro and in vivo. **Journal of Materials Science: Materials in Medicine**, v. 22, n. 11, p. 2525-2535, Aug. 2011. DOI. 10.1007/s10856-011-4427-z.

CHEN, K. K.; CHAO, C. Y.; CHEN, J. H.; WU, J. H.; CHANG, Y. H.; DU, J. K. Effect of Low Copper Addition to As-Forged 304 Stainless Steel for Dental Applications. **Metals**, v. 11, n. 1, p. 43, Dec. 2020. DOI. 10.3390/met11010043.

COLIN, M.; CHARPENTIER, E.; KLINGELSCHMITT, F.; BONTEMPS, C.; CHAMPS, C.; REFFUVEILLE, F.; GANGLOFF, S. C. Specific antibacterial activity of copper alloy touch surfaces in five long-term care facilities for older adults. **Journal of Hospital Infection**, v. 104, n. 3, p. 283-292, Mar. 2020. DOI. 10.1016/j.jhin.2019.11.021.

COOPER, A. J.; COOPER, N. I.; DHERS, J.; SHERRY, A. H. Effect of Oxygen Content Upon the Microstructural and Mechanical Properties of Type 316L Austenitic Stainless Steel Manufactured by Hot Isostatic Pressing. **Metallurgical and Materials Transactions A**, v. 47, n. 9, p. 4467-4475, Jun. 2016. DOI. 10.1007/s11661-016-3612-6.

DURMOO, S.; RICHARD, C.; BERANGER, G.; MOUTIA, Y. Biocorrosion of stainless steel grade 304L (SS304L) in sugar cane juice. **Electrochimica Acta**, v. 54, n. 1, p. 74-79, Dec. 2008. DOI. 10.1016/j.electacta.2008.06.028.

GILCRIST, K. E.; PRESTON, S. D. The Thermal Diffusivity/Conductivity of 316 Stainless Steel Powders in Air and Nitric Acid Mixtures at Room Temperature. **Thermal Conductivity**, v. 18, p. 713-722, 1985. DOI. 10.1007/978-1-4684-4916-7_67.

GOMES, R.; HENKE, S.; D'OLIVEIRA, A. S. C. M. Microstructural control of Co-based PTA coatings. **Materials Research**, v. 15, n. 5, p. 796-800, Aug. 2012. DOI. 10.1590/s1516-14392012005000099.

GRASS, G.; RENSING, C.; SOLIOZ, M. Metallic Copper as an Antimicrobial Surface. **Applied and Environmental Microbiology**, v. 77, n. 5, p. 1541-1547, Mar. 2011. DOI. 10.1128/aem.02766-10.

HASAN, S. S.; KOW, C. S.; ZAIDI, S. T. R. Social distancing and the use of PPE by community pharmacy personnel: does evidence support these measures?. **Research in Social and Administrative Pharmacy**, v. 17, n. 2, p. 456-459, Feb. 2021. DOI. 10.1016/j.sapharm.2020.04.033.

HO, C. Y.; POWELL, R. W.; LILEY, P. E. Thermal Conductivity of the Elements. **Journal of Physical and Chemical Reference Data**, v. 1, n. 2, p. 279-421, Apr. 1972. DOI. 10.1063/1.3253100.

JIA, R.; UNSAL, T.; XU, D.; LEKBACH, Y.; GU, T. Microbiologically influenced corrosion and current mitigation strategies: a state of the art review. **International Biodeterioration & Biodegradation**, v. 137, p. 42-58, Feb. 2019. DOI. 10.1016/j.ibiod.2018.11.007.

KAMPF, G.; TODT, D.; PFAENDER, S.; STEINMANN, E. Persistence of coronaviruses on inanimate surfaces and their inactivation with biocidal agents. **Journal of Hospital Infection**, v. 104, n. 3, p. 246-251, Mar. 2020. DOI. 10.1016/j.jhin.2020.01.022.

KASNOWSKI, M. C.; MANTILLA, S. P. S.; OLIVEIRA, L. A. T. Formação de biofilme na indústria de alimentos e métodos de validação de superfícies. **Revista Científica Eletrônica de Medicina Veterinária**, v. 15, p. 1-23. 2010.

LIU, M.; LIN, M. C.; WANG, C. Enhancements of thermal conductivities with Cu, CuO, and carbon nanotube nanofluids and application of MWNT/water nanofluid on a water chiller system. **Nanoscale Research Letters**, v. 6, n. 1, Apr. 2011. DOI. 10.1186/1556-276x-6-297.

LIU, Y.; NING, Z.; CHEN, Y.; GUO, M.; LIU, Y.; GALI, N. K.; SUN, L.; DUAN, Y.; CAI, J.; WESTERDAHL, D. Aerodynamic analysis of SARS-CoV-2 in two Wuhan hospitals. **Nature**, v. 582, n. 7813, p. 557-560, Apr. 2020. DOI. 10.1038/s41586-020-2271-3.

MACEDO, J. A. B. Biofilmes bacterianos, uma preocupação da indústria de farmacêutica. **Revista Fármacos & Medicamentos**, v. 2, n. 7, p. 19-24. 2000.

MATHEWS, S.; KUMAR, R.; SOLIOZ, M. Copper Reduction and Contact Killing of Bacteria by Iron Surfaces. **Applied and Environmental Microbiology**, v. 81, n. 18, p. 6399-6403, Sep. 2015. DOI. 10.1128/aem.01725-15.

MAZUR, V. T.; MAZUR, M. M.; D'OLIVEIRA, A. S. C. M. Graded Inconel 625 coatings with in-situ processing of Ni3Al. **Surface and Coatings Technology**, v. 445, p. 128660, Sep. 2022. DOI. 10.1016/j.surfcoat.2022.128660.

PALZA, H.; NUÑEZ, M.; BASTÍAS, R.; DELGADO, K. In situ antimicrobial behavior of materials with copper-based additives in a hospital environment. Inte**rnational Journal of Antimicrobial Agents**, v. 51, n. 6, p. 912-917, Jun. 2018. DOI. 10.1016/j.ijantimicag.2018.02.007.

SILVA, F.S.; CINCA, N.; DOSTA, S.; CANO, I.G.; GUILEMANY, J.M.; CAIRES, C.S.A.; LIMA, A.R.; SILVA, C.M.; OLIVEIRA, S.L.; CAIRES, A.R.L. Corrosion resistance and antibacterial properties of copper coating deposited by cold gas spray. **Surface and Coatings Technology**, v. 361, p. 292-301, Mar. 2019. DOI. 10.1016/j.surfcoat.2019.01.029.

SLAVIN, Y. N.; ASNIS, J.; HÄFELI, U. O.; BACH, H. Metal nanoparticles: understanding the mechanisms behind antibacterial activity. **Journal of Nanobiotechnology**, v. 15, n. 1, Oct. 2017. DOI. 10.1186/s12951-017-0308-z.

TAKANO, E. H.; QUEIROZ, D.; D'OLIVEIRA, A. S. C. M. Evaluation of processing parameters on PTA hardfacing surfaces. **Welding International**, v. 24, n. 3, p. 241-248, Mar. 2010. DOI. 10.1080/09507110902843974.

VAN DOREMALEN, N.; BUSHMAKER, T.; MORRIS, D. H.; HOLBROOK, M. G.; GAMBLE, A.; WILLIAMSON, B. N.; TAMIN, A.; HARCOURT, J. L.; THORNBURG, N. J.; GERBER, S. I. Aerosol and Surface Stability of SARS-CoV-2 as Compared with SARS-CoV-1. **New England Journal of Medicine**, v. 382, n. 16, p. 1564-1567, Apr. 2020. DOI. 10.1056/nejmc2004973.

WARNES, S. L.; LITTLE, Z. R.; KEEVIL, C. W. Human Coronavirus 229E Remains Infectious on Common Touch Surface Materials. **Mbio**, v. 6, n. 6, Dec. 2015. DOI. 10.1128/mbio.01697-15.

WU, Y.; WU, W.; ZHAO, W.; LAN, X. Revealing the antibacterial mechanism of copper surfaces with controllable microstructures. **Surface and Coatings Technology**, v. 395, p. 125911, Aug. 2020. DOI. 10.1016/j.surfcoat.2020.125911.

XI, T.; SHAHZAD, M. B.; XU, D.; SUN, Z.; ZHAO, J.; YANG, C.; QI, M.; YANG, K. Effect of copper addition on mechanical properties, corrosion resistance and antibacterial property of 316L stainless steel. **Materials Science and Engineering**: C, v. 71, p. 1079-1085, Feb. 2017. DOI. 10.1016/j.msec.2016.11.022.

XI, T.; SHAHZAD, M. B.; XU, D.; ZHAO, J.; YANG, C.; QI, M.; YANG, K. Copper precipitation behavior and mechanical properties of Cu-bearing 316L austenitic stainless steel: a comprehensive cross-correlation study. **Materials Science and Engineering**: A, v. 675, p. 243-252, Oct. 2016. DOI. 10.1016/j.msea.2016.08.058.

ZHANG, J.; SHAO, P.; WANG, X.; FAN, D. Improving weld penetration by two-TIG arc activated via mixing oxygen into shielding gas. **The International Journal of Advanced Manufacturing Technology**, v. 125, n. 1-2, p. 169-181, Dec. 2022. DOI. 10.1007/s00170-022-10703-4.

ZHANG, Z.; ZHANG, X. R.; JIN, T.; YANG, C. G.; SUN, Y. P; LI, Q.; YANG, K. Antibacterial mechanism of Cu-bearing 430 ferritic stainless steel. **Rare Metals**, v. 41, n. 2, p. 559-569, Jun. 2021. DOI. 10.1007/s12598-021-01751-y.

ZOU, Y.; UEJI, R.; FUJII, H. Effect of oxygen on weld shape and crystallographic orientation of duplex stainless steel weld using advanced A-TIG (AA-TIG) welding

method. **Materials Characterization**, v. 91, p. 42-49, May 2014. DOI. 10.1016/j.matchar.2014.02.006.

4.4 EFFECT OF CU ADDITIONS ON MICROSTRUCTURE AND WEAR PERFORMANCE OF AISI 316L MANUFACTURED BY PLASMA TRANSFERRED ARC

ABSTRACT

Cu additions to austenitic stainless steel enhance properties such as thermal conductivity and mechanical strength. Cu nanoparticles (NPs) are particularly effective, though their impact depends on the processing technique, which controls their distribution within the microstructure and influences material properties. The present study contributes to this discussion as it addresses the relationship between chemical composition, microstructure and wear performance. Cu was added to stainless steel powder in three forms: Cu microparticles (1 and 5 wt% Cu MP), Cu nanoparticles (1 wt% Cu NP), and CuO nanoparticles (1 wt% CuO NP). Plasma Transferred Arc (PTA-DED) was used to fabricate single-walls, which were characterized in two conditions, as-deposited and heat treated by solubilization at 1100 °C for 0.5 h, followed by aging at 700 °C for 3 h. The PTA-DED process achieved powder catchment efficiency above 93 % and cross-section density over 99.85 %. As-deposited microstructure analysis revealed grain refinement following Cu additions. Additionally, heat treatment of the richer Cu deposits induced a hardening effect due to Cu precipitation. Sliding wear tests using a 100Cr6 ball-on-disk at 5.0 N, 125 rpm, and 2500 laps. Wear track was analyzed by laser confocal microscopy and worn surface was characterized by SEM-EDS. Results revealed that Cu content plays a more important role in wear performance than grain refinement alone. Higher Cu content promoted adhesive interactions, facilitating the formation of oxide tribolayer, which acts as a barrier against abrasive wear, contributing to the reduced COF and wear coefficient.

Keywords: Nanoparticles, Plasma Transferred Arc, 316L, Cu, CuO, Wear performance.

INTRODUCTION

Additive Manufacturing (AM) is an advanced technology capable of producing metallic parts with complex geometry directly from digital models (Rasiya; Shukla; Saran, 2021). The technology is based on the fabrication of parts layer-by-layer from wire or powder feedstock (Armstrong; Mehrabi; Naveed, 2022). Two AM techniques are commonly used for manufacturing metallic components: powder bed fusion (PBF), which employs a laser or electron beam to selectively melt metallic feedstock on a powder bed, forming a solid layer with the desired geometry; and directed energy deposition (DED), where a nozzle directs both the feedstock (wire or powder) and heat source (electric arc, plasma, laser and electron beam) along a defined path to create the desired geometry (Kladovasilakis et al., 2021). A cost-effective alternative to laser-based DED processes is Plasma Transferred Arc (PTA-DED), which is a competitive technique, particularly suited for producing coatings and multilayer depositions (Alberti; Bueno; d'Oliveira, 2015; Sawant; Jain, 2018; Sadasivam; Amirthalingam, 2022). PTA-DED offers high powder catchment efficiency due to the strong interaction between the plasma arc and the feedstock, allowing for the deposition of powder feedstock with diverse morphologies, including nanoparticles doped powders (Cardozo et al., 2018; Prass; d'Oliveira, 2023).

In recent years, AM processes have been applied with a variety of materials, such as aluminum alloys, copper alloys, nickel alloys, titanium alloys, carbon steels, tool steels and stainless steels (Armstrong; Mehrabi; Naveed, 2022). Among these, AISI 316L stainless steel is widely used in AM due to its excellent corrosion resistance, good weldability, high strength and ductility (Revilla et al., 2020; Saboori et al., 2020; Wang et al., 2020; Astafurov; Astafurova, 2021). 316L is used across various applications, ranging from implants used in the biomedical industry to offshore pipelines in the oil and gas sector (D'Andrea, 2023). However, for certain applications such as automotive bearings, landing gear, valve and pump components, ship propellers, surgical tools and implants, good wear resistance is necessary (Vishnu et al., 2024). In this context, recent research has been exploring the influence of AM processes on microstructure and its effect on wear performance. A brief literature review of the tribological behavior of AISI 316L obtained by AM techniques is presented in Table 22.

Table 22 - Brief literature review of the tribological behavior of AISI 316L obtained by AM techniques

Reference	Material / Process	Remarks
Vishnu et al., 2024	316L powder/ L-PBF	The wear mechanism was a combination of oxidation, abrasion, and adhesion when tested against a chrome steel counter body. The AM sample demonstrated a lower wear coefficient compared to the conventionally manufactured 316L sample, attributed to the finer microstructure produced by the AM process.
Upadhyay; Kumar, 2020	316L powder/ L-PBF	The conventionally manufactured (cold-rolled) sample exhibited higher friction and wear coefficient compared to the AM sample. The formation of a tribo-film on the sliding surface had a lubricating effect, leading to a reduction in friction.
Özer; Kisasöz, 2022	316L powder/ L-PBF+HT	As heat treatment (HT) temperature increased, hardness decreased, and wear coefficient increased. The worn surface displayed a mix of abrasive and adhesive wear mechanisms.
Tascioglu; Karabulut; Kaynak, 2020	316L powder/ L-PBF+HT	Wear resistance was strongly affected by porosity. Hence, the AM sample, with its higher porosity, exhibited a higher wear coefficient compared to the wrought 316L sample. However, heat treatment improved wear resistance.
Li et al., 2018	316L powder/ L-PBF	The build direction had no significant impact on the coefficient of friction or wear coefficient. At higher wear test temperatures, the coefficient of friction decreased, with oxide layers serving as solid lubricants.
Alvi; Saeidi; Akhtar, 2020	316L powder/ L-PBF	At room temperature, the wear test for both conventional and AM samples showed similar wear performance. However, at high temperature, AM samples benefited from their refined microstructure, which facilitated the formation of a stable oxide glaze.
Mandal et al., 2020	Gr-reinforced 316L/ L-PBF	This study prepared a graphene (Gr)-reinforced metal matrix composite. The addition of Gr led to an increase in hardness and a significant reduction in wear coefficient, attributed to the lubricating properties of Gr.
Han et al., 2020	316 powder/ L-DED	An increase in oxygen suggests an oxidation reaction, with oxide films serving as a protective layer. Analysis of the worn surface revealed a combination of oxidative, abrasive, and adhesive wear mechanisms. Additionally, as increase in C content led to a reduced wear coefficient.

Source: Authors (2025).

Literature reports that austenitic stainless steel obtained by laser-based AM techniques generally exhibits a reduced wear coefficient compared to conventionally manufactured 316L. Nevertheless, porosity inherent to AM methods can be detrimental to wear resistance. The formation of an oxide tribolayer can serve as a solid lubricant, preventing further material removal. Additionally, changes in chemical composition and the incorporation of nanoparticles have been found to enhance the wear performance of 316L. While the tribological behavior of 316L fabricated by PBF has been widely addressed, research on the wear performance of 316L fabricated by DED techniques remains limited. This study aims to contribute to this discussion by

evaluating the effect of Cu additions on microstructure and wear performance of AISI 316L manufactured by PTA-DED. The impact of Cu content, Cu particles morphology and nanoparticle composition were assessed. To the best of our knowledge, this is the first-ever tribological investigation on stainless steel powder processed by PTA-DED incorporating Cu microparticles, Cu nanoparticles, and CuO nanoparticles.

MATERIALS AND METHODS

Feedstock preparation and characterization

Five powder mixtures were prepared using gas-atomized AISI 316L stainless steel as main powder (grain size between 85 and 150 μm). Cu was added in three distinct forms: Cu microparticles (Cu MP - grain size between 89 and 143 μm), Cu nanoparticles (Cu NP - particle size of about 500 nm) and CuO nanoparticles (CuO NP - particle size of about 40 nm). The AISI 316L powder was mixed with 1 wt% and 5 wt% Cu MP, 1 wt% Cu NP and 1 wt% CuO NP. The chemical compositions of the powder mixtures are shown in Table 23.

Table 23 - Powder mixtures chemical composition in weight percentage

Powder mixture	Fe	Cr	Ni	Mo	Mn	S	Si	Cu	O	Source
AISI 316L	Bal.	17.64	12.52	3.34	1.72	0.69	0.53	-	-	XRF
AISI 316L + 5 wt% Cu MP	Bal.	16.76	11.89	3.17	1.63	0.66	0.50	5.00	-	Calculated
AISI 316L + 1 wt% Cu MP	Bal.	17.47	12.40	3.31	1.70	0.69	0.52	1.00	-	Calculated
AISI 316L + 1 wt% Cu NP	Bal.	17.47	12.40	3.31	1.70	0.69	0.52	1.00	-	Calculated
AISI 316L + 1 wt% CuO NP	Bal.	17.47	12.40	3.31	1.70	0.69	0.52	0.80	0.20	Calculated

Source: Authors (2025).

AISI 316L and Cu MP powders were dried at 80 °C for 2 h and mixed in a Y-type mixer for 2 h. For powder mixtures containing NP, due to their elevated surface energy, and to prevent the inherent tendency of NP to agglomerate into clusters, the NP powders were dispersed in an ultrasonic bath with ethanol for 300 s, before being mechanically stirred with the stainless-steel powder for 2 h. The wet mixture was dried at 50 °C for 24 h and mixed in a Y-type mixer for 12 h. Powder mixtures and particles morphology were assessed by scanning electron microscopy (SEM) with a secondary electron (SE) detector, operating at 15 kV and 30 μm aperture. Due to its

non-conductive nature, CuO NPs powder mixture was analyzed under 10 kV to decrease the SEM charging effect.

Single-walls deposition and heat treatment

Plasma Transferred Arc (PTA) was used to deposit powders mixtures as single-walls on AISI 304L stainless steel substrates (12 × 32 × 160 mm). Before deposition, the substrate was ground and cleaned with ethanol. To guarantee the dilution between the first deposited layer and the substrate, a deposition current of 120 A was used for the first layer. In addition, to prevent overheating during subsequent layer processing, deposition current was reduced to 80 A, maintaining an interlayer temperature at 150 °C. The PTA deposition parameters are detailed in Table 24.

Table 24 - PTA deposition parameters

Parameter (unit)	**Value**
Protective gas	Argon 99 %
Carrier gas flow (L/min)	0.8
Plasma gas flow (L/min)	2
Shield gas flow (L/min)	15
Nozzle-plate distance (mm)	10
Powder feed rate (g/min)	6
Deposition current (A)	120 (first layer), 80 (subsequent layers)
Deposition speed (mm/min)	100
Interlayer temperature (°C)	150

Source: Authors (2025).

During deposition, the plasma arc is established between the tungsten electrode and the metallic substrate, offering a good interaction between powder feedstock, heat source and melt pool. Consequently, PTA may exhibit superior powder catchment efficiency when compared to other Directed Energy Deposition (DED) techniques. As the PTA nozzle moves, the melt pool starts to solidify, forming a single bead. As successive layers are deposited, a single-wall is formed, Figure 56a.

Figure 56 - (a) Schematic representation of PTA single-wall deposition process, and (b) photographs of the single-walls deposited by PTA with different Cu additions

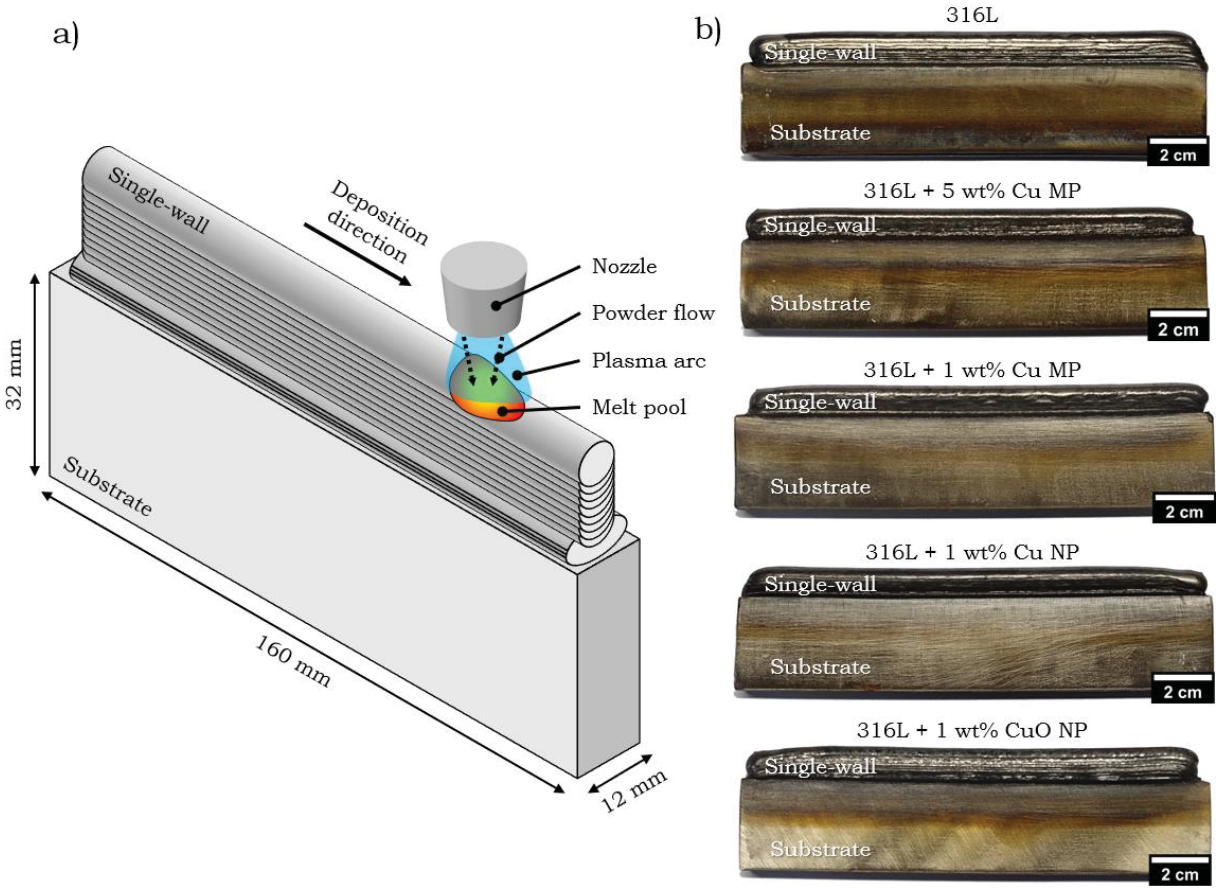

Source: Authors (2025).

Single-walls produced with different powder mixture containing Cu were deposited by PTA, with a total of 11 layers, Figure 56b. The deposited materials were exposed to a solubilization heat treatment at 1100 °C for 0.5 h, followed by cooling in air. Solubilization was succeeded by aging heat treatment at 700 °C for 3 h, followed by cooling in air.

Single-walls characterization

The PTA-DED single-walls were characterized by X-ray fluorescence spectrometry (XRF) to assess the impact of PTA processing on chemical compositions of powder mixtures. For each single-wall, three cross-sections were ground and polished with diamond paste (1 μm) to obtain a mirror-like finish. For the density and porosity analysis, micrographs of the polished specimens were obtained by optical microscopy (OM), covering all the transverse cross-section of the top 10

layers, resulting in grids of more than 60 images. The micrograph grids were analyzed using *ImageJ* software. Powder catchment efficiency (Koti *et al.,* 2023), was calculated from the equation:

$$PCE\ (\%) = ((A \times V \times \rho \times D_{IMAGE}) / (N_{LAYERS} \times P_{FR})) \times 100 \quad (1)$$

where *PCE* is the powder catchment efficiency (%), *A* is the cross-section area of the top layers disregarding the first deposited layer (mm²), *V* is the deposition speed (mm/min), ρ is the theoretical material density (g/mm³), D_{IMAGE} is the cross-section mean density (%), N_{LAYERS} is the number of layers and P_{FR} is the powder feed rate (g/min).

The microstructure analysis of the topmost deposited layer was performed on the polished specimens, which were etched by an 8 second immersion in Marbles solution (4 g $CuSO_4$ + 20 ml HCl + 20 mL H_2O). SEM analysis was conducted using a SE detector, under 10 kV and 60 µm aperture. The mean equiaxed dendrite size was determined by measuring the area of a minimum of 15 dendrites within the equiaxed dendritic region. Semi-quantitative chemical analysis of the dendritic and interdendritic zones within the equiaxed dendritic region of the top layer was carried out by energy-dispersive X-ray spectroscopy (EDS).

X-ray diffraction (XRD) was carried out on as deposited and heat treated (solubilization + ageing) materials. The tests were performed in an X-ray diffractometer with scanning angle 2θ ranging from 40º to 55º with scanning speed of 1 º/min with Cu-Ka radiation (λ = 0.15406 nm) at 40 kV and 20 mA. The substrate and the first layer were removed prior to the XRD analysis, and the cross-sections were oriented on the sample holder randomly to the build direction.

Variations due to different Cu additions and heat treatments applied were assessed through microhardness measurements using a Vickers micro indenter with a test load of 300 g (2.9 N) and a dwell time of 10 seconds. Mean hardness values were determined by averaging three hardness profile measurements along the central portion of the transverse cross-section, from the first deposited layer to the topmost layer, with a 0.5 mm spacing between indentations.

Sliding wear tests

Sliding wear tests were performed on a ball-on-disk tribometer at room temperature under dry conditions. The set-up used to evaluate the effects of Cu additions and heat treatment to 316L stainless steel consists of a 100Cr6 ball (3 mm diameter) counter body that slides against the transverse cross-section of the PTA-DED single-walls. The wear tests were carried out in the as deposited and in the heat-treated condition (solubilized + aged). Prior to testing, the specimen surfaces were ground using 1200-grit SiC sandpaper and ultrasonic cleaned in acetone. The ball-on-disk wear test conditions are summarized on Table 25. Preliminary testing was conducted to determine the number of laps required to achieve a steady-state condition.

Table 25 - Ball-on-disk wear test conditions

Test conditions (unit)	**Value**
Ball material	100Cr6
Ball diameter (mm)	3
Wear track radius (mm)	2.5
Load (N)	5
Rotation (RPM)	125
Number of laps	2500
Sliding distance (m)	Approx. 40
Sliding time (min)	20
Temperature (°C)	Approx. 25
Relative Humidity (%)	42 - 54

Source: Authors (2025).

Coefficient of friction (COF) was measured in real-time using a load cell integrated with the tribometer, with a data acquisition rate of 10 Hz. Wear track cross-section profile areas were measured using laser confocal microscopy (LCM) at 12 locations, evenly spaced at 30° around the wear track. Based on Archard's model (Archard, 1953), the wear coefficient was calculated from the equation:

$$\textit{Wear coefficient } [mm^3 / (Nm)] = (2 \times \pi \times r \times S) / (L_n \times D) \quad (2)$$

where r is the wear track radius (mm), S is the mean cross-section profile area measured (mm²), L_n is the normal load applied (N) *and* D is the total sliding distance (m).

Worn surface morphology was analyzed by SEM equipped with a SE detector, operating at 15 kV with a 60 μm aperture. The area covered by tribolayer and semi-quantitative chemical analysis of the tribolayer were assessed using SEM with a backscattered electron detector (BSD) and EDS, operated at 10 kV voltage and with a 60 μm aperture.

RESULTS AND DISCUSSION

Effect of feedstock on single-walls processability

Gas-atomized AISI 316L stainless steel particles (Figure 57a) are mostly spherical with a few satellite particles attached whereas Cu MP are irregular in shape (Figure 57c). Cu MP and the stainless steel powder grains are in the same size range and their mixing process resulted in powder mixtures with uniformly distributed Cu MP for both 1 wt% and 5 wt% Cu content added. XRF chemical composition analysis of the single-wall cross-sections (Table 26) shows that the Cu MP additions were successfully fed into the plasma arc and consequently to the melt pool. However, semi-quantitative XRF analysis indicates slight variations in composition compared to the initial powder mixtures, with Cu content reductions of 6 % and 10 % for powder mixtures containing 1 wt% and 5 wt% Cu MP respectively. These minor reductions in Cu content can be attributed to the irregular shape of the Cu MP, which can be detrimental to their flowability and lead to inconsistencies in powder feeding.

Powder mixtures with NP have different features, as the volume of a single Cu NP is approximately 13 million times smaller than the volume of one AISI 316L particle, this allows for Cu NP to adhere and partially cover the surface of all stainless steel particles (Figure 57b). CuO NP has a volume of about 26 billion times smaller than stainless steel individual grains, as a result, CuO NP can be seen covering most of the carrier particle surface (Figure 57d), forming clusters. Additionally, Cu NP have a lower surface-area-to-volume ratio than CuO NP. This reduced surface area results in weaker adhesion forces, making Cu NP more susceptible to detaching from the stainless steels particles during the feeding process of the powder mixture compared to CuO NP. This behavior is reflected in the chemical composition of the single-walls deposited by PTA-DED, where powder mixtures containing Cu NP and CuO NP resulted in a Cu content reduction of 27 % and 13 %, respectively. This fluctuation

may be attributed to some NPs detaching from the stainless steel particle surface, which may lead to loss of NPs during handling and processing.

Figure 57 - SEM micrographs of (a) 316L particle, (b) Cu MP, (c) Cu NPs attached on the surface of 316L particle, and (d) CuO NPs attached on the surface of 316L particle

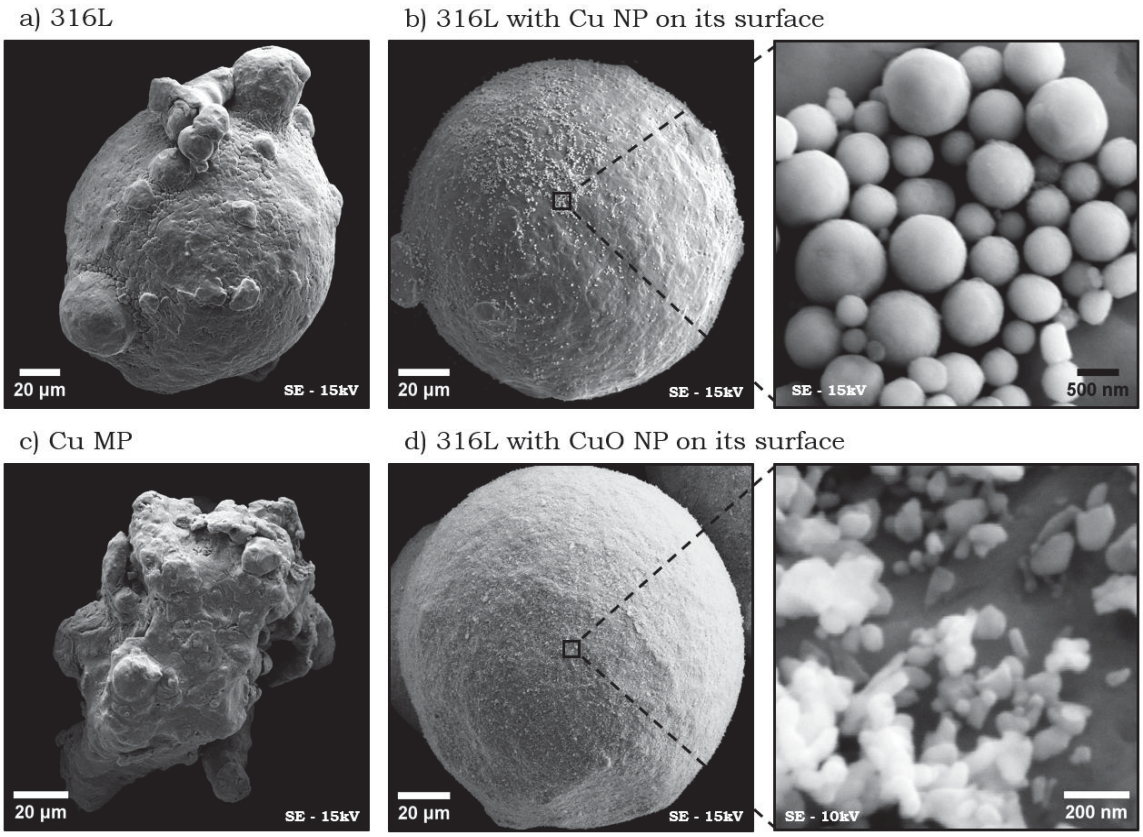

Source: Authors (2025).

Table 26 - XRF chemical analysis of the deposited materials in weight percentage

Material	Fe	Cr	Ni	Mo	Mn	S	Si	Cu
AISI 316L	Bal.	17.41	12.38	2.56	1.57	1.05	0.74	-
AISI 316L + 5 wt% Cu MP	Bal.	16.65	11.81	2.45	1.50	0.98	0.55	4.50
AISI 316L + 1 wt% Cu MP	Bal.	17.30	12.29	2.56	1.53	1.03	0.50	0.94
AISI 316L + 1 wt% Cu NP	Bal.	17.35	12.41	2.59	1.55	1.03	0.56	0.73
AISI 316L + 1 wt% CuO NP	Bal.	17.26	12.39	2.58	1.38	1.03	0.55	0.70

Source: Authors (2025).

Additionally, as reported in previous research (Prass; d'Oliveira, 2023), during the PTA-DED process, the powder mixture is fed directly into the plasma arc column and part of the Cu NP and CuO NP that are directly in touch with the plasma arc may evaporate due to its high temperatures. NPs have a lower melting point than their bulk counterparts due to the higher proportion of surface atoms, which have a

lower coordination number. As the particle size decreases, the influence of surface atoms increases, leading to further reduction in the melting temperature (Jena; Castleman Jr., 2010). These effects are enhanced by the high thermal conductivity of Cu and the high surface-area-to-volume ratio of NPs, which allows them to rapidly absorb heat and reach vaporization temperatures much faster than larger particles.

To evaluate the proportion of the deposited powder that effectively reached the melt poll and composed the processed part, the cross-section area was measured for all feedstock materials maintaining the same powder feed rate. By considering the theoretical material density, cross-section porosity, and number of deposited layers, the powder catchment efficiency (PCE) for each feedstock powder was calculated (Figure 58a). According to the literature, PCE values for AISI 316L deposited by Laser Directed Energy Deposition typically range from 65 % to 90 % following parameter optimization (Koti *et al.,* 2023). In contrast, the PCE measured for the PTA-DED process ranged from 93 to 99 %. This indicates that the PTA-DED of powder feedstock is competitive with other DED techniques, even without parameter optimization for improved PCE. The notable high PCE observed in the single-walls deposited implies excellent material utilization, translating to a reduced wastage of feedstock material, a critical advantage for both economic and environmental considerations. Since Cu MP, Cu NP and CuO NP were added in small quantities to the stainless steel powder, the variations in PCE are proportional to the scale of these additions. As data indicates, only minor variations in PCE were observed with the incorporation of Cu. However, a slight decrease in PCE was noted with the addition of 1 wt% Cu NP. As suggested in previous research (Prass; d'Oliveira, 2023), when exposed to the high temperatures of the plasma arc column, Cu NP attached to the stainless steel particles melt and form a thin liquid layer around them. This liquid film acts as a thermal barrier, absorbing energy from plasma and reducing the heat available to melt the stainless steel particles. Consequently, the stainless steel particles receive less energy while passing through the plasma arc column, leading to a slight reduction in PCE.

Figure 58 - (a) Powder catchment efficiency, (b) density on cross-section, (c) pore count, and (d) average pore size

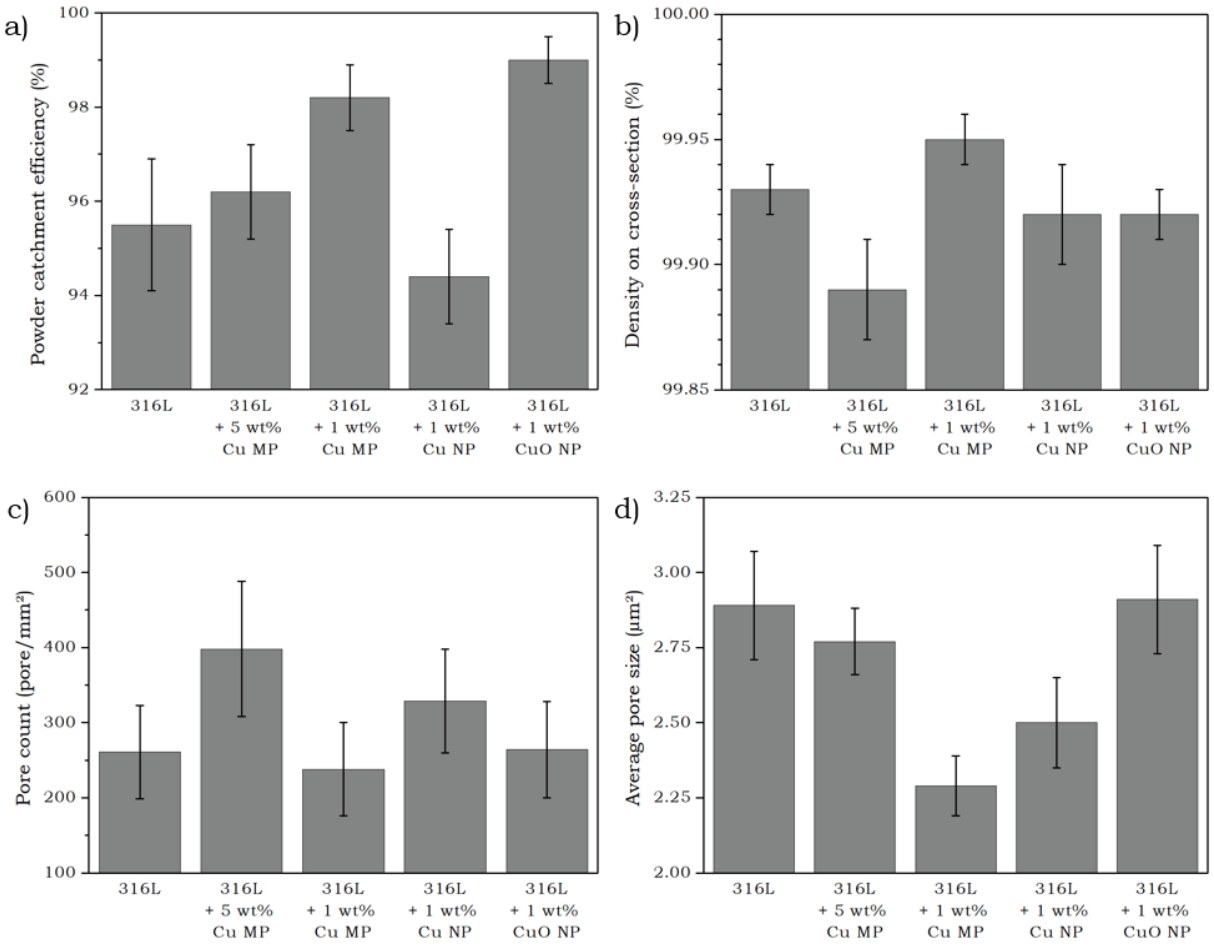

Source: Authors (2025).

According to the literature, as-cast AISI 316L parts typically exhibits cross-section density around 99.90 %, with average pore size ranging from 1 to 10 µm^2 (Ralls *et al.,* 2022). In additive manufacturing, components can be considered near-fully dense when their cross-section density exceeds 99 % (Choo *et al.,* 2019; Kamath *et al.,* 2014). Within this context, the evaluation of density and porosity at the transverse cross-section provide additional insights into the interaction dynamics between distinct feedstock powders and the plasma arc. Figure 58b shows the cross-section density on the single-walls, assessed through pore counting of OM grid images. Given the small variations of the chemical composition between the powder mixtures, ranging from 0 to 5 wt% Cu, only slight variations in cross-section density were expected. Single-walls processed with powder mixtures achieved a density above 99.85 %, confirming that PTA-DED is a viable technique for depositing dense components, comparable to those obtained through casting and other AM methods.

However, a noticeable increase in pore count was observed in the samples produced with 5 wt% Cu MP (Figure 58c), accounting for the slight reduction in density. This effect can be related to the increase in thermal conductivity of the deposited material resulting from the higher Cu content, which increases the solidification rate of the melt pool (Mirzababaei et al., 2023). Rapid solidification favors the entrapment of processing gases, promoting the formation of gas porosities. Notably, while maintaining the average pore size, the increase in pore count indicates greater retention of processing gases within the solidified single-walls. Nevertheless, the average pore size observed in PTA deposits ranged from 2.2 to 3.0 μm^2, regardless of feedstock used (Figure 58d), which falls within the range reported for as-cast AISI 316L components (Ralls et al., 2022).

The microstructure and solidification mode of stainless steels are influenced by the chemical composition of the feedstock and the thermal conditions imposed by the processing technique. According to the literature (Bond; d'Oliveira, 2012; Gomes; Henke; d'Oliveira, 2012), the solidification of the melt pool generated by PTA process leads to the formations of distinct microstructures along the height of the deposited layer, driven by variations in cooling rate. Typically, a planar growth region forms near the unmelted substrate, which transitions into columnar dendrites in the middle of the layer and equiaxed dendrites at the top of the deposit. Figure 59 presents the microstructure of the topmost layer in the as deposited single-walls. As expected, the overall microstructure produced by PTA-DED shows a columnar dendritic solidification pattern, with dendrite growth direction aligned with built direction (Figure 59b). As the heat source moves during the deposition, different solidification conditions occur throughout the melt pool. And near the top of the melt pool, a transition from columnar dendritic to equiaxed dendritic can be observed, regardless of the powder mixture (Figure 59a).

Figure 59 - Microstructure of the topmost layer in the as deposited single-walls

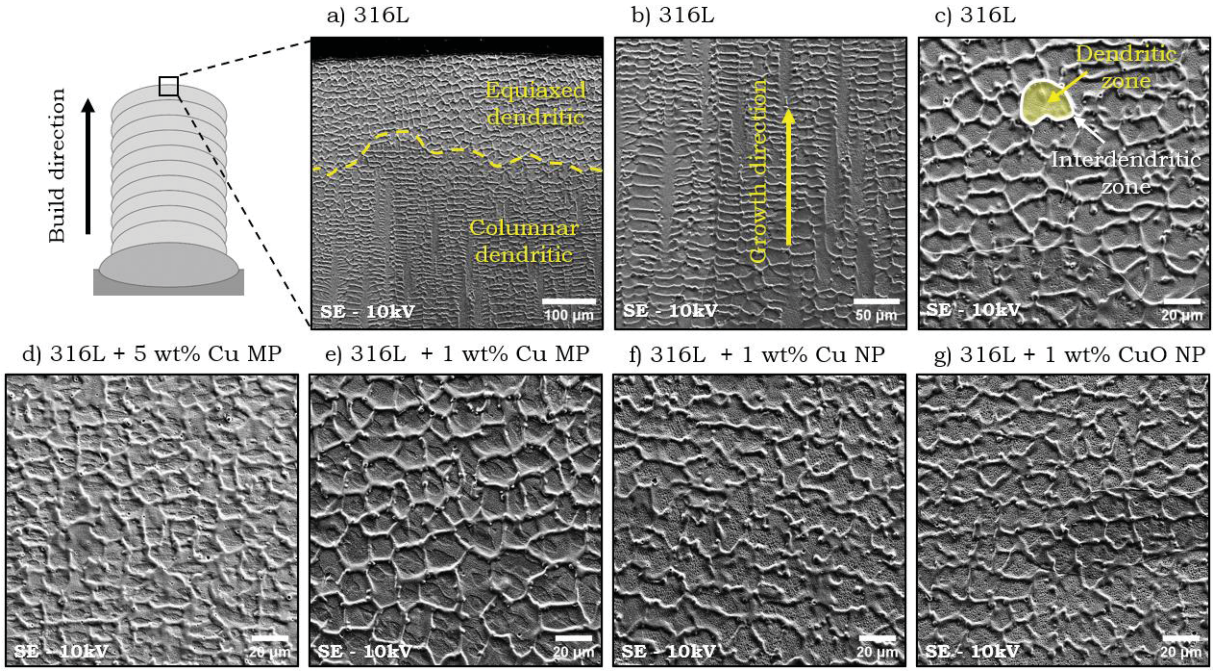

Source: Authors (2025).

The welding of austenitic stainless steel can result in two distinct solidification modes, primary ferrite and primary austenite. In the primary ferrite mode, solidification begins with the formation of Cr-rich δ-ferrite crystals, causing Ni to segregate to the remaining melt pool. In contrast, the primary austenite mode initiates with the formation of γ-austenite, which is depleted both in Cr and Ni, therefore enriching the liquid phase with these elements (Folkhard, 1988; Kou, 2002). Cu in stainless steels, similar to Ni, acts as an austenite-stabilizing element, thus, its addition to the powder feedstock is expected to promote primary austenite solidification (Kou, 2002; Saluja; Moeed, 2012; Niu *et al*., 2022). In the SEM images using a SE detector (Figure 59c), the dendritic zones appear darker than the interdendritic zones, suggesting the segregation of corrosion-resistance elements occurred due to the rapid cooling rates during solidification (Xie; Xue; Ren, 2020; Bernauer et al., 2023). This interpretation is supported by semi-quantitative EDS analysis on both dendritic and interdendritic zones (Table 27), which confirms the segregation of both Ni and Cr during solidification, strongly suggesting that the deposition of the powder mixtures with PTA-DED resulted in primary austenite solidification mode. It is also worth noting that in austenitic stainless steels, the solubility of Cu in austenite is approximately 7.5 wt% at 1100°C and 3.0 wt% at

835°C (Folkhard, 1988). This behavior contributes to the observed accumulation of Cu in the interdendritic zone, especially for the single-wall deposited with powder mixture containing 5 wt% Cu MP.

Table 27 - Semi-quantitative chemical analysis by EDS of dendritic and interdendritic zones at the top layer equiaxed dendritic region (normalized wt.%)

Material	Zone	Fe	Cr	Ni	Mo	Mn	Si	Cu
AISI 316L	Dendritic	67.84	16.16	12.51	1.79	1.15	0.56	-
	Interdendritic	62.65	17.61	15.08	2.56	1.39	0.71	-
AISI 316L + 5 wt% Cu MP	Dendritic	65.17	14.92	10.61	1.74	1.14	0.50	5.91
	Interdendritic	58.78	15.61	11.78	2.64	1.53	0.76	8.89
AISI 316L + 1 wt% Cu MP	Dendritic	68.20	15.37	11.90	1.65	1.10	0.53	1.24
	Interdendritic	62.67	17.49	12.65	3.23	1.51	0.86	1.59
AISI 316L + 1 wt% Cu NP	Dendritic	68.27	15.65	11.83	1.73	1.14	0.56	0.82
	Interdendritic	61.90	17.16	14.11	2.98	1.63	0.80	1.41
AISI 316L + 1 wt% CuO NP	Dendritic	68.32	15.92	11.49	1.84	1.25	0.51	0.67
	Interdendritic	64.00	17.33	12.67	2.95	1.30	0.74	1.01

Source: Authors (2025).

Cu additions impacted grain refinement, as assessed by measuring the equiaxed dendrite size (Figure 59c - 30g). Compared to the deposits processed with 316L, which exhibited a mean equiaxed dendrite size of 183 ± 49 μm^2, additions of 1 wt% and 5 wt% Cu MP reduced dendrite size to 167 ± 42 μm^2 and 119 ± 21 μm^2, respectively. Similarly, a microstructure refinement was measured in single-walls processed with powder mixtures containing 1 wt% Cu NP and 1 wt% CuO NP, with dendrite size of 153 ± 42 μm^2 and 152 ± 31 μm^2, respectively. These findings can be accounted by different operating mechanisms depending on the feedstock used, higher Cu content enhances thermal conductivity and increases cooling rate, producing more refined microstructures. This agrees with the lower cross-section density observed, as faster solidification rates tend to trap processing gases within the solidifying material. Although statistically comparable, the equiaxed dendrite sizes of specimens with 1 wt% Cu NP and 1 wt% CuO NP were slightly smaller to those with 1 wt% Cu MP. This can be attributed to partial Cu evaporation prior to reaching the melt pool, which also correlates with the slightly lower density measured.

Although Cu might influence the thermal conductivity and solidification rate of the deposited materials, the addition of Cu MP, Cu NP and CuO NP did not affect the formation of the austenitic phase during the processing of single-walls with PTA (Figure 60). This outcome is expected, since Cu is an austenite-stabilizing element

that favors primary austenite solidification, as shown before and supported by Folkhard, 1988; Saluja; Moeed, 2012; Niu *et al*., 2022. Notwithstanding, Cu additions led to a reduction in the lattice parameters of austenite in the as deposited condition, as determined by Brag's law (Table 28). This rightward peak shift can be attributed to lattice distortion induced by the increased Cu content in solid solution and the presence of Cu-rich precipitates (Prass; d'Oliveira, 2023). Segregation of Cu into the interdendritic region is confirmed by the higher Cu content measured (Table 27), that might promote the formation of Cu-rich phases (Alaneme *et al.,* 2010; Hauser *et al.,* 2023). However, no distinct diffraction peaks corresponding to Cu-rich phases were observed. This might be attributed to the coherency of Cu-rich precipitates with the austenitic phase and their sharing of a face-centered cubic (FCC) crystal lattice and similar diffraction angles (Sen *et al.,* 2011; Chi *et al.,* 2012). Additionally, the volume fraction of the Cu-rich precipitates in the microstructure is possibly too low for detection by XRD.

Figure 60 - XRD patterns of the single-walls with different Cu additions

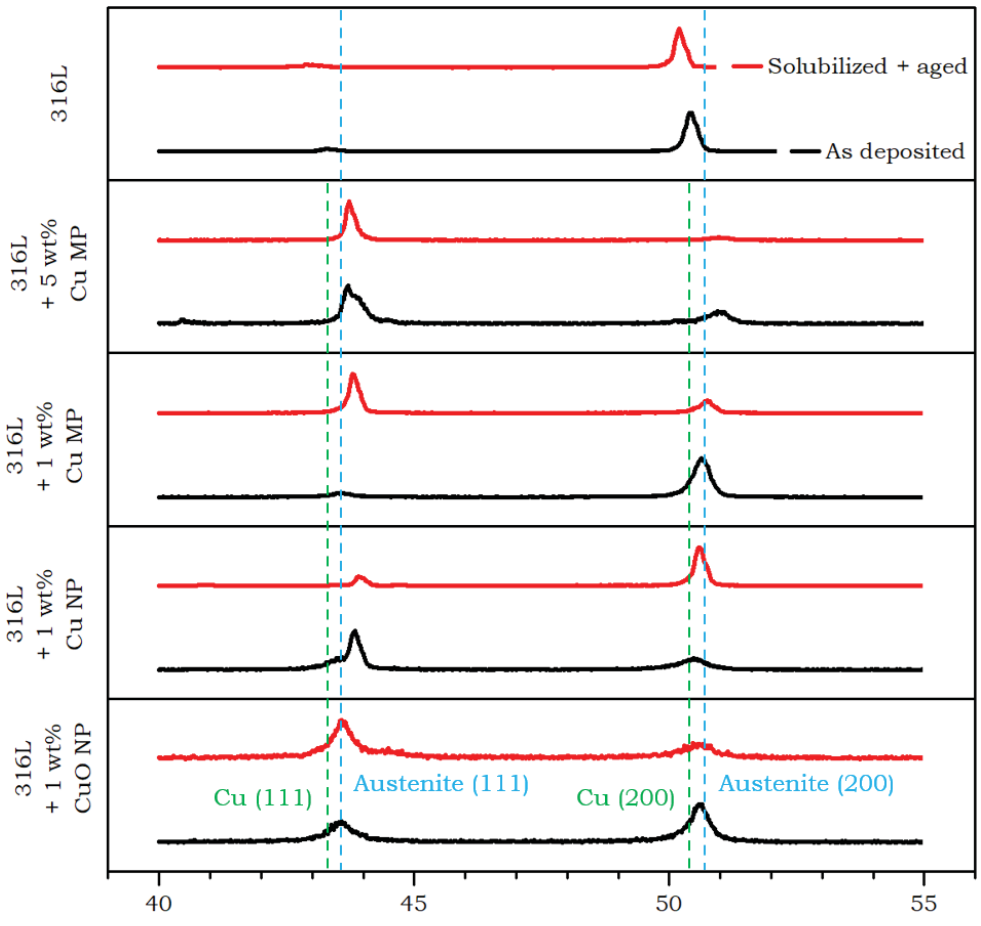

Source: Authors (2025).

Table 28 - Peak angle and lattice parameter for austenite (111) crystallographic plane

Material	Condition	2 Theta (º)	Lattice parameter (Å)
AISI 316L	As deposited	43.33	2.087
	Solubilized + aged	42.96	2.104
AISI 316L + 5 wt% Cu MP	As deposited	43.78	2.066
	Solubilized + aged	43.75	2.067
AISI 316L + 1 wt% Cu MP	As deposited	43.57	2.076
	Solubilized + aged	43.82	2.064
AISI 316L + 1 wt% Cu NP	As deposited	43.85	2.063
	Solubilized + aged	43.95	2.059
AISI 316L + 1 wt% CuO NP	As deposited	43.57	2.076
	Solubilized + aged	43.59	2.075
Austenite (#33-397)	-	43.62	2.073
Cu (#4-836)	-	43.29	2.088

Source: Authors (2025).

Stainless steels processed by AM techniques are usually subjected to solubilization heat treatment to dissolve precipitates and reduce residual stresses that are caused by the rapid cooling and solidification of the molten material (Aversa *et al.,* 2020; Mohyla *et al.,* 2022; Hauser et al., 2023). In the case of PTA-DED materials containing Cu, it is expected that after solubilization, Cu will be present in a saturated solid solution (SSS) within the austenitic matrix. From the SSS, it is possible to promote the formation of nano-sized Cu precipitates through ageing heat treatment (Chi *et al.,* 2012; Xi *et al.,* 2017). In this study, a combination of solubilization and ageing heat treatments was applied to enhance the formation of Cu-rich precipitates, which can potentially modify the material properties. This approach aimed to optimize the effects of Cu addition, even at relatively low concentrations of 1 wt% Cu. As expected, the heat treatment of 316L reduced residual stress and dissolved precipitates, as evidenced by an increase in austenite lattice parameter (Table 28). In contrast, for the specimen containing 1 wt% of Cu MP, a reduction in the lattice parameter indicates the presence of the Cu-rich precipitates after heat treatment (Table 28). Notably, this reduction was not observed on AISI 316L with 5 wt% Cu MP, which strongly suggests that Cu-rich precipitates were formed during deposition, prior to heat treatment. The mean hardness of AISI 316L measured in the as deposited condition is 180 ± 12 HV (Figure 61a). However, the addition of 1 wt% Cu MP and 5 wt% Cu MP slightly reduced the as deposited mean hardness to 177 ± 9 and 171 ± 11 HV, respectively, despite the refinement measured in the dendritic structure with increased Cu content. This decrease in

hardness is attributed to Cu being present in solid solution within the austenitic matrix (Xi *et al.,* 2017; Prass; d'Oliveira, 2023). After ageing, both 1 wt% Cu MP and 5 wt% Cu MP specimens exhibited an increase in the mean hardness of approximately 5 % and 14 %, respectively. Increase attributed to the availability of Cu in solid solution, which promotes the formation of Cu-rich precipitates coherent with the austenitic matrix during aging (Xi *et al.,* 2016; Xi *et al.,* 2017).

Figure 61 - Single-walls mean hardness

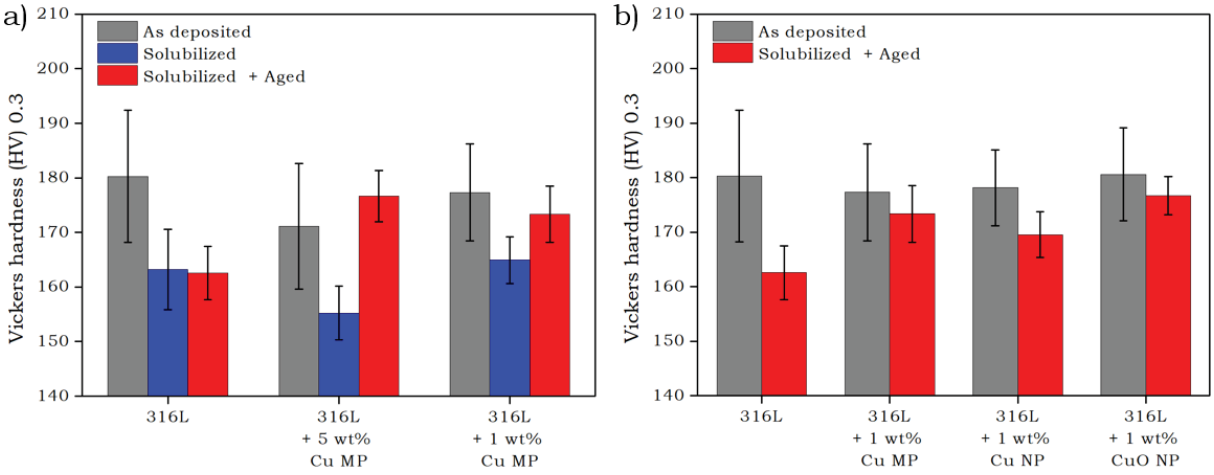

Source: Authors (2025).

The addition of 1 wt% of Cu NP and 1 wt% CuO NP to the stainless steel, resulted in hardness values comparable to those measured with 1 wt% Cu MP (Figure 61b). This suggests that the Cu particle morphology and the observed changes in microstructure did not significantly affect the hardness of the PTA-DED material in the as deposited condition. As expected, solubilization led to a decrease in mean hardness of all powder mixtures, including those with Cu NP and CuO NP. This decrease is associated with the dissolution of precipitates which previously distorted the crystal lattice and acted as obstacles to dislocation movement (Aversa *et al.,* 2020; Mohyla *et al.,* 2022; Bernauer *et al.,* 2023). Notably, AISI 316L modified with 1 wt% CuO NP exhibited a mean hardness with a minimal reduction of approximately 3.5 % after solubilization, maintaining a significantly higher hardness compared to the other compositions in the solubilized condition. This difference is attributed to the formation of oxide nano-inclusions during the deposition process, that were not dissolved during solubilization and are a possible cause for hardness increase (Saeidi et al., 2015; Zhong et al., 2016). Following ageing, both

compositions originally containing 1 wt% Cu NP and 1 wt% CuO NP experienced a slight increase in hardness, around 3.0 % and 1.5 %, respectively. Despite their lower Cu content in solid solution (Table 26), this increase is consistent with the precipitation of Cu-rich phases during ageing.

Wear performance

The wear performance of the PTA-DED materials was evaluated considering both the influence of Cu content (1 wt% and 5 wt% Cu MP) and Cu particle morphology (1 wt% Cu NP and 1 wt% CuO NP). Which involved determining the coefficient of friction (COF) and wear coefficient under both as deposited and heat-treated conditions. The COF is a dimensionless number defined as the ration between the normal load applied to two contacting surfaces and the resulting force resisting the movement between them. In contrast, the wear coefficient quantifies the volume of material removed from a surface per unit of normal load and sliding distance. In practical terms, a lower COF indicates lower frictional resistance between two surfaces in relative motion, while a lower wear coefficient indicates better wear resistance due to reduced material loss. During sliding wear tests performed on a ball-on-disk tribometer, the COF typically changes during an initial running-in step before stabilizing at a steady-state value (da Silva; d'Oliveira, 2016). Figure 62 shows the variation of the coefficient of friction as a function of the number of laps for 316L deposited by PTA, tested against a 100Cr6 counter ball. All powder mixture investigated exhibited similar COF evolution curves, with a behavior comparable to 316L during both the running-in and steady-state stages.

Prior to testing, the specimen surface is macroscopically flat with micro-asperities resulting from the surface preparation using 1200-grit SiC sandpaper. At the beginning of the dry sliding wear test, contact between the flat surface of the material and the counter ball occurs primarily at the tips of the asperities. This minimal contact area leads to high contact pressure, consequently, an initial peak in the COF of approximately 0.7 is observed. As the wear test progresses, the interaction between the specimen and counter body leads to the gradual breakdown of surface asperities, smoothing the sliding contact surfaces of the tribological pair (Sousa et al., 2022). This smoothing of asperities causes the COF to decrease to around 0.5 (a reduction of approximately 20%) as surface micro-roughness reduces.

Simultaneously, material is removed from the specimen's surface, generating a wear track profile closely linked to the geometry of the counter ball, increasing the contact area and causing a gradual rise in COF. The running-in step is completed once the COF reaches a steady value, after approximately 1500 laps under the tested conditions, indicating the transition to the steady-state stage. During this stage, wear debris can accumulate on the worn surface, contributing to the formation of a stable tribolayer (da Silva; d'Oliveira, 2016). This tribolayer helps maintain a constant COF and serves as a protective barrier against further material loss.

Figure 62 - Coefficient of friction variation with number of laps for 316L in the as deposited condition

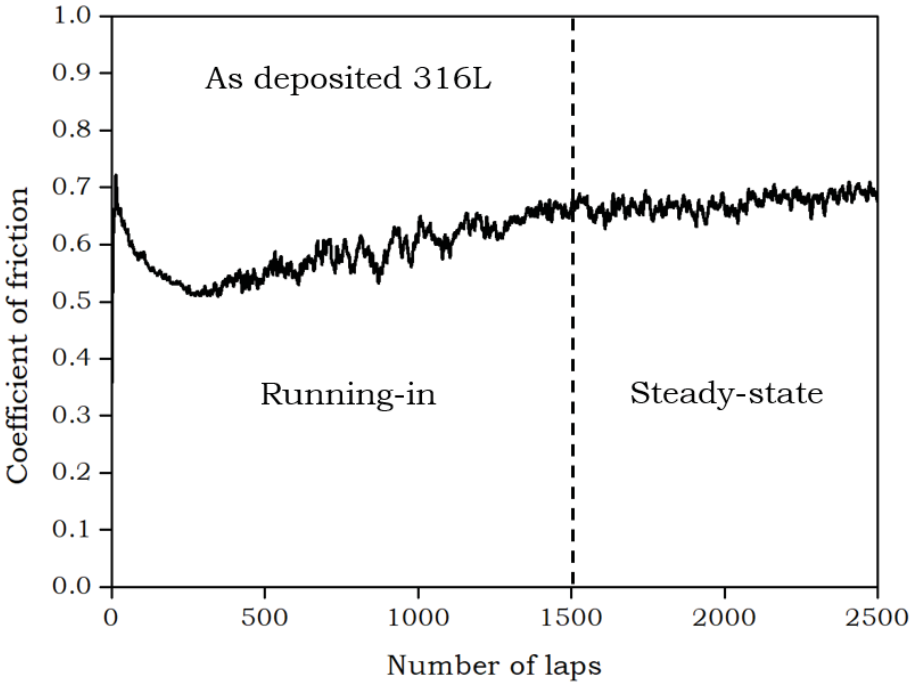

Source: Authors (2025).

The mean COF was calculated as the average value measured between laps 2000 to 2500 (Figure 63a) and corresponds to the steady-state stage of the wear test. As the baseline material, the COF of 316L was statistically equal in both as deposited (0.68 ± 0.044) and heat treated (0.66 ± 0.036) conditions. The impact of Cu in the deposited material is identified when processing powder mixtures with the addition of 5 wt% Cu MP. Which led to a notable reduction on COF measured, with values of 0.62 ± 0.041 and 0.59 ± 0.042 in the as deposited and heat treated conditions, respectively. Furthermore, a substantial decrease in the wear coefficient was measured for the single-wall richer in Cu (Figure 63b), dropping from

approximately 6.1 and 6.6 mm^3/Nm in 316L to around 2.7 and 3.0 mm^3/Nm in the 5 wt% Cu MP single-wall. Extrapolating data that associates microstructure refinement with improved wear performance (Upadhyay; Kumar, 2020; Vishnu et al., 2024), the observed grain refinement with the addition of 5 wt% Cu MP might be contributing to the reduction of COF and wear coefficient. In contrast, the addition of 1 wt% Cu MP resulted in COF and wear coefficient values similar to those of the unmodified 316L (Figure 63), despite the slight grain refinement observed. This suggests that Cu content plays a more important role in wear performance than grain refinement alone. Supporting this, single-walls processed with powder mixtures containing 1 wt% Cu NP and 1 wt% CuO NP also exhibited COF and wear performance similar to those observed with 1 wt% Cu MP, even though the NP additions promoted more noticeable microstructural refinement. These findings reinforce that a higher Cu content is more effective in enhancing wear performance than differences in particle morphology. Regardless of chemical composition, no statistically significant variation in COF or wear coefficient was observed after heat treatment, suggesting that the precipitation of Cu-rich phases promoted by ageing did not influence wear performance under the tested conditions.

Figure 63 - (a) Coefficient of friction and (b) Wear coefficient

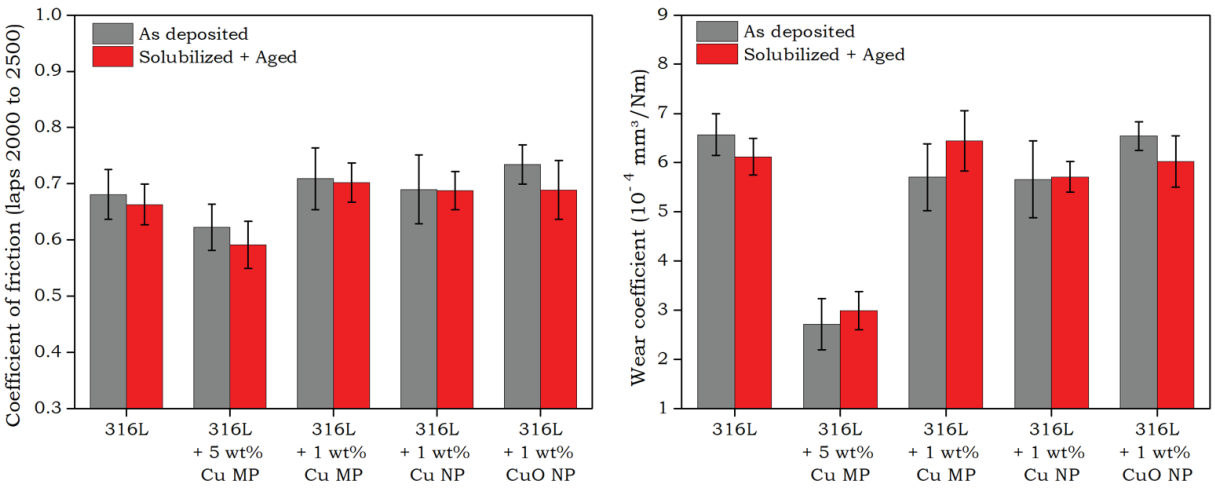

Source: Authors (2025).

Since no significant variation in wear performance was measured after heat treatment, tribolayer characterization was focused in the as deposited condition. Analysis of the tribolayers, supported by oxygen mapping and semi-quantitative

chemical analysis by EDS (Figure 64), confirmed the presence of oxygen within the tribolayer. This observation suggests that the heat generated at the contact interface during the sliding against the chromium steel ball increases temperature locally, which promotes the oxidation of the worn surface. The resulting oxides are progressively removed from the worn surface, contributing to the formation of oxidized wear debris. The agglomeration and compaction of these wear debris promotes the formation of a stable oxide tribolayer. A compact tribolayer refers to a tribological surface film that is dense, uniform and well adhered to the worn surface, with minimal fragmentation and fewer loose wear debris (da Silva; d'Oliveira, 2016). It should be noted that, the tribolayer observed in the specimen with 5 wt% Cu MP (Figure 64b) appears more compact than that in the 1 wt% Cu MP specimen (Figure 64c), showing less fragmentation on the edges of the tribolayer and fewer detached particles. This increased compaction enhances the stability of the tribolayer, which can improve wear performance. In addition, the chemical analysis (Figure 64f) revealed that the addition of higher Cu content produces a tribolayer richer in oxygen, suggesting that Cu facilitates oxidation at the worn surface. This contributes to the formation of oxidized wear debris, which are then compacted into a tribolayer that acts as a barrier against further material loss, agreeing with the lower wear coefficient observed in the single-wall with 5 wt% Cu MP (Figure 63b). However, the tribolayer is not composed only of oxides, it is composed of a mixture of matrix material and oxidized debris, as evidenced by the areas with varying oxygen content (Figure 64e). Despite the presence of cracks within the tribolayers, which indicate their fragile nature under frictional stresses, they can serve as an effective barrier, reducing further wear (Figure 64d).

Figure 64 - (a-e) BSE micrographs with EDS mapping of tribolayer and (f) semi-quantitative chemical analysis of tribolayer by EDS

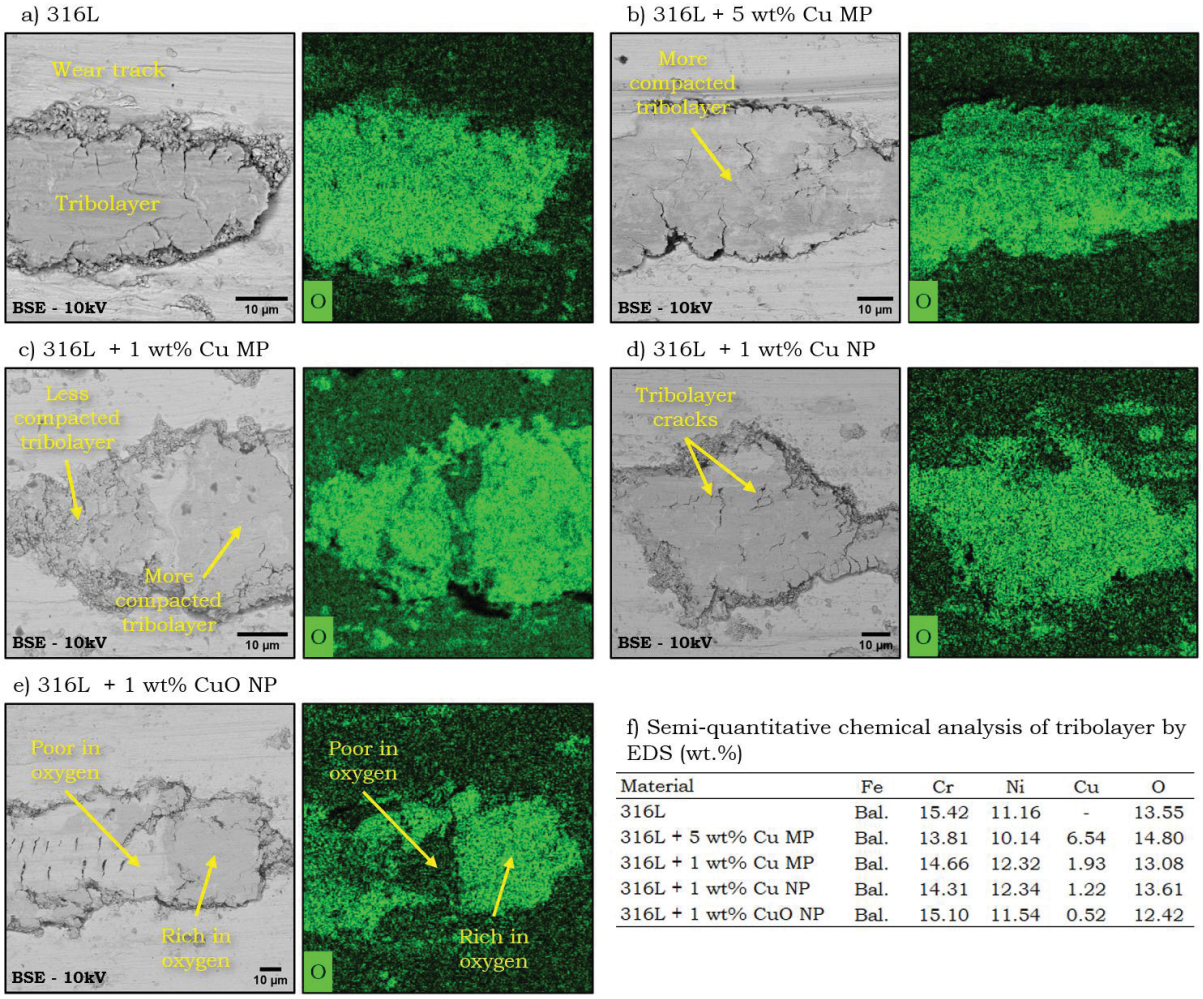

f) Semi-quantitative chemical analysis of tribolayer by EDS (wt.%)

Material	Fe	Cr	Ni	Cu	O
316L	Bal.	15.42	11.16	-	13.55
316L + 5 wt% Cu MP	Bal.	13.81	10.14	6.54	14.80
316L + 1 wt% Cu MP	Bal.	14.66	12.32	1.93	13.08
316L + 1 wt% Cu NP	Bal.	14.31	12.34	1.22	13.61
316L + 1 wt% CuO NP	Bal.	15.10	11.54	0.52	12.42

Source: Authors (2025).

Figure 65 illustrates the extent of tribolayer coverage at the worn surfaces of the as deposited specimens. All micrographs were captured from the same region of the wear track, with the relative ball sliding direction moving from left to right in a counterclockwise motion (Figure 65a). Analysis of the wear scar and tribolayer reveals that, across all processed material, tribolayers formed via the agglomeration and compaction of wear debris are dispersed along the worn surface (Figure 65a-e). As previously described, a more compacted tribolayer is characterized by reduced fragmentation of the edges of the tribolayer with fewer loose wear debris (Figure 64c). Regardless of the powder feedstock used, variations in the compactness of tribolayers can be observed across the wear scar, some tribolayer are dense and well-compacted, while others are more fragmented and loosely compacted. These differences reflect both local variation in debris compaction and the possible

breakdown of a previously dense tribolayer, consistent with their fragile nature, as evidenced previously by the presence of cracks within the tribolayers (Figure 64d). However, the influence of Cu in the deposited material becomes evident through the varying levels of tribolayer coverage along the wear track (Figure 65g). The quantitative analysis indicates that the presence of Cu leads to a greater portion of the wear scar being covered by oxide tribolayers. Notably, the worn surface of 316L with 5 wt% Cu MP (Figure 65c) exhibits significantly higher tribolayer coverage compared to the unmodified 316L (Figure 65b), with 28 % and 11 % of the area covered by tribolayer, respectively. These findings agree with the lower COF and reduced wear coefficient measured in the 5 wt% Cu MP specimen (Figure 63). The improved wear performance can be attributed to the presence of compact tribolayer with high coverage and the self-lubricating properties of Cu-rich oxides, which can act as solid lubricant and provide a barrier against further material removal (Li et al., 2018; Upadhyay; Kumar, 2020; Alvi; Saeidi; Akhtar, 2020; Chi et al., 2023). For single-walls deposited with 1 wt% Cu MP, 1 wt% Cu NP and 1 wt% CuO NP, the relatively small variations in Cu content accounted for a modest increase in tribolayer coverage along the wear track (Figure 65g). This observation is consistent with the comparable COF and wear coefficient values measured for these specimens, further reinforcing that Cu content is a key factor influencing wear performance, rather than particle morphology under the tested conditions.

Figure 65 - (a-f) BSE micrographs of at the center of the wear tracks and (g) percentage of wear track area covered by tribolayer

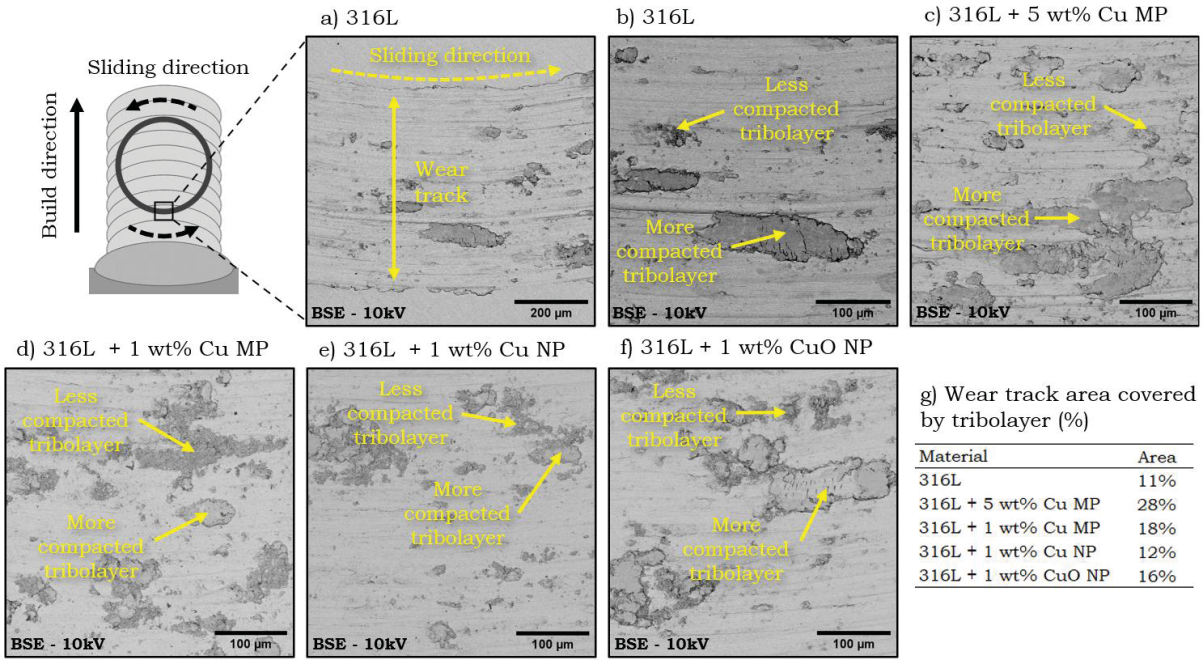

g) Wear track area covered by tribolayer (%)

Material	Area
316L	11%
316L + 5 wt% Cu MP	28%
316L + 1 wt% Cu MP	18%
316L + 1 wt% Cu NP	12%
316L + 1 wt% CuO NP	16%

Source: Authors (2025).

The active wear mechanisms observed on the worn surfaces are illustrated in Figure 66. Across all specimens, regardless of Cu content and particle morphology, the wear tracks displayed the formation of grooves aligned with the sliding direction, indicative of abrasive wear (Figure 66a-e). This behavior can be attributed to the relatively high hardness of the chrome steel counter ball compared to the deposited stainless steel, which led to micro-ploughing of the softer material under repeated sliding contact. In addition to abrasion, signs of adhesive wear are evident. During sliding, superficial asperities of the tribological pair come into direct contact under localized stress, resulting in severe plastic deformation of the stainless steel surface. Material from the softer specimen surface adhere to the harder counter ball (Figure 67), and may be transferred back to the wear track. The adhered material can either detach as loose wear debris or agglomerate into the surface, contributing to the formation of the tribolayers. Additionally, plastic deformation is seen at the interface between the wear track (zone 1) and the original surface of the specimen (zone 2) (Figure 66a), further confirming the role of localized sliding stress and severe plastic deformation in the adhesive wear. The greater tribolayer coverage measured on the wear track of the 5 wt% Cu MP single-wall (Figure 65g), suggests that higher Cu content promotes adhesive interactions, facilitating the formation of oxide tribolayer,

which acts as a barrier against abrasive wear, contributing to the reduced COF and wear coefficient observed. Furthermore, the oxygen content analysis (Figure 66f) reveals an increase in oxygen concentration within the wear track, confirming that oxidation occurred during testing. This suggests that frictional heating at the contact interface elevates surface temperature sufficiently to promote surface oxidation. The weak adhesion of the resulting oxide films, paired with high localized stresses, leads to their removal during sliding, generating oxide wear debris that can subsequently be compacted into a tribolayer. Taken together, these observations indicate that a combination of abrasive, adhesive and oxidative mechanisms were acting simultaneously under the tested conditions. These findings are consistent with findings reported for 316L produced by laser-based AM techniques (Han et al., 2020; Özer; Kisasöz, 2022; Vishnu et al., 2024).

Figure 66 - (a-e) SE micrographs of the interface between the original surface and wear track and (f) oxygen content analysis by EDS

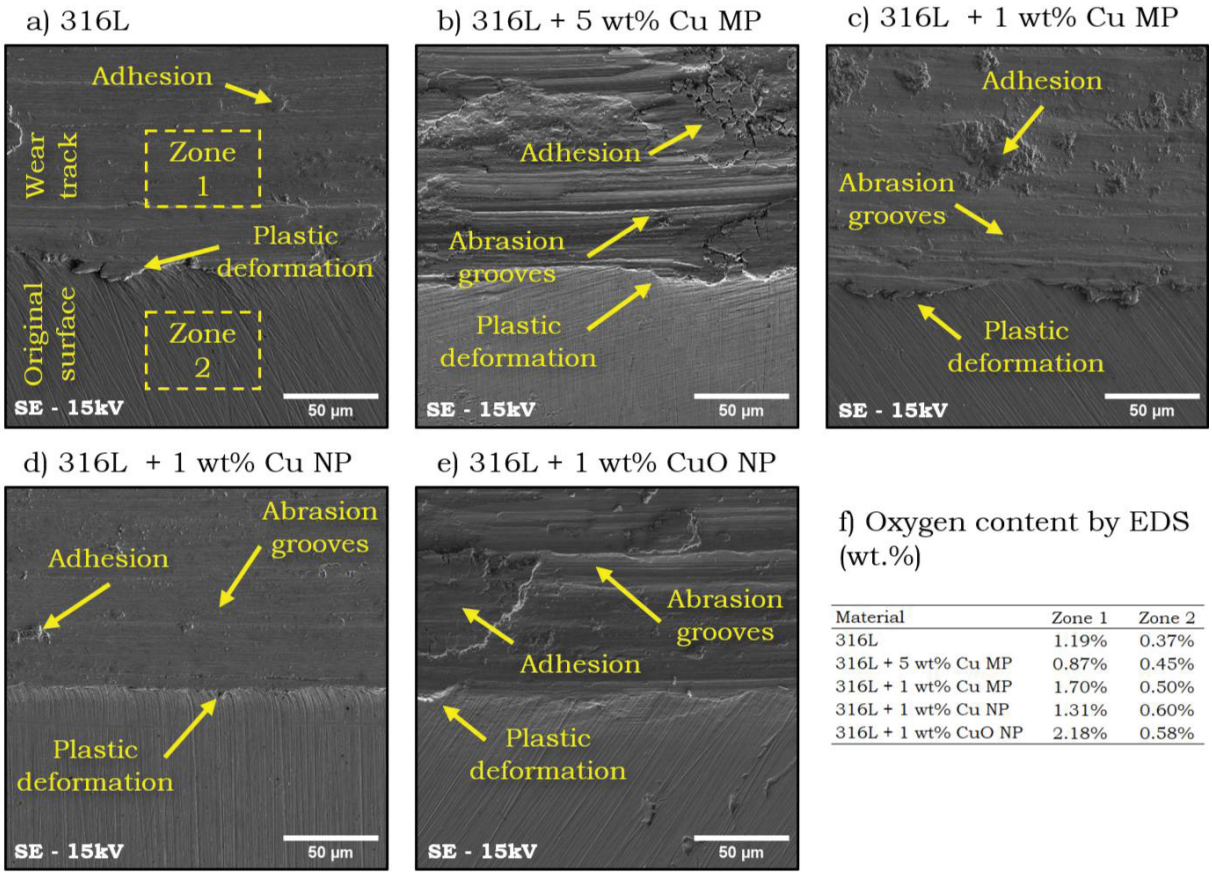

f) Oxygen content by EDS (wt.%)

Material	Zone 1	Zone 2
316L	1.19%	0.37%
316L + 5 wt% Cu MP	0.87%	0.45%
316L + 1 wt% Cu MP	1.70%	0.50%
316L + 1 wt% Cu NP	1.31%	0.60%
316L + 1 wt% CuO NP	2.18%	0.58%

Source: Authors (2025).

Figure 67 - Adhesion of wear debris at the surface of the 100Cr6 counter ball.

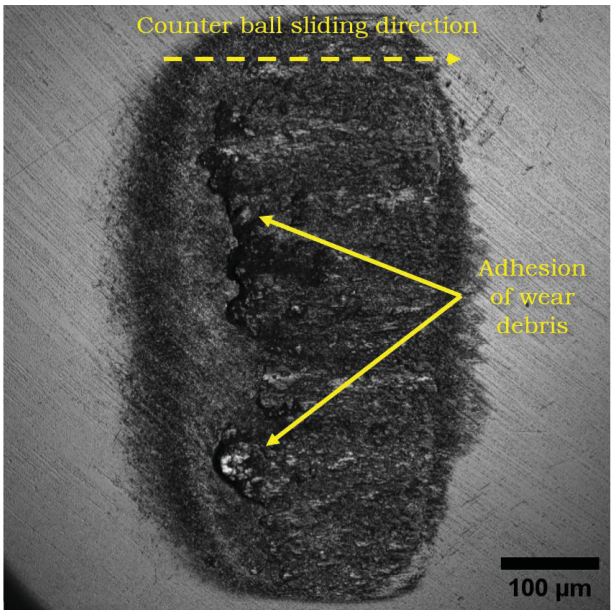

Source: Authors (2025).

CONCLUSIONS

This study evaluated wear performance of 316L stainless steel single-walls manufactured by PTA-DED against a chromium steel counter ball, a typical pairing in sliding applications for conventionally manufactured 316L. The impact of Cu content (1 and 5 wt% Cu MP added to the atomized stainless steel) and Cu particles morphology (1 wt% Cu NP, and 1 wt% CuO NP) on the dry sliding wear was examined under both as deposited and heat treated conditions. Based on the results obtained, the following conclusions can be drawn:

- Five powder mixtures of 316L with Cu additions, were successfully deposited as single-walls by PTA-DED. The chemical composition of the deposited materials closely matched with the powder mixture prepared, though a slight reduction in Cu content (6 to 12 %) was observed in specimens with Cu MP. However, larger Cu variations were observed in specimens with Cu NP and CuO NP, with reductions of 27 and 13%, respectively, attributed to the partial vaporization of nanoparticles in the plasma arc.
- PTA-DED proved to be a competitive technique compared to laser-based AM processes, being able to deposit powder feedstock with nanoparticles while achieving powder catchment efficiency above 93 %. Due to the high

interaction between the feedstock and the plasma arc, the defect-free deposited single-walls exhibited cross-sectional densities exceeding 99.85 %.

- As deposited single-walls microstructure consisted of columnar dendrites oriented in the build direction, transitioning to equiaxed dendrites near the top of the melt pool. The microstructure became more refined with increasing Cu content, which is associated with an increase in cooling rate. In compositions with 1 wt% Cu content, the microstructure was slightly finer with the addition of nanoparticles.
- The addition of 5 wt% Cu MP to the 316L manufactured by PTA-DED significantly decreased the COF and wear coefficient, attributed to the formation of more compact tribolayers on the worn surface. In contrast, the addition of 1 wt% Cu MP, 1 wt% Cu NP, and 1 wt% CuO NP did not affect COF and wear coefficient. Induced by heat treatment, the variations in hardness had no impact on wear performance.
- Under the tested conditions, the wear mechanism consisted of a combination of abrasive, adhesive, and oxidative modes. The tribolayers that adhered to the worn surfaces were formed by the agglomeration and compaction of oxide wear debris, acting as a solid lubricant and protecting against further material loss.

ACKNOWLEDGMENTS

The authors acknowledge CAPES, the National Council for Scientific and Technological Development (CNPq), the Laboratory of X-Ray Optics and Instrumentation (LORXI) of UFPR, and the Laboratory of Advanced Materials and Surface Engineering (LAMSE) of UFPR.

REFERENCES

ALANEME, K. K.; HONG, S. M.; SEN, Indrani; FLEURY, E.; RAMAMURTY, U. Effect of copper addition on the fracture and fatigue crack growth behavior of solution heat-treated SUS 304H austenitic steel. **Materials Science and Engineering**: A, v. 527, n. 18-19, p. 4600-4604, Jul. 2010. DOI. 10.1016/j.msea.2010.04.018.

ALBERTI, E. A.; BUENO, B. M. P.; D'OLIVEIRA, A. S. C. M. Additive manufacturing using plasma transferred arc. **The International Journal of Advanced**

Manufacturing Technology, v. 83, n. 9-12, p. 1861-1871, Aug. 2015. DOI. 10.1007/s00170-015-7697-7.

ALVI, S.; SAEIDI, K.; AKHTAR, F. High temperature tribology and wear of selective laser melted (SLM) 316L stainless steel. **Wear**, v. 448-449, p. 203228, May 2020. DOI. 10.1016/j.wear.2020.203228.

ARCHARD, J. F. Contact and Rubbing of Flat Surfaces. **Journal of Applied Physics,** v. 24, n. 8, p. 981-988, Aug. 1953. DOI. 10.1063/1.1721448.

ARMSTRONG, M.; MEHRABI, H.; NAVEED, N. An overview of modern metal additive manufacturing technology. **Journal of Manufacturing Processes**, v. 84, p. 1001-1029, Dec. 2022. DOI. 10.1016/j.jmapro.2022.10.060.

ASTAFUROV, S.; ASTAFUROVA, E. Phase Composition of Austenitic Stainless Steels in Additive Manufacturing: a review. **Metals**, v. 11, n. 7, p. 1052, Jun. 2021. DOI. 10.3390/met11071052.

AVERSA, A.; PISCOPO, G.; SALMI, A.; LOMBARDI, M. Effect of Heat Treatments on Residual Stress and Properties of AISI 316L Steel Processed by Directed Energy Deposition. **Journal of Materials Engineering and Performance**, v. 29, n. 9, p. 6002-6013, Sep. 2020. DOI. 10.1007/s11665-020-05061-9.

BERNAUER, C.; SIGL, M. E.; GRABMANN, S.; MERK, T.; ZAPATA, A.; ZAEH, M. F. Effects of the thermal history on the microstructural and the mechanical properties of stainless steel 316L parts produced by wire-based laser metal deposition. **Materials Science and Engineering**: A, v. 889, p. 145862, Jan. 2024. DOI. 10.1016/j.msea.2023.145862.

BOND, D.; D'OLIVEIRA, A. S. C. M. Effect of current and atomized grain size distribution on the solidification of Plasma Transferred Arc coatings. **Materials Research**, v. 15, n. 5, p. 770-774, Aug. 2012. DOI. 10.1590/s1516-14392012005000101.

CARDOZO, E. P.; RÍOS, S.; GANGULY, S.; D'OLIVEIRA, A. S. C. M. Assessment of the effect of different forms of Inconel 625 alloy feedstock in Plasma Transferred Arc (PTA) additive manufacturing. **The International Journal of Advanced Manufacturing Technology**, v. 98, n. 5-8, p. 1695-1705, Jun. 2018. DOI. 10.1007/s00170-018-2340-z.

CHI, C. Y.; YU, H. Y.; DONG, J. X.; LIU, W. Q.; CHENG, S. C.; LIU, Z. D.; XIE, X. S. The precipitation strengthening behavior of Cu-rich phase in Nb contained advanced Fe-Cr-Ni type austenitic heat resistant steel for USC power plant application. **Progress in Natural Science**: Materials International, v. 22, n. 3, p. 175-185, Jun. 2012. DOI. 10.1016/j.pnsc.2012.05.002.

CHI, X.; YUAN, J.; LI, J.; PAN, G.; CUI, Y.; LI, X. Effect of Cu on the high-temperature wear behavior of FeAl-TiB2 coatings produced by extreme high-speed laser cladding. **Applied Surface Science Advances**, v. 17, p. 100439, Oct. 2023. DOI. 10.1016/j.apsadv.2023.100439.

CHOO, H.; SHAM, K. L.; BOHLING, J.; NGO, A.; XIAO, X.; REN, Y.; DEPOND, P. J.; MATTHEWS, M. J.; GARLEA, E. Effect of laser power on defect, texture, and microstructure of a laser powder bed fusion processed 316L stainless steel. **Materials & Design**, v. 164, p. 107534, Feb. 2019. DOI. 10.1016/j.matdes.2018.12.006.

da SILVA, L. J.; D'OLIVEIRA, A. S. C. M. NiCrSiBC coatings: effect of dilution on microstructure and high temperature tribological behavior. **Wear**, v. 350-351, p. 130-140, Mar. 2016. DOI. 10.1016/j.wear.2016.01.015.

D'ANDREA, D. Additive Manufacturing of AISI 316L Stainless Steel: a review. **Metals**, v. 13, n. 8, p. 1370, Jul. 2023. DOI. 10.3390/met13081370.

FOLKHARD, Erich. **Welding Metallurgy of Stainless Steels**. Kapfenberg: Springer Vienna, 1988.

GOMES, R.; HENKE, S.; D'OLIVEIRA, A. S. C. M. Microstructural control of Co-based PTA coatings. **Materials Research**, v. 15, n. 5, p. 796-800, Aug. 2012. DOI. 10.1590/s1516-14392012005000099.

HAN, Y.; ZHANG, C.; CUI, X.; ZHANG, S.; CHEN, J.; DONG, S.; ABDULLAH, A.O. Microstructure and properties of a novel wear- and corrosion-resistant stainless steel fabricated by laser melting deposition. **Journal of Materials Research**, v. 35, n. 15, p. 2006-2015, Apr. 2020. DOI. 10.1557/jmr.2020.70.

HAUSER, M.; NITZSCHE, P.; WEIDNER, A.; HENKEL, S.; BIERMANN, H.; VOLKOVA, O.; WENDLER, M. Effect of Cu addition on solidification, precipitation behavior and mechanical properties in austenitic CrNi-N stainless steel. **Materials Science and Engineering**: A, v. 862, p. 144422, Jan. 2023. DOI. 10.1016/j.msea.2022.144422.

JENA, P.; CASTLEMAN, A.W. Introduction to Atomic Clusters. **Science and Technology of Atomic, Molecular, Condensed Matter & Biological Systems**, p. 1-36, 2010. http://dx.doi.org/10.1016/b978-0-444-53440-8.00001-x.

KAMATH, C.; EL-DASHER, B.; GALLEGOS, G. F.; KING, W. E.; SISTO, A. Density of additively-manufactured, 316L SS parts using laser powder-bed fusion at powers up to 400 W. **The International Journal of Advanced Manufacturing Technology**, v. 74, n. 1-4, p. 65-78, May 2014. DOI. 10.1007/s00170-014-5954-9.

KLADOVASILAKIS, N.; CHARALAMPOUS, P.; KOSTAVELIS, I.; TZETZIS, D.; TZOVARAS, D. Impact of metal additive manufacturing parameters on the powder bed fusion and direct energy deposition processes: a comprehensive review. **Progress in Additive Manufacturing**, v. 6, n. 3, p. 349-365, Apr. 2021. DOI. 10.1007/s40964-021-00180-8.

KOTI, D.; POWELL, J.; NAESSTROEM, H.; VOISEY, K. T. Powder catchment efficiency in laser cladding (directed energy deposition). An investigation into

standard laser cladding and the ABA cladding technique. **Journal of Laser Applications**, v. 35, n. 1, Feb. 2023. DOI. 10.2351/7.0000904.

KOU, S. Welding metallurgy. Hoboken: John Wiley & Sons, 2002.

LI, H.; RAMEZANI, M.; LI, M.; MA, C.; WANG, J. Tribological performance of selective laser melted 316L stainless steel. **Tribology International**, v. 128, p. 121-129, Dec. 2018. DOI. 10.1016/j.triboint.2018.07.021.

MANDAL, A.; TIWARI, J.K.; ALMANGOUR, B.; SATHISH, N.; KUMAR, S.; KAMARAJ, M.; ASHIQ, M.; SRIVASTAVA, A.K. Tribological behavior of graphene-reinforced 316L stainless-steel composite prepared via selective laser melting. **Tribology International**, v. 151, p. 106525, Nov. 2020. DOI. 10.1016/j.triboint.2020.106525.

MIRZABABAEI, S.; DODDAPANENI, V.; LEE, K.; PAUL, G.E.; PIRGAZI, H.; TAN, K.; ERTORER, O.; CHANG, C.; PAUL, B.K.; PASEBANI, S. Remarkable enhancement in thermal conductivity of stainless-steel leveraging metal composite via laser powder bed fusion: 316l-Cu composite. **Additive Manufacturing**, v. 70, p. 103576, May 2023. DOI. 10.1016/j.addma.2023.103576.

MOHYLA, P.; HAJNYS, J.; GEMBALOVÁ, L.; ZAPLETALOVÁ, A.; KRPEC, P. Influence of Heat Treatment of Steel AISI316L Produced by the Selective Laser Melting Method on the Properties of Welded Joint. **Materials**, v. 15, n. 5, p. 1690, Feb. 2022. DOI. 10.3390/ma15051690.

NIU, M.C.; YANG, K.; LUAN, J.H.; WANG, W.; JIAO, Z.B. Cu-assisted austenite reversion and enhanced TRIP effect in maraging stainless steels. **Journal of Materials Science & Technology**, v. 104, p. 52-58, Mar. 2022. DOI. 10.1016/j.jmst.2021.06.055.

ÖZER, G.; KISASÖZ, A. The role of heat treatments on wear behaviour of 316L stainless steel produced by additive manufacturing. **Materials Letters**, v. 327, p. 133014, Nov. 2022. DOI. 10.1016/j.matlet.2022.133014.

PRASS, G. S.; D'OLIVEIRA, A. S. C. M. Processing and characterization of AISI 316L coatings modified with Cu and CuO nanoparticles. **Surface and Coatings Technology**, v. 461, p. 129465, May 2023. DOI. 10.1016/j.surfcoat.2023.129465.

RALLS, A. M.; DAROONPARVAR, M.; SIKDAR, S.; RAHMAN, M. H.; MONWAR, M.; WATSON, K.; KAY, C. M.; MENEZES, P. L. Tribological and Corrosion Behavior of High Pressure Cold Sprayed Duplex 316 L Stainless Steel. **Tribology International**, v. 169, p. 107471, May 2022. DOI. 10.1016/j.triboint.2022.107471

RASIYA, G.; SHUKLA, A.; SARAN, K. Additive Manufacturing - A Review. **Materials Today**: Proceedings, v. 47, p. 6896-6901, 2021. DOI. 10.1016/j.matpr.2021.05.181.

REVILLA, R.I.; VAN CALSTER, M.; RAES, M.; ARROUD, G.; ANDREATTA, F.; PYL, L.; GUILLAUME, P.; GRAEVE, I. Microstructure and corrosion behavior of 316L stainless steel prepared using different additive manufacturing methods: a

comparative study bringing insights into the impact of microstructure on their passivity. **Corrosion Science**, v. 176, p. 108914, Nov. 2020. DOI. 10.1016/j.corsci.2020.108914.

SABOORI, A.; AVERSA, A.; MARCHESE, G.; BIAMINO, S.; LOMBARDI, M.; FINO, P. Microstructure and Mechanical Properties of AISI 316L Produced by Directed Energy Deposition-Based Additive Manufacturing: a review. **Applied Sciences**, v. 10, n. 9, p. 3310, May 2020. DOI.10.3390/app10093310.

SADASIVAM, P.; AMIRTHALINGAM, M. Design and fabrication of micro-plasma transferred wire arc additive manufacturing system. **CIRP Journal of Manufacturing Science and Technology**, v. 37, p. 185-195, May 2022. DOI. 10.1016/j.cirpj.2022.01.014.

SAEIDI, K.; KVETKOVÁ, L.; LOFAJ, F.; SHEN, Z. Austenitic stainless steel strengthened by the in situ formation of oxide nanoinclusions. **RSC Advances**, v. 5, n. 27, p. 20747-20750, 2015. DOI. 10.1039/c4ra16721j.

SALUJA, R. P.; MOEED, K. The emphasis of phase transformations and alloying constituents on hot cracking susceptibility of type 304L and 316L stainless steel welds. **International Journal of Engineering Science and Technology**, v. 4, p. 2206-2216, 2012.

SAWANT, M. S.; JAIN, N. K. Investigations on Additive Manufacturing of Ti-6Al-4V by Microplasma Transferred Arc Powder Deposition Process. **Journal of Manufacturing Science and Engineering**, v. 140, n. 8, Jun. 2018. DOI. 10.1115/1.4040324.

SEN, I.; AMANKWAH, E.; KUMAR, N.S.; FLEURY, E.; OH-ISHI, K.; HONO, K.; RAMAMURTY, U. Microstructure and mechanical properties of annealed SUS 304H austenitic stainless steel with copper. **Materials Science and Engineering**: A, v. 528, n. 13-14, p. 4491-4499, May 2011. DOI. 10.1016/j.msea.2011.02.019.

SOUSA, J.M.S.; PEREIRA, A.S.P.; SILVA, R.G.N.; PEREIRA, M.; CASTRO, R.M.; CURI, E.I.M.; MACHADO, P.C. Tribological performance of Ni-Cr-B-Si coatings deposited via laser cladding process. **Surface Topography**: Metrology and Properties, v. 10, n. 3, p. 034008, Sep. 2022. DOI. 10.1088/2051-672x/ac97af.

TASCIOGLU, E.; KARABULUT, Y.; KAYNAK, Y. Influence of heat treatment temperature on the microstructural, mechanical, and wear behavior of 316L stainless steel fabricated by laser powder bed additive manufacturing. The International **Journal of Advanced Manufacturing Technology**, v. 107, n. 5-6, p. 1947-1956, Feb. 2020. DOI. 10.1007/s00170-020-04972-0.

UPADHYAY, R.K.; KUMAR, A. Scratch and wear resistance of additive manufactured 316L stainless steel sample fabricated by laser powder bed fusion technique. **Wear**, v. 458-459, p. 203437, Oct. 2020. DOI. 10.1016/j.wear.2020.203437.

VISHNU, V.; PRABHU, T.R.; IMAM, M.; VINEESH, K.P. High-temperature dry sliding wear behavior of additively manufactured austenitic stainless steel (316L). **Wear**, v. 540-541, p. 205259, Mar. 2024. DOI. 10.1016/j.wear.2024.205259.

WANG, C.; LIU, T.G.; ZHU, P.; LU, Y.H.; SHOJI, T. Study on microstructure and tensile properties of 316L stainless steel fabricated by CMT wire and arc additive manufacturing. **Materials Science and Engineering**: A, v. 796, p. 140006, Oct. 2020. DOI. 10.1016/j.msea.2020.140006.

XI, T.; SHAHZAD, M. B.; XU, D.; SUN, Z.; ZHAO, J.; YANG, C.; QI, M.; YANG, K. Effect of copper addition on mechanical properties, corrosion resistance and antibacterial property of 316L stainless steel. **Materials Science and Engineering**: C, v. 71, p. 1079-1085, Feb. 2017. DOI. 10.1016/j.msec.2016.11.022.

XI, T.; SHAHZAD, M. B.; XU, D.; ZHAO, J.; YANG, C.; QI, M.; YANG, K. Copper precipitation behavior and mechanical properties of Cu-bearing 316L austenitic stainless steel: a comprehensive cross-correlation study. **Materials Science and Engineering**: A, v. 675, p. 243-252, Oct. 2016. DOI. 10.1016/j.msea.2016.08.058.

XIE, B.; XUE, J.; REN, X. Wire Arc Deposition Additive Manufacturing and Experimental Study of 316L Stainless Steel by CMT + P Process. **Metals**, v. 10, n. 11, p. 1419, Oct. 2020. DOI. 10.3390/met10111419.

ZHONG, Y.; LIU, L.; WIKMAN, S.; CUI, D.; SHEN, Z. Intragranular cellular segregation network structure strengthening 316L stainless steel prepared by selective laser melting. **Journal of Nuclear Materials**, v. 470, p. 170-178, Mar. 2016. DOI. 10.1016/j.jnucmat.2015.12.034.

4.5 OPTIMIZATION OF LASER POWDER BED FUSION PROCESSING PARAMETERS FOR IN-SITU ALLOYING 316L STAINLESS STEEL WITH CU

ABSTRACT

This study optimizes the Laser Powder Bed Fusion (L-PBF) processing parameters for 316L stainless steel with and without Cu additions, aiming to enhance part density, microstructural integrity, and mechanical properties. The mixture between 316L stainless steel powder added with 5 wt% Cu powder was assessed for flowability, particle size, morphology and homogeneity. Using a full factorial design of experiments (DoE), the effects of laser power, scan speed, and hatch distance on Archimedes density and hardness were systematically evaluated. Post-optimization characterization includes cross-section density via SEM, melt pool dimensions and microstructure analysis through optical microscopy and SEM, phase identification by XRD, and crystallographic orientation and grain size determination using EBSD. Additionally, the influence of three energy density levels on the mechanical properties of 316L and 316L with Cu was examined. The results demonstrate that precise control of processing parameters significantly enhances part density, achieving 99.99% for 316L and 99.96% for 316L + 5% Cu. However, the addition of Cu led to a reduction in hardness and tensile mechanical properties of the stainless steel. Moreover, lower energy density levels increased yield strength, ultimate tensile strength (UTS), and strain at UTS.

Keywords: Laser Powder Bed Fusion, 316L, Cu, Design of Experiments, Mechanical Properties.

INTRODUCTION

Additive Manufacturing (AM) permits the production of intricate metallic components, processing and consolidating the added feedstock material in a layer-by-layer manner (Huang *et al.*, 2015). Among the feedstock used, metal powders stand out for their flexibility in tailoring the chemical composition, making it possible to design materials with specific properties (Li *et al.*, 2019; Dong *et al.*, 2020; Cui *et al.*, 2022). In Laser Powder Bed Fusion (L-PBF) processes, it is essential to distribute a thin and uniform layer of powder to ensure high part density and structural integrity

(Avrampos; Vosniakos, 2022; Abu-Lebdeh *et al.*, 2022). Therefore, advancing material development for AM relies on a comprehensive understanding of how powder characteristics interact with processing conditions, influencing the resulting mechanical properties.

Table 29 presents a brief literature review on L-PBF of 316L with Cu additions, showing the material composition and the main objectives of the study. The main goal of adding Cu to austenitic stainless steel is to improve target property, such as thermal conductivity, without negatively affecting other characteristics, such as mechanical properties and corrosion resistance. The studies summarized in Table 29 demonstrate that Cu addition can not only improve thermal conductivity but also antimicrobial performance. And when combined with post-processing heat treatments, Cu can promote the precipitation of Cu-rich phases, contributing to improved mechanical properties.

Table 29 - Brief literature review on L-PBF of 316L with Cu additions

Reference	**Material Composition (weight %)**	**Main objectives**
Wang et al., 2016	316L + 4.5 % Cu	Antimicrobial properties and biocompatibility
Rankouhi et al., 2021	316L + 25, 50, 75, 100 % Cu	Compositional grading
Foadian et al., 2023	316L + 1 and 5 % Cu	Mechanical properties
Mirzababaei et al., 2023	316L + 20, 30, 50, 60 % Cu	Thermal conductivity
Behjat et al., 2024	316L + 3.5 % Cu	Antimicrobial properties
Behjat et al., 2024	316L + 2.5 % Cu	Mechanical properties

Source: Authors (2025).

However, there is a gap in the literature regarding the systematic optimization of processing parameters for the in-situ alloying of 316L with Cu, particularly with the goal of maximizing the density of the final part. In this context, this study uses a full factorial design of experiments to optimize the L-PBF processing parameters for 316L with 5 wt% Cu additions, establishing the relationship between chemical composition, processing parameters, melt pool dimensions, microstructure, density and mechanical properties.

MATERIALS AND METHODS

As described in section 1.3.1, two feedstock materials were used, 316L and 316L with the addition of 5 wt% Cu. The morphology of the powder mixture particles was characterized by scanning electron microscopy (SEM) and the Cu particle distribution among the stainless steel particles was assessed by energy-dispersive X-ray spectroscopy (EDS) mapping. The overall effects of the powder mixing process were evaluated by particle size analysis (PSA) and flowability tests, which were conducted on the primary powders and the powder mixture.

A full-factorial Design of Experiments (DoE) was conducted for both materials to systematically evaluate the effects of 3 factors (laser powder, scan speed and hatch distance) on Archimedes density and hardness. The processing parameters selected for L-PBF are presented in Table 30.

Table 30 - Range of processing parameters selected for L-PBF

Parameter (unit)	**Value**
Machine	Concept Laser M2 Cusing
Substrate	Stainless steel
Protective gas	Argon
Scanning strategy	Islands (5 x 5 mm)
Layer thickness (µm)	30
Laser power (W)	150, 200, 250
Scan speed (mm/s)	500, 750, 1000
Hatch distance (µm)	70, 90, 110

Source: Authors (2025).

Each set of parameters (27 in total) was used to manufacture one individual cube (10 × 10 × 10 mm), using a constant layer thickness and an island scanning strategy. As presented in Figure 16b, the island scanning strategy consists of dividing the part cross section into smaller islands (5 × 5 mm), where every neighboring island is scanned perpendicular to the other neighboring island. In the successive layer scan, the islands are shifted in 1 mm in both the x and y direction, perpendicular to the build direction, in addition to rotating the scan direction within an island by 90 degrees.

After this systematic evaluation, 9 specimens for each material were selected for further analysis, based on the hatch distance that achieved the highest Archimedes density and hardness. With the hatch distance fixed, the influence of laser power and scan speed on the microstructure and mechanical properties was examined in detail. The cross-section density was measured by SEM on the polished

specimens, with an image analysis software (ImageJ). The polished specimens were etched with Marbles' reagent (4 g $CuSO_4$ + 20 ml HCl + 20 mL H_2O) to reveal the melt pool boundaries and microstructure, which were evaluated by Optical Microscopy (OM) and SEM. Chemical composition was determined by EDS analysis, crystallographic phases and lattice parameters by XRD, crystallographic orientation and grain size by Electron Backscattered Diffraction (EBSD).

The effects of Cu addition and energy density on the mechanical properties of 316L stainless steel were assessed by testing tensile specimens with 3 laser power, based on ASTM E8 standard. The tensile specimen's thickness is 1.5 mm, and the other dimensions are presented in Figure 68. Three replicates were tested for each condition and the fractography analysis was done by SEM.

Figure 68 - Tensile specimen dimensions based on ASTM E8 standard

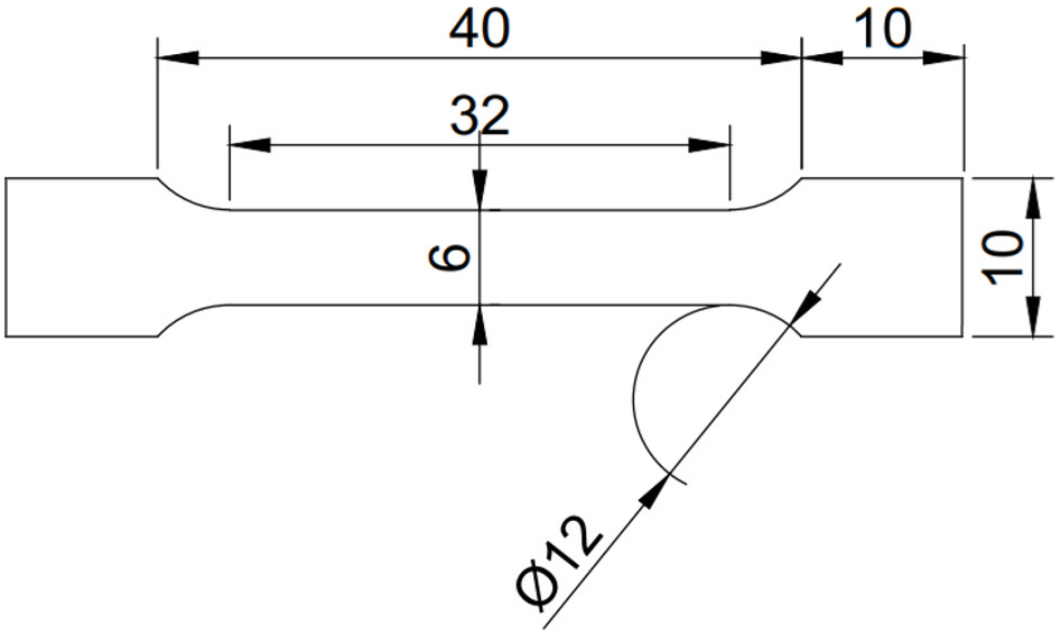

Source: Authors (2025).

RESULTS AND DISCUSSION

Powders characterization

Figure 69a shows the overall morphology of the powder particles after mixing AISI 316L with 5 wt% Cu. The particles are mostly spherical, with smaller satellites attached to their surfaces. The Cu particles are well distributed among the stainless

steel particles, as observed in Figure 69b. As seen in Figure 70a, both primary powders are within the same size range, with Cu being slightly smaller than the 316L. In terms of powder size percentiles (d10 and d90), stainless steel and Cu ranges from 20 to 49 µm and 17 to 44 µm, respectively. However, the powder mixture ranges from 22 to 55 µm, indicating that some particles were deformed or agglomerated during the mixing procedure, causing the increase in size.

Figure 69 - (a) SEM micrograph and (b) EDS mapping of the powder mixture

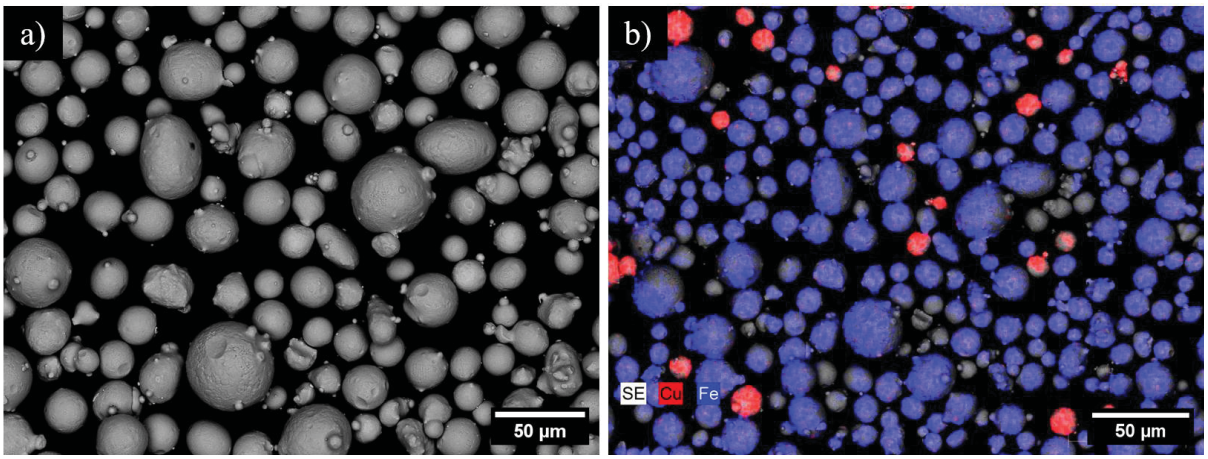

Source: Authors (2025).

Figure 70 - (a) Particle size distribution and (b) powder flowability

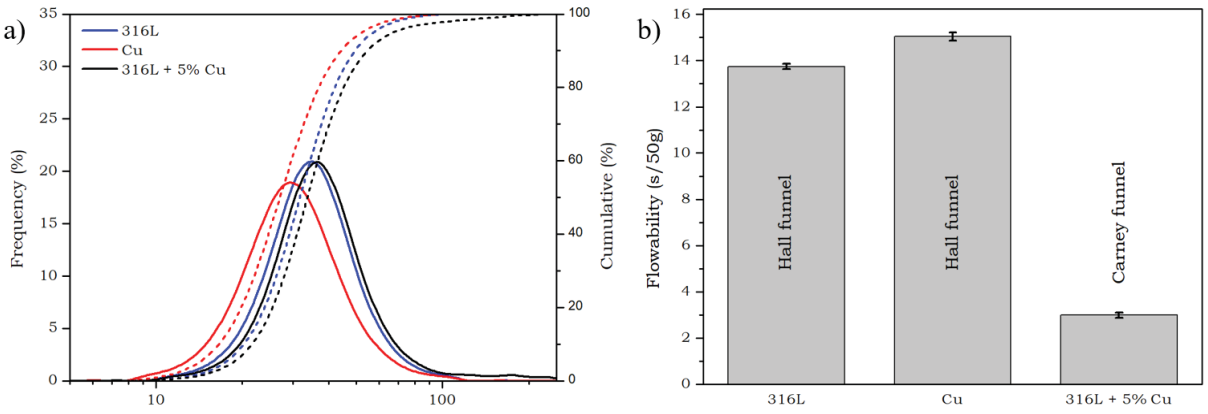

Source: Authors (2025).

Powder flowability is one of the main factors that indicates its behavior during the L-PBF process. Powders with good flowability (low flow time) tend to form a uniform powder bed when spread by the recoater, favoring material processability. The flowability tests were conducted using a Hall funnel, and if the powder did not

flow through it, a Carney Funnel was used. As shown in Figure 70b, both 316L and Cu powders exhibited excellent flowability in the Hall funnel, taking approximately 15 seconds to flow 50 g of powder. The powder mixture did not flow through the Hall funnel, indicating poor flowability. However, it did flow through the Carney funnel, which has a bigger aperture.

L-PBF process optimization

The effects of laser power, scan speed and hatch distance on Archimedes density for both 316L and 316L + 5 % Cu specimens are presented on Figure 71. The mean Archimedes densities are shown by dashed lines on Figure 71a and Figure 71b, with values of 7.868 g/cm³ for 316L and 7.856 g/cm³ for 316L + 5 % Cu. For both materials, the density was mostly influenced by scan speed, with 500 mm/s resulting in the lowest density and 750 mm/s producing the highest density among the tested parameters.

The interaction plots for Archimedes density are presented in Figure 71c and Figure 71d. A similar behavior is observed in both powders processed, with Cu-containg specimens showing slightly lower density. The interaction between scan speed and laser powder is evident, at the lowest speed, increasing laser powder results in reduced density, while at the highest scan speed, lowering laser powder also leads to reduced density. Theses effects highlight the role of energy density, where both insufficient or excessive energy input negatively impact material consolidation, and consequently, density. The effects of excessive energy are also observed in the interation between scan speed and hatch distance, wherea combintaion of low hatch distance and low scan speed produce generates high energy input, resulting in parts with reduced density.

The Archimedes density countour plots for 316L and 316L + 5 % Cu are given in Figure 71e and Figure 71f. These plots can be used as maps for the selection of optimal processing parameters. For instance, at the lowest scan speed, only the lowest laser power should be used to produce parts with high density. Nevertheless, the highest density can be achieved using a scan speed between 750 and 1000 mm/s paired with a laser power between 200 and 250 W.

Figure 71 - Archimedes density of 316L and 316L + 5 % Cu: (a, b) Main effects plots, (c, d) interaction plots, and (e, f) contour plots.

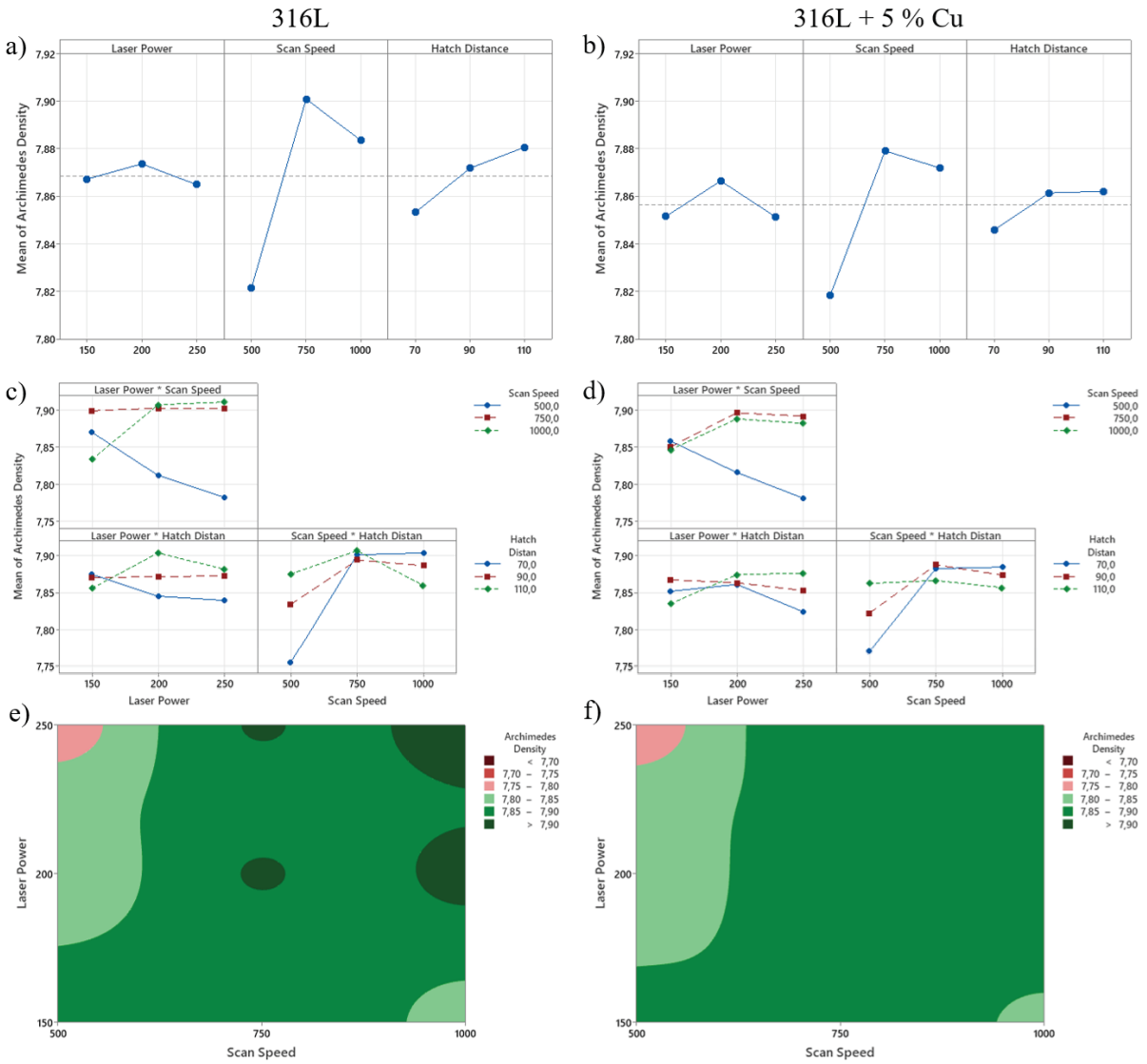

Source: Authors (2025).

The effects of laser power, scan speed and hatch distance on Vicker hardness for both 316L and 316L + 5 % Cu specimens are presented on Figure 72. The mean hardness are shown by dashed lines on Figure 72a and Figure 72b, with values of 216.8 HV for 316L and 205.4 HV for 316L + 5 % Cu, indicating a reduction in hardness with the addition of Cu. Increasing laser power results in a reduced hardness for 316L, while it has the opposite effect for 316L + 5 % Cu. These contrasting results suggest that Cu plays an important role in both the processability and mechanical properties of the material. The reduction in hardness observed in 316L with increased laser power is likely due to grain coarsening caused by higher energy density. A similar trend is seen with scan speed, where lower scan speeds,

corresponding to higher energy input, promote the formation of larger grains and consequently result in reduced hardness.

Figure 72 - Vicker hardness of 316L and 316L + 5 % Cu: (a, b) Main effects plots, (c, d) interaction plots, and (e, f) contour plots.

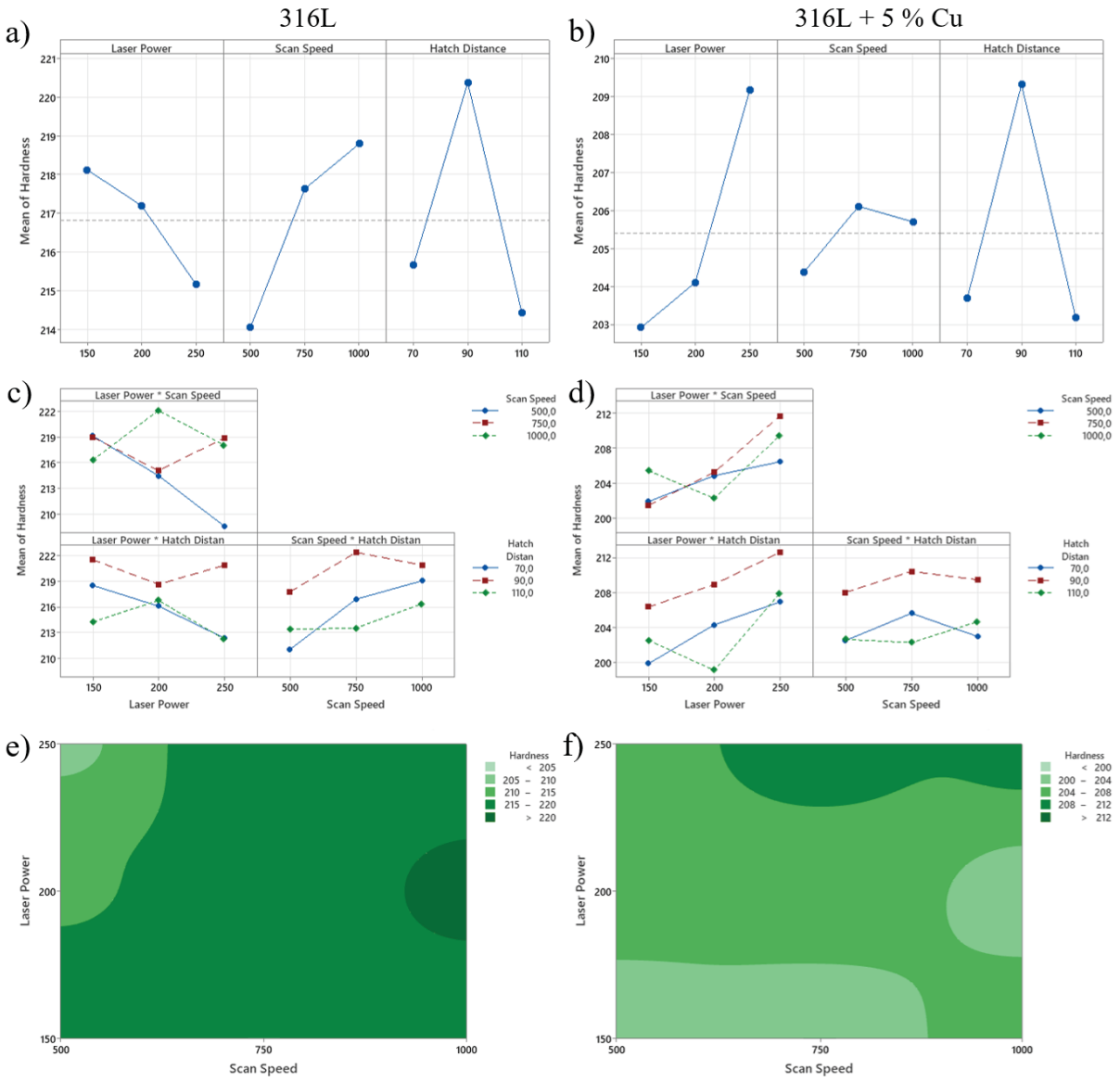

Source: Authors (2025).

The influence of hatch distance is evident, with 90 µm resulting in the highest hardness for both 316L and 316L + 5 % Cu. The interaction plots presented in Figure 72c and Figure 72d further demonstrate that a hatch distance of 90 µm produces the highest hardness across all test ranges of laser power and scan speed. Hatch distance determines the spacing of scan lines, controlling the overlap between successive laser passes. Affecting energy input, cooling rate, grain growth,

microstructure, and mechanical properties. The contour plots presented in Figure 72e and Figure 72f show the regions for achieving the highest hardness. For 316L, a higher scan speed leads to increased hardness, while for 316L + 5 % Cu, higher laser power results in higher hardness.

Cross-section density, melt pool geometry and microstructure

Further characterization was carried out on specimens produced with a hatch distance of 90 µm, which produced the optimal combination of Archimedes density and Vicker hardness. Table 31 presents the cross-section density, indicating the relationship between feedstock material, scan speed, laser power and mean density. In accordance with the measured Archimedes density (Figure 71), the highest cross-section densities are obtained with a scan speed of 750 mm/s. At this scan speed, the addition of Cu caused a slight reduction in cross-section density, with mean values of 99.98 % for 316L and 99.96 % for 316L + 5 % Cu. Under the tested conditions, the optimal energy density range for achieving the best cross-section density lies between 74 and 123 J/mm³.

Table 31 - Density obtained by SEM imaging on the cross-section of specimens

Scan speed (mm/s)	Laser power (W)	Energy density (J/mm³)	Mean density (316L)	SD	Mean density (316L + 5 % Cu)	SD
500	150	111	99.87%	0.12%	99.88%	0.12%
500	200	148	99.29%	0.24%	99.51%	0.13%
500	250	185	98.93%	0.26%	99.38%	0.24%
750	150	74	99.97%	0.03%	99.95%	0.03%
750	200	99	99.99%	0.01%	99.96%	0.04%
750	250	123	99.99%	0.01%	99.96%	0.04%
1000	150	56	98.94%	0.18%	99.72%	0.11%
1000	200	74	99.99%	0.01%	99.94%	0.05%
1000	250	93	99.99%	0.01%	99.90%	0.08%

Source: Authors (2025).

Within the optimal processing parameters range, the high density parts produced showed minimal porosities. Figure 73 shows the microstructure on the perpendicular and parallel planes relative to the build direction of two specimens with the highest density, processed with a layer thickness of 30 µm, hatch distance of 90 µm, laser power of 250 W and scan speed of 750 mm/s. On the planes parallel to the

build direction, the successive stacking of layers can be seen, showing the characteristic microstructure obtained by the L-PBF layer-by-layer building process. In the perpendicular plane, the intersecting melt pool lines originate from the 90º rotation of the scan direction between layers, defined on the scanning strategy.

Figure 73 - Microstructure on perpendicular and parallel planes relative to the build direction

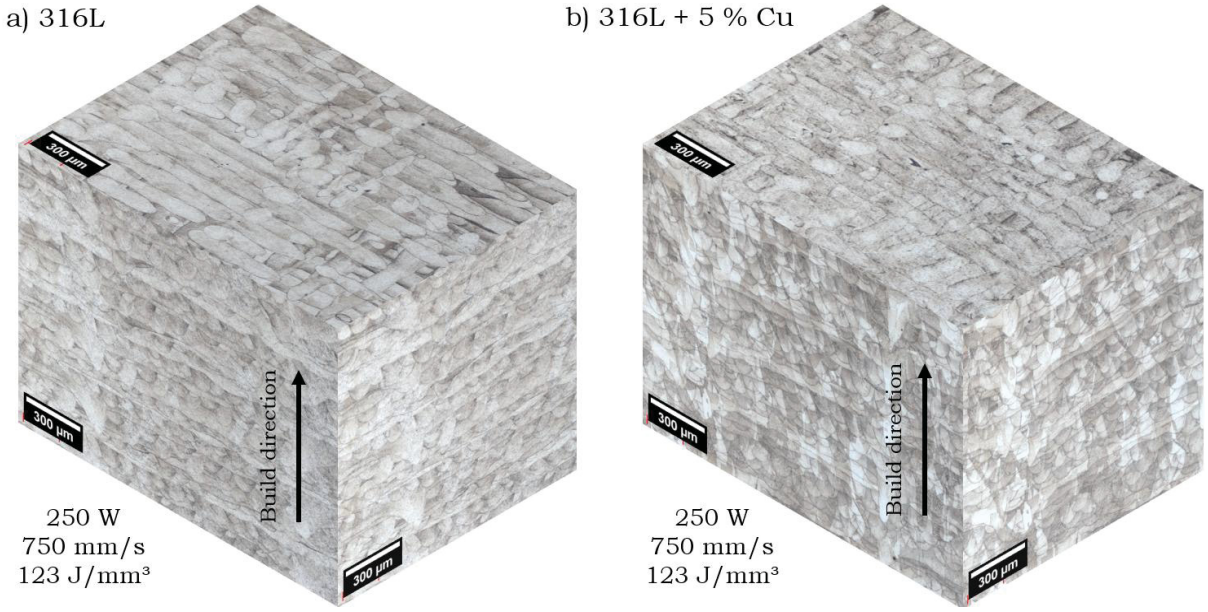

Source: Authors (2025).

Figure 74 summarizes the effects of laser power and scan speed on the melt pool width (w) and melt pool depth (d) of both materials. Overall, both melt pool dimensions tend to increase with higher laser power and decrease as scan speed increases. Across all processing parameters tested, the addition of Cu increased melt pool width and melt pool depth by approximately 15 % and 22 %, respectively. This effect can be attributed to the higher thermal conductivity and lower melting point of Cu, when compared to 316L.

Figure 74 - Effects of laser power and scan speed on (a, b) melt pool width and (c, d) melt pool depth

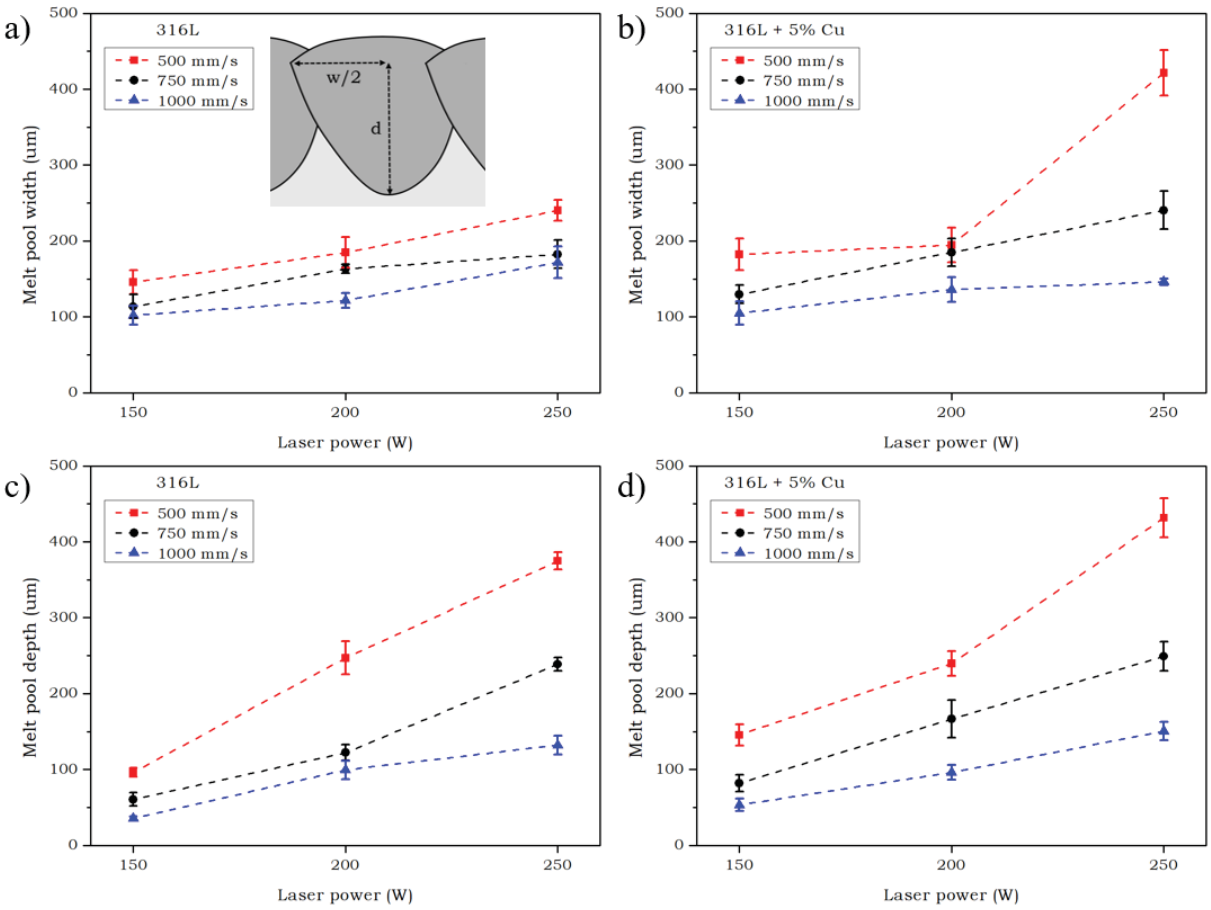

Source: Authors (2025).

The effects of laser power and scan speed on melt pool geometry for 316L and 316L + 5 % Cu can be seen on the micrographs shown in Figure 75. The melt pool boundaries are delineated with red dotted lines, outlining the overall geometry under specific energy density levels. At a laser power of 150 W and a scan speed of 1000 mm/s, the energy density is the at its lowest, 56 J/mm³, resulting in a minimal melt pool size. As shown in Figure 74, the mean melt pool depth is 35 µm for 316L and 53 µm for 316L + 5 % Cu. Consequently, a few pores can be observed in 316L, attributed to lack of fusion (Figure 75a). However, for 316L + 5 % Cu, at the same energy density level, etching revealed incomplete homogenization of Cu within the stainless steel matrix, evidenced by dark stains in areas with possible higher Cu concentration (Figure 75b).

Figure 75 - Melt pool micrographs for (a) 316L and (b) 316L + 5 % Cu

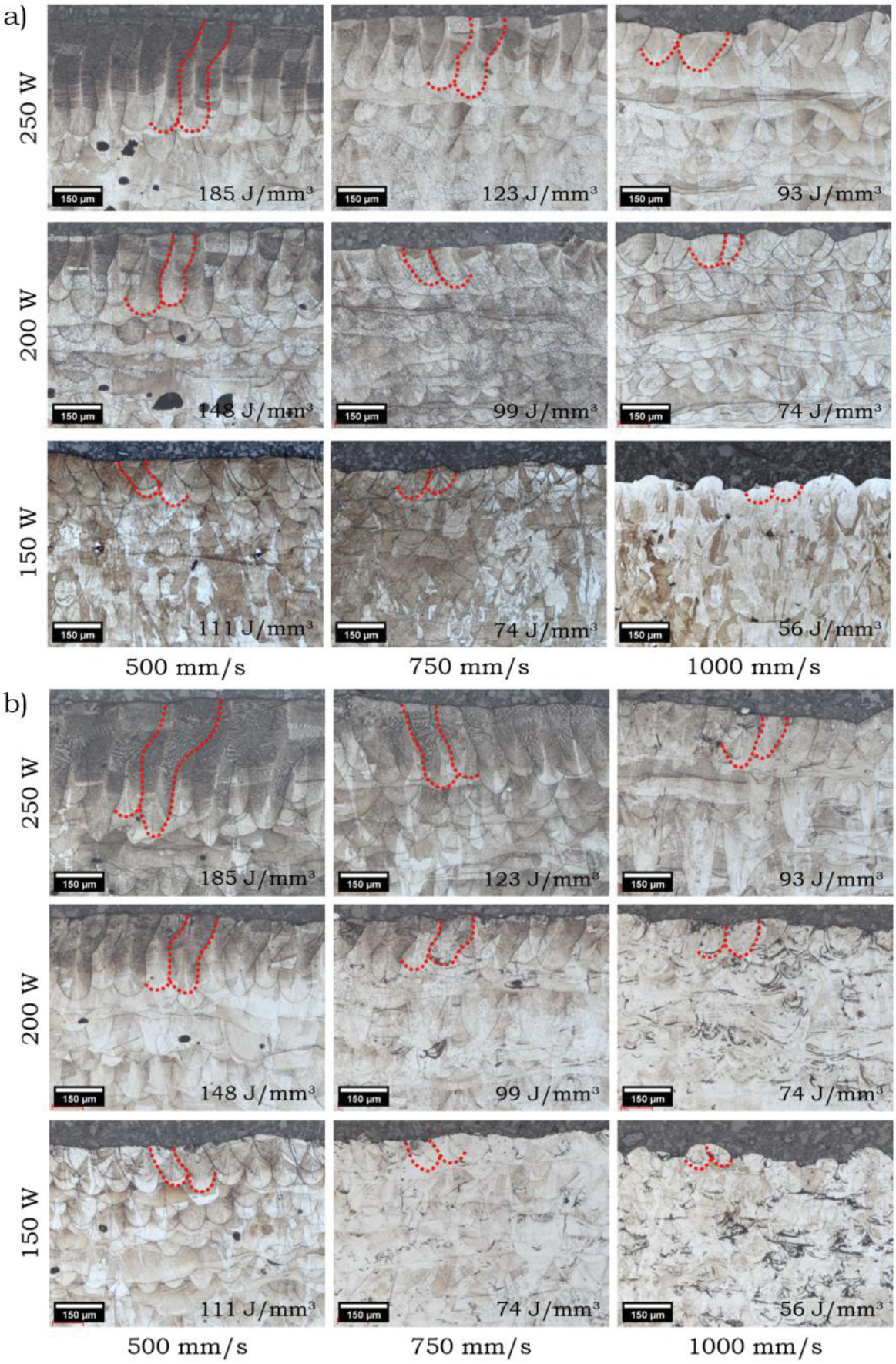

Source: Authors (2025).

At a laser power of 250 W and a scan speed of 500 mm/s, the energy density is at its highest, 185 J/mm³, resulting in the largest melt pool size. As shown in Figure 74, the mean melt pool depth is 375 µm for 316L and 432 µm for 316L + 5 % Cu. Given a layer thickness of 30 µm, each laser scan remelts approximately 12.5 layers for 316L and 14.4 layers for 316L + 5 % Cu, leading to complete homogenization of Cu within the stainless steel matrix (Figure 75b). However, at this high energy density, keyhole pores are observed (Figure 75a).

The SEM micrographs of 316L and 316L + 5 % Cu processed under different energy densities are shown in Figure 76 and Figure 77, respectively. Melt pool boundaries are delineated with yellow dashed lines, illustrating the increase in melt pool size with higher energy density, as previously discussed. At higher magnifications, it becomes evident that higher energy density leads to the coarsening of columnar dendrites.

Figure 76 - SEM micrographs of 316L processed with different energy densities

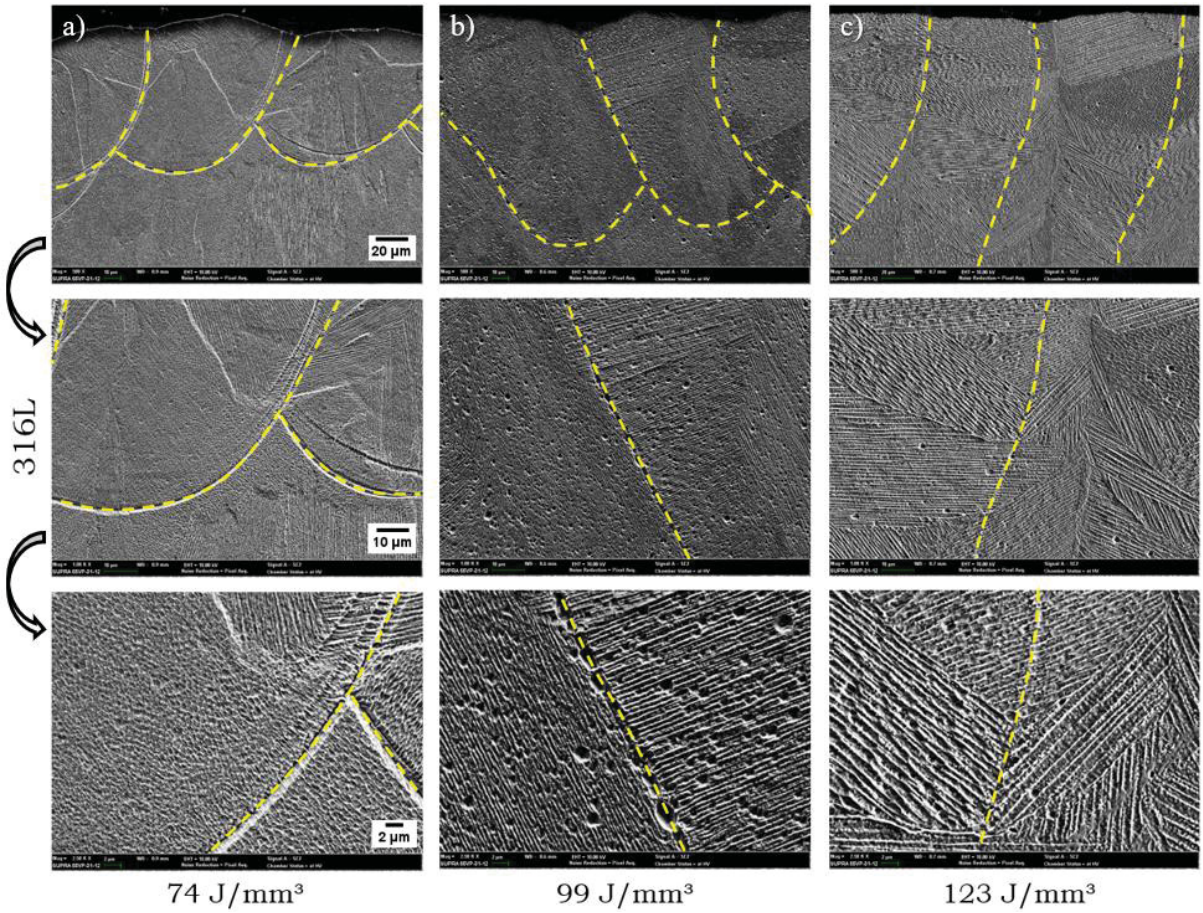

Source: Authors (2025).

The incomplete homogenization of Cu within the stainless steel matrix can be seen in Figure 77a. As previously discussed, the low energy input (74 J/mm³) resulted in a shallow melt pool, preventing the full remelt of the previous layer. This limited remelt led to localized regions with higher Cu concentration, as revealed by etching. At higher energy density (99 and 123 J/mm³), a complete homogenization of Cu was achieved.

Figure 77 - SEM micrographs of 316L + 5 % Cu processed with different energy densities

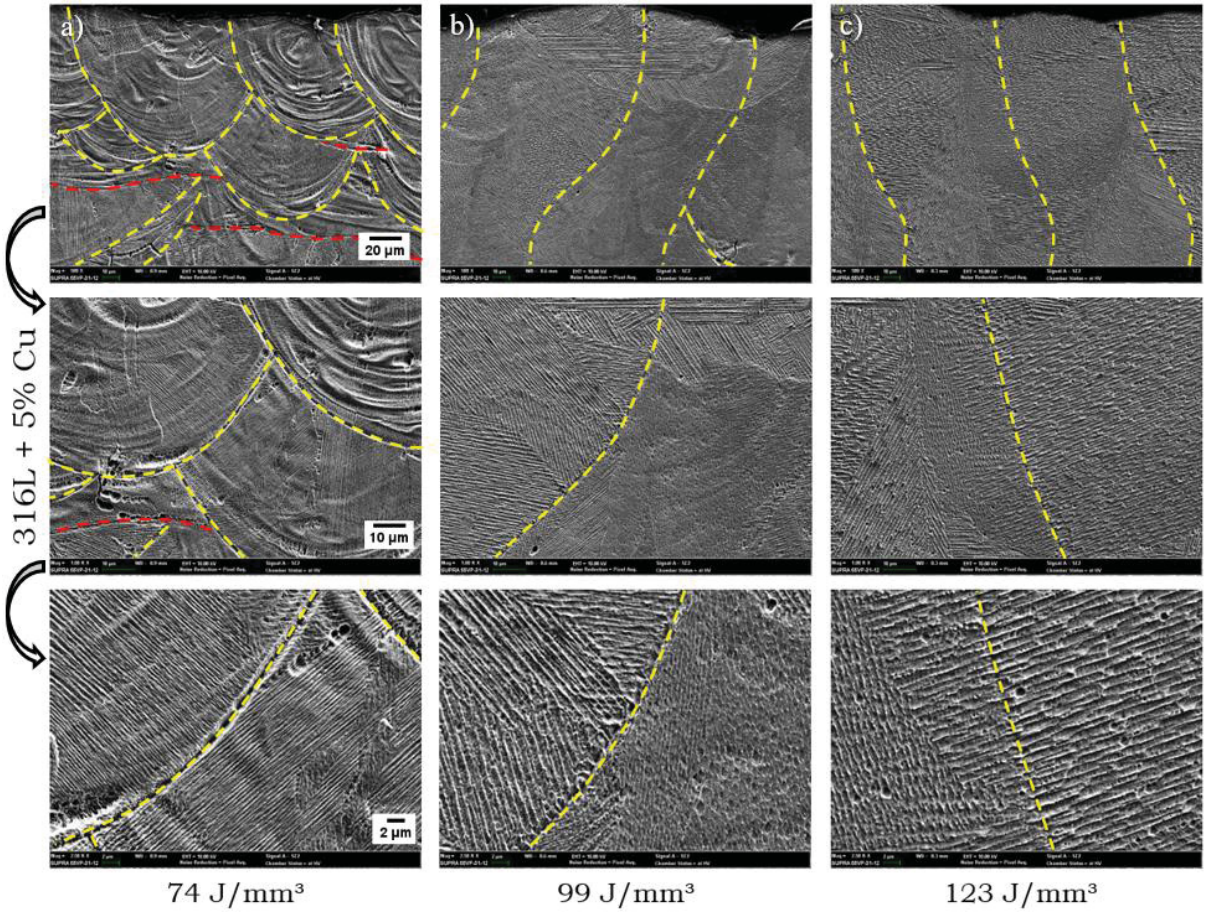

Source: Authors (2025).

Figure 78 presents the XRD patterns for 316L and 316L + 5 % Cu processed under different energy densities. The austenitic (111) and (200) peaks are identified in both materials. As summarized in Table 32, energy density had no significant effect on the peak angles. However, the addition of Cu caused a peak shift to the left, resulting in an increase in lattice parameter.

Figure 78 - XRD patterns for 316L and 316L + 5 % Cu processed with different energy densities

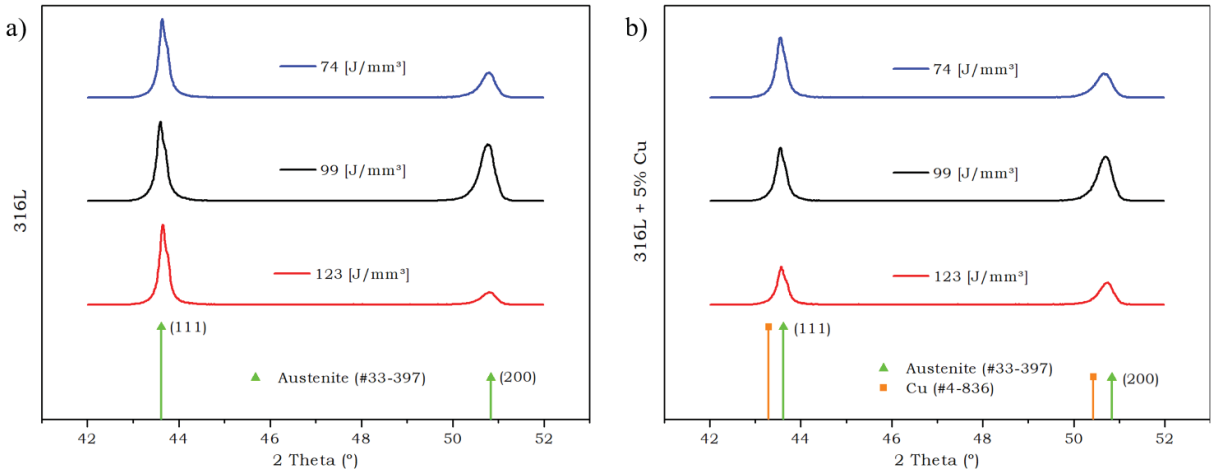

Source: Authors (2025).

Table 32 - Peak angle and lattice parameter for (111) and (200) crystallographic planes

Material	Energy density level (J/mm³)	(111)		(200)	
		2 Theta (°)	Lattice parameter (Å)	2 Theta (°)	Lattice parameter (Å)
316L	74	43.66	2.072	50.79	1.796
	99	43.62	2.074	50.77	1.797
	123	43.67	2.071	50.81	1.796
316L + 5% Cu	74	43.56	2.076	50.67	1.800
	99	43.56	2.076	50.69	1.800
	123	43.58	2.075	50.72	1.798
Austenite (33-397)	-	43.62	2.073	50.84	1.795
Cu (4-836)	-	43.29	2.088	50.43	1.808

Source: Authors (2025).

Figure 79 shows the crystallographic orientation and grain size distribution of 316L and 316L + 5 % Cu in the as built condition, processed under an energy density of 123 J/mm³. Overall, the grain growth appears to be aligned with the build direction. The inverted pole figures indicate the presence of similar texture in both materials. However, the addition of Cu to the stainless steel resulted in a decrease in mean grain size, from 51.8 to 44.2 µm, which can be attributed to a faster cooling rate due to the higher thermal conductivity of Cu.

Figure 79 - Crystallographic orientation and grain size distribution in the as built condition

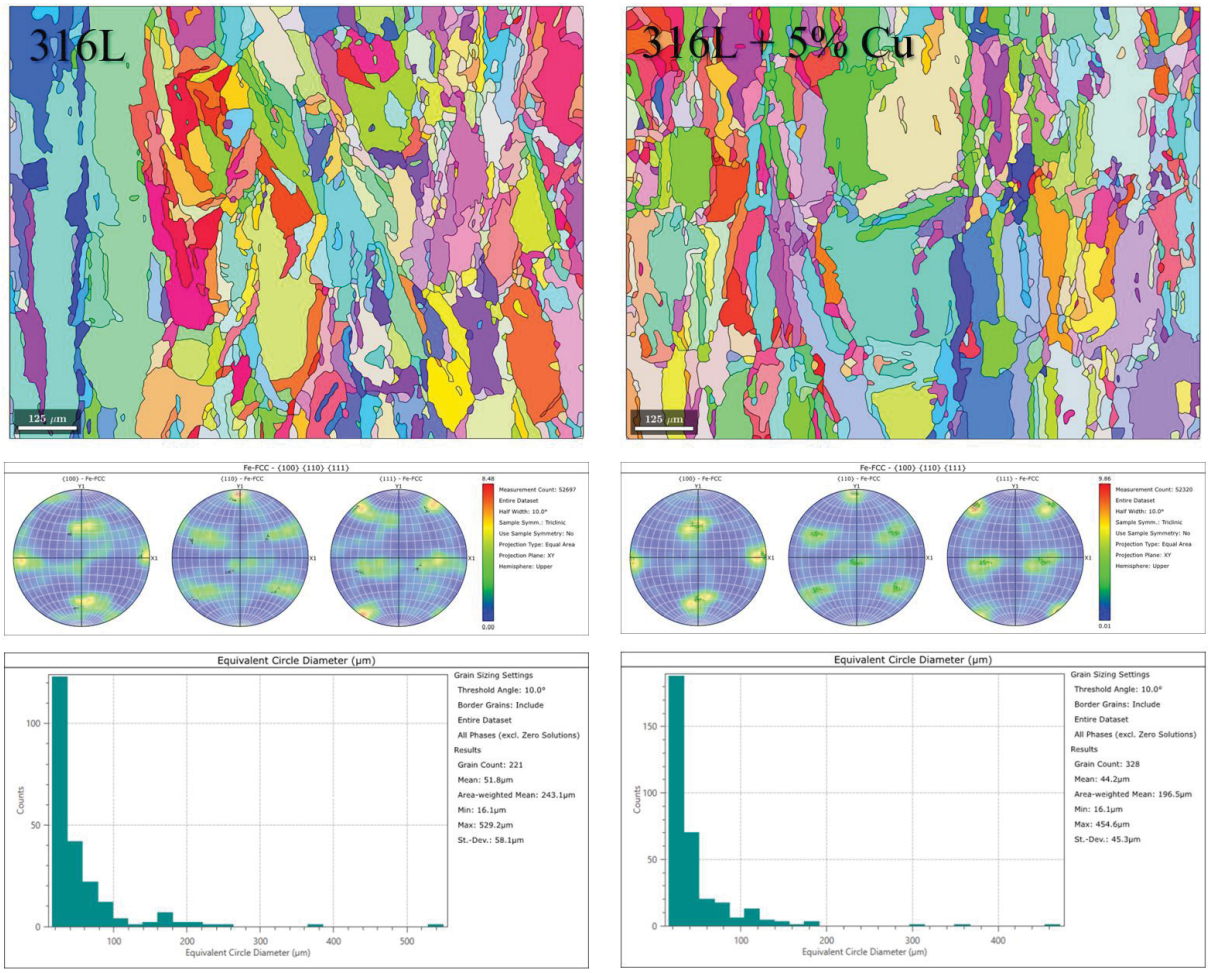

Source: Authors (2025).

Influence of Cu addition and energy density on mechanical properties

Figure 80 summarizes the mechanical testing results for 316L and 316L + 5 % Cu processed under different energy densities. Figure 80a presents the stress-strain curves, showing that the addition of Cu leads to a notable reduction in fracture strain. This decrease in strain for Cu-containing specimens is further evidenced by the necking region in the tensile specimens after fracture. As shown in Figure 81, the necking effect, originated by plastic deformation, is more pronounced in the 316L specimens compared to those with 5 % Cu addition. As shown in Figure 76, the microstructure becomes coarser at higher energy densities, resulting in a decrease in yield strength, UTS and strain at UTS for 316L with increasing energy density. This effect is less pronounced in samples containing Cu, likely due to the incomplete

homogenization of Cu in specimens processed at 74 J/mm³ (Figure 77). Overall, the addition of Cu diminished the mechanical properties of the 316L.

Figure 80 - Mechanical testing: (a) Stress-strain curves, (b) Yield strength versus energy density, (c) UTS versus energy density, and (d) Strain at UTS versus energy density

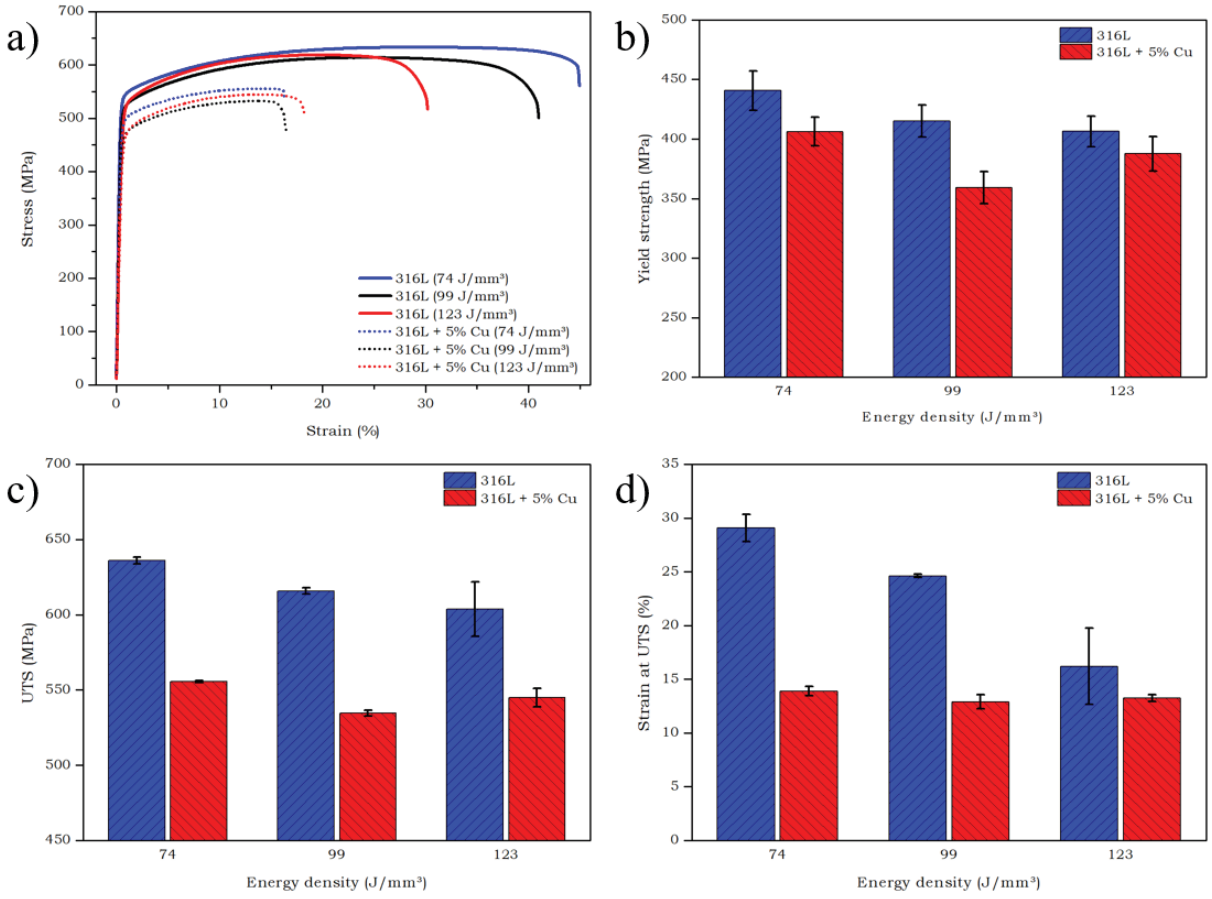

Source: Authors (2025).

Figure 82 presents the micrographs of the specimen fracture surface. For 316L specimens, the presence of dimples on the fracture surface indicates a predominantly ductile fracture mode, which indicates that the material undergoes significant elongation before failure. The specimens containing Cu showed a mix-mode fracture, with a fracture surface exhibiting a combination of ductile and brittle characteristics. The dimples regions indicate a ductile regimen, while the flatter, faceted areas indicate a brittle fracture. This mixed-mode fracture led to the overall reduction on the mechanical properties described earlier.

Figure 81 - Macrographs of tensile specimens after testing

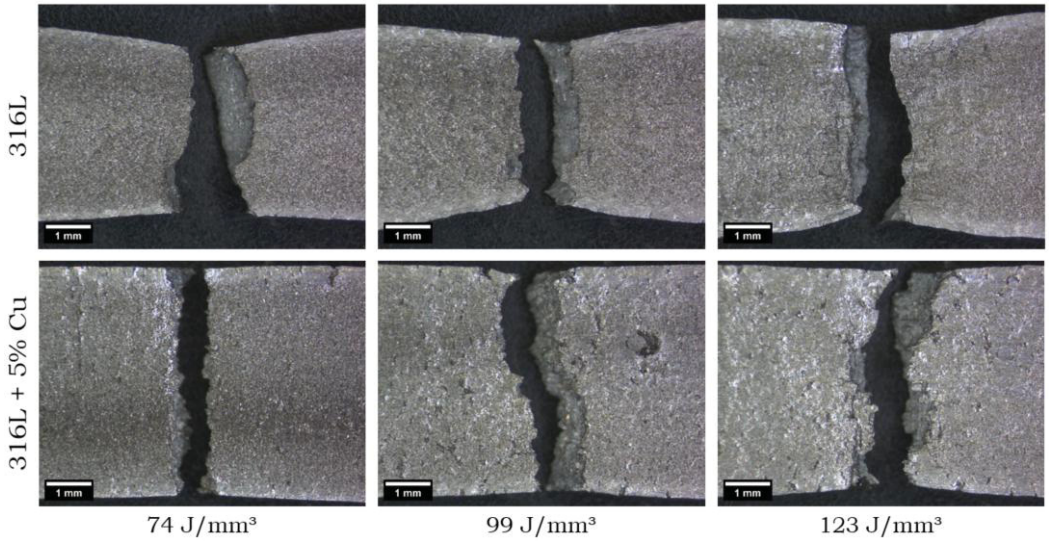

Source: Authors (2025).

Figure 82 - SEM micrographs of tensile specimen fracture surface

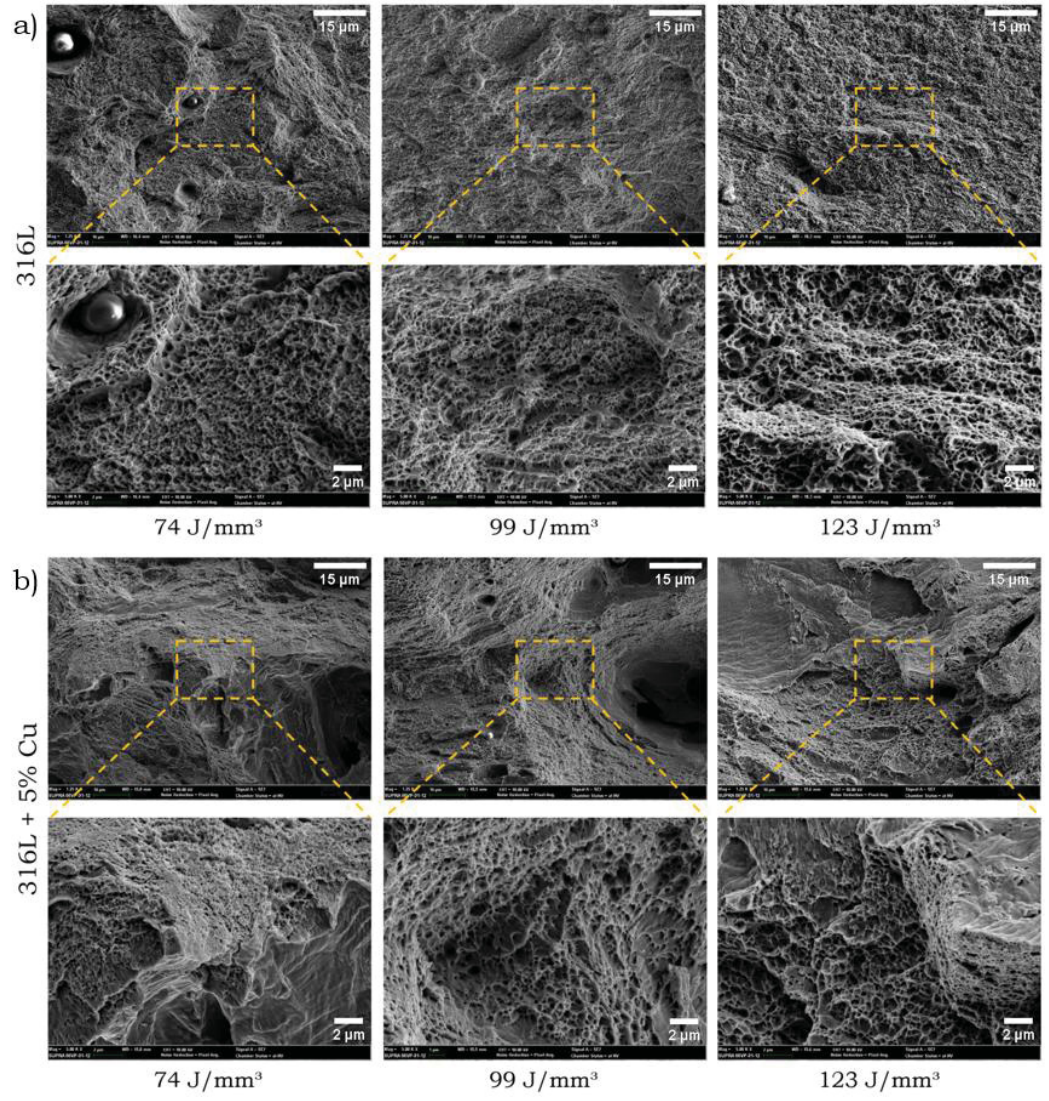

Source: Authors (2025).

CONCLUSIONS

In this study, in-situ alloying of a powder mixture of 316L stainless steel and Cu was achieved via additive manufacturing. The optimization of the Laser Powder Bed Fusion (L-PBF) processing parameters, using a full factorial design of experiments, enabled improvements in part density, microstructural integrity and mechanical properties. The main conclusions are as follows:

- The powder mixture of 316L with 5 wt% Cu exhibited suitable characteristics for L-PBF processing, including flowability, particle size distribution, morphology, and homogeneity. The results confirmed the feasibility of in-situ synthesis, showing that L-PBF can be employed to produce solid parts with tailored chemical composition.
- The effects of laser power, scan speed and hatch distance on the Archimedes density and hardness were systematically assessed using a full factorial design of experiments. Optimum processing parameters were identified for both 316L and the powder mixture with Cu, achieving a maximum cross-sectional density of 99.99% for 316L and 99.96% for 316L + 5 wt% Cu.
- The relationship between chemical composition, energy density levels, melt pool dimensions, microstructure, and mechanical properties was established. Cu addition resulted in decreased hardness and tensile strength. In addition, lower energy levels led to reduced melt pool dimensions, refined grain sizes, and optimized mechanical properties, including higher yield strength, ultimate tensile strength, and strain at UTS.

ACKNOWLEDGMENTS

This study was financed in part by the *Coordenação de Aperfeiçoamento de Pessoal de Nível Superior* (CAPES) - Finance Code 001. The authors acknowledge CAPES, the Advanced Material Processing Laboratory (AMPLab) of the University of Birmingham, and the Laboratory of Advanced Materials and Surface Engineering (LAMSE) of UFPR.

REFERENCES

ABU-LEBDEH, T. M.; DAMPTEY, R.; UNGUREANU, L. M.; PETRESCU, F. I. T. A Ternary Model for Particle Packing Optimization. **Journal of Composites Science**, v. 6, n. 4, p. 113, Apr. 2022. DOI. 10.3390/jcs6040113.

AVRAMPOS, P.; VOSNIAKOS, G. C. A review of powder deposition in additive manufacturing by powder bed fusion. **Journal of Manufacturing Processes**, v. 74, p. 332-352, Feb. 2022. DOI. 10.1016/j.jmapro.2021.12.021.

BEHJAT, A.; SHAMANIAN, M.; IULIANO, L.; SABOORI, A. Laser powder bed fusion in situ alloying of AISI 316L-2.5%Cu alloy: microstructure and mechanical properties evolution. **Progress In Additive Manufacturing**, Jan. 2024. DOI. 10.1007/s40964-023-00557-x.

BEHJAT, A.; SHAMANIAN, M.; SADEGHI, F.; IULIANO, L.; SABOORI, A. Additive manufacturing of a novel in-situ alloyed AISI316L-Cu stainless steel: microstructure and antibacterial properties. **Materials Letters**, v. 355, p. 135363, Jan. 2024. DOI. 10.1016/j.matlet.2023.135363.

CUI, C.; BECKER, L.; GÄRTNER, E.; BOES, J.; LENTZ, J.; UHLENWINKEL, V.; STEINBACHER, M.; WEBER, S.; FECHTE-HEINEN, R. Laser Additive Manufacturing of Duplex Stainless Steel via Powder Mixture. **Journal of Manufacturing and Materials Processing**, v. 6, n. 4, p. 72, Jul. 2022. DOI. 10.3390/jmmp6040072.

DONG, Y.; LI, Y.; EBEL, T.; YAN, M. Cost-affordable, high-performance Ti-TiB composite for selective laser melting additive manufacturing. **Journal of Materials Research**, v. 35, n. 15, p. 1922-1935, Jan. 2020. DOI. 10.1557/jmr.2019.389.

FOADIAN, F.; KREMER, R.; POST, M.; TABRIZI, A. T.; AGHAJANI, H. Investigation of In-Situ Low Copper Alloying of 316L Using the Powder Bed Fusion Process. **Solids**, v. 4, n. 3, p. 156-165, Jun. 2023. DOI. 10.3390/solids4030010.

HUANG, Y.; LEU, M. C.; MAZUMDER, J.; DONMEZ, A. Additive Manufacturing: current state, future potential, gaps and needs, and recommendations. **Journal of Manufacturing Science and Engineering**, v. 137, n. 1, Feb. 2015. DOI. 10.1115/1.4028725.

LI, N.; HUANG, S.; ZHANG, G.; QIN, R.; LIU, W.; XIONG, H.; SHI, G.; BLACKBURN, J. Progress in additive manufacturing on new materials: a review. **Journal of Materials Science & Technolo**gy, v. 35, n. 2, p. 242-269, Feb. 2019. DOI. 10.1016/j.jmst.2018.09.002.

MIRZABABAEI, S.; DODDAPANENI, V.; LEE, K.; PAUL, G.E.; PIRGAZI, H.; TAN, K.; ERTORER, O.; CHANG, C.; PAUL, B.K.; PASEBANI, S. Remarkable enhancement in thermal conductivity of stainless-steel leveraging metal composite via laser powder bed fusion: 316l-Cu composite. **Additive Manufacturing**, v. 70, p. 103576, May 2023. DOI. 10.1016/j.addma.2023.103576.

RANKOUHI, B.; JAHANI, S.; PFEFFERKORN, F.E.; THOMA, D.J. Compositional grading of a 316L-Cu multi-material part using machine learning for the determination of selective laser melting process parameters. **Additive Manufacturing**, v. 38, p. 101836, Feb. 2021. DOI. 10.1016/j.addma.2021.101836.

WANG, Q.; REN, L.; LI, X.; ZHANG, S.; SERCOMBE, T. B.; YANG, K. Antimicrobial Cu-bearing stainless steel scaffolds. **Materials Science and Engineering**: C, v. 68, p. 519-522, Nov. 2016. DOI. 10.1016/j.msec.2016.06.038.

5 CONCLUSIONS

In this research, the additive manufacturing of 316L stainless steel modified with Cu additions was investigated. Under the tested conditions, it is possible to conclude that:

- The methodology for preparing powder mixture and nanocomposite powder of gas atomized stainless steel with Cu microparticles, Cu nanoparticles and CuO nanoparticles proved effective. The homogeneous distribution between host powder and guest particles enabled the successful use of PTA-DED as a technique to in-situ alloying, producing dense parts from these customized powders. However, the strong influence of nanoparticles on the flow time and processability indicates that specific procedures are necessary for the mixing, handling, and processing of nanoparticle-containing powders.
- The deposition of single-track coatings enabled a systematic understanding of PTA-DED processing parameters for 316L, demonstrating the relationship between deposition current and deposition speed on both hardness and geometric characteristics. This process window mapping provides a foundation for selecting optimal parameters to achieve sound single-track coating with controlled geometry, an important step toward using PTA-DED as a viable additive manufacturing technique. Additionally, the hardness of the 316L coatings remained consistent across the entire tested parameters range, highlighting the stability of the mechanical properties achieved.
- The processing of 316L stainless steel with the incorporation of Cu MP, Cu NP and CuO NP via PTA-DED contributes to the understanding of how the feedstock influences the processability and metallurgical characteristics of the coatings. It was revealed that the addition of Cu MP and Cu NP affected dilution and wettability, requiring higher deposition current to prevent lack of fusion.
- During interaction with the plasma arc, CuO NP is decomposed, releasing oxygen, which changes the dynamics of the molten pool, increasing dilution despite the low wettability. The introduction of Cu NP and CuO NP led to a loss of Cu during handling and processing, as the interaction between plasma arc and the powder feedstock caused the partial vaporization of the nanoparticles, altering the final chemical composition of the coating.

- PTA-DED has proven to be a competitive AM technique compared to laser-based DED methods, achieving high powder catchment efficiency while producing dense, defect-free single-walls. The single-walls microstructure is characterized by columnar dendrites oriented in the build direction, which transition to equiaxed dendrites near the top of the melt pool. Notably, higher Cu content and the presence of NP contribute to dendrite refinement.
- Preliminary antimicrobial assessment of single-walls deposited by PTA-DED in the as-deposited condition indicates that the addition of Cu to the stainless steel tends to reduce the number of *E. coli* colonies after a 24 hour incubation period, although it does not significantly affect *S. aureus*. Solubilization followed by ageing heat treatment of the Cu-containing stainless steel specimens leads to the formation of Cu-rich precipitates, as evidenced by an increase in hardness. compositions with higher Cu content exhibit a more pronounced increase in hardness. Thus, this higher Cu content, combined with heat treatment, is expected to enhance the antimicrobial activity observed, though results for the heat treated specimens are still pending.
- Regarding the wear performance, the addition of 5 wt% Cu MP was found to significantly reduce the coefficient of friction and wear rate, attributed to the formation of compact tribolayers on the worn surfaces, while other compositions did not influence wear performance despite variations in hardness due to heat treatment. The observed wear mechanisms included abrasive, adhesive, and oxidative modes, with the generated tribolayers acting as solid lubricants, mitigating material loss. This demonstrates the potential for improved wear resistance in Cu-modified 316L stainless steel in sliding applications.
- The corrosion behavior of PTA-DED single-walls was evaluated in comparison to high-velocity oxy-fuel (HVOF) and bulk materials. The 316L processed with PTA-DED showed a more noble behavior than 316L bulk and 316L processed by HVOF. The results also indicate that increasing Cu content correlates with a decrease in open circuit potential. However, all PTA-DED compositions exhibited corrosion behavior comparable or superior to that of 316L bulk, which can be related to a more refined microstructure.

- L-PBF has the capability to induce multiple remelting cycles during processing, which significantly influences the final properties of the manufactured parts. The productions of Cu-containing specimens via L-PBF allow the establishment of the relationship between processing parameters, microstructure and mechanical properties. The optimization process conducted individually for 316L and 316L with Cu led to optimized sets of parameters that enabled the fabrication of dense defect-free specimens. The addition of Cu was found to reduce both the specimen density and hardness of the stainless steel specimen, requiring higher energy density for effective processing.
- At low energy density, both 316L and 316L with Cu exhibited a more refined microstructure, which enhanced the mechanical properties of 316L. However, the same lower energy density led to incomplete homogenization of Cu within the stainless steel matrix, due to a shallower melt pool, which prevented the full remelting of the previous layer. The fracture surface analysis of 316L specimens revealed a predominantly ductile fracture mode, characterized by the presence of dimples that indicate significant elongation before failure. In contrast, the specimens containing Cu exhibited both ductile and brittle characteristics, contributing to the overall reduction in the mechanical properties observed in the Cu-containing specimens.

REFERENCES

Following the recommendations of "*Manual de normalização de documentos científicos de acordo com as normas da ABNT*" made available in 2024 by the "*Sistema de Bibliotecas da UFPR",* all documents cited on this work are listed below.

ABREU-CASTILLO, H.O.; BUENO, B.P.; D'OLIVEIRA, A.S.C.M. In situ processing aluminide coatings with and without tungsten carbide. **The International Journal of Advanced Manufacturing Technology**, v. 119, n. 1-2, p. 477-488, Nov. 2021. DOI. 10.1007/s00170-021-08032-z.

ABREU-CASTILLO, H.O.; D'OLIVEIRA, A.S.C.M. Challenges of nanoparticle-reinforced NiAl-based coatings processed by in situ synthesis of the aluminide. **The International Journal of Advanced Manufacturing Technology**, v. 134, n. 3-4, p. 1547-1561, Aug. 2024. DOI. 10.1007/s00170-024-14162-x.

ABU-LEBDEH, T. M.; DAMPTEY, R.; UNGUREANU, L. M.; PETRESCU, F. I. T. A Ternary Model for Particle Packing Optimization. **Journal of Composites Science**, v. 6, n. 4, p. 113, Apr. 2022. DOI. 10.3390/jcs6040113.

ALANEME, K. K.; HONG, S. M.; SEN, Indrani; FLEURY, E.; RAMAMURTY, U. Effect of copper addition on the fracture and fatigue crack growth behavior of solution heat-treated SUS 304H austenitic steel. **Materials Science and Engineering**: A, v. 527, n. 18-19, p. 4600-4604, Jul. 2010. DOI. 10.1016/j.msea.2010.04.018.

ALBERTI, E. A.; BUENO, B. M. P.; D'OLIVEIRA, A. S. C. M. Additive manufacturing using plasma transferred arc. **The International Journal of Advanced Manufacturing Technology**, v. 83, n. 9-12, p. 1861-1871, Aug. 2015. DOI. 10.1007/s00170-015-7697-7.

ALVI, S.; SAEIDI, K.; AKHTAR, F. High temperature tribology and wear of selective laser melted (SLM) 316L stainless steel. **Wear**, v. 448-449, p. 203228, May 2020. DOI. 10.1016/j.wear.2020.203228.

AMERICAN SOCIETY FOR TESTING AND MATERIALS. **ASTM A941-15**: Standard Terminology Relating to Steel, Stainless Steel, Related Alloys, and Ferroalloys. New York, 2015.

AMERICAN SOCIETY FOR TESTING AND MATERIALS. **ASTM B213-20**: Standard Test Methods for Flow Rate of Metal Powders Using the Hall Flowmeter Funnel. New York, 2020.

AMERICAN SOCIETY FOR TESTING AND MATERIALS. **ASTM B822-20**: Standard Test Method for Particle Size Distribution of Metal Powders and Related Compounds by Light Scattering. New York, 2020.

AMERICAN SOCIETY FOR TESTING AND MATERIALS. **ASTM E8/E8M**: Standard Test Methods for Tensile Testing of Metallic Materials. New York, 2022.

ARCHARD, J. F. Contact and Rubbing of Flat Surfaces. **Journal of Applied Physics,** v. 24, n. 8, p. 981-988, Aug. 1953. DOI. 10.1063/1.1721448.

ARMSTRONG, M.; MEHRABI, H.; NAVEED, N. An overview of modern metal additive manufacturing technology. **Journal of Manufacturing Processes**, v. 84, p. 1001-1029, Dec. 2022. DOI. 10.1016/j.jmapro.2022.10.060.

ASM INTERNATIONAL. **ASM Handbook**: Volume 3: Alloy Phase Diagrams. 1992.

ASTAFUROV, S.; ASTAFUROVA, E. Phase Composition of Austenitic Stainless Steels in Additive Manufacturing: a review. **Metals**, v. 11, n. 7, p. 1052, Jun. 2021. DOI. 10.3390/met11071052.

AVERSA, A.; PISCOPO, G.; SALMI, A.; LOMBARDI, M. Effect of Heat Treatments on Residual Stress and Properties of AISI 316L Steel Processed by Directed Energy Deposition. **Journal of Materials Engineering and Performance**, v. 29, n. 9, p. 6002-6013, Sep. 2020. DOI. 10.1007/s11665-020-05061-9.

AVRAMPOS, P.; VOSNIAKOS, G. C. A review of powder deposition in additive manufacturing by powder bed fusion. **Journal of Manufacturing Processes**, v. 74, p. 332-352, Feb. 2022. DOI. 10.1016/j.jmapro.2021.12.021.

BAHNINI, I.; RIVETTE, M.; RECHIA, A.; SIADAT, A.; ELMESBAHI, A. Additive manufacturing technology: the status, applications, and prospects. **The International Journal of Advanced Manufacturing Technology**, v. 97, n. 1-4, p. 147-161, Mar. 2018. DOI. 10.1007/s00170-018-1932-y.

BALASUBRAMANIAM, B.; PRATEEK; RANJAN, S.; SARAF, M.; KAR, P.; SINGH, S. P.; THAKUR, V. K.; SINGH, A.; GUPTA, R. K. Antibacterial and Antiviral Functional Materials: chemistry and biological activity toward tackling covid-19-like pandemics. **ACS Pharmacology & Translational Science**, v. 4, n. 1, p. 8-54, Dec. 2020. DOI. 10.1021/acsptsci.0c00174.

BEHJAT, A.; SHAMANIAN, M.; IULIANO, L.; SABOORI, A. Laser powder bed fusion in situ alloying of AISI 316L-2.5%Cu alloy: microstructure and mechanical properties evolution. **Progress In Additive Manufacturing**, Jan. 2024. DOI. 10.1007/s40964-023-00557-x.

BEHJAT, A.; SHAMANIAN, M.; SADEGHI, F.; IULIANO, L.; SABOORI, A. Additive manufacturing of a novel in-situ alloyed AISI316L-Cu stainless steel: microstructure and antibacterial properties. **Materials Letters**, v. 355, p. 135363, Jan. 2024. DOI. 10.1016/j.matlet.2023.135363.

BENAKIS, M.; COSTANZO, D.; PATRAN, A. Current mode effects on weld bead geometry and heat affected zone in pulsed wire arc additive manufacturing of Ti-6-4 and Inconel 718. **Journal of Manufacturing Processes**, v. 60, p. 61-74, Dec. 2020. DOI. 10.1016/j.jmapro.2020.10.018.

BERNAUER, C.; SIGL, M. E.; GRABMANN, S.; MERK, T.; ZAPATA, A.; ZAEH, M. F. Effects of the thermal history on the microstructural and the mechanical properties of stainless steel 316L parts produced by wire-based laser metal deposition. **Materials Science and Engineering**: A, v. 889, p. 145862, Jan. 2024. DOI. 10.1016/j.msea.2023.145862.

BHARATH, R. R.; RAMANATHAN, R.; SUNDARARAJAN, B.; SRINIVASAN, P. B. Optimization of process parameters for deposition of Stellite on X45CrSi93 steel by plasma transferred arc technique. **Materials & Design**, v. 29, n. 9, p. 1725-1731, Out. 2008. DOI. 10.1016/j.matdes.2008.03.020.

BOND, D.; D'OLIVEIRA, A. S. C. M. Effect of current and atomized grain size distribution on the solidification of Plasma Transferred Arc coatings. **Materials Research**, v. 15, n. 5, p. 770-774, Aug. 2012. DOI. 10.1590/s1516-14392012005000101.

BRANDT, M. **Laser Additive Manufacturing**: Materials, Design, Technologies, and Applications. Elsevier, 2017.

CARDOZO, E. P.; RÍOS, S.; GANGULY, S.; D'OLIVEIRA, A. S. C. M. Assessment of the effect of different forms of Inconel 625 alloy feedstock in Plasma Transferred Arc (PTA) additive manufacturing. **The International Journal of Advanced Manufacturing Technology**, v. 98, n. 5-8, p. 1695-1705, Jun. 2018. DOI. 10.1007/s00170-018-2340-z.

CHAI, H.; GUO, L.; WANG, X.; FU, Y.; GUAN, J.; TAN, L.; REN, L.; YANG, K. Antibacterial effect of 317L stainless steel contained copper in prevention of implant-related infection in vitro and in vivo. **Journal of Materials Science: Materials in Medicin**e, v. 22, n. 11, p. 2525-2535, Aug. 2011. DOI. 10.1007/s10856-011-4427-z.

CHEN, G.; SUN, Y.; WANG, C. DING, J.; SUDER, W.; LI, Z.; WILLIAMS, S. Characterising and modelling plasma transferred arc for additive manufacturing. **International Journal of Heat and Mass Transfer,** v. 241, p. 126735, May 2025. DOI. 10.1016/j.ijheatmasstransfer.2025.126735.

CHEN, K. K.; CHAO, C. Y.; CHEN, J. H.; WU, J. H.; CHANG, Y. H.; DU, J. K. Effect of Low Copper Addition to As-Forged 304 Stainless Steel for Dental Applications. **Metals**, v. 11, n. 1, p. 43, Dec. 2020. DOI. 10.3390/met11010043.

CHEN, X.; WANG, C.; DING, J.; BRIDGEMAN, P.; WILLIAMS, S. A three-dimensional wire-feeding model for heat and metal transfer, fluid flow, and bead shape in wire plasma arc additive manufacturing. **Journal of Manufacturing Processes**, v. 83, p. 300-312, Nov. 2022. DOI. 10.1016/j.jmapro.2022.09.012.

CHI, C. Y.; YU, H. Y.; DONG, J. X.; LIU, W. Q.; CHENG, S. C.; LIU, Z. D.; XIE, X. S. The precipitation strengthening behavior of Cu-rich phase in Nb contained advanced Fe-Cr-Ni type austenitic heat resistant steel for USC power plant application. **Progress in Natural Science**: Materials International, v. 22, n. 3, p. 175-185, Jun. 2012. DOI. 10.1016/j.pnsc.2012.05.002.

CHI, X.; YUAN, J.; LI, J.; PAN, G.; CUI, Y.; LI, X. Effect of Cu on the high-temperature wear behavior of FeAl-TiB2 coatings produced by extreme high-speed laser cladding. **Applied Surface Science Advances**, v. 17, p. 100439, Oct. 2023. DOI. 10.1016/j.apsadv.2023.100439.

CHOO, H.; SHAM, K. L.; BOHLING, J.; NGO, A.; XIAO, X.; REN, Y.; DEPOND, P. J.; MATTHEWS, M. J.; GARLEA, E. Effect of laser power on defect, texture, and microstructure of a laser powder bed fusion processed 316L stainless steel. **Materials & Design**, v. 164, p. 107534, Feb. 2019. DOI. 10.1016/j.matdes.2018.12.006.

CHU, F.; ZHANG, K.; SHEN, H.; LIU, M.; HUANG, W.; ZHANG, X.; LIANG, E.; ZHOU, Z.; LEI, L.; HOU, J. Influence of satellite and agglomeration of powder on the processability of AlSi10Mg powder in Laser Powder Bed Fusion. **Journal of Materials Research and Technology**, v. 11, p. 2059-2073, Mar. 2021. DOI. 10.1016/j.jmrt.2021.02.015.

COLIN, M.; CHARPENTIER, E.; KLINGELSCHMITT, F.; BONTEMPS, C.; CHAMPS, C.; REFFUVEILLE, F.; GANGLOFF, S. C. Specific antibacterial activity of copper alloy touch surfaces in five long-term care facilities for older adults. **Journal of Hospital Infection**, v. 104, n. 3, p. 283-292, Mar. 2020. DOI. 10.1016/j.jhin.2019.11.021.

COOPER, A. J.; COOPER, N. I.; DHERS, J.; SHERRY, A. H. Effect of Oxygen Content Upon the Microstructural and Mechanical Properties of Type 316L Austenitic Stainless Steel Manufactured by Hot Isostatic Pressing. **Metallurgical and Materials Transactions A**, v. 47, n. 9, p. 4467-4475, Jun. 2016. DOI. 10.1007/s11661-016-3612-6.

CUI, C.; BECKER, L.; GÄRTNER, E.; BOES, J.; LENTZ, J.; UHLENWINKEL, V.; STEINBACHER, M.; WEBER, S.; FECHTE-HEINEN, R. Laser Additive Manufacturing of Duplex Stainless Steel via Powder Mixture. **Journal of Manufacturing and Materials Processing**, v. 6, n. 4, p. 72, Jul. 2022. DOI. 10.3390/jmmp6040072.

D'ANDREA, D. Additive Manufacturing of AISI 316L Stainless Steel: a review. **Metals**, v. 13, n. 8, p. 1370, Jul. 2023. DOI. 10.3390/met13081370.

DÁVILA, J.L.; INFORÇATTI, P.; NORITOMI, P.Y.; COELHO, R.T.; SILVA, J.V.L. Hybrid manufacturing: a review of the synergy between directed energy deposition and subtractive processes. **The International Journal of Advanced Manufacturing Technology**, v. 110, n. 11-12, p. 3377-3390, Sep. 2020. DOI. 10.1007/s00170-020-06062-7.

DAVIS, J.R. **ASM Specialty Handbook**: Stainless Steels. ASM International, 1999.

DEBROY, T.; WEI, H.L.; ZUBACK, J.S.; MUKHERJEE, T.; ELMER, J.W.; MILEWSKI, J.O.; BEESE, A.M.; WILSON-HEID, A.; DE, A.; ZHANG, W. Additive manufacturing of metallic components - Process, structure and properties. **Progress**

in Materials Science, v. 92, p. 112-224, Mar. 2018. DOI. 10.1016/j.pmatsci.2017.10.001.

DONG, Y.; LI, Y.; EBEL, T.; YAN, M. Cost-affordable, high-performance Ti-TiB composite for selective laser melting additive manufacturing. **Journal of Materials Research**, v. 35, n. 15, p. 1922-1935, Jan. 2020. DOI. 10.1557/jmr.2019.389.

DU, X.; XI, T.; YANG, C.; ZHAO, H.; YANG, K. Cu addition retards the static recrystallization of cold-deformed 316L biomedical stainless steel. **Journal of Materials Research and Technology**, v. 19, p. 1673-1677, Jul. 2022. DOI. 10.1016/j.jmrt.2022.05.155.

DURMOO, S.; RICHARD, C.; BERANGER, G.; MOUTIA, Y. Biocorrosion of stainless steel grade 304L (SS304L) in sugar cane juice. **Electrochimica Acta**, v. 54, n. 1, p. 74-79, Dec. 2008. DOI. 10.1016/j.electacta.2008.06.028.

FOADIAN, F.; KREMER, R.; POST, M.; TABRIZI, A. T.; AGHAJANI, H. Investigation of In-Situ Low Copper Alloying of 316L Using the Powder Bed Fusion Process. **Solids**, v. 4, n. 3, p. 156-165, Jun. 2023. DOI. 10.3390/solids4030010.

FOLKHARD, Erich. **Welding Metallurgy of Stainless Steels**. Kapfenberg: Springer Vienna, 1988.

GARG, R.; DHAMI, H. S.; PANDA, P. R.; VISWANATHAN, K. Evaluating gas-driven flow mechanics of non-spherical powders for directed energy deposition. **Journal of Manufacturing Processes**, v. 99, p. 260-271, Aug. 2023. DOI. 10.1016/j.jmapro.2023.04.057.

GILCRIST, K. E.; PRESTON, S. D. The Thermal Diffusivity/Conductivity of 316 Stainless Steel Powders in Air and Nitric Acid Mixtures at Room Temperature. **Thermal Conductivity**, v. 18, p. 713-722, 1985. DOI. 10.1007/978-1-4684-4916-7_67.

GOMES, R.; HENKE, S.; D'OLIVEIRA, A. S. C. M. Microstructural control of Co-based PTA coatings. **Materials Research**, v. 15, n. 5, p. 796-800, Aug. 2012. DOI. 10.1590/s1516-14392012005000099.

GRASS, G.; RENSING, C.; SOLIOZ, M. Metallic Copper as an Antimicrobial Surface. **Applied and Environmental Microbiology**, v. 77, n. 5, p. 1541-1547, Mar. 2011. DOI. 10.1128/aem.02766-10.

GUTJAHR, J. **Método de Reutilização de Pó de Aço Inoxidável 316L Processado por Deposição por Energia Direcionada a Laser**. 2022. 256 f. Thesis (PhD) - Mechanical Engineering Department, Universidade Federal de Santa Catarina, Florianópolis, 2022.

HAFERKAMP, L. **Effect of the Particle Size Distribution and Morphology on Powder Processability in Laser Powder Bed Fusion**. 2022. 130 f. Thesis (PhD) - ETH Zurich, Zurich, 2022.

HAN, Y.; ZHANG, C.; CUI, X.; ZHANG, S.; CHEN, J.; DONG, S.; ABDULLAH, A.O. Microstructure and properties of a novel wear- and corrosion-resistant stainless steel fabricated by laser melting deposition. **Journal of Materials Research**, v. 35, n. 15, p. 2006-2015, Apr. 2020. DOI. 10.1557/jmr.2020.70.

HASAN, S. S.; KOW, C. S.; ZAIDI, S. T. R. Social distancing and the use of PPE by community pharmacy personnel: does evidence support these measures?. **Research in Social and Administrative Pharmacy**, v. 17, n. 2, p. 456-459, Feb. 2021. DOI. 10.1016/j.sapharm.2020.04.033.

HAUSER, M.; NITZSCHE, P.; WEIDNER, A.; HENKEL, S.; BIERMANN, H.; VOLKOVA, O.; WENDLER, M. Effect of Cu addition on solidification, precipitation behavior and mechanical properties in austenitic CrNi-N stainless steel. **Materials Science and Engineering**: A, v. 862, p. 144422, Jan. 2023. DOI. 10.1016/j.msea.2022.144422.

HO, C. Y.; POWELL, R. W.; LILEY, P. E. Thermal Conductivity of the Elements. **Journal of Physical and Chemical Reference Data**, v. 1, n. 2, p. 279-421, Apr. 1972. DOI. 10.1063/1.3253100.

HUANG, A.; WANG, K.; ZHAO, Y.; WANG, W.; WEI, X.; PENG, J. Effect of Copper Addition on the Formability of 304L Austenitic Stainless Steel. **Journal of Materials Engineering and Performance**, v. 32, n. 8, p. 3563-3570, Sep. 2022. DOI. 10.1007/s11665-022-07367-2.

HUANG, Y.; LEU, M. C.; MAZUMDER, J.; DONMEZ, A. Additive Manufacturing: current state, future potential, gaps and needs, and recommendations. **Journal of Manufacturing Science and Engineering**, v. 137, n. 1, Feb. 2015. DOI. 10.1115/1.4028725.

HUNG, T.; CHEN, T.; CHEN, H.; TSAY, L. The effects of Cr and Ni equivalents on the microstructure and corrosion resistance of austenitic stainless steels fabricated by laser powder bed fusion. **Journal of Manufacturing Processes**, v. 90, p. 69-79, Mar. 2023. DOI. 10.1016/j.jmapro.2023.01.081.

JAVIDI, M.J.; HOSSEINI, S.M.; KHODABAKHSHI, F.; MOHAMMADI, M.; OROVCIK, L.; TREMBOŁOVÁ, V.N.; NAGY, Š.; NOSKO, M. Laser powder bed fusion of 316L stainless steel/Al2O3 nanocomposites: taguchi analysis and material characterization. **Optics & Laser Technology**, v. 158, p. 108883, Feb. 2023. DOI. 10.1016/j.optlastec.2022.108883.

JENA, P.; CASTLEMAN, A.W. Introduction to Atomic Clusters. **Science and Technology of Atomic, Molecular, Condensed Matter & Biological Systems**, p. 1-36, 2010. http://dx.doi.org/10.1016/b978-0-444-53440-8.00001-x.

JIA, R.; UNSAL, T.; XU, D.; LEKBACH, Y.; GU, T. Microbiologically influenced corrosion and current mitigation strategies: a state of the art review**. International Biodeterioration & Biodegradation**, v. 137, p. 42-58, Feb. 2019. DOI. 10.1016/j.ibiod.2018.11.007.

JHAVAR, S.; PAUL, C.P.; JAIN, N.K. Micro-Plasma Transferred Arc Additive Manufacturing for Die and Mold Surface Remanufacturing. **Journal of the Minerals, Metals & Material Society**, v. 68, n. 7, p. 1801-1809, May. 2016. DOI. 10.1007/s11837-016-1932-z.

KAMATH, C.; EL-DASHER, B.; GALLEGOS, G. F.; KING, W. E.; SISTO, A. Density of additively-manufactured, 316L SS parts using laser powder-bed fusion at powers up to 400 W. **The International Journal of Advanced Manufacturing Technology**, v. 74, n. 1-4, p. 65-78, May 2014. DOI. 10.1007/s00170-014-5954-9.

KAMPF, G.; TODT, D.; PFAENDER, S.; STEINMANN, E. Persistence of coronaviruses on inanimate surfaces and their inactivation with biocidal agents. **Journal of Hospital Infection**, v. 104, n. 3, p. 246-251, Mar. 2020. DOI. 10.1016/j.jhin.2020.01.022.

KARAPUZHA, A. S.; FRASER, D.; ZHU, Y.; WU, X.; HUANG, A. Effect of solution heat treatment and hot isostatic pressing on the microstructure and mechanical properties of Hastelloy X manufactured by electron beam powder bed fusion. **Journal of Materials Science & Technology**, v. 98, p. 99-117, Jan. 2022. DOI. 10.1016/j.jmst.2021.04.059.

KASNOWSKI, M. C.; MANTILLA, S. P. S.; OLIVEIRA, L. A. T. Formação de biofilme na indústria de alimentos e métodos de validação de superfícies. **Revista Científica Eletrônica de Medicina Veterinária**, v. 15, p. 1-23. 2010.

KASSYM, K.; PERVEEN, A. Atomization processes of metal powders for 3D printing. **Materials Today**: Proceedings, v. 26, p. 1727-1733, 2020. DOI. 10.1016/j.matpr.2020.02.364.

KAYALI, Y.; TALAŞ, Ş. Investigation of Wear and Corrosion Behaviour of AISI 316 L Stainless Steel Coated By ESD Surface Modification. **Protection of Metals and Physical Chemistry of Surfaces**, v. 55, n. 6, p. 1148-1153, Nov. 2019. DOI. 10.1134/s2070205119060170.

KLADOVASILAKIS, N.; CHARALAMPOUS, P.; KOSTAVELIS, I.; TZETZIS, D.; TZOVARAS, D. Impact of metal additive manufacturing parameters on the powder bed fusion and direct energy deposition processes: a comprehensive review. **Progress in Additive Manufacturing**, v. 6, n. 3, p. 349-365, Apr. 2021. DOI. 10.1007/s40964-021-00180-8.

KOTECKI, D.J.; SIEWERT, T.A. WRC-1992 Constitution Diagram for Stainless Steel Weld Metals: A Modification of the WRC-1988 Diagram. **Welding Journal**, v. 71, n. 5, 1992.

KOTI, D.; POWELL, J.; NAESSTROEM, H.; VOISEY, K. T. Powder catchment efficiency in laser cladding (directed energy deposition). An investigation into standard laser cladding and the ABA cladding technique. **Journal of Laser Applications**, v. 35, n. 1, Feb. 2023. DOI. 10.2351/7.0000904.

KOU, S. **Welding metallurgy**. Hoboken: John Wiley & Sons, 2002.

KUMAR, P.; SAWANT, M. S.; JAIN, N. K. Optimization of process parameters in micro-plasma transferred arc deposition process for cobalt-based alloy. **Materials Today**: Proceedings, v. 44, p. 1681-1686, 2021. DOI. 10.1016/j.matpr.2020.11.840.

KUMAR, R.; ARYA, H. K. Experimental Determination of Cooling Rate and its Effect on Microhardness in Submerged Arc Welding of Mild Steel Plate (Grade c-25 as per IS 1570). **Journal of Material Science & Engineering**, v. 03, n. 02, 2013. DOI. 10.4172/2169-0022.1000138.

KUMAR, P.; JAIN, N.K. Surface roughness prediction in micro-plasma transferred arc metal additive manufacturing process using K-nearest neighbors algorithm. **The International Journal of Advanced Manufacturing Technology**, v. 119, n. 5-6, p. 2985-2997, Jan. 2022. DOI. 10.1007/s00170-021-08639-2.

LASHGARI, H. R.; LI, S.; KONG, C.; ASNAVANDI, M.; ZANGENEH, S. Rotary friction welding of additively manufactured 17-4PH stainless steel. Journal of **Manufacturing Processes**, v. 64, p. 1517-1528, Apr. 2021. DOI. 10.1016/j.jmapro.2021.03.008.

LI, H.; RAMEZANI, M.; LI, M.; MA, C.; WANG, J. Tribological performance of selective laser melted 316L stainless steel. **Tribology International**, v. 128, p. 121-129, Dec. 2018. DOI. 10.1016/j.triboint.2018.07.021.

LI, N.; HUANG, S.; ZHANG, G.; QIN, R.; LIU, W.; XIONG, H.; SHI, G.; BLACKBURN, J. Progress in additive manufacturing on new materials: a review. **Journal of Materials Science & Technolo**gy, v. 35, n. 2, p. 242-269, Feb. 2019. DOI. 10.1016/j.jmst.2018.09.002.

LI, R.; JIN, M.; PAQUIT, V. C. Geometrical defect detection for additive manufacturing with machine learning models. **Materials & Design**, v. 206, p. 109726, Aug. 2021. DOI. 10.1016/j.matdes.2021.109726.

LIAN, T.; ZHAO, J.; YANG, C.; YANG, K. Environment-friendly antifouling coating of Cu-bearing stainless steel prepared by pre-alloyed powder. **Materials Letters**, v. 344, p. 134439, Aug. 2023. DOI. 10.1016/j.matlet.2023.134439

LIPPOLD, J.C.; KOTECKI, D.J. **Welding metallurgy and weldability of stainless steels**. New Jersey: John Wiley & Sons, 2005.

LIU, H.; XU, D.; YANG, K.; LIU, H.; CHENG, Y. F. Corrosion of antibacterial Cu-bearing 316L stainless steels in the presence of sulfate reducing bacteria. **Corrosion Science**, v. 132, p. 46-55, Mar. 2018. DOI. 10.1016/j.corsci.2017.12.006.

LIU, M.; LIN, M. C.; WANG, C. Enhancements of thermal conductivities with Cu, CuO, and carbon nanotube nanofluids and application of MWNT/water nanofluid on a water chiller system. **Nanoscale Research Letters**, v. 6, n. 1, Apr. 2011. DOI. 10.1186/1556-276x-6-297.

LIU, Y.; NING, Z.; CHEN, Y.; GUO, M.; LIU, Y.; GALI, N. K.; SUN, L.; DUAN, Y.; CAI, J.; WESTERDAHL, D. Aerodynamic analysis of SARS-CoV-2 in two Wuhan hospitals. **Nature**, v. 582, n. 7813, p. 557-560, Apr. 2020. DOI. 10.1038/s41586-020-2271-3.

LIU, Y.; YANG, J.; YANG, H.; LI, K.; QIU, Y.; ZHANG, W.; ZHOU, S. Cu-bearing 316L stainless steel coatings produced by laser melting deposition: microstructure and corrosion behavior in simulated body fluids. **Surface and Coatings Technology**, v. 428, p. 127868, Dec. 2021. DOI. 10.1016/j.surfcoat.2021.127868.

MACEDO, J. A. B. Biofilmes bacterianos, uma preocupação da indústria de farmacêutica. **Revista Fármacos & Medicamentos**, v. 2, n. 7, p. 19-24. 2000.

MANDAL, A.; TIWARI, J.K.; ALMANGOUR, B.; SATHISH, N.; KUMAR, S.; KAMARAJ, M.; ASHIQ, M.; SRIVASTAVA, A.K. Tribological behavior of graphene-reinforced 316L stainless-steel composite prepared via selective laser melting. **Tribology International**, v. 151, p. 106525, Nov. 2020. DOI. 10.1016/j.triboint.2020.106525.

MATHEWS, S.; KUMAR, R.; SOLIOZ, M. Copper Reduction and Contact Killing of Bacteria by Iron Surfaces. **Applied and Environmental Microbiology**, v. 81, n. 18, p. 6399-6403, Sep. 2015. DOI. 10.1128/aem.01725-15.

MAZUR, V. T.; MAZUR, M. M.; D'OLIVEIRA, A. S. C. M. Graded Inconel 625 coatings with in-situ processing of Ni3Al. **Surface and Coatings Technology**, v. 445, p. 128660, Sep. 2022. DOI. 10.1016/j.surfcoat.2022.128660.

MELLIN, P.; LYCKFELDT, O.; HARLIN, P.; BRODIN, H.; BLOM, H.; STRONDL, A. Evaluating flowability of additive manufacturing powders, using the Gustavsson flow meter. **Metal Powder Report**, v. 72, n. 5, p. 322-326, Sep. 2017. DOI. 10.1016/j.mprp.2017.06.003.

METTLER TOLEDO. Measuring Density with Laboratory Balance. Available at: https://www.mt.com/us/en/home/applications/Laboratory_weighing/density-measurement.html#overviewaf. Accessed on: 06 Jun 2025.

MIRZABABAEI, S.; DODDAPANENI, V.; LEE, K.; PAUL, G.E.; PIRGAZI, H.; TAN, K.; ERTORER, O.; CHANG, C.; PAUL, B.K.; PASEBANI, S. Remarkable enhancement in thermal conductivity of stainless-steel leveraging metal composite via laser powder bed fusion: 316l-Cu composite. **Additive Manufacturing**, v. 70, p. 103576, May 2023. DOI. 10.1016/j.addma.2023.103576.

MOHYLA, P.; HAJNYS, J.; GEMBALOVÁ, L.; ZAPLETALOVÁ, A.; KRPEC, P. Influence of Heat Treatment of Steel AISI316L Produced by the Selective Laser Melting Method on the Properties of Welded Joint. **Materials**, v. 15, n. 5, p. 1690, Feb. 2022. DOI. 10.3390/ma15051690.

MOMIN, A. G.; KHATRI, B. C.; CHAUDHARI, M.; SHAH, U. V.; VALAKI, J. Parameters for cladding using plasma transfer arc welding - A critical. **Materials Today**: Proceedings, v. 77, p. 614-618, 2023. DOI. 10.1016/j.matpr.2022.11.009.

NATIONAL COMMITTEE FOR CLINICAL LABORATORY STANDARDS. **NCCLS M31-A2**: Performance Standards for Antimicrobial Disk and Dilution Susceptibility Tests for Bacteria Isolated from Animals, Approved Standard. Wayne, 2002.

NIE, Y.; TANG, J.; TENG, J.; YE, X.; YANG, B.; HUANG, J.; YU, S.; LI, Y. Particle defects and related properties of metallic powders produced by plasma rotating electrode process. **Advanced Powder Technology**, v. 31, n. 7, p. 2912-2920, Jul. 2020. DOI. 10.1016/j.apt.2020.05.018.

NIKAM, S.H.; JAIN, N.K.; SAWANT, M.S. Optimization of parameters of micro-plasma transferred arc additive manufacturing process using real coded genetic algorithm. **The International Journal of Advanced Manufacturing Technology**, v. 106, n. 3-4, p. 1239-1252, Dec. 2019. DOI. 10.1007/s00170-019-04658-2.

NIU, M.C.; YANG, K.; LUAN, J.H.; WANG, W.; JIAO, Z.B. Cu-assisted austenite reversion and enhanced TRIP effect in maraging stainless steels. **Journal of Materials Science & Technology**, v. 104, p. 52-58, Mar. 2022. DOI. 10.1016/j.jmst.2021.06.055.

OROPEZA, D.; HOFMANN, D. C.; WILLIAMS, K.; FIRDOSY, S.; BORDEENITHIKASEM, P.; SOKOLUK, M.; LIESE, M.; LIU, J.; LI, X. Welding and additive manufacturing with nanoparticle-enhanced aluminum 7075 wire. **Journal of Alloys and Compounds**, v. 834, p. 154987, Sep. 2020. DOI. 10.1016/j.jallcom.2020.154987.

ÖZER, G.; KISASÖZ, A. The role of heat treatments on wear behaviour of 316L stainless steel produced by additive manufacturing. **Materials Letters**, v. 327, p. 133014, Nov. 2022. DOI. 10.1016/j.matlet.2022.133014.

PACHECO, J.T.; D'OLIVEIRA, A.S.C.M. Additive manufacturing of duplex stainless steels: assessment of deposition processes, microstructure, and properties. **The International Journal of Advanced Manufacturing Technology**, v. 127, n. 11-12, p. 5013-5030, Jul. 2023. DOI. 10.1007/s00170-023-11947-4.

PALZA, H.; NUÑEZ, M.; BASTÍAS, R.; DELGADO, K. In situ antimicrobial behavior of materials with copper-based additives in a hospital environment. **International Journal of Antimicrobial Agents**, v. 51, n. 6, p. 912-917, Jun. 2018. DOI. 10.1016/j.ijantimicag.2018.02.007.

PARK, S. H.; SON, S. J.; LEE, S. B.; YU, J. H.; AHN, S. J.; CHOI, Y. S. Surface machining effect on material behavior of additive manufactured SUS 316L. Journal of **Materials Research and Technology**, v. 13, p. 38-47, Jul. 2021. DOI. 10.1016/j.jmrt.2021.04.031.

PRASS, G. S.; D'OLIVEIRA, A. S. C. M. Processing and characterization of AISI 316L coatings modified with Cu and CuO nanoparticles. **Surface and Coatings Technology**, v. 461, p. 129465, May 2023. DOI. 10.1016/j.surfcoat.2023.129465.

PRIARONE, P. C.; CAMPATELLI, G.; CATALANO, A. R.; BAFFA, F. Life-cycle energy and carbon saving potential of Wire Arc Additive Manufacturing for the repair of mold inserts. **CIRP Journal of Manufacturing Science and Technology**, v. 35, p. 943-958, Nov. 2021. DOI. 10.1016/j.cirpj.2021.10.007.

RALLS, A. M.; DAROONPARVAR, M.; SIKDAR, S.; RAHMAN, M. H.; MONWAR, M.; WATSON, K.; KAY, C. M.; MENEZES, P. L. Tribological and Corrosion Behavior of High Pressure Cold Sprayed Duplex 316 L Stainless Steel. **Tribology International**, v. 169, p. 107471, May 2022. DOI. 10.1016/j.triboint.2022.107471.

RAMAKRISHNAN, A.; RAMESHKUMAR, T.; RAJAMURUGAN, G.; SUNDARRAJU, G.; SELVAMUTHUKUMARAN, D. Experimental investigation on mechanical properties of TIG welded dissimilar AISI 304 and AISI 316 stainless steel using 308 filler rod. **Materials Today**: Proceedings, v. 45, p. 8207-8211, 2021. DOI. 10.1016/j.matpr.2021.03.502.

RANKOUHI, B.; JAHANI, S.; PFEFFERKORN, F.E.; THOMA, D.J. Compositional grading of a 316L-Cu multi-material part using machine learning for the determination of selective laser melting process parameters. **Additive Manufacturing**, v. 38, p. 101836, Feb. 2021. DOI. 10.1016/j.addma.2021.101836.

RASIYA, G.; SHUKLA, A.; SARAN, K. Additive Manufacturing - A Review. **Materials Today**: Proceedings, v. 47, p. 6896-6901, 2021. DOI. 10.1016/j.matpr.2021.05.181.

REVILLA, R.I.; VAN CALSTER, M.; RAES, M.; ARROUD, G.; ANDREATTA, F.; PYL, L.; GUILLAUME, P.; GRAEVE, I. Microstructure and corrosion behavior of 316L stainless steel prepared using different additive manufacturing methods: a comparative study bringing insights into the impact of microstructure on their passivity. **Corrosion Science**, v. 176, p. 108914, Nov. 2020. DOI. 10.1016/j.corsci.2020.108914.

RIQUELME, A.; CANDELA, C. S. R.; RODRIGO, P.; RAMS, J. Influence of process parameters in additive manufacturing of highly reinforced 316L / SiCp composites. **Journal of Materials Processing Technology**, v. 299, p. 117325, Jan. 2022. DOI. 10.1016/j.jmatprotec.2021.117325.

ROJAS, J.G.M.; WOLFE, T.; FLECK, B.A.; QURESHI, A. J. Plasma transferred arc additive manufacturing of Nickel metal matrix composites. **Manufacturing Letters**, v. 18, p. 31-34, Oct. 2018. DOI. 10.1016/j.mfglet.2018.10.001.

ROMERO-RESENDIZ, L.; KONG, H.J.; ZHANG, T.; NI, H.; CHEN, S.; NAEEM, M.; ZHU, Y.T. Achieving antimicrobial and superior mechanical properties in a scalable and cost-effective heterostructured stainless steel. **Materials Science and Engineering**: A, v. 886, p. 145676, Oct. 2023. DOI. 10.1016/j.msea.2023.145676.

SABOORI, A.; AVERSA, A.; MARCHESE, G.; BIAMINO, S.; LOMBARDI, M.; FINO, P. Microstructure and Mechanical Properties of AISI 316L Produced by Directed Energy Deposition-Based Additive Manufacturing: a review. **Applied Sciences**, v. 10, n. 9, p. 3310, May 2020. DOI.10.3390/app10093310.

SADASIVAM, P.; AMIRTHALINGAM, M. Design and fabrication of micro-plasma transferred wire arc additive manufacturing system. **CIRP Journal of Manufacturing Science and Technology**, v. 37, p. 185-195, May 2022. DOI. 10.1016/j.cirpj.2022.01.014.

SAEIDI, K.; KVETKOVÁ, L.; LOFAJ, F.; SHEN, Z. Austenitic stainless steel strengthened by the in situ formation of oxide nanoinclusions. **RSC Advances**, v. 5, n. 27, p. 20747-20750, 2015. DOI. 10.1039/c4ra16721j.

SAHOO, A.; TRIPATHY, S. Development in plasma arc welding process: a review. **Materials Today**: Proceedings, v. 41, p. 363-368, 2021. DOI. 10.1016/j.matpr.2020.09.562.

SALUJA, R. P.; MOEED, K. The emphasis of phase transformations and alloying constituents on hot cracking susceptibility of type 304L and 316L stainless steel welds. **International Journal of Engineering Science and Technology**, v. 4, p. 2206-2216, 2012.

SANTOS, A. X.; MACIEL, T. M.; COSTA, J. D.; SOUSA, M. B.; PRASAD, S.; CAMPOS, A. R. N.; SANTANA, R. A. C. Study on influence of the PTA-P welding process parameters on corrosion behavior of Inconel 625 coatings. **Matéria (Rio de Janeiro)**, v. 24, n. 1, 2019. DOI. 10.1590/s1517-707620190001.0619.

SAWANT, M. S.; JAIN, N. K. Investigations on Additive Manufacturing of Ti-6Al-4V by Microplasma Transferred Arc Powder Deposition Process. **Journal of Manufacturing Science and Engineering**, v. 140, n. 8, Jun. 2018. DOI. 10.1115/1.4040324.

SEN, I.; AMANKWAH, E.; KUMAR, N.S.; FLEURY, E.; OH-ISHI, K.; HONO, K.; RAMAMURTY, U. Microstructure and mechanical properties of annealed SUS 304H austenitic stainless steel with copper. **Materials Science and Engineering**: A, v. 528, n. 13-14, p. 4491-4499, May 2011. DOI. 10.1016/j.msea.2011.02.019.

SHARMA, R.; SETIA, G. Mechanical dry particle coating on cohesive pharmaceutical powders for improving flowability - A review. **Powder Technology**, v. 356, p. 458-479, Nov. 2019. DOI. 10.1016/j.powtec.2019.08.009.

SILVA, F.S.; CINCA, N.; DOSTA, S.; CANO, I.G.; GUILEMANY, J.M.; CAIRES, C.S.A.; LIMA, A.R.; SILVA, C.M.; OLIVEIRA, S.L.; CAIRES, A.R.L. Corrosion resistance and antibacterial properties of copper coating deposited by cold gas spray. **Surface and Coatings Technology**, v. 361, p. 292-301, Mar. 2019. DOI. 10.1016/j.surfcoat.2019.01.029.

SILVA, L. J.; D'OLIVEIRA, A. S. C. M. NiCrSiBC coatings: effect of dilution on microstructure and high temperature tribological behavior. **Wear**, v. 350-351, p. 130-140, Mar. 2016. DOI. 10.1016/j.wear.2016.01.015.

SLAVIN, Y. N.; ASNIS, J.; HÄFELI, U. O.; BACH, H. Metal nanoparticles: understanding the mechanisms behind antibacterial activity. **Journal of Nanobiotechnology**, v. 15, n. 1, Oct. 2017. DOI. 10.1186/s12951-017-0308-z.

SOULIER, M.; BENAYAD, A.; TEULON, L.; OUDART, Y.; SENOL, S.; VANMEENSEL, K. Nanocomposite powder for powder-bed-based additive manufacturing obtained by dry particle coating. **Powder Technology**, v. 404, p. 117474, May 2022. DOI. 10.1016/j.powtec.2022.117474.

SOUSA, J.M.S.; PEREIRA, A.S.P.; SILVA, R.G.N.; PEREIRA, M.; CASTRO, R.M.; CURI, E.I.M.; MACHADO, P.C. Tribological performance of Ni-Cr-B-Si coatings deposited via laser cladding process. **Surface Topography**: Metrology and Properties, v. 10, n. 3, p. 034008, Sep. 2022. DOI. 10.1088/2051-672x/ac97af.

SPIERINGS, A.B.; VOEGTLIN, M.; BAUER, T.; WEGENER, K. Powder flowability characterisation methodology for powder-bed-based metal additive manufacturing. **Progress in Additive Manufacturing**, v. 1, n. 1-2, p. 9-20, Jul. 2015. DOI. 10.1007/s40964-015-0001-4.

SVAHN, F.; MISHRA, P.; EDIN, E.; ÅKERFELDT, P.; ANTTI, M.L. Microstructure and mechanical properties of a modified 316 austenitic stainless steel alloy manufactured by laser powder bed fusion. **Journal of Materials Research and Technology**, v. 28, p. 1452-1462, Jan. 2024. DOI. 10.1016/j.jmrt.2023.12.063.

TAKANO, E. H.; QUEIROZ, D.; D'OLIVEIRA, A. S. C. M. Avaliação dos Parâmetros de Processamento por PTA nas Superfícies Processadas. **Soldagem & Inspeção**, v. 13, n. 3, p. 210-218, Sep. 2008.

TAKANO, E. H.; QUEIROZ, D.; D'OLIVEIRA, A. S. C. M. Evaluation of processing parameters on PTA hardfacing surfaces. **Welding International**, v. 24, n. 3, p. 241-248, Mar. 2010. DOI. 10.1080/09507110902843974.

TANG, Z.; KONG, N.; ZHANG, X.; LIU, Y.; HU, P.; MOU, S.; LILJESTRÖM, P.; SHI, J.; TAN, W.; KIM, J. S. A materials-science perspective on tackling COVID-19. **Nature Reviews Materials**, v. 5, n. 11, p. 847-860, Oct. 2020. DOI. 10.1038/s41578-020-00247-y.

TASCIOGLU, E.; KARABULUT, Y.; KAYNAK, Y. Influence of heat treatment temperature on the microstructural, mechanical, and wear behavior of 316L stainless steel fabricated by laser powder bed additive manufacturing. The International **Journal of Advanced Manufacturing Technology**, v. 107, n. 5-6, p. 1947-1956, Feb. 2020. DOI. 10.1007/s00170-020-04972-0.

THOMPSON, M. K.; MORONI, G.; VANEKER, T.; FADEL, G.; CAMPBELL, R.I.; GIBSON, I.; BERNARD, A.; SCHULZ, J.; GRAF, P.; AHUJA, B. Design for Additive Manufacturing: trends, opportunities, considerations, and constraints. **Cirp Annals**, v. 65, n. 2, p. 737-760, 2016. DOI. 10.1016/j.cirp.2016.05.004.

TWI. What is directed energy deposition (DED). Available at: https://www.twi-global.com/technical-knowledge/faqs/directed-energy-deposition. Accessed on: 21 may 2021.

UPADHYAY, R.K.; KUMAR, A. Scratch and wear resistance of additive manufactured 316L stainless steel sample fabricated by laser powder bed fusion technique. **Wear**, v. 458-459, p. 203437, Oct. 2020. DOI. 10.1016/j.wear.2020.203437.

VAN DOREMALEN, N.; BUSHMAKER, T.; MORRIS, D. H.; HOLBROOK, M. G.; GAMBLE, A.; WILLIAMSON, B. N.; TAMIN, A.; HARCOURT, J. L.; THORNBURG, N. J.; GERBER, S. I. Aerosol and Surface Stability of SARS-CoV-2 as Compared with SARS-CoV-1. **New England Journal of Medicine**, v. 382, n. 16, p. 1564-1567, Apr. 2020. DOI. 10.1056/nejmc2004973.

VISHNU, V.; PRABHU, T.R.; IMAM, M.; VINEESH, K.P. High-temperature dry sliding wear behavior of additively manufactured austenitic stainless steel (316L). **Wear**, v. 540-541, p. 205259, Mar. 2024. DOI. 10.1016/j.wear.2024.205259.

WAN, H. Y.; YANG, W. K.; WANG, L. Y.; ZHOU, Z. J.; LI, C. P.; CHEN, G. F.; LEI, L. M.; ZHANG, G. P. Toward qualification of additively manufactured metal parts: tensile and fatigue properties of selective laser melted inconel 718 evaluated using miniature specimens. **Journal of Materials Science & Technology**, v. 97, p. 239-253, Jan. 2022. DOI. 10.1016/j.jmst.2021.04.049.

WANG, C.; LIU, T.G.; ZHU, P.; LU, Y.H.; SHOJI, T. Study on microstructure and tensile properties of 316L stainless steel fabricated by CMT wire and arc additive manufacturing. **Materials Science and Engineering**: A, v. 796, p. 140006, Oct. 2020. DOI. 10.1016/j.msea.2020.140006.

WANG, D.; ZHANG, J.; ZHANG, S.; WEI, Y.; HOU, L.; WU, P.; ZHANG, Y.; ZHANG, J.; LIU, B. Simultaneous optimization of corrosion resistance and mechanical properties of LMD-processed 316L austenitic stainless steel by adding Ti nanoparticles in a simulated environment for proton exchange membrane fuel cells. **Vacuum**, v. 237, p. 114205, Jul. 2025. DOI. 10.1016/j.vacuum.2025.114205.

WANG, Q.; REN, L.; LI, X.; ZHANG, S.; SERCOMBE, T. B.; YANG, K. Antimicrobial Cu-bearing stainless steel scaffolds. **Materials Science and Engineering**: C, v. 68, p. 519-522, Nov. 2016. DOI. 10.1016/j.msec.2016.06.038.

WANG, R.; XI, L.; DING, K. GÖKCE, B.; BARCIKOWSKI, S.; GU, D. Powder preparation during ball milling and laser additive manufacturing of aluminum matrix nanocomposites: powder properties, processability and mechanical property. **Advanced Powder Technology**, v. 33, n. 8, p. 103687, Aug. 2022. DOI. 10.1016/j.apt.2022.103687.

WARNES, S. L.; LITTLE, Z. R.; KEEVIL, C. W. Human Coronavirus 229E Remains Infectious on Common Touch Surface Materials. **Mbio**, v. 6, n. 6, Dec. 2015. DOI. 10.1128/mbio.01697-15.

WEI, Y.; CHEN, G.; WANG, H.; TAO, N. High-precision laser powder bed fusion of 316L stainless steel and its SiC reinforcement composite materials. **Optics & Laser Technology**, v. 190, p. 113267, Nov. 2025. DOI. 10.1016/j.optlastec.2025.113267.

WEI, Y.; WEI, X. S.; CHEN, B.; ZUO, J. Y.; MA, T. C.; SHEN, J. Parameter optimization for tungsten carbide/Ni-based composite coating deposited by plasma transferred arc hardfacing. **Transactions of Nonferrous Metals Society of China**, v. 28, n. 12, p. 2511-2519, Dec. 2018. DOI. 10.1016/s1003-6326(18)64897-6.

WU, Y.; WU, W.; ZHAO, W.; LAN, X. Revealing the antibacterial mechanism of copper surfaces with controllable microstructures. **Surface and Coatings Technology**, v. 395, p. 125911, Aug. 2020. DOI. 10.1016/j.surfcoat.2020.125911.

XI, T.; SHAHZAD, M. B.; XU, D.; SUN, Z.; ZHAO, J.; YANG, C.; QI, M.; YANG, K. Effect of copper addition on mechanical properties, corrosion resistance and antibacterial property of 316L stainless steel. **Materials Science and Engineering**: C, v. 71, p. 1079-1085, Feb. 2017. DOI. 10.1016/j.msec.2016.11.022.

XI, T.; SHAHZAD, M. B.; XU, D.; ZHAO, J.; YANG, C.; QI, M.; YANG, K. Copper precipitation behavior and mechanical properties of Cu-bearing 316L austenitic stainless steel: a comprehensive cross-correlation study. **Materials Science and Engineering**: A, v. 675, p. 243-252, Oct. 2016. DOI. 10.1016/j.msea.2016.08.058.

XIE, B.; XUE, J.; REN, X. Wire Arc Deposition Additive Manufacturing and Experimental Study of 316L Stainless Steel by CMT + P Process. **Metals**, v. 10, n. 11, p. 1419, Oct. 2020. DOI. 10.3390/met10111419.

XIONG, Z.; LI, H.; YANG, H.; YANG, Y.; LIU, Y.; CUI, L.; LI, X.; MASSELING, L.; SHEN, L.; HAO, S. Micro laser powder bed fusion of NiTi alloys with superior mechanical property and shape recovery function. **Additive Manufacturing**, v. 57, p. 102960, Sep. 2022. DOI. 10.1016/j.addma.2022.102960.

YADAV, S.; JINOOP, A. N.; SINHA, N.; PAUL, C. P.; BINDRA, K. S. Parametric investigation and characterization of laser directed energy deposited copper-nickel graded layers. **The International Journal of Advanced Manufacturing Technology**, v. 108, n. 11-12, p. 3779-3791, Jun. 2020. DOI. 10.1007/s00170-020-05644-9.

YAEDU, A. E.; D'OLIVEIRA, A. S. C. M. Cobalt based alloy PTA hardfacing on different substrate steels. **Materials Science and Technology**, v. 21, n. 4, p. 459-466, Apr. 2005. DOI. 10.1179/174328413x13789824293380.

YANG, H.; LIU, Y.; JIN, J.; LI, K.; YANG, J.; MENG, L.; LI, C.; ZHANG, W.; ZHOU, S. Effect of Heat Treatment on Microstructure and Mechanical Behavior of Cu-Bearing 316L Stainless Steel Produced by Selective Laser Melting. **Acta Metallurgica Sinica (English Letters)**, v. 37, n. 1, p. 169-180, Jan. 2024. DOI. 10.1007/s40195-023-01643-3.

YIN, H.; YANG, J.; ZHANG, Y.; CRILLY, L.; JACKSON, R.L.; LOU, X. Carbon nanotube (CNT) reinforced 316L stainless steel composites made by laser powder bed fusion: microstructure and wear response. **Wear**, v. 496-497, p. 204281, May 2022. DOI. 10.1016/j.wear.2022.204281.

ZHAI, W.; ZHOU, W.; NAI, S.M.L. Grain refinement and strengthening of 316L stainless steel through addition of TiC nanoparticles and selective laser melting. **Materials Science and Engineering**: A, v. 832, p. 142460, Jan 2022. DOI. 10.1016/j.msea.2021.142460.

ZHAI, W.; ZHOU, W.; NAI, S.M.L. Fabrication of TiC strengthened 316L composites and nanocomposites using laser powder bed fusion. **Materials Today**: Proceedings, v. 70, p. 212-217, 2022. DOI. 10.1016/j.matpr.2022.09.023.

ZHANG, J.; SHAO, P.; WANG, X.; FAN, D. Improving weld penetration by two-TIG arc activated via mixing oxygen into shielding gas. **The International Journal of Advanced Manufacturing Technology**, v. 125, n. 1-2, p. 169-181, Dec. 2022. DOI. 10.1007/s00170-022-10703-4.

ZHANG, Z.; ZHANG, X. R.; JIN, T.; YANG, C. G.; SUN, Y. P; LI, Q.; YANG, K. Antibacterial mechanism of Cu-bearing 430 ferritic stainless steel. **Rare Metals**, v. 41, n. 2, p. 559-569, Jun. 2021. DOI. 10.1007/s12598-021-01751-y.

ZHAO, H.; DING, Y.; LI, J.; WEI, G.; ZHANG, M. Corrosion resistance of laser melting deposited Cu-bearing 316L stainless steel coating in 0.5 M H2SO4 solution. **Materials Chemistry and Physics**, v. 291, p. 126572, Nov. 2022. DOI. 10.1016/j.matchemphys.2022.126572.

ZHONG, Y.; LIU, L.; WIKMAN, S.; CUI, D.; SHEN, Z. Intragranular cellular segregation network structure strengthening 316L stainless steel prepared by selective laser melting. **Journal of Nuclear Materials**, v. 470, p. 170-178, Mar. 2016. DOI. 10.1016/j.jnucmat.2015.12.034.

ZHUANG, J.; GU, D.; XI, L.; LIN, K.; FANG, Y.; WANG, R. Preparation method and underlying mechanism of MWCNTs/Ti6Al4V nanocomposite powder for selective laser melting additive manufacturing. **Powder Technology**, v. 368, p. 59-69, May 2020. DOI. 10.1016/j.powtec.2020.04.041.

ZOU, Y.; UEJI, R.; FUJII, H. Effect of oxygen on weld shape and crystallographic orientation of duplex stainless steel weld using advanced A-TIG (AA-TIG) welding method. **Materials Characterization**, v. 91, p. 42-49, May 2014. DOI. 10.1016/j.matchar.2014.02.006.

APPENDIX A - ANTIMICROBIAL ASSESSMENT

This work is being developed with the expertise in microbiology contributed by Professor Wesley Mauricio de Souza from the Federal University of Paraná. This assessment is currently under development and materials, methods and results are partially summarized below.

MATERIALS AND METHODS

As described in Figure 15b, PTA-DED was used to prepare AISI 316L single-wall multilayers with different Cu addition. In this section, the processed materials tested include 316L, 316L with Cu MP (1 and 5 wt%), 316L with 1 wt% Cu NP, and 316L with 1 wt% CuO. Initially, these specimens were evaluated in the as-deposited condition. Additionally, they are currently being tested following solubilization (0.5 h at 1100ºC) and ageing (3 h at 700ºC) heat treatments.

To assess the antimicrobial properties of the processed materials, two standard bacteria with different cell wall structures were selected, consequently displaying different sensitivity to sterilization methods. A Gram-negative, *Escherichia coli* ATCC 25922 and, a Gram-positive, *Staphylococcus aureus* ATCC 6538. Two methods were used, agar diffusion method and plaque count method. Prior to testing, the surfaces of the plates (processed materials) were ground with 1200 grit SiC abrasive paper, sonicated for 10 min, respectively, in ethanol and ultrapure water and left to air dry for at least 12 h. Once dried, the plates were autoclaved at 121 °C for 15 min and dried in oven at 50 °C.

For the agar diffusion method, bacterial cultures (*E. coli* and *S. aureus*) were sourced from standard ATCC strains. Susceptibility tests were conducted following the Kirby-Bauer method (NCCLS, 2002). Microbial cultures were prepped 24 hours prior to testing. Bacterial suspensions were prepared in sterile saline solution (0.85%) using a 0.5 McFarland standard, resulting in final concentrations ranging from approximately 1.0 to 6.0 x 10^5 CFU/ml. These suspensions were then inoculated onto Mueller Hinton (MH) agar using sterile cotton swabs. The sterilized plates were placed on MH agar previously inoculated with bacterial suspensions. Incubation took place at 37 °C for 18 h. Following incubation, plates were examined for inhibition zones (halos).

For the plaque count method, 20 Erlenmeyer flasks (25 mL) were prepared, 6 for each bacterium (3 for control and 3 for testing). 10 mL of Brain-Heart Infusion Broth (BHIB) was added to each Erlenmeyer flask, which was sealed with cotton plugs. Additionally, tubes containing saline solution (NaCl - 0.85%) were prepared for bacterial inoculation. The Erlenmeyer flasks, the saline solution tubes, and metal tweezers were sterilized by autoclaving at 121°C for 15 min. Bacteria (*S. aureus* and *E. coli*) stored at -80°C with 20% glycerol were reactivated on brain-heart infusion agar plates (BHIA) at 36 °C for 24 h. An inoculum was prepared in saline solution with turbidity equivalent to 0.5 McFarland scale (approximately 1.0 x 10^8 CFU/mL), from which, 1 mL was added to 9 mL of saline solution, resulting in a 1.0 x 10^7 CFU/mL suspension. From this suspension, 100 µL were added to each of the 6 Erlenmeyer flasks containing BHIB for each bacterium, resulting in an inoculum of 1.0 x 10^5 CFU/mL. Immediately after the sterile plates were added, one per Erlenmeyer flasks, using sterile metal tweezers.

The Erlenmeyer flasks were incubated at 36°C for 18 h with agitation (43 Hz). Subsequently, the plates were removed from the Erlenmeyer flasks using sterile metal tweezers and placed in sterile, semi-sealed tubes, left to air dry at 36 °C, and maintained in the incubator for 24 hours. The control plates (no 24 h incubation time) and the test plates (after 24 h incubation time) were added, using sterile metal tweezers, to Erlenmeyer flasks (25 mL) with 10 mL of sterile saline solution and sonicated for 10 min. From 1mL of this suspension, serial dilutions were made in saline (1:100, 1:1000 and, 1:10000). From each dilution, 100 µL were inoculated onto BHIA and incubated at 36 °C for 18 h. Additionally, the treated plates were removed using sterile metal tweezers and placed in tubes containing BHIB and incubated at 36 °C for 18 h to verify growth or sterility. The bacterial colonies grown on the plates were multiplied by the corresponding dilution factor and the number of colonies was expressed as Log10 CFU/mL. The plaque count experiment was repeated 3 times.

SUMMARY OF THE RESULTS

For the agar diffusion method, after the incubation of the plates (processed materials) at 37 °C for 18 h, no halos were identified around the plates, indicating the presence of *E. coli* and *S. aureus* colonies around the materials. To compare the antimicrobial action, the plaque count method was required. For both Gram-positive

and Gram-negative bacteria, there was a slight reduction in the number of colonies after a 24 h incubation for all the tested materials (Figure 83). Adding Cu to the stainless steel shows a tendency of decreasing the number of colonies of the Gram-negative bacterium, *E. coli*. However, adding Cu did not impact on the number of colonies of the Gram-positive bacterium, S. aureus.

The inhibition rate was calculated comparing the number of colonies with the control plaque (without the 24 h incubation period), and the results are shown in Table 33. The addition of CuO NP did not affect the inhibition rate of stainless steel, on the other hand, the addition of Cu NP showed the highest inhibition rate against both bacteria, around 17 % for *E. coli* and 10 % to *S. aureus*.

Xi et al. (2017) showed that the inhibition rate for *E. coli* for cast AISI 316L with 3.5 wt% Cu in the solubilized condition was around 25 % for a 24 h incubation time, and after an ageing heat treatment, it went up to around 98 % associated with the formation of Cu rich precipitates. The processed materials were tested in the as deposited condition; therefore, the low antimicrobial action can be associated with Cu being in solid solution in the austenitic matrix. Further testing for the heat treated specimens is being conducted and awaiting results.

Figure 83 - Number of colonies obtained by the plaque count method after 24 h incubation time

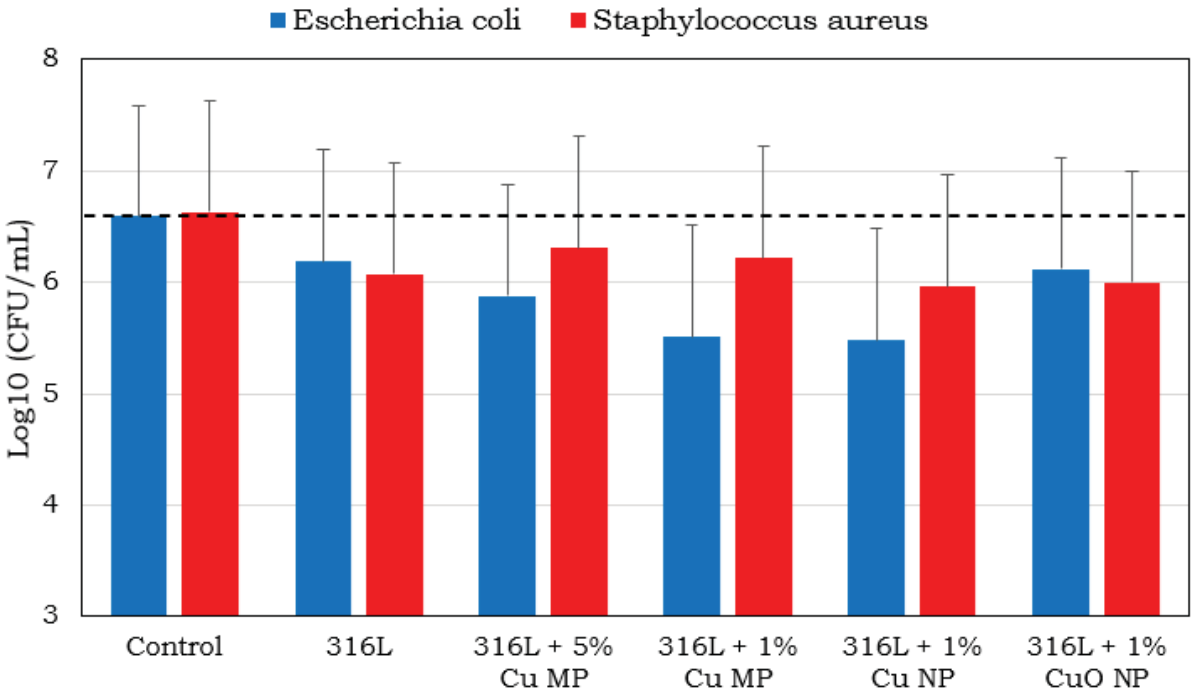

Source: Authors (2025).

Table 33 - Inhibition rate obtained on plaque count method after 24 h incubation time

Specimen	Escherichia coli inhibition (%)	Staphylococcus aureus inhibition (%)
Control	0.0	0.0
316L	6.07	8.44
316L + 5% Cu MP	10.77	4.82
316L + 1% Cu MP	16.38	6.18
316L + 1% Cu NP	16.84	10.10
316L + 1% CuO NP	7.13	9.50

Source: Authors (2025).

REFERENCES

NATIONAL COMMITTEE FOR CLINICAL LABORATORY STANDARDS. **NCCLS M31-A2**: Performance Standards for Antimicrobial Disk and Dilution Susceptibility Tests for Bacteria Isolated from Animals, Approved Standard. Wayne, 2002.

XI, T.; SHAHZAD, M. B.; XU, D.; SUN, Z.; ZHAO, J.; YANG, C.; QI, M.; YANG, K. Effect of copper addition on mechanical properties, corrosion resistance and antibacterial property of 316L stainless steel. **Materials Science and Engineering**: C, v. 71, p. 1079-1085, Feb. 2017. DOI. 10.1016/j.msec.2016.11.022.

APPENDIX B - CORROSION RESISTANCE

This work is being developed with the expertise in corrosion and HVOF contributed by Professor Juliane Ribeiro da Cruz Alves, formerly a postdoctoral researcher at the Federal University of Paraná and currently an Assistant Professor at the University of São Paulo.

The effects of Cu content (1 and 5 wt%), Cu particle size (Cu MP, Cu NP and CuO NP) and processing technique (PTA-DED and HVOF: High Velocity Oxy-Fuel) on the corrosion behavior of the AISI 316L stainless steel are evaluated. This research is currently under development and materials, methods and results are partially summarized below.

MATERIALS AND METHODS

PTA-DED was used to process single-wall multilayers (Figure 15b) with a total of 11 layers deposited on AISI 316L substrates. Five powder compositions (Table 34) were prepared (Figure 13) prior the PTA-DED processing, while the alloying occurs *in-situ*. HVOF was used to obtain coatings of three powder compositions (Table 34). The processing parameters adopted for PTA-DED and HVOF are presented at Table 35 and Table 36, respectively.

Table 34 - Composition of powder mixtures and processing technique

Powder mixture composition	**Processing technique**
316L	PTA-DED and HVOF
316L + 5 wt% Cu MP	PTA-DED and HVOF
316L + 1 wt% Cu MP	PTA-DED
316L + 1 wt% Cu NP	PTA-DED
316L + 1 wt% CuO NP	PTA-DED
Cu	HVOF

Source: Authors (2025).

The processed materials were cut, ground and polished following standard metallographic procedures to attain a mirror-like finish. Solidification microstructure was revealed by etching with Marble's solution (4 g $CuSO_4$ + 20 ml HCl + 20 mL H_2O) and captured using optical microscopy. High resolution scanning electron microscopy (SEM) equipped with energy dispersive x-ray spectroscopy (EDS) was

done after polishing in a vibratory polisher with colloidal silica suspension of 40 nm for 12 h, followed by ion beam polishing for 20 min. Polishing, SEM and EDS were done at the Brazilian Nanotechnology National Laboratory (LNNano) from the Brazilian Center for Research in Energy and Materials (CNPEM), Campinas.

Table 35 - Processing parameters used in PTA-DED single-wall multilayers

Parameter (unit)	**Value**
Substrate	AISI 304L
Protective gas	Argon 99 %
Carrier gas flow (L/min)	0.8
Plasma gas flow (L/min)	2
Shield gas flow (L/min)	15
Nozzle-plate distance (mm)	10
Powder flow rate (g/min)	6
Deposition current (A)	120 (first layer), 80 (subsequent layers)
Deposition speed (mm/min)	100
Temperature between layers (°C)	150

Source: Authors (2025).

Table 36 - Processing parameters used in HVOF coatings

Parameter (unit)	**316L**	**316L + 5 wt% Cu**	**Cu**
Substrate material	Cu	AISI 316L	AISI 316L
Substrate thickness (mm)	3.2	3.0	3.0
Oxygen flow (scfh)	1900	1900	1600
Kerosene (gal/h)	6	6	5
O/F ratio	1.16	1.16	1.16
Carrier gas - Nitrogen (scfh)	20	20	21
Combustion pressure (psi)	101	101	83
Barrel length (in)	6	6	4
Feed rate (g/min)	30	30	30
Spray distance (mm)	305	406	406
Raster speed (mm/s)	500	500	500
Step size (mm)	5	5	4
Number of passes	20	26	20

Source: Authors (2025).

To evaluate the corrosion behavior, the open circuit potential (OCP) was measured after 3 h of stabilization, followed by cyclic polarization testing in naturally aerated NaCl solution (3.5 %). An electrochemical cell with three electrodes was used, where the saturated calomel electrode (SCE) served as the reference electrode, and a coiled platinum electrode (CPE) was used as the counter electrode. The scan started at -150 mV vs. OCP and went up to +850 mV vs. reference

electrode, then returned until passing the repassivation potential (approximately -400 mV vs. the reference electrode), at a scan rate of 1 mV/s. Tafel analysis was used to determined corrosion current (I_{corr}) and corrosion potential (E_{corr}). To compare the corrosion behavior of the processed materials with materials obtained by conventional manufacturing routes, three commercially available materials were tested, AISI 316L stainless steel, commercially pure Cu and a superduplex stainless steel.

SUMMARY OF THE RESULTS

The morphology of the four primary powders used in the PTA-DED process is presented in Figure 84. The gas atomized AISI 316L is composed mostly of spherical particles with a few satellites while the Cu MP is composed of irregularly shaped particles. Further powder characterization was discussed in Chapter 3. However, the high resolution SEM images allow for the observation of both nanoparticle clusters in detail. It is shown that the Cu NP are mostly spherical with mean size of around 500 nm. The CuO NP are smaller in size, with a mean size of approximately 40 nm, and its morphology consists of well-rounded elongated particles.

The primary powders used for HVOF coatings deposition are shown in Figure 85. Both powders are within the same size range with a narrow particle size distribution. HVOF powders are usually required to have near-spherical particle shapes to improve flowability and promote a uniform coating deposition. And as can be seen, both powders are well-rounded and spherical in shape.

During the PTA-deposition process the power feedstock material is fed into the plasma arc, which melts the powder and part of the substrate or previous deposited layer. This allows for the in situ alloying between stainless steel and Cu, generating a layer with homogeneous chemical composition. The stainless steel with 5 wt% Cu processed by PTA-DED presents a typical columnar dendritic microstructure (Figure 86a) that can be seen at this magnification without the presence of Cu rich phases. In contrast, due to the nature of the HVOF process, islands of Cu can be seen within the stainless steel coating (Figure 86b).

Figure 84 - SEM images of powders used for PTA-DED

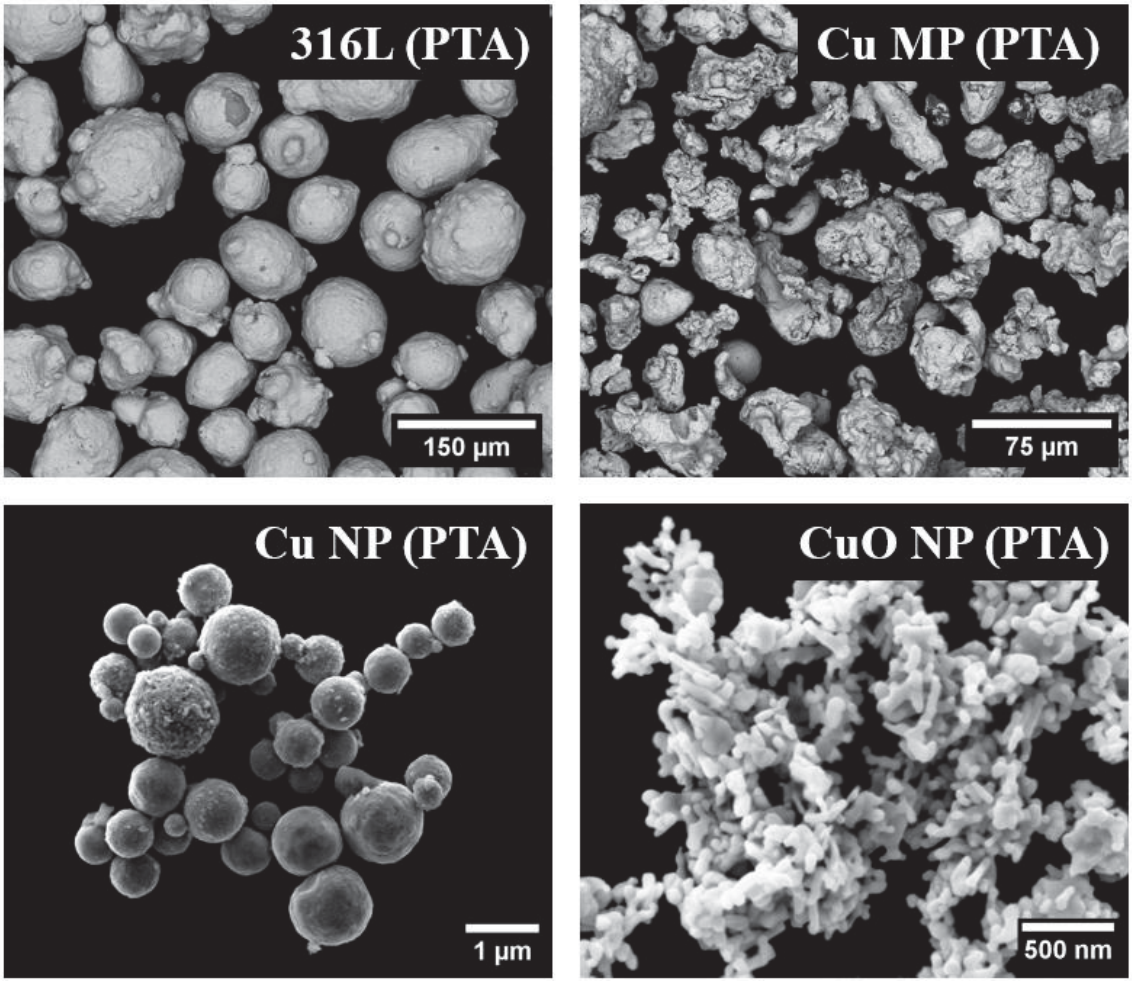

Source: Authors (2025).

Figure 85 - SEM images of powders used for HVOF

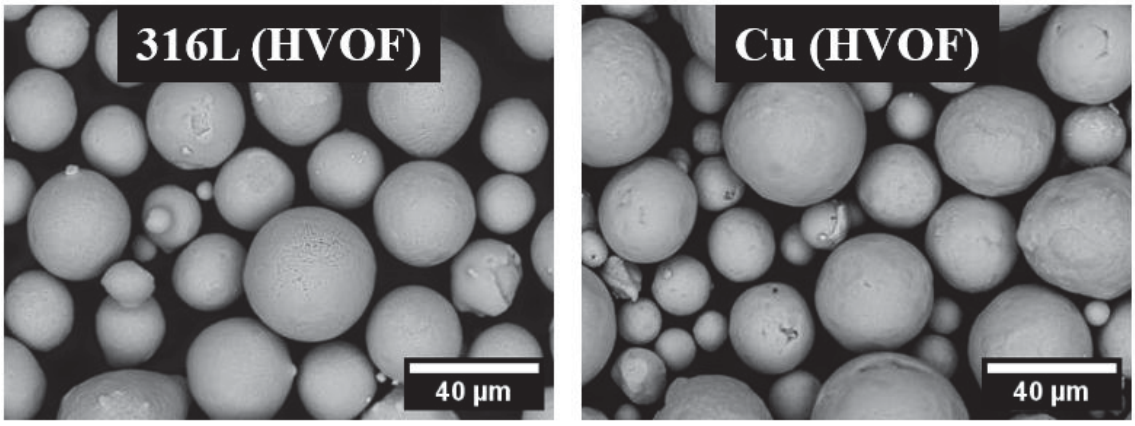

Source: Authors (2025).

Figure 86 - Microstructure of AISI 316L with 5 wt% Cu MP processed by PTA-DED and HVOF in the as built condition

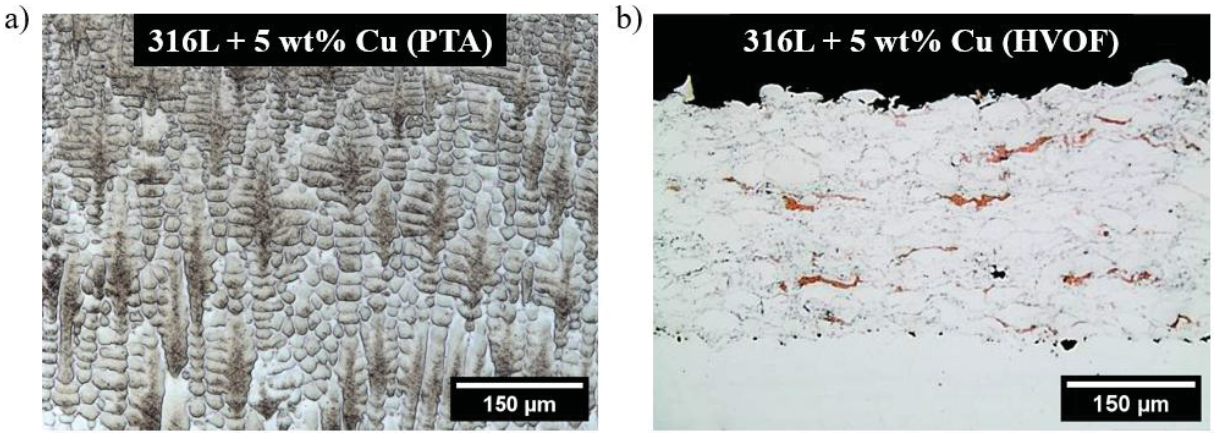

Source: Authors (2025).

In Figure 87, Cu precipitates with a few nanometers in size are shown, these precipitates are located within the austenitic matrix in the interdrendritic region of stainless steel with 5 wt% of Cu deposited by PTA-DED. This indicates that Cu is partitioning to the interdendritic region during the solidification.

Figure 87 - Elemental mapping of interdendritic region in AISI 316L with 5 wt% Cu MP processed by PTA-DED

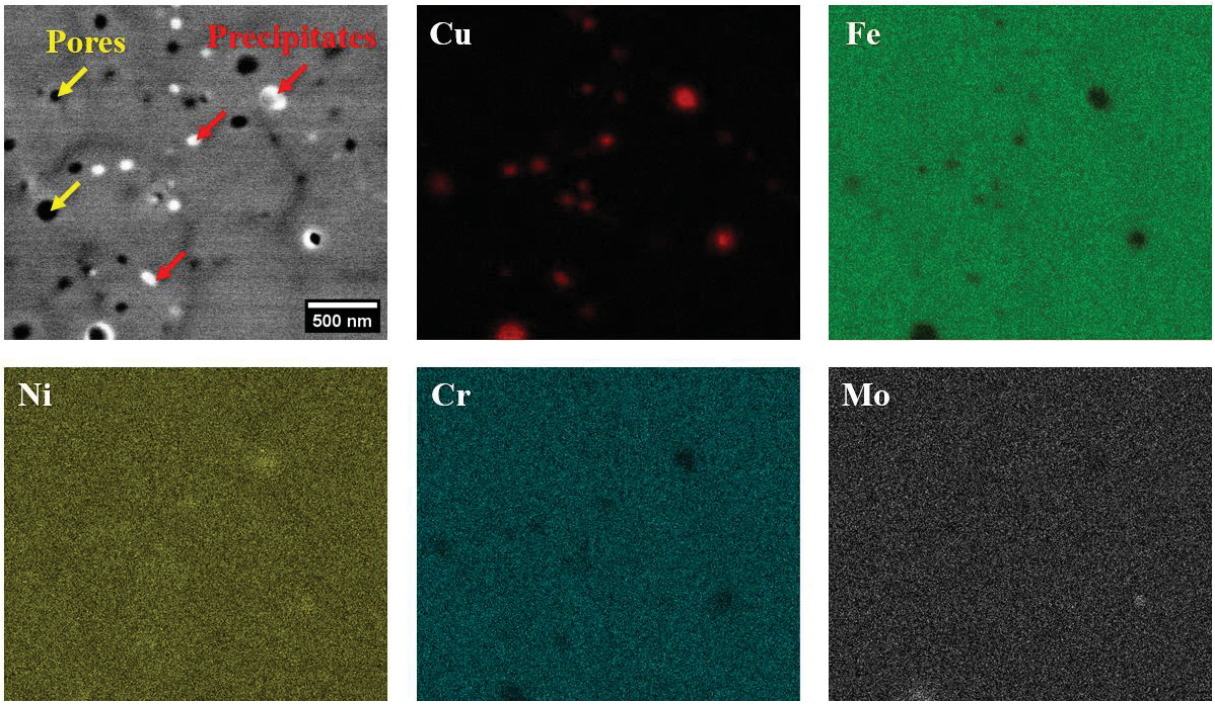

Source: Authors (2025).

The effect of processing technique on OCP over time of AISI 316L and Cu is presented in Figure 88a. During OCP testing, the material interacts with the solution without external current or voltage applied, and less negative the voltage, more noble the material. It can be seen that the Cu bulk (commercial reference) is less noble than the 316L bulk and has a similar behavior than Cu HVOF. The 316L processed with PTA-DED showed a more noble behavior than 316L bulk, however 316L processed by HVOF showed a less noble OCP. The summarized effects of processing and chemical composition in shown in Figure 88b. PTA-DED deposited materials showed a tendency to decrease OCP with the increase in Cu content, while HVOF coatings OCP increased with the addition of Cu.

Figure 88 - (a) Effect of processing on OCP over time of AISI 316L and Cu and (b) summarized effects of processing and chemical composition on OCP

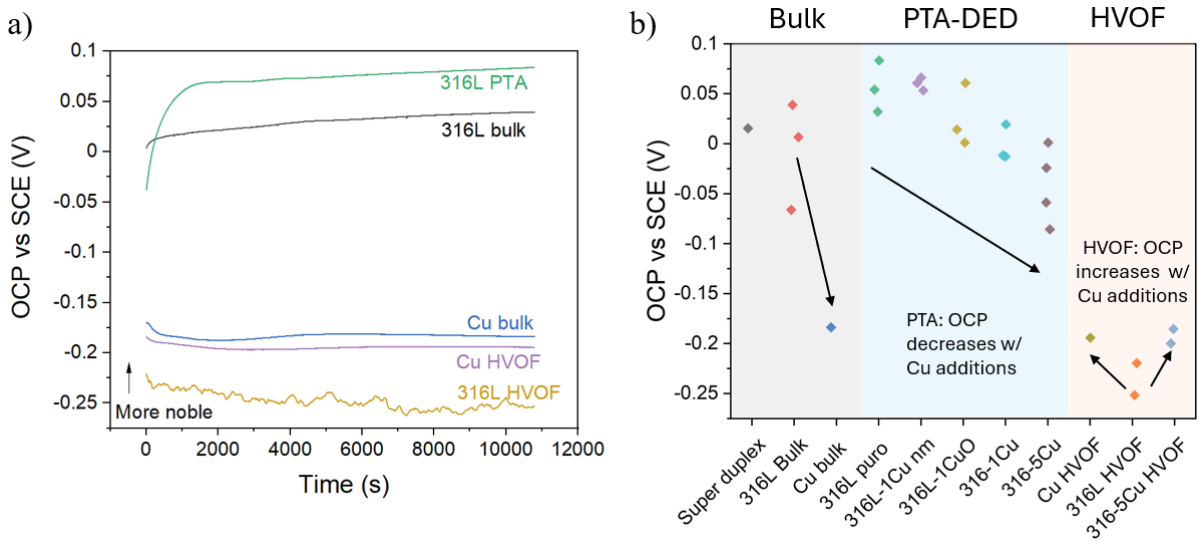

Source: Authors (2025).

The cyclic polarization curves for 316L bulk and Cu bulk (Figure 89a) that the stainless steel have a more noble corrosion behavior with more positive corrosion potential and lower corrosion rate. And the polarization curves for 316L processed with different techniques (Figure 89b) show that 316L processed with PTA-DED had better performance than 316L bulk, which can be related to a more refined microstructure. While 316L processed with HVOF showed inferior performance, with less noble potential and higher corrosion rate.

Figure 89 - Cyclic polarization curves comparing (a) bulk AISI 316L and bulk Cu and (b) AISI 316L processed by different techniques

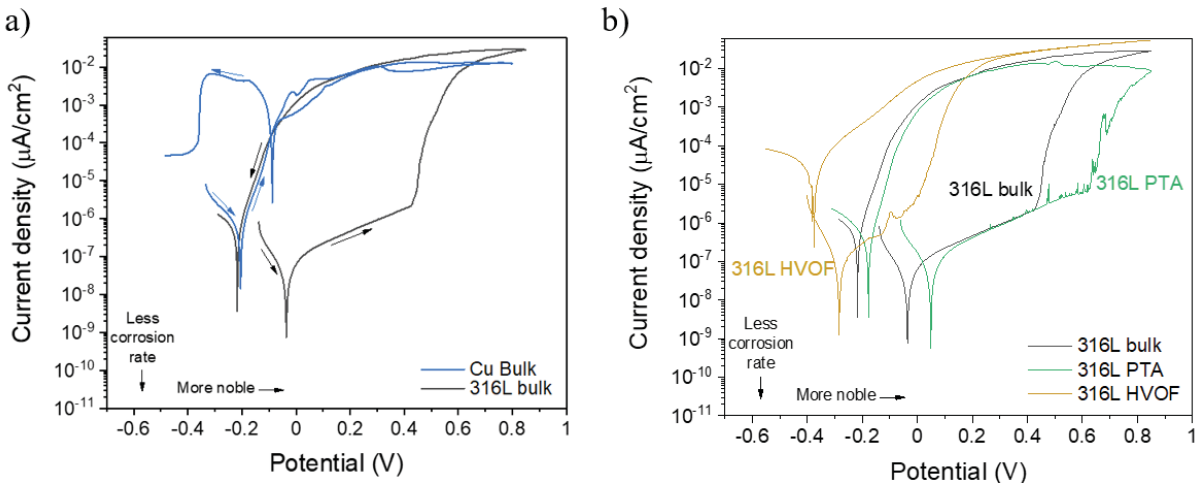

Source: Authors (2025).

From the Tafel curves, E_{corr} and I_{corr} were measured, and the summarized effects of processing and chemical composition are shown in Figure 90. As a general trend, Cu presented a more negative E_{corr} than the 316L stainless steel and the superduplex steel. PTA-DED showed improved performance, with E_{corr} higher than 316L bulk, however, higher Cu contend decreased its corrosion potential. HVOF processed materials presented less noble E_{corr}, which increases with the addition of Cu. It should be noted that all PTA-DED materials showed similar I_{corr} than 316L bulk (Figure 90b). In addition, HVOF coatings with Cu showed a high corrosion rate (Figure 90b), related to the selective pitting corrosion of the Cu phases.

Figure 90 - Summarized effects of processing and chemical composition on (a) corrosion potential and (b) corrosion current

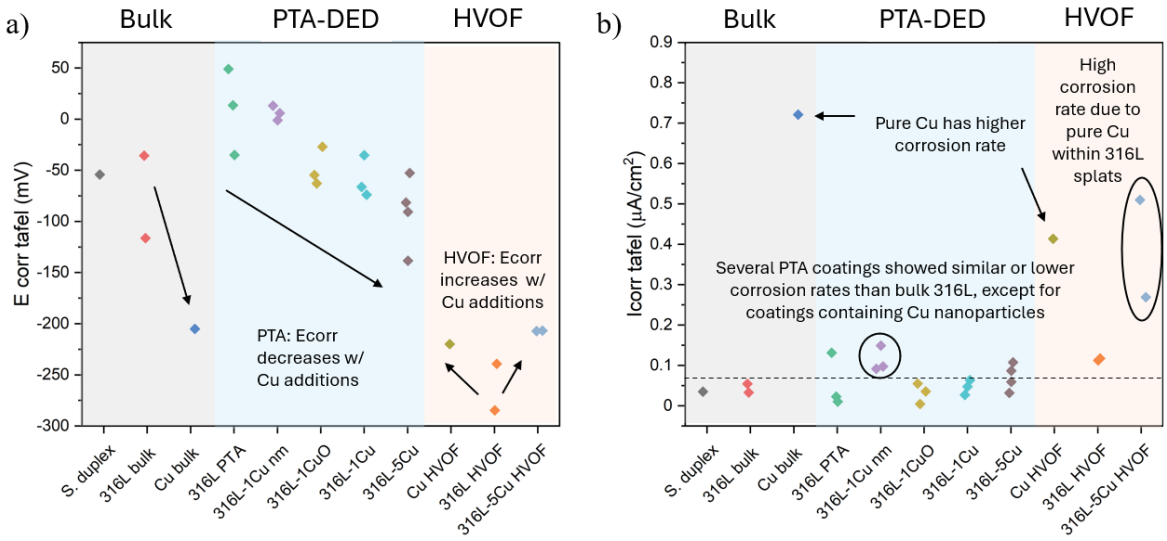

Source: Authors (2025).

APPENDIX C - L-PBF WITH HEAT TREATMENT

Impact of heat treatments on mechanical properties and wear resistance of in-situ alloyed Cu-bearing 316L stainless steel produced by Laser Powder Bed Fusion

Abstract: This study investigates the effects of different heat treatments (HT) on the mechanical properties and wear resistance of 316L and 316L with 5 wt% Cu, both produced by Laser Powder Bed Fusion (L-PBF). The material was assessed in four conditions: as-built, aged (700°C for 3 hours), solubilized (1100°C for 30 minutes), and solubilized + aged. The influence of HT on hardness, microstructure, phase composition, mechanical properties, coefficient of friction, and wear rate was evaluated. Solubilization at high temperature dissolved precipitates, eliminating micro-segregations that form during rapid solidification typical of L-PBF, resulting in a more homogeneous microstructure. In the aged condition, the micro-segregation was preserved. In the as-built condition, 316L showed a higher hardness than 316L with Cu, however, the contrary was observed in the solubilized + aged condition, indicating that the precipitation of the Cu-rich phase happened in favor of hardness. Overall, there is a tendency to decrease hardness after HT. In general, the HT decreased yield strength and ultimate tensile strength (UTS) while significantly increasing the strain at UTS for both chemical compositions. For specimens containing Cu, ageing done directly after building and after solubilization increased the UTS and strain at UTS. Wear testing results are currently being analyzed.

PREVIEW OF THE RESULTS

The following is a preliminary overview of the results, which will serve as the basis for a more detailed discussion in a future scientific paper. A comprehensive analysis and interpretation of the data collected is still to be made.

Figure 91 - Variation of Vickers hardness with chemical composition and heat treatment

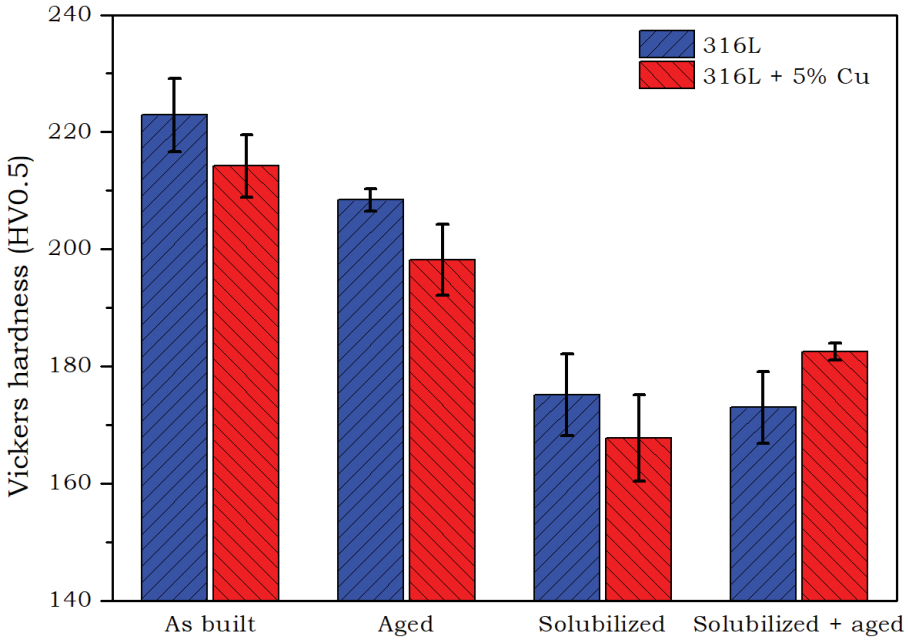

Source: Authors (2025).

Figure 92 - Variation of microstructural features with heat treatments

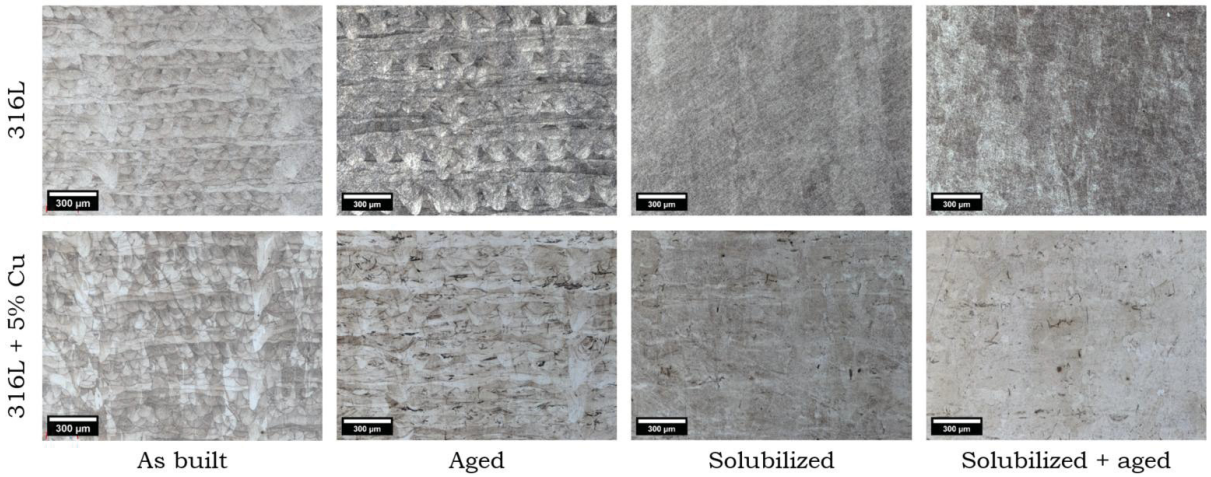

Source: Authors (2025).

Figure 93 - XRD patterns for 316L and 316L + 5% Cu in different heat treatment conditions

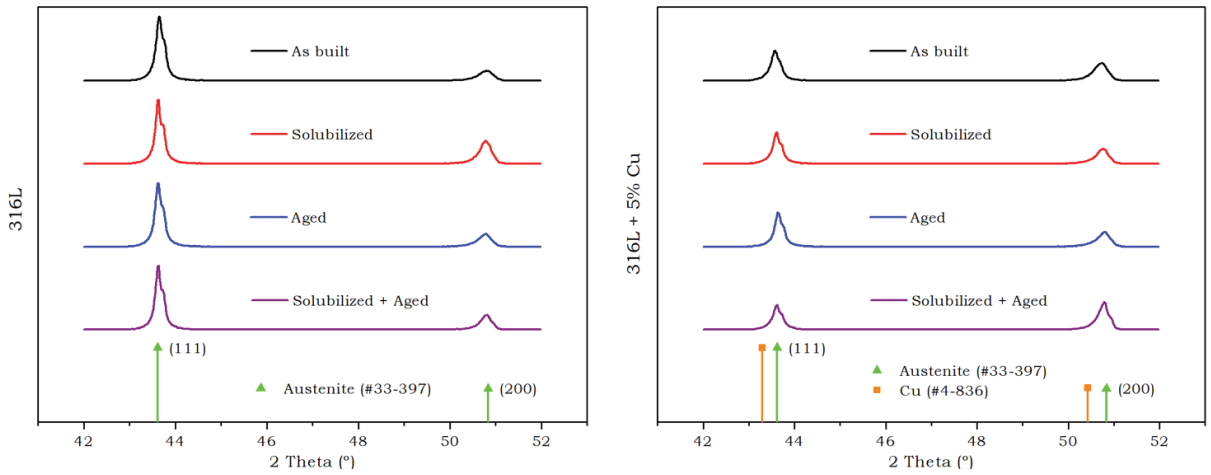

Source: Authors (2025).

Table 37 - Peak angle and lattice parameter for (111) and (200) crystallographic planes

Material	Condition	(111)		(200)	
		2 Theta (°)	Lattice parameter (Å)	2 Theta (°)	Lattice parameter (Å)
316L	As built	43.67	2.071	50.81	1.796
	Aged	43.65	2.072	50.79	1.796
	Solubilized	43.65	2.072	50.78	1.797
	Solubilized + Aged	43.65	2.072	50.80	1.796
316L + 5% Cu	As built	43.58	2.075	50.72	1.798
	Aged	43.62	2.073	50.76	1.797
	Solubilized	43.66	2.072	50.79	1.796
	Solubilized + Aged	43.62	2.073	50.78	1.797
Austenite (33-397)	-	43.62	2.073	50.84	1.795
Cu (4-836)	-	43.29	2.088	50.43	1.808

Source: Authors (2025).

Figure 94 - Crystallographic orientation and grain size distribution after solubilization heat treatment

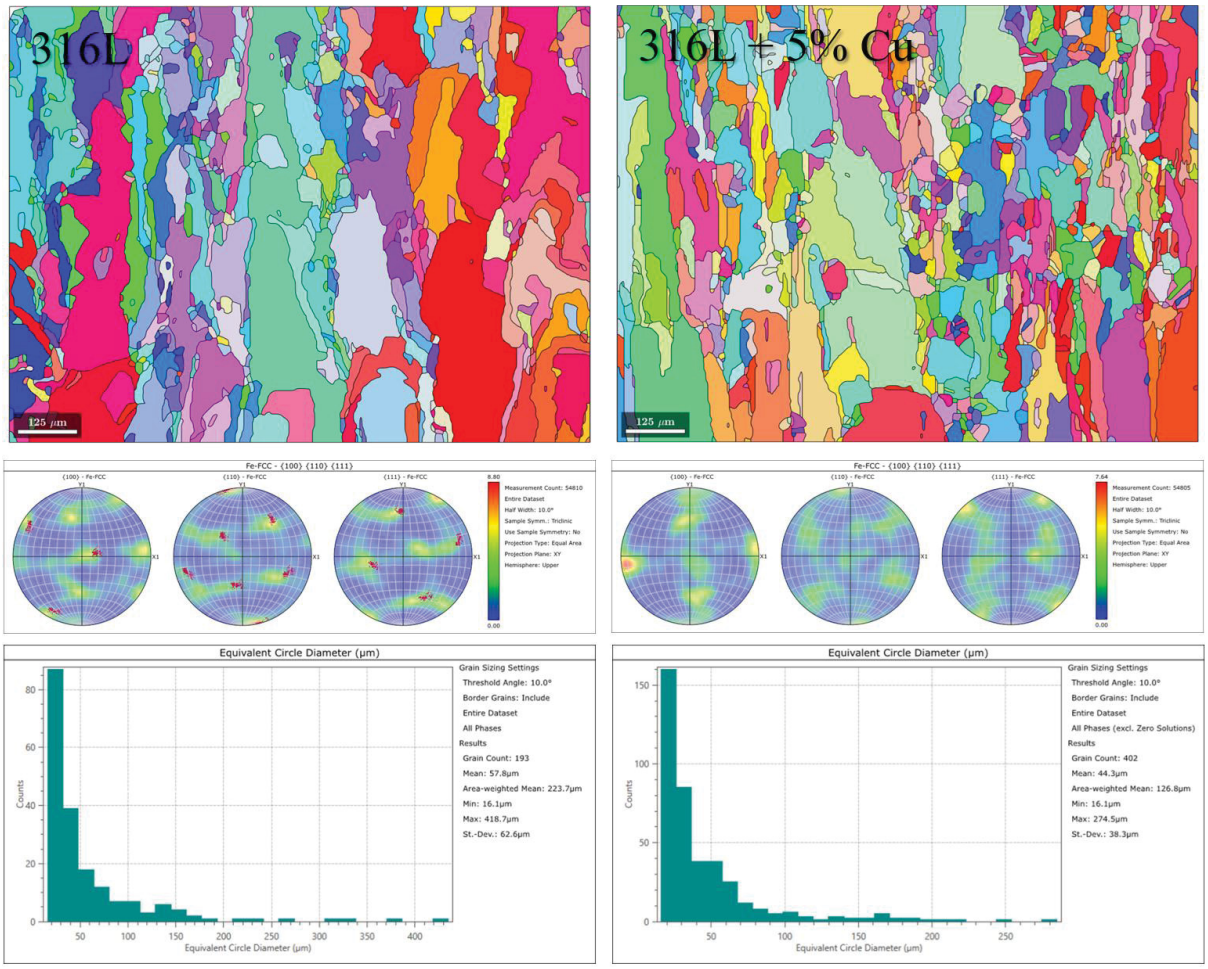

Source: Authors (2025).

Figure 95 - Stress-strain curves for 316L and 316L + 5 % Cu in different heat treated conditions

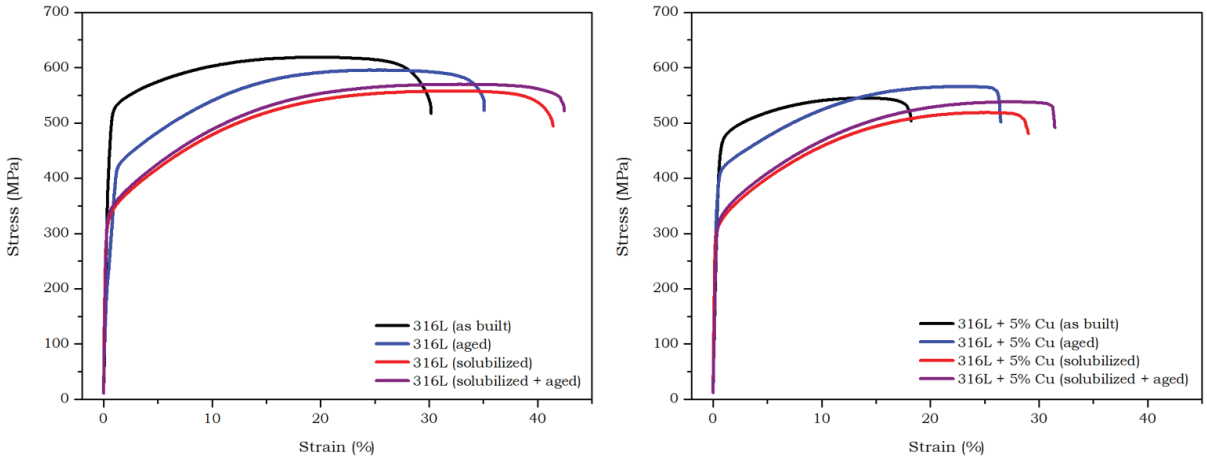

Source: Authors (2025).

Figure 96 - Yield strength, UTS and strain at UTS for 316L and 316L + 5% Cu in different heat treated conditions

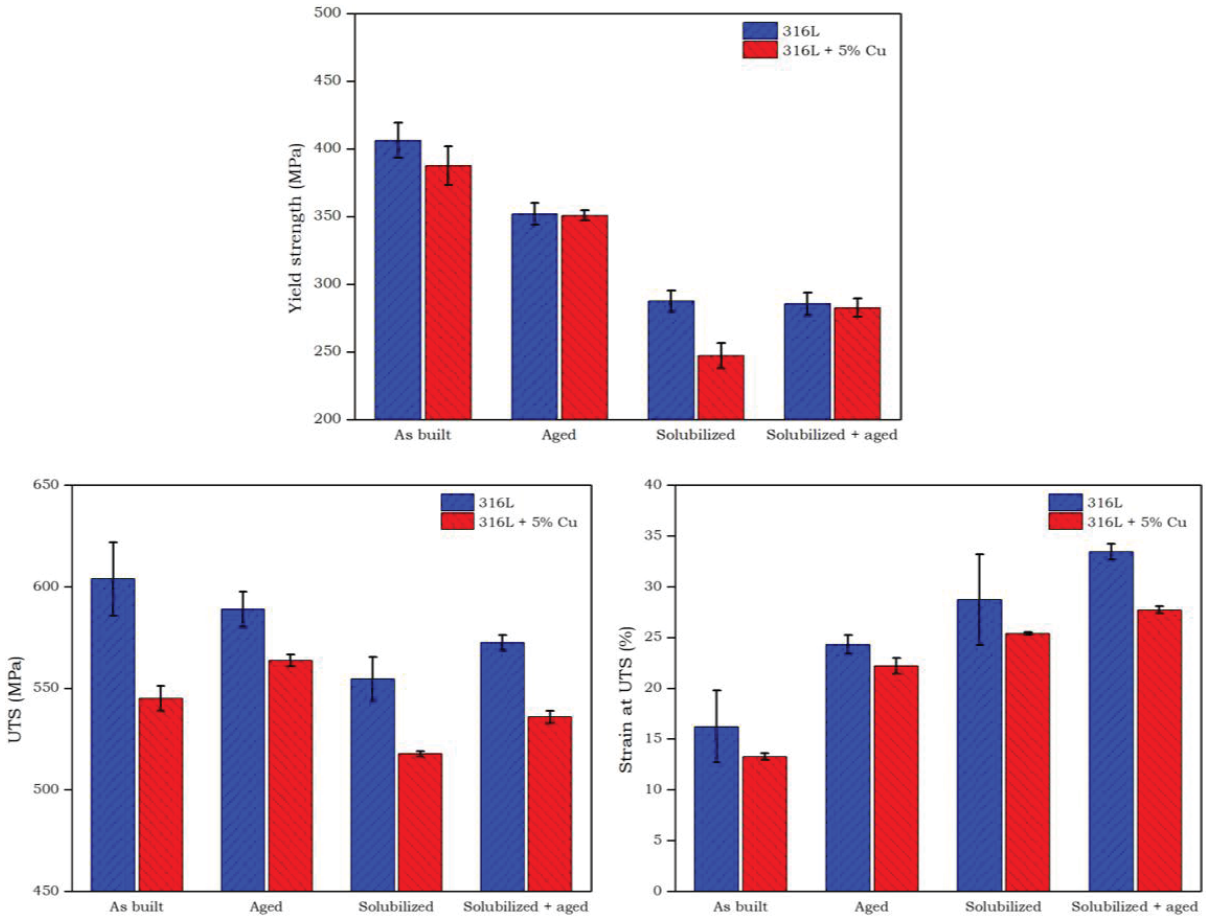

Source: Authors (2025).

Figure 97 - Macrographs of tensile specimens after testing

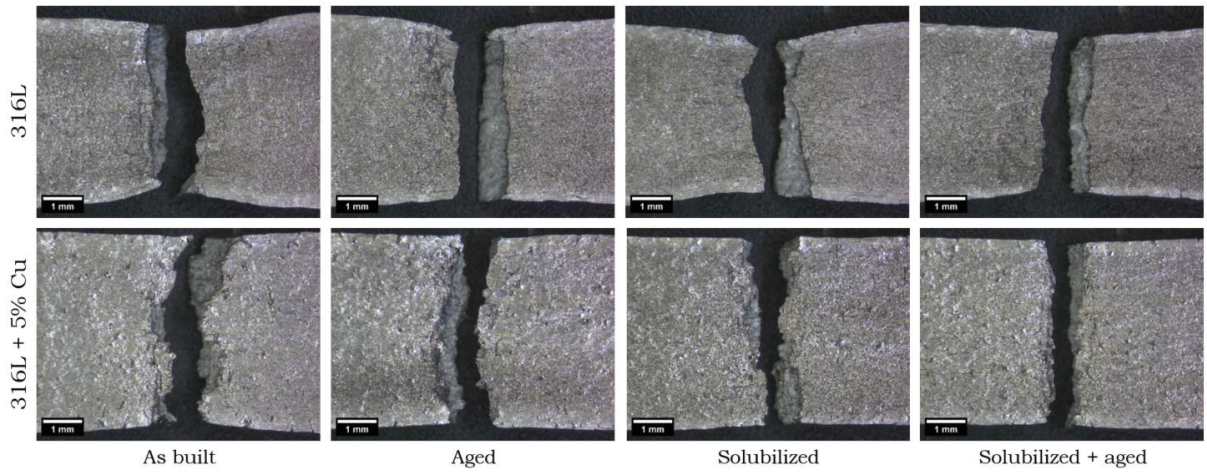

Source: Authors (2025).

Figure 98 - SEM micrographs of 316L tensile specimen fracture surface

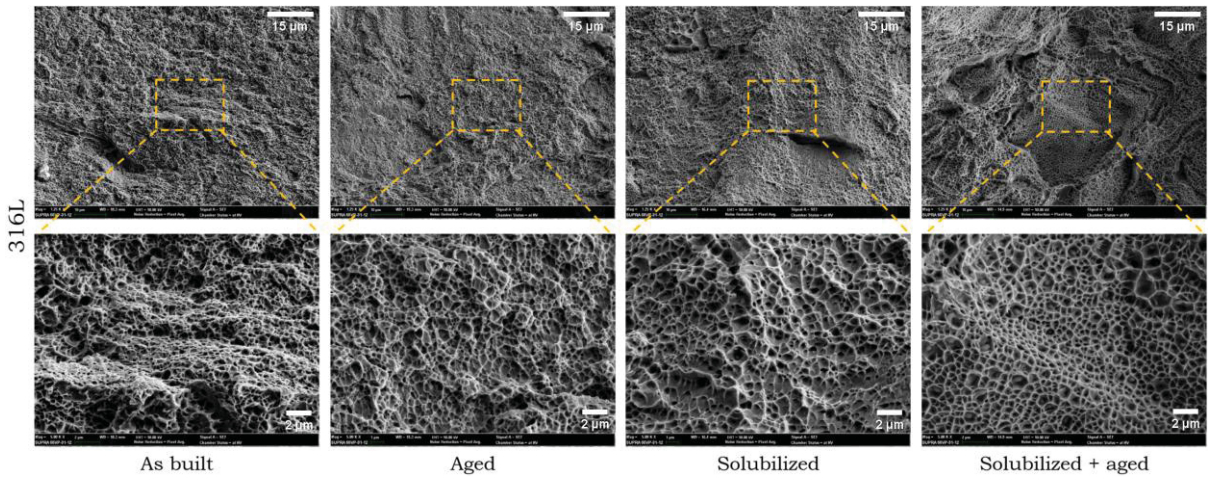

Source: Authors (2025).

Figure 99 - SEM micrographs of 316L + 5% Cu tensile specimen fracture surface

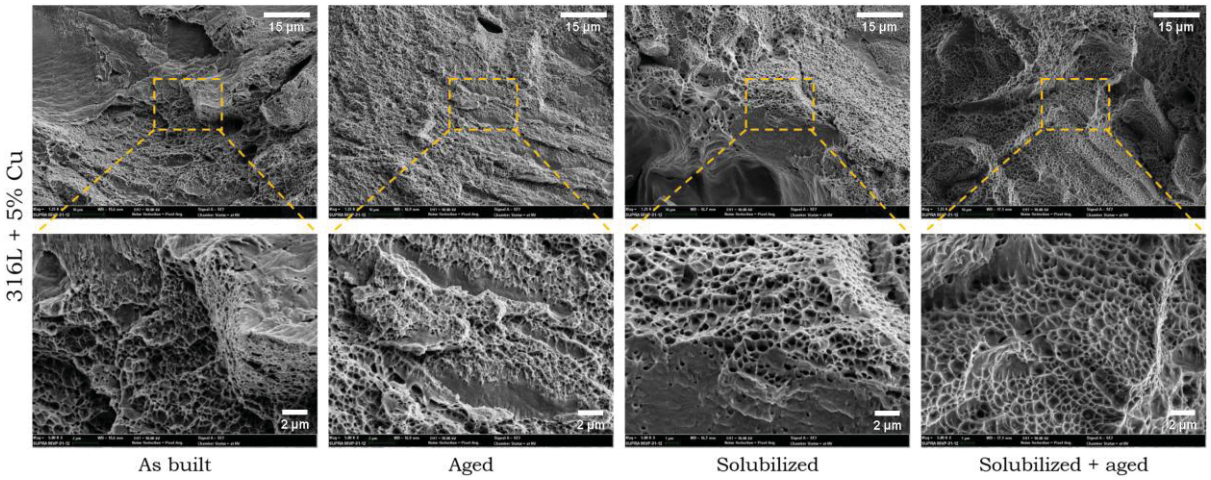

Source: Authors (2025).

Figure 100 - Coefficient of friction of heat treated L-PBF specimens

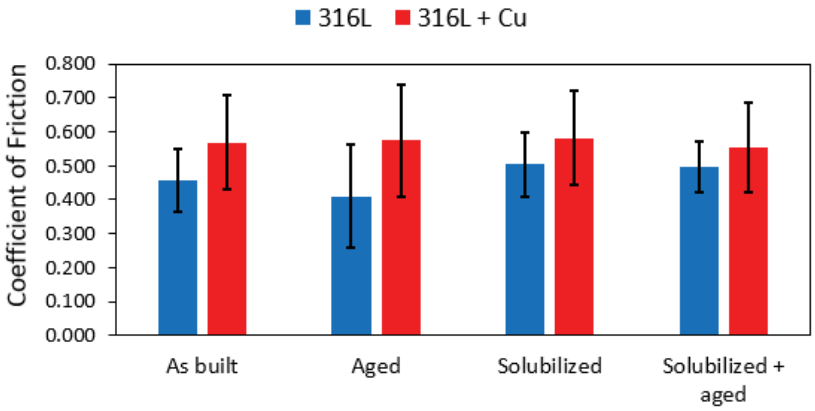

Source: Authors (2025).

Figure 101 - Wear rate of heat treated L-PBF specimens

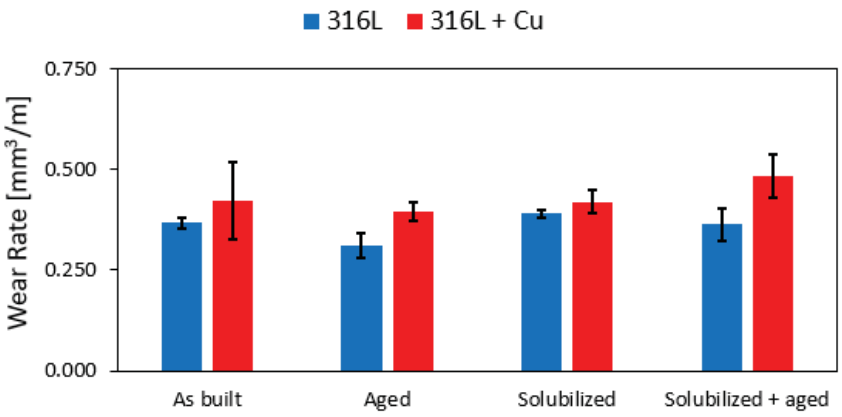

Source: Authors (2025).

APPENDIX D - MATERIALS AND EQUIPMENTS

Table 38 present a short list of materials and suppliers used in this work.

Table 38 - List of materials and suppliers

Material	Size	Supplier
AISI 316L powders	85 - 150 µm	Höganäs
	20 - 49 µm	Carpenter Additive
Cu powders	89 - 143 µm	Höganäs
	16 - 44 µm	Carpenter Additive
Cu nanoparticles	500 nm	Skyspring Nanomaterials
CuO nanoparticles	40 nm	Skyspring Nanomaterials

Source: Authors (2025).

Table 39 and Table 40 present a non-exhaustive list of techniques and equipment used during the experimental development of this thesis. UFPR is in Curitiba, Instituto Senai de Inovação em Processamento a Laser (ISI Laser) is in Joinville, and University of Birmingham (UoB) is in Birmingham, United Kingdom.

Table 39 - List of techniques, equipment and location - part 1

Technique	Equipment	Location
Plasma Transferred Arc	PTA Starweld 300	UFPR
Laser Powder Bed Fusion	Concept Laser M2	UoB
Optical Microscopy	Olympus BX51M	UFPR
	Zeiss Axio M2M	ISI Laser
Confocal Laser Microscopy	Olympus LEXT OLS4000	UFPR
Optical Stereoscopy	Zeiss V8	ISI Laser
Scanning Electron Microscopy	ThermoFisher Phenom	ISI Laser
	Zeiss Supra 55VP	ISI Laser
	ThermoScientific Apreo 2C	UoB
Energy Dispersive Spectroscopy	Brucker Quantax	ISI Laser
	Brucker Quantax	UoB

Source: Authors (2025).

Table 40 - List of techniques, equipment and location - part 2

Electron Backscatter Diffraction	Jeol JSM-7000F	UoB
Microhardness indenter	Anton Paar MHT	UFPR
	Wilson 402 MVD	ISI Laser
	Buhler	UoB
Tribometer	Anton Paar THT	UFPR
X-ray fluorescence	Shimadzu EDX-80HS	UFPR
X-ray diffraction	Shimadzu XRD-7000	UFPR
	Proto AXRD Benchtop	UoB
Dynamic Image Analysis	Particle Insight	ISI Laser
Particle Size Analysis	Microtrac MRB Flowsync	UoB
Universal Testing Machine	ZWICK/ROELL Zmart.Pro	UoB

Source: Authors (2025).

APPENDIX E - SCIENTIFIC OUTPUT

1. Academic Exchange

- **Sandwich doctorate period at the University of Birmingham, United Kingdom,** under the supervision of Professor Moataz M. Attallah, PhD., under the *Programa Institucional de Internacionalização* (CAPES-PrInt), between February 2024 and July 2024.

2. Scientific papers

- **Scientific paper published:** Prass, G.S.; d'Oliveira, A.S.C.M. (2023). "Processing and characterization of AISI 316L coatings modified with Cu and CuO nanoparticles". Surface and Coatings Technology (Vol. 461, p. 129465). DOI. 10.1016/j.surfcoat.2023.129465.
- **Scientific paper submitted and under review:** "Effect of Cu additions on microstructure and wear performance of AISI 316L manufactured by Plasma Transferred Arc".
- **Scientific paper planned:** "Optimization of Laser Powder Bed Fusion processing parameters for in-situ alloying 316L stainless steel with Cu".
- **Scientific paper planned:** "Impact of heat treatments on mechanical properties and wear resistance of in-situ alloyed Cu-bearing 316L stainless steel produced by Laser Powder Bed Fusion".
- **Scientific paper planned:** "Corrosion behavior and antimicrobial properties of Cu-bearing AISI 316L prepared by PTA-DED and HVOF".

3. Book chapter

- **Conference paper published as book chapter:** Prass, G.S.; Mattioli, P.W.; d'Oliveira, A.S.C.M. (2023). "Effects of PTA deposition parameters on geometry and hardness of AISI 316L single-tracks". ABCM Series on Mechanical Sciences and Engineering. COBEF 2023. Springer, Cham. DOI. 10.1007/978-3-031-43555-3_13.

4. Awards

- **Bernhard Gross Award received for the best oral presentation of Symposium U - Surface ad Engineering at the XX Brazilian Materials Research Society Meeting (SBPMat 2022):** Prass, G.S.; d'Oliveira, A.S.C.M. "Processing and characterization of AISI 316L coating reinforced with Cu and CuO nanoparticles". Foz do Iguaçu-PR. September 2022.

5. Conferences

- **Oral presentation at the 11th Brazilian Congress of Manufacturing Engineering (COBEF 2021):** Prass, G.S.; d'Oliveira, A.S.C.M. "Effect of Cu on multilayer PTA deposition of AISI 316 stainless steel". Curitiba-PR. May 2021.
- **Oral presentation at the XIX Brazilian Materials Research Society Meeting (SBPMat 2021):** Prass, G.S.; d'Oliveira, A.S.C.M. "Multilayer DED-PTA of AISI 316 stainless steel: effect of Cu addition on geometry and hardness". Foz do Iguaçu-PR. September 2021.
- **Oral presentation at the XX Brazilian Materials Research Society Meeting (SBPMat 2022):** Prass, G.S.; d'Oliveira, A.S.C.M. "Processing and characterization of AISI 316L coating reinforced with Cu and CuO nanoparticles". Foz do Iguaçu-PR. September 2022.
- **Oral presentation at the XX Brazilian Materials Research Society Meeting (SBPMat 2022):** Cruz, J.R.; Prass, G.S.; d'Oliveira, A.S.C.M. "Processing and electrochemical functionalities of 316L stainless steel coatings with copper additions". Foz do Iguaçu-PR. September 2022.
- **Poster presentation at the *Congresso Brasileiro de Engenharia e Ciência dos Materiais* (CBECiMat 2022):** Mazur, V.T.; Mazur, M.M.; Prass, G.S.; d'Oliveira, A.S.C.M. "Dispositivo de alinhamento a laser de baixo custo aplicado na manufatura aditiva por deposição direcionada de energia com plasma de arco transferido". Águas de Lindóia-SP. November 2022.
- **Oral presentation at the 12th Brazilian Congress of Manufacturing Engineering (COBEF 2023):** Prass, G.S.; Mattioli, P.W.; d'Oliveira, A.S.C.M. "Effects of PTA deposition parameters on geometry and hardness of AISI 316L single-tracks". Brasília-DF. May 2023.

- **Poster presentation at the XXI Brazilian Materials Research Society Meeting (SBPMat 2023):** Prass, G.S.; d'Oliveira, A.S.C.M. "Effect of Cu additions on the wear behavior of AISI 316L single-walls manufactured by Plasma Transferred Arc". Maceió-AL. October 2023.
- **Oral presentation at the International Congress of Mechanical Engineering (COBEM 2023):** Prass, G.S.; Chastinet, V.L.; d'Oliveira, A.S.C.M. "Characterization of nanocomposite powders for additive manufacturing". Florianópolis-SC. December 2023.